CITY UNIVERSITY LONDON

School of Engineering and Mathematical Sciences

Electrical, Electronic and Information Engineering

Development of Methodologies for the Solution of the Forward Problem in Magnetic-Field Tomography (MFT) Based on Magnetoencephalography (MEG)

Kirill Aristovich

Thesis submitted for the fulfilment of the requirements for the degree of Doctor of Philosophy of the City University London

October 2011

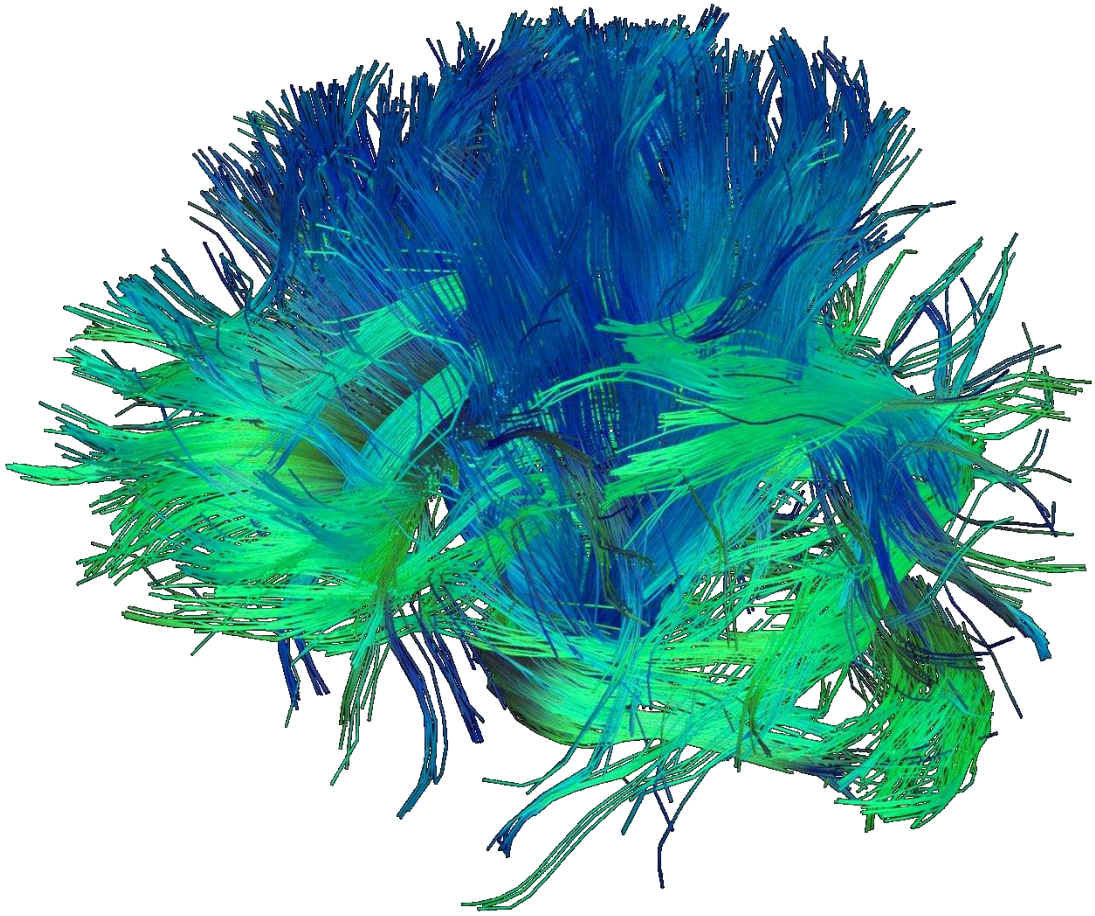

Acknowledgements

To many people who made it possible, participated, and supported this project

I would like to thank my supervisor Prof. Sanowar H. Khan who is behind the scene on every page of this report, and who was also my *Teacher* all the way through the lifetime of this project, helping me not only with actual work, but also with all other aspects of my life.

I would also like to thank all my friends and colleagues at City University for their support and attention. They made this project stayed on track filling me up with loads of brilliant ideas.

And finally I would like to specifically thank all my family. Particularly my wife who sacrificed a lot in order to let me make and finalize this project, and my parents who were so helpful, supportive, and patient to me.

Abstract

The prime topic of research presented in this report is the development and validation of methodologies for the solution of the forward problem in Magnetic field Tomography based on Magnetoencephalography. Throughout the report full aspects of the accurate solution are discussed, including the development of algorithms and methods for realistic brain model, development of realistic neuronal source, computational approaches, and validation techniques.

Every delivered methodology is tested and analyzed in terms of mathematical and computational errors. Optimizations required for error minimization are performed and discussed. Presented techniques are successfully integrated together for different test problems. Results were compared to experimental data where possible for the most of calculated cases.

Designed human brain model reconstruction algorithms and techniques, which are based on MRI (Magnetic Resonance Imaging) modality, are proved to be the most accurate among existing in terms of geometrical and material properties. Error estimations and algorithm structure delivers the resolution of the model to be the same as practical imaging resolution of the MRI equipment (for presented case was less than 1mm).

Novel neuronal source modelling approach was also presented with partial experimental validation showing improved results in comparison to all existing methods. At the same time developed mathematical basis for practical realization of discussed approach allows computer simulations of any known neuronal formation. Also it is the most suitable method for Finite Element Method (FEM) which was proved to be the best computer solver for complex bio-electrical problems.

The mathematical structure for Inverse problem solution which is based on integrated human brain modelling technique and neuronal source modelling approach is delivered and briefly discussed.

In the concluding part of the report the practical application case of developed techniques is performed and discussed.

Table of Contents

List of Figures

List of Tables

Chapter 1

Introduction

1.1 Preface

The term magnetic-field tomography (MFT) refers to a relatively new imaging modality which involves localization and subsequent imaging of active areas in the brain by measuring the extremely weak neuromagnetic fields (10–100 fT) produced by neural currents in these areas associated with cognitive processing (magnetoencephalogram). This approach, called the magnetoencephalography (MEG) technique (recording of magnetic fields produced by electrical activity in the brain), is the only truly non-invasive method which could provide information about functional brain activity.

The MFT, based on MEG data, would provide images of the brain “at work” and, as such, could have major implications for neurology and neuropsychiatry, in general, and new instrumentation for diagnosis in particular. Compared to other imaging modalities [e.g., computed tomography (CT), positron emission tomography (PET), single photon emission computed tomography (SPECT), magnetic resonance imaging (MRI)], the MEG technique is the only imaging modality that combines high temporal with high spatial resolution.

Due to its advanced properties, MEG can be used in the wide range of clinical applications which requires very precise knowledge about working human brain. It was shown to have enormous potential to be used in the study of stroke, autism, schizophrenia, Alzheimer's disease, Parkinson's disease, and cognitive and mental disorders.

Similar to any other tomographic technique, MFT involves the solution of two distinct problems: 1) the forward problem of calculating the magnetic-field distribution from

known generators (sources) in the brain and 2) the inverse problem of localizing and imaging the generators by using MEG data measured around the head, and the data obtained from the forward solution. Besides, an accurate solution of the forward problem has implications for design, configuration, and placement of superconducting quantum interference device (SQUID) sensors, used to measure the neuromagnetic fields around the head, and which constitute the sensing subsystem of the MFT system. Thus, the successful solution of the inverse problem and, hence, the effectiveness of the MFT as a whole is very much dependent upon the accurate solution of the forward problem.

Despite the growing interest of MEG application in clinical studies, the main research activity is focusing on inverse problem solution in order to accelerate the beginning of successful clinical implementation. However, recent studies highlighted the growing gap between the accuracy of forward problem solution and inverse solution methods. None of the existing methodologies can satisfy the accuracy requirements which are dictated by the theoretical assumptions underlying already existing methods of the inverse problem solution.

At the same time new hardware and components were introduced by various MEG equipment manufacturers. A number of these components allow improving the accuracy of acquiring data and measurements of the magnetic fields around the human head, and reducing background noise. All together in combination with the improving signal processing methodologies it also illuminates the need of improvement for the methodologies of the forward problem solution.

This work presents the complete set of methodologies for accurate solution of the forward problem via incorporating realistic brain geometry and inhomogeneous anisotropic material properties coupled with the new realistic neuronal current source approximations.

Each of described methods is delivered on the basis of realistic physical assumptions and carefully tested with the comparison to real data obtained by various laboratories across the world.

As a result of this research, the most accurate among existing models for the considered propose 3D mathematical model of the brain was developed and detailed magnetic field distributions for known neuronal current sources were computed.

The number of computational techniques, data visualisation tools, image processing algorithms, advanced geometrical modelling techniques, and data processing software were also developed and briefly discussed in associated chapters of this report.

1.2 Aims and Objectives

Based on the existing research problems discovered during the literature survey (see Chapter 2) and on-going research activity observation the following aims can be formulated:

Aim 1: Improve the methodologies for the human brain modelling for forward solution MFT based on MEG. This aim refers to the following objectives:

1) Develop and test the realistic brain model according to fundamental physiological, biological and geometrical basis
2) Create algorithms and procedures for automatic brain model reconstruction with required optimization of parameters and accuracy. Developed methodologies must be patient (subject) specific

Aim 2: Develop methodologies for neuronal current source modelling for forward and inverse problem in MFT based on MEG. Objectives related to this aim are:

1) Create realistic neuronal source model for MEG forward problem calculations based on the bio-electro-physical underlying assumptions
2) Develop algorithms and procedures for implementation of the neuronal current source model into the human brain model for the full branch of possible problems related to the forward problem solution
3) Prove that developed neuronal source model can be used for inverse problem solution

Aim 3: Approximate possible errors of developed methodologies and experimentally validate them. Specified aim leads to the following list of objectives:

1) Obtain optimal modelling and solution parameters for required accuracy
2) Achieve the required computational accuracy using developed model for the simple testing solution
3) Test realistic brain model in combination with the realistic neuronal source model (also relates to aims 2 and 3)

4) Simulate known realistic neuronal source, obtained from clinical studies and compare the results of simulation with real magnetic field, obtained from clinical MEG tomography

Chapter 2

Literature Survey

2.1 History of Magnetoencephalography (MEG)

The history of non-invasive medical neuroimaging began with the radiographic technique introduction by Professor Wilhelm Conrad Roentgen [1]. It was a great step towards understanding of how human brain works and at that time the only non-invasive method of clinical studies and monitoring. The idea of radiographic technique is based on the evaluation of internal body images using the X-ray. This technique could provide these pictures for internal human body and therefore the brain because of difference in absorption of X-ray in different tissues. Unfortunately human brain is almost entirely composed of soft tissues that are not radio-opaque, and it is almost impossible to see the structure of the tissues inside the brain for adult people. This is also true for the most brain abnormalities, especially those ones which do not affect density changes. At the same time radiographic technique is very dangerous due to high level of radiation dose which patient receives when doing X-ray scan.

Later, in 1918 the American neurosurgeon Walter Dandy introduced the venticulography as a novel approach to display entire ventricular system. Internal images were obtained by injection of filtered air into one or both lateral ventricles of the brain via small trephine holes drilled in the skull under local anesthesia. This approach was pseudo-noninvasive, as a whole process of imaging itself was based on radiographic technique, and apart from drilling holes there were no damaging of the brain. This method was extremely dangerous though and caused different types of irreversible brain damages. Nevertheless the surgical information given by this method was often remarkably precise and greatly enlarged the capabilities and accuracy of neurosurgical treatment.

Modern noninvasive medical neuroimaging started with the development of cerebral angiography [2]. This method is based on injection of the radioactive contrast into the blood system, and then detection of the traces produced by this contrast. This technique is used nowadays with slight modification of processes and allows very accurate imaging of blood vessels in the entire human brain.

Computerized Tomography (CT) and Magnetic Resonance Imaging (MRI), together with functional MRI, Positron-Emission Tomography (PET), and Single Photon Emission Computed Tomography (SPECT) are the main established methods which nowadays are used to provide noninvasive brain scanning, but all of them have their limitations, practical and theoretical. CT does not provide enough accuracy and it is relatively destructive. MRI has low spatial resolution, which cannot be improved theoretically due to fundamental limitations. PET and SPECT are extremely destructive because of the radioactive contrast.

There is also a technique have been developed in the field of combining these procedures [3] in order to get more accurate images and make described modalities less dangerous. The combination of several methods implemented together to work simultaneously is called Multimodal Neuroimaging.

At present there are only two known fundamental non-invasive ways of measuring working brain activity. First method is based on physiological processes of increasing element adsorption by the working cells. All techniques involving this method are based on the measuring of contrast concentration changes and thus evaluating the areas of current brain activity. This idea works perfectly for macroscopic imaging, however has poor spatial accuracy and sufficient limitations in temporal resolution.

Another class of methods is based on the measuring self-induced neuronal electric or magnetic fields. Due to the fact that all meaningful processes inside the brain are electromagnetic, these modalities theoretically allow getting full information about brain activity without theoretical (but with a lot of practical) limitations on time and spatial resolutions. The electrical activity of neuronal cells can be obtained using Electroencephalography (EEG) technique. EEG involves placing the electrodes around the head and measuring electric potentials in each electrode. Obtained

electrode signal however consists of not only the electrical signal of neuronal activity, but also contains entire intercellular eddy currents and external noise.

The limitations of EEG have been successfully passed with the development of Magnetoencephalography (MEG) method and the Magnetic-Field Tomography (MFT) related to it. As mentioned earlier in Chapter 1, MEG deals with measuring the neuromagnetic fields produced by neural currents in these areas associated with cognitive processing.

First magnetoencephalogram was measured by University of Illinois physicist David Cohen in 1968 [4] using only a copper induction coil as the magnetic field detector. The measurements were made in a magnetically shielded room in order to reduce the magnetic background noise. However, the insensitivity of this detector resulted in poor, noisy MEG signals, which were difficult to use. Then later he built a better shielded room, and used one of the first Superconductive Quantum Interference Devices (SQUID), just developed by James E. Zimmerman, a researcher at Ford Motor Company [5] to measure the MEG again [4]. This time the signals were almost as clear as an EEG. Obtained results stimulated the interest of physicists who had begun looking for uses of SQUIDs.

Nowadays MEG is the most promising technique (it is currently on the experimental stage) because it is the only imaging modality that combines high temporal with high spatial resolution. As mentioned before, it is relatively young and not fully developed yet mainly due to lack of understanding of electromagnetic processes involved in cognitive activity.

Thus, the successful solution of the inverse problem and, hence, the effectiveness of the MFT as a whole is very much dependent upon the accurate solution of the forward problem.

2.2 Principles of MEG

Human brain consists of the assembly of neurons, which generate electrical activity (electrical impulses) and exchange this activity with each other [6]. The structure of the single neuron is shown in Figure 2.2-1. Single neuron consists of a cell body which is the central part, axons, dendrites, and synaptic terminals. Neuronal axon is the main electrical signal provider. Dendrites are the signal receivers, and synaptic transmitters are playing electrochemical neuron-to-neuron signal exchange role.

Neurons are generally combined into the formations. Clustered formations of the neurons in cerebral cortex are also known as neuroclusters. All together they form neo-cortex, which is so-called grey matter. Grey matter is the thin (2-3mm [7]) layer which covers the brain volume and thought to be the part of the brain responsible for cognitive activity. The internal part of the brain is called white matter. White matter mostly consists of neuronal chains called neurotracts or fibertracts as they form a fiber structure. There are two types of fibertracts depending on the surrounding cells: myelinated and unmyelinated. Myelinated tracts consist of neurons which are surrounded by myelin shield. Myelin acts as ion source protector and at the same time provides mineral's supply to the neuron. Unmyelinated fibertracts are mostly located in very packed areas of the nervous system (such as areas which are close to cerebral cortex or cerebellum).

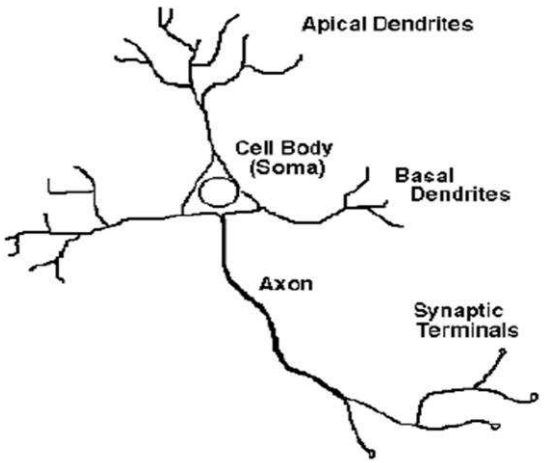

Figure 2.2-1. Single neuron structure

Due to the intracellular and extracellular electrochemical activity of neuronal cell and mechanisms of electric impulses propagation neurons act as magnetic and electric fields generators. Magnetic field produced by neuronal activity can be measured and associated to bio-chemical activity. Collected data could provide essential information about initial electrical activity, such as position of activated neurons and internal current paths between different brain zones.

As described before, MEG use the SQUID sensors positioned around the human head in order to perform required measurements. Obtained information then is meant to be processed and interpreted by medics according to physiological and personal structures for particular subject. Basic MEG-based magnetic field tomography scheme is demonstrated in Figure 2.2-2.

The outline and structure of SQUID sensor is shown in Figure 2.2-3. Main constructive element of the sensor is the coil which is made of superconductive material. This coil is sensible to external magnetic field according to the Faraday's Law [8]. Superconductivity effect in collaboration with high quality shielding from the external noises is used for detection in order to improve the quality of recordings (magnetic fields produced by neuronal activity are very weak).

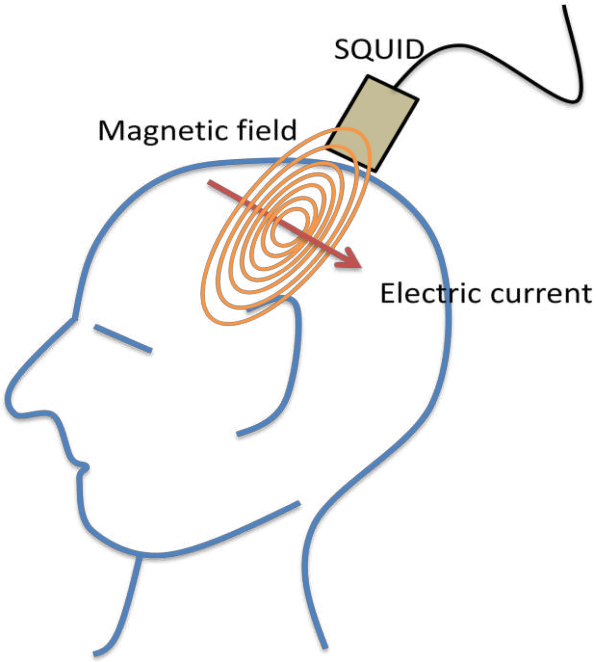

Figure 2.2-2. Measuring MEG

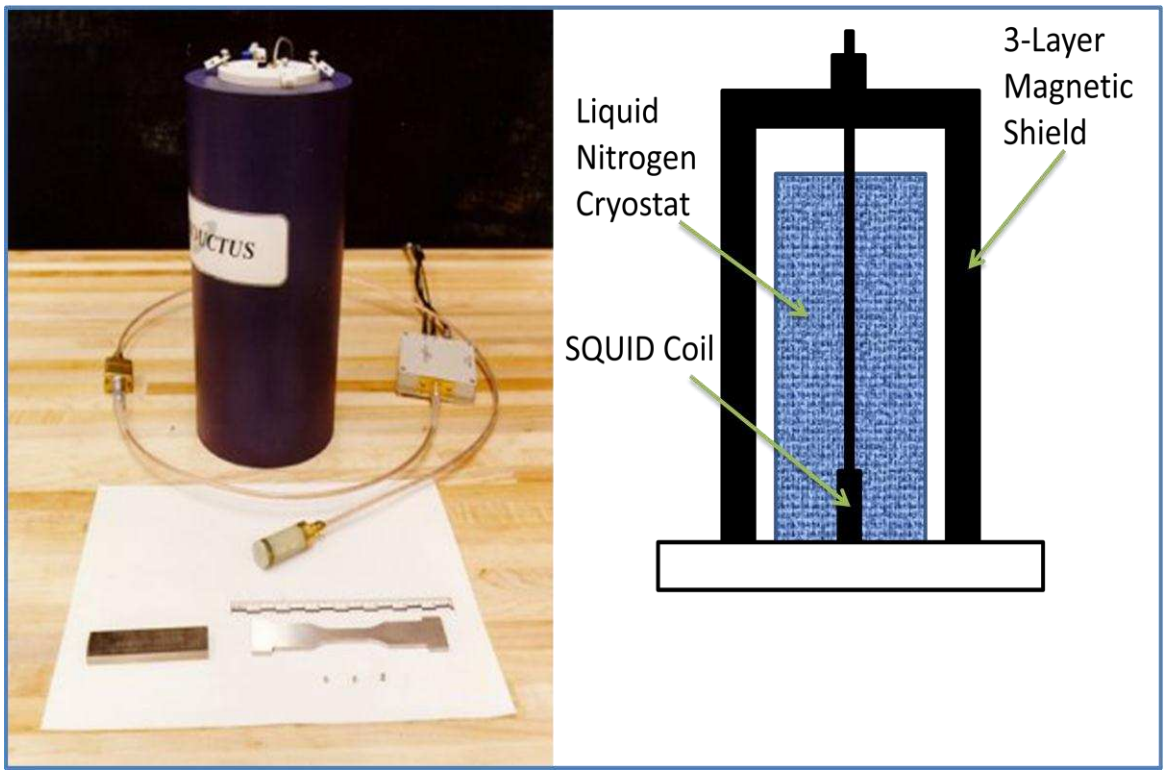

Figure 2.2-3. SQUID sensor device

The magnetic superconductive coil itself is not simple and is based on state-of-the-art technology which involves inclusion of complex superconductive wires in optimally-shaped superconductive metal loop. Example of modern coil could be seen in Figure 2.2-4 [9]. Generally MEG measurements involve information processing from several sensors placed around the head of the analyzed subject. It is now convenient to use about 140-300 sensors [10] in order to get acceptable accuracy for the following signal processing procedure. However the number of electrodes and its placements are still open questions for researchers. One of the relatively new MEG machine can be seen in Figure 2.2-5. The illustrative layout of SQUID sensors within this particular machine can be found in Figure 2.2-6 [11].

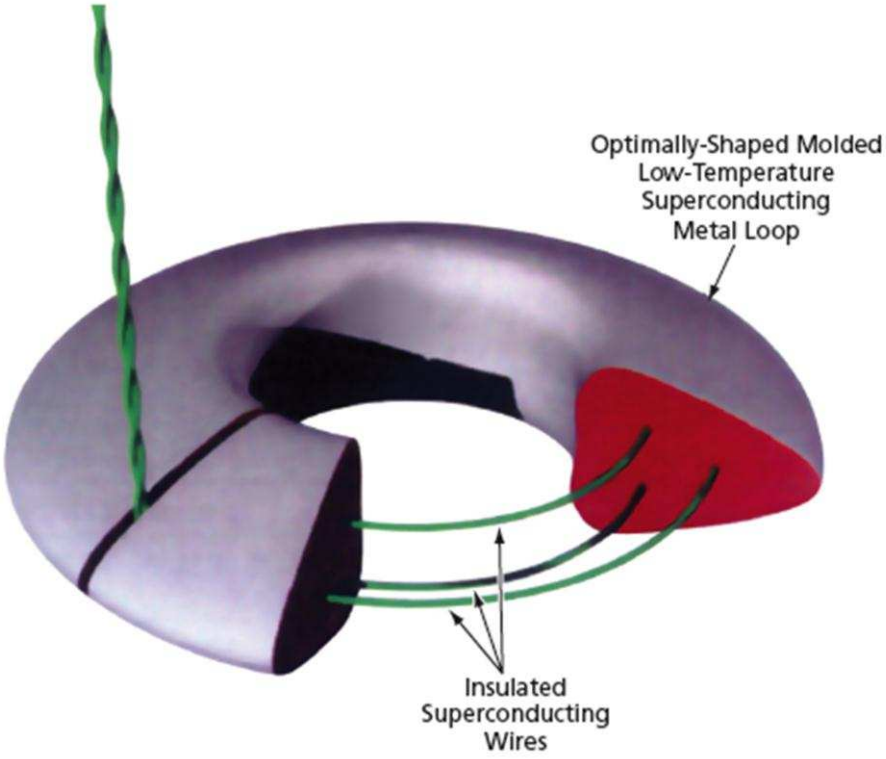

Figure 2.2-4. Modern coil for SQUID [9]

Figure 2.2-5. MEG tomography machine [11]

Figure 2.2-6. MEG tomography machine SQUID sensors layout [11]

2.3 Basics of the Forward Problem

Like every other tomography technique, MEG involves solution of two different problems, which are both important for understanding of the relations between measured data and actual physical processes, actual hardware manufacturing, data processing, results interpretation, and clinical applications. The idea of forward and inverse problems specification is illustrated in Figure 2.3-1.

The forward problem generally must be solved prior to any further processing. This helps exploring possible practical outcome from the theoretical assumptions, understanding the relation between underlying assumptions and collected data, and which is more important, recognizing possible limitations and accuracy of the method. Inverse problem, in opposite, solves the question of practical reconstruction of the required data with the help of collected measurements and forward problem solution. In case of MEG tomography, forward problem is formulated in general using the following proposals: there is known information about active parts of the brain obtained from the medical studies. This information could be retransferred to the specific neuronal current sources within the human brain. The problem requires

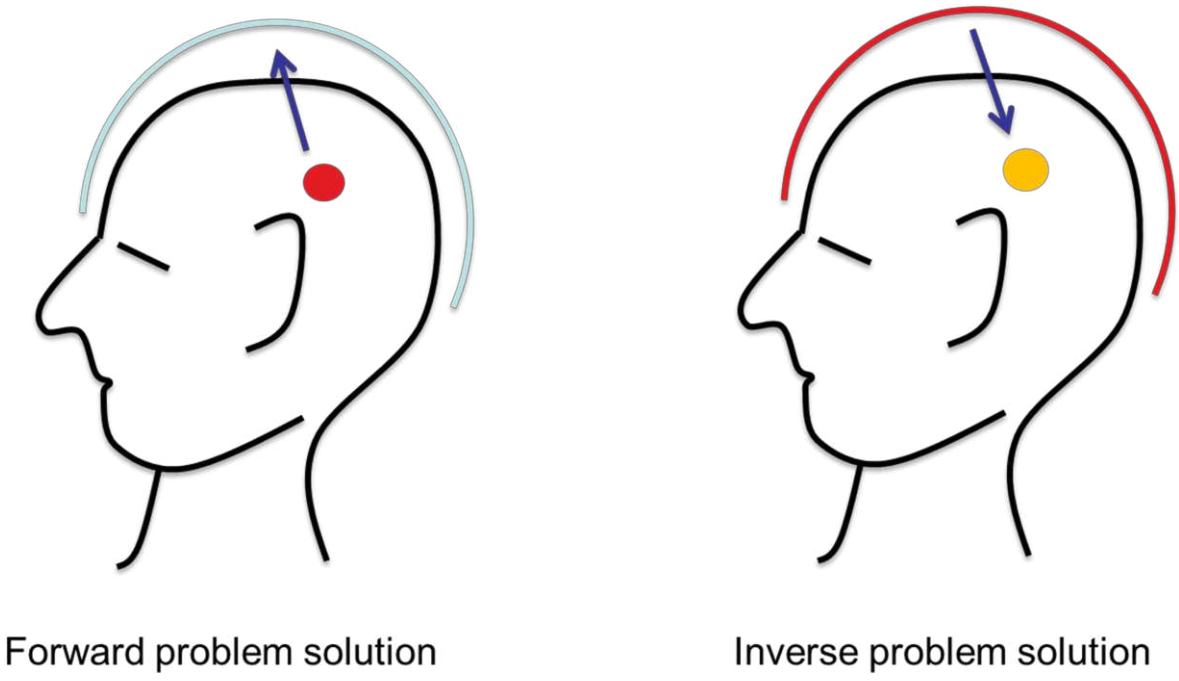

Figure 2.3-1. Illustration of the forward and inverse problems

obtaining magnetic fields around the head as much close to reality as possible. Basically, forward problem in case of MEG includes simulation of whole electromagnetic processes within the head and validation of the results with the experimental data. This simulation requires performing of all range of engineering routines, from the very abstract mathematical problem formulation to the complex numerical analysis, optimization, accuracy estimation etc.

In order to create a good basis for inverse problem solution it is important do discover all possible ways of mathematical simulation and to obtain the best possible way of modelling for such complex process. Successful forward problem solution allows optimization in terms of accuracy, time of computation, practical realization and cost-effectiveness of the required methodologies and apparatus [12]. There are many different ways of doing so (as shown in next Section) and one of the main proposes of this study is to choose or create the more reliable one from the very beginning.

In Figure 2.3-2 the main procedure for forward and inverse problem solution is schematically shown via routine blocks. First step is the mathematical problem formulation and the right solution method discovery (which is essential as was discussed before). Then the routine continues with the creation of appropriate model (mathematical representation) for considering physical object, which is the human brain in case of MEG tomography. After that the neuronal source model must be created and implemented into the model of the object. The next step involves required simulations to be done and results to be obtained. If resulting detected field around the object do not match the experimental field measured with the same conditions with required accuracy, the optimization procedure must be started and required improvements to the object model or source model must be performed. The basic mathematical structure must be changed In case of impossibility of such improvement, and routine starts from the beginning.

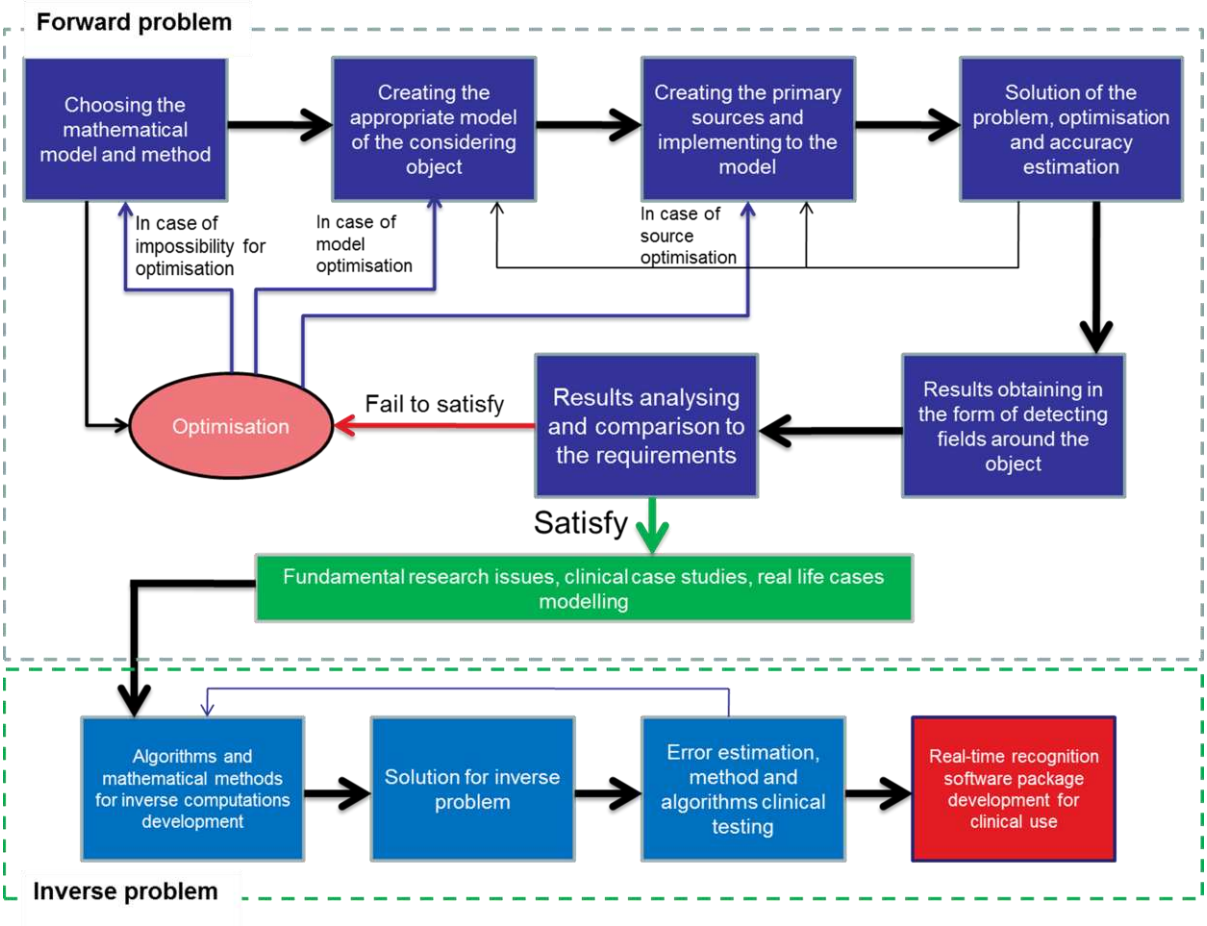

Figure 2.3-2. Forward and inverse problems schematic view

Forward model is ready for investigation after all computational requirements are achieved. Initial study usually involves realistic simulation tests. This is essential in order to get methodology restrictions and computational restrictions. Also forward modelling tests are required for understanding fundamental theory of processes, which take place within human brain. A part of investigation activity is concentrated in the field of exploring the mechanisms of different diseases such as epilepsy, Parkinson's disease, etc. Huge research interest is also associated with the mechanisms of the human thinking process as it is still unknown. It is also very important to have a right computational model with the ability of simulations to be performed for the different neuronal sources activation approaches. Thus for all of research activity which is based on the forward problem it is essential to be sure that forward model has good predictability and accuracy.

As mentioned before the significant part of research activity which is based on forward modelling is focused on the brain matter disorders. Forward model must predict the electromagnetic processes which take place inside the degraded human brain (without one or many functional parts). The most known case of such brain matter disorder is Alzheimer disease. The brain of the subject affected with disease has strongly degenerative matter. There is a huge interest in understanding the way that signals are processed inside neuronal structure of the brain degraded by this disease. Successful forward problem solution in combination with the latest imaging technologies could help create the fundamental structure for further experimental investigations.

Forward problem in application to MEG tomography consists of three fundamental concepts (first three boxes in Figure 2.3-2), that has to be defined before starting any simulations and investigations. First of all it is the type of the brain model, which would be considered in the analysis in form of modeled physical object. It can have geometrical representation (spherical, realistic-shaped, etc.), or some abstract mathematical interpretation and should satisfy the forward problem conditions. Second concept is the type of neuronal current source which is used as an electrical source for forward model (existing approaches to current source modelling is shown in next chapter). Finally, it is essential to choose computational method for solving the appropriate system of mathematical equations followed from the mathematical model.

The mathematical structure of the forward MEG problem is fully determined by the physical Maxwell equations, discussed in Chapter 3, therefore the first box in Figure 2.3-2 for MEG involves only simplification of mathematical model and investigation of the solution method. The requirements for the human brain model and neuronal source model (such as geometrical and material accuracy) are much stronger than solution method parameters (such as time of computation or cost-effectiveness). Hence in case of MEG the brain model and source are determined first and then the right solution method is revised.

All the previous work found in literature is accurately shown in next Section, which is structured with respect to three fundamental concepts discussed before. All

previously discovered methods and forward problem solutions are also grouped and the very brief summary of each group is discussed.

2.4 Literature Survey

2.4.1 Models of the Human Brain

The importance of accurate human brain reconstruction is followed from the Maxwell equations and it is one of the most discussed topics inside the scientific society related to the tomography problems. Great influence of even small particular disturbance of the input data on the final solution is specifically mentioned in wide range of papers [13-18]. However, all possible brain models will be revised in this paragraph in order to show the historical developing and possible basic engineering solutions for solving this problem.

2.4.1.1 Spherical and Ellipsoidal Models

Early stages of research related to MEG tomography forward problem were quite basic due to the lack of the computational resources. The aim of forward modelling at that time was to understand the possible ways of obtaining the solution on primitive level. Most of the methods which were used during the studies are formulated in general with the simple example which is placed in order to illustrate the method and to get engineering approximation of the solution.

The spherical brain model was considered as a good computational approximation at the very beginning of the MFT development. Spherical models in papers [19-27] showed the limitations of MEG technique in general and were used to obtain the preliminary range of possible ways to improve the computational technique and the solution method. However, the results obtained with spherical models were very inaccurate, and it was shown [17, 18, 20, 28-32] that they cannot be used to calculate magnetic fields around the head in any case of practical application.

The simplest possible spherical model is homogeneous (in terms of modelling properties, electrical conductivity and magnetic permeability) solid sphere (Figure 2.4-1). With this type of model, mathematical equations underlying the modelling can be easily solved and this process does not require any additional computer computations. This model was used in papers [20, 33], where the very basic

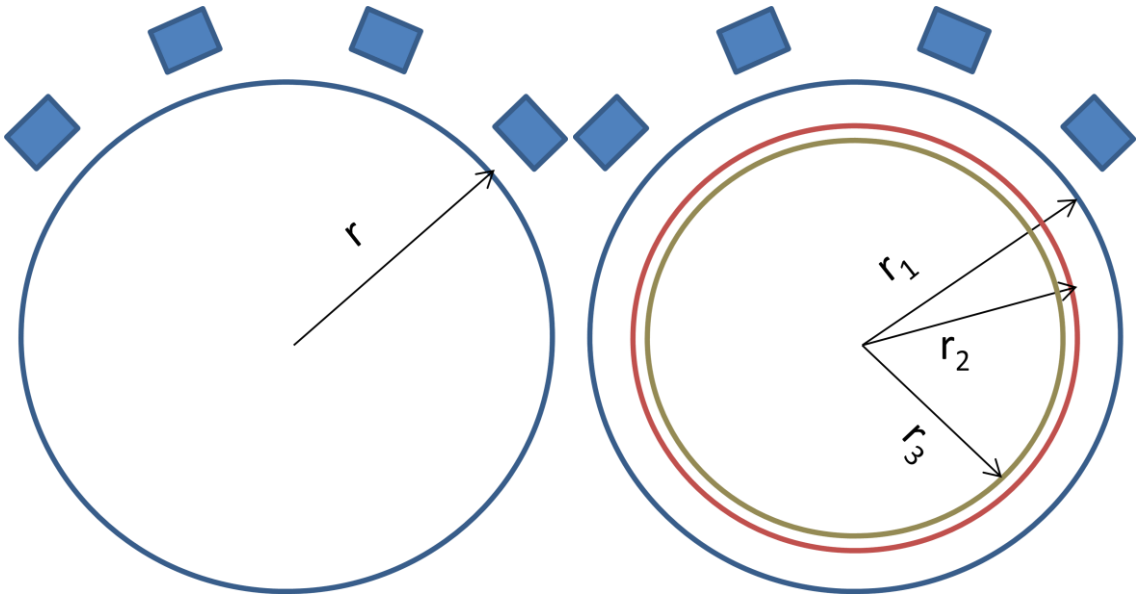

Figure 2.4-1. Spherical models of the human head, Homogeneous solid sphere (left) and layered sphere with scull (r_1), grey (r_2) and white (r_3) matter representation.

resulting magnetic fields were obtained and the direction of improvement work has been set up. The solutions of the problem, as stated before, were far beyond the limits of accuracy [22].

The layered spherical brain model has been developed as an improvement to the single solid sphere. Each single layer of the model represents different tissues of the physical human head. There could be different number of layers, but the most common is 3 layer schemes with scull bone, white and grey matter subdivision (Figure 2.4-1).

The layered spherical model shows almost the same poor accuracy of the solution as a homogeneous one and it was shown [22] that the main influence on the accuracy is the geometrical shape of the head, which is far away from spherical in reality. The first attempt of the shape improvement was made by assuming the head to be an ellipsoid [29, 34, 35]. This was quite reasonable engineering improvement considering the fact that elliptical model still allows analytical computation of the magnetic field around the head. Also ellipsoidal model gave quite a few improvements to the final forward problem solution. However the resulting magnetic field distributions were found not matching any reasonable limit of accuracy. The main weak point of any 'fit-in' geometry model is that the real surfaces of the grey

and white matter of the brain are much more complex in terms of geometry than any smooth-surfaced structure. In order to understand this complexity and difference with the ellipsoid let us consider the following example.

Imagine the flat A4-formatted piece of paper. If wrinkled (see Figure 2.4-2) this object can visually represent the brain surface layout with approximately the same geometrical level of complexity. The external shape of wrinkled sheet can be approximated by ellipsoid. The area of approximating elliptical body will be more than 6 times less than the initial area of A4. Thus even rough estimation shows the difference of the resulting solution to be more than 6 times. In reality the difference can be more than 20 times (mostly due to the hidden high-packed surface areas such as cerebellum). So even if one needs to calculate the simple area of the surface for grey matter, in reality this is much bigger than in case of spherical or ellipsoidal shape.

Studies show that all sufficient matter transition regions are very important during the simulations [30]. Therefore the realistic shape of the model is strongly required for forward problem solution. The improvement and sufficient increase of the accuracy due to realistic shape modelling is observed in next paragraph.

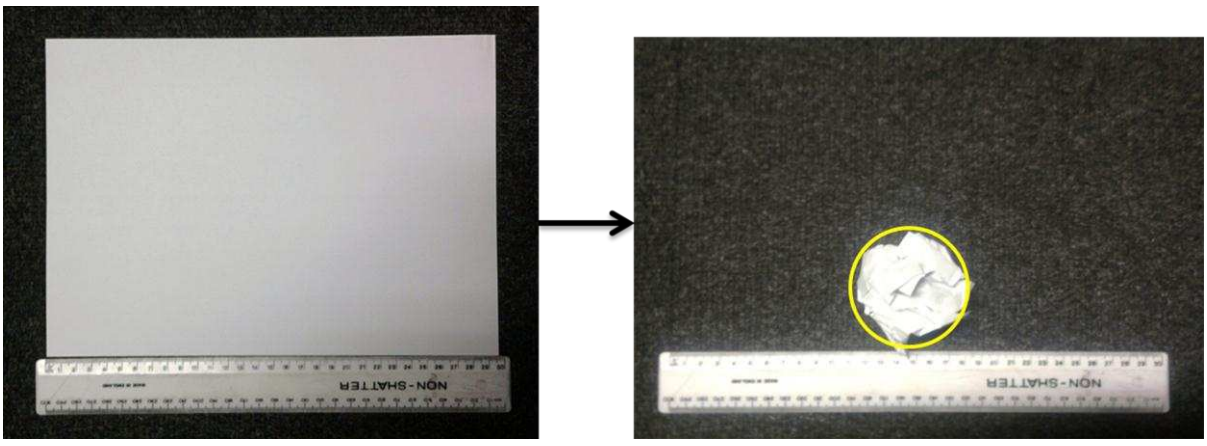

Figure 2.4-2. Surface difference example. Flat sheet (Left) has surface area of more than 6 times bigger than the area of the ellipsoid approximating the same wrinkled sheet (Right)

2.4.1.2 Realistically Shaped Brain Models

Increased computational resources and computer evolution allow solving the problem in constructing realistically shaped brain models. In paper [20] the influence of the human brain shape was first introduced and studied. The strong difference between spherical and realistically shaped models for MEG forward simulations was shown. Also the importance of complexity of the brain external structure was discovered. The model itself is illustrated in Figure 2.4-3. Despite the fact that even this shape is far beyond the realistic, the difference between this and elliptical model was sufficient enough to propose realistic brain model as gold standard for such simulations. Further investigations showed even more the importance of the brain geometrical shape being accurately modeled. In work [18] the internal structure of the brain tissues was found as one of the main influence on the accuracy of the solution. The main advantage of the work was in the comparison of the simulating results with experimental data. The magnetic field mapping indicated similarity of the magnetic field outline to the maps obtained from experiment. However the numerical values were found not matching experimental ones.

At the same time, the complexity of the tissue structures and difference in the conductivity of different tissues required more complex models being developed not only from geometrical modelling point of view, but also with appropriate material properties consideration. In works [17, 32, 36] the realistic geometrical brain shape which is closer to actual than ever before had been developed. The model was obtained with the tissue segmentation technique allowing matching at least external

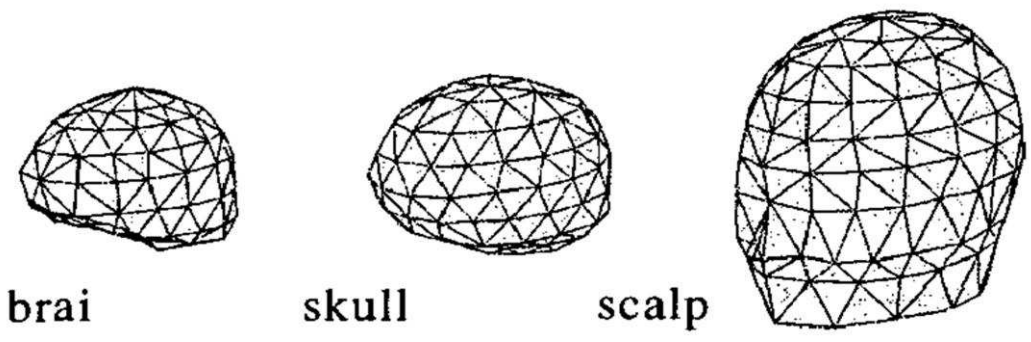

Figure 2.4-3. Early realistic shaped brain model [17]

geometry of the grey matter. At the same time different material properties have been applied to the parts of the model corresponding to grey, white matter and cerebrospinal fluid (CSF). In Figure 2.4-4 an example of such model is shown [32]. The work mainly concentrated on EEG forward simulations. For EEG analysis the muscle and scull tissues are important due to current redistribution, therefore the main part of the model consists of mainly these tissues with the lack of geometrical detailing within the brain itself. For MEG forward simulations it is unnecessary to consider muscle, scull and CSF due to high conductivity contrast between brain matter and other surrounding tissues.

In works [16, 17] the importance of the material properties being considered properly is also confirmed. The simple division on grey and white matter, which is considered in majority of previous work, is found to be not enough in order to satisfy the requirements of the forward problem solution. Further investigations with the new imaging modality called Diffusion Tensor Magnetic Resonance Imaging (DTMRI) proposed new method for material properties extraction on the very high level of accuracy. This method highlighted very high anisotropy of the material properties, particularly electrical conductivity, within the brain white matter. The only attempt to

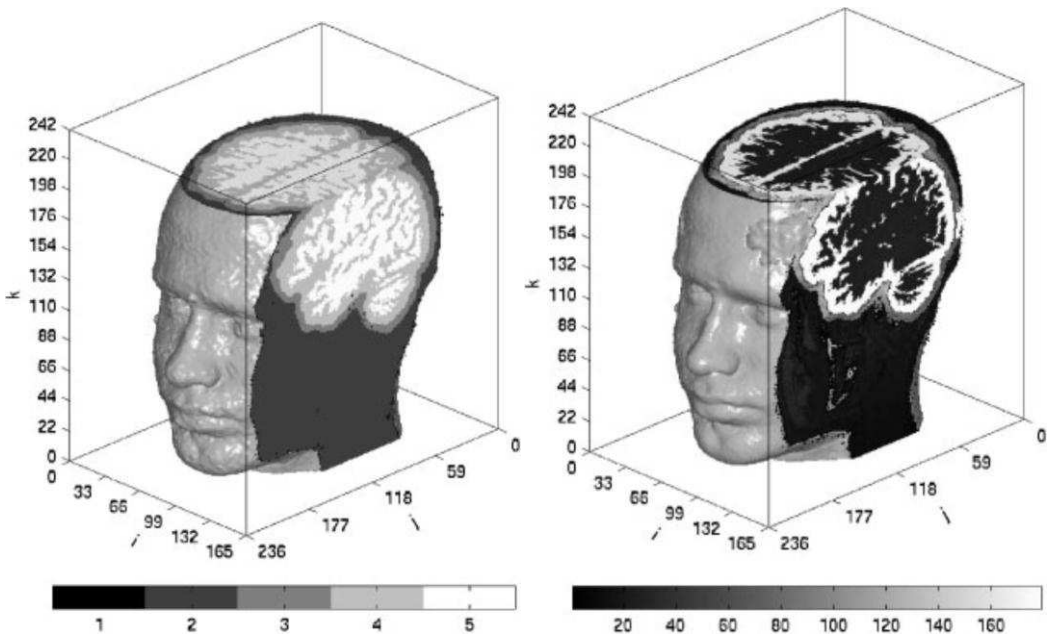

Figure 2.4-4. Realistic brain model with different material properties in terms of conductivity [29]

apply such complex conductivity properties was made in paper [32]. The overview of the brain model with anisotropic properties which has been used in this study is shown in Figure 2.4-5.

High influence of the conductivity tensor anisotropy on forward problem solution results was highlighted. However in this paper a relatively complicated algorithm was introduced and unusual software package was developed in order to allow such computations. Due to the methodology that was chosen to introduce these computations it is very difficult to use models developed in [32] for the following research. Particularly, this algorithm does not allow applying realistic current sources. Due to internal format which is used for anisotropy classification and storage of analyzing data it is very difficult to convert and transfer the modeled geometry and material properties to other formats and computational packages.

In recent years several papers were published where attempts of combination with using different types of models and realistic material properties were made in application to MEG research and particularly forward problem solution. For example, elliptical brain model was combined with realistic material properties in [34]. Also some improvements were made to geometrical modelling of the human brain in [37, 38]. In this entire branch of works the importance of accurate geometrical in combination with accurate material properties modelling is proved. However there is a big gap in terms of practical application for those mathematical methods and integration of models into the forward solution.

The main problem nowadays is flexibility of the model. No models were met in literature, that combine flexibility in terms of geometrical changes with flexibility in terms of different types of neuronal sources application.

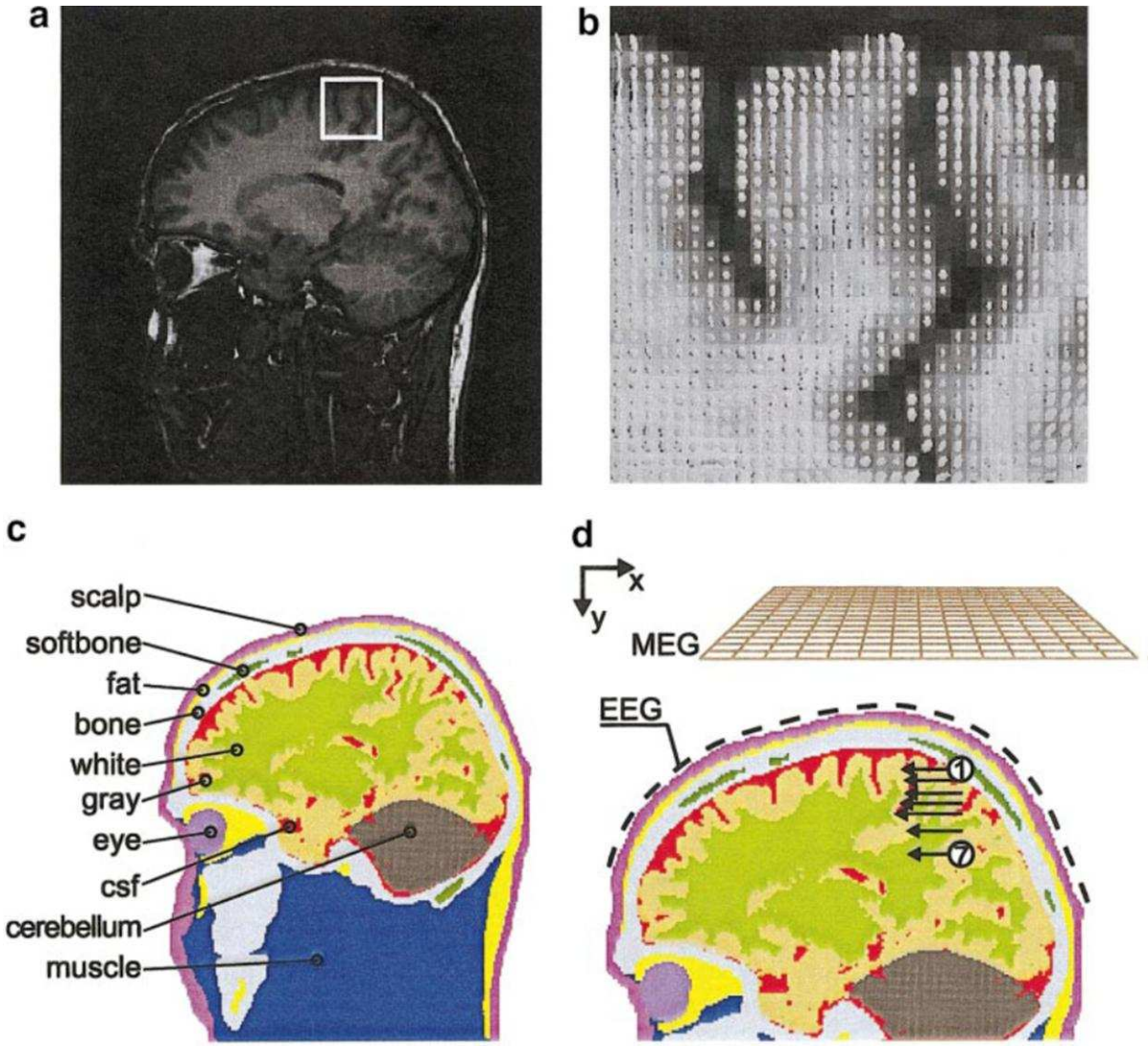

Figure 2.4-5. Coregistered T1-weighted magnetic resonance image (a) and diffusion tensor (b), FEM model cross section (c), and setup for the simulations (d). The white square in (a) indicates the region of interest enlarged in (b). The diffusion tensor image was interpolated to match the spatial resolution of the T1 image. The ellipsoids depict the local diffusion tensor. The ellipsoid axes are oriented in the direction of the tensor eigenvectors and scaled according to the eigenvalues. The origin of the coordinate system is at the upper left corner of the first MR slice. The position of the dipoles 1 to 7 is indicated by the tip of the arrows (d). The dashed line in (d) illustrates the coverage of the electrodes only. The electric potential was actually computed at 300 single surface nodes of the FEM model [29]

2.4.2 Models of the Neuronal Current Source

Neuronal current source which is applied in forward problem traditionally is described considering biological formations as a single neuron, neuronal chain, or neuronal cluster (assemble of neurons). Neuronal chains also can create assemblies known as neurotracts, or fibertracts. Entire white matter mostly consists of neurotracts, although grey matter in general is the assembly of neuronal clusters [39]. The neurons of the grey matter (cerebral cortex) are known as main functional cells of the brain responsible for cognitive activity, and therefore in almost all MEG research papers only this type of neurons is considered (Figure 2.4-6). Typical cortical neuronal distribution in grey matter is shown in Figure 2.4-7.

The electrical activity of the neuron, which produces the magnetic field, is caused by underlying electrochemical activity mechanism of the Action Potential propagation along the neuronal axon. The detailed description of Action Potential will be considered later in Chapter 5. According to this mechanism in wide range of papers the quasistatic approach in combination with symmetry of the neuronal axon lead to consider the current flowing along the axon as a primary source. Thus there are several ways found in literature of describing this type of current source and implementing it in a brain model.

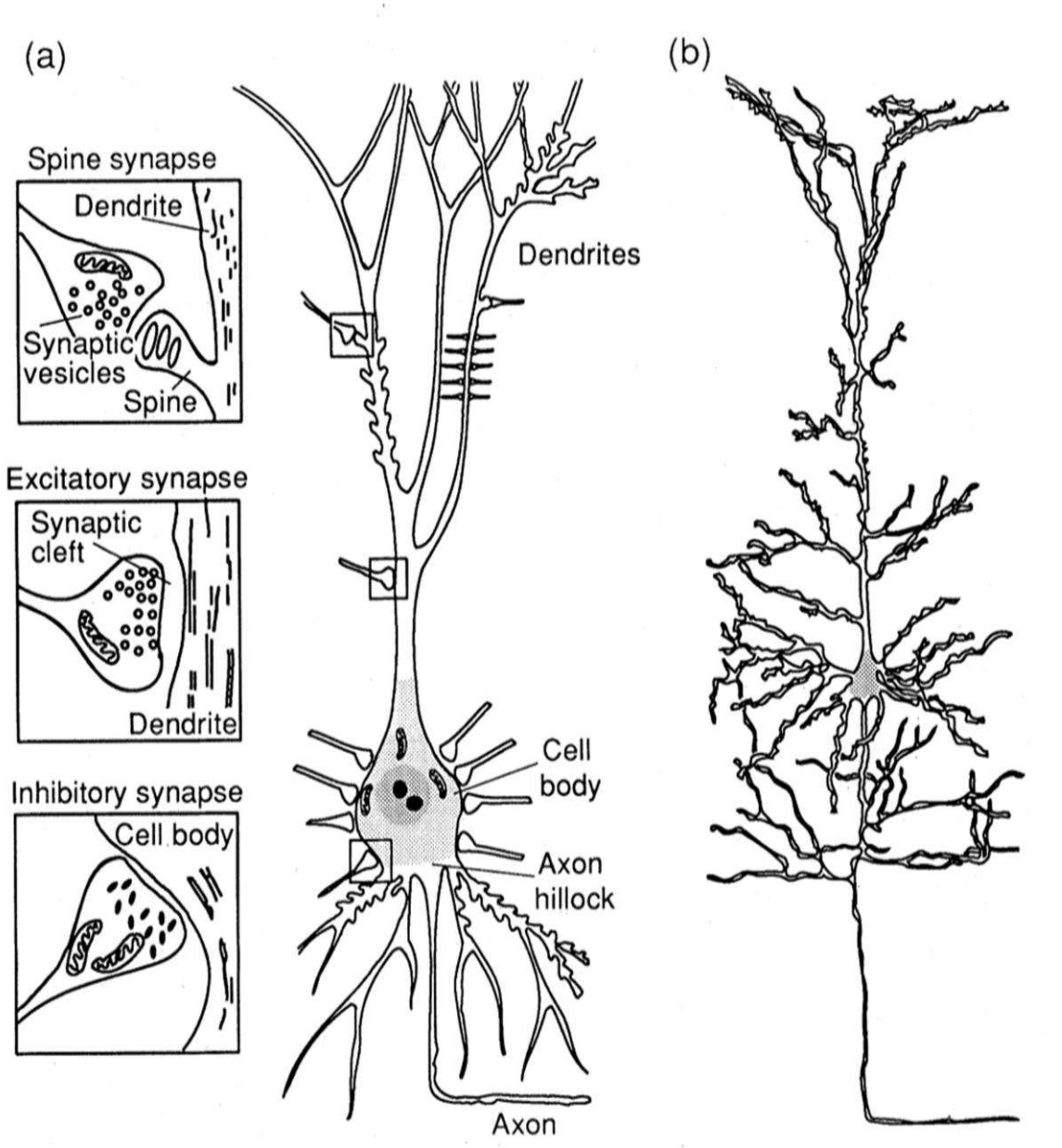

Figure 2.4-6. Cortical neuron structure. (a) Schematic illustration with synapses, and (b) actual typical configuration [39]

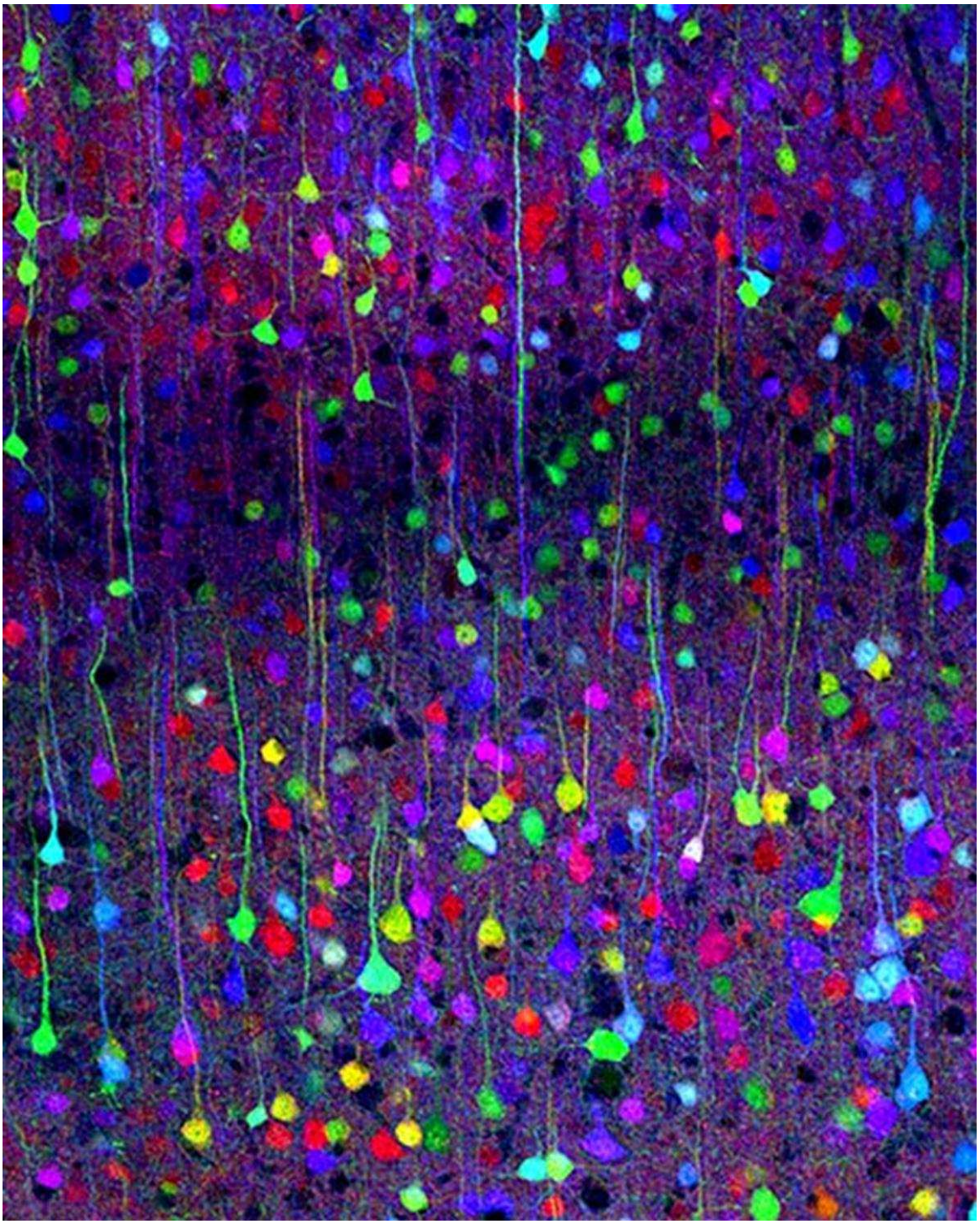

Figure 2.4-7. Typical cortical neuronal distribution [39]

2.4.2.1 Single Dipole Model

In the MEG and EEG research work the dipole approximation of the neuronal current source is mostly considered to be convenient to use. The basics of this approach was introduced in work [22] where the assumption of quasistatic behavior was considered and required accuracy for the linear solution and solid spherical brain model was obtained. The hypothesis of the dipole current source was given based on the fact that neuronal impulse which passes along the axon is very short in space and time; however post-synaptic electrochemical activity (the ionic current which flows between two neuronal terminals) was thought to have activation time much larger than actual axonal impulse. Therefore it could be assumed that the neuron is very short and thin current conductor that carries the current during a small period of time (between two neuronal terminals). It is very reasonable computational model for the preliminary approach because it simplifies solved equations without obvious decreasing in accuracy. In paper [23] the solution for forward problem was obtained in general form with the help of dipole model approximation. Major investigation has also been done based on the single dipole model in the field of understanding of the mechanism of current redistribution. In paper [18] the influence of the volume currents redistribution was discovered. In this work abstract conductive regions were considered, which are schematically illustrated in Figure 2.4-8, and solution was obtained in parametric form.

The importance of the volume currents was proved by calculations of the error in the dipole localization after forward and inverse problem solution. The average error without volume currents consideration (up to 62mm) was significantly larger than the error with such consideration (maximum error was 6mm).

Although the single dipole model was perfect for discovering computational methods and approaches, this model does not provide any realistic behavior of the neuronal current sources and thus cannot be used in the forward and inverse modelling in application to realistic problems. This decision was proved in paper [23] where different models were compared to each other. The disadvantages in terms of accuracy with using single dipole model were shown via performing simulation with

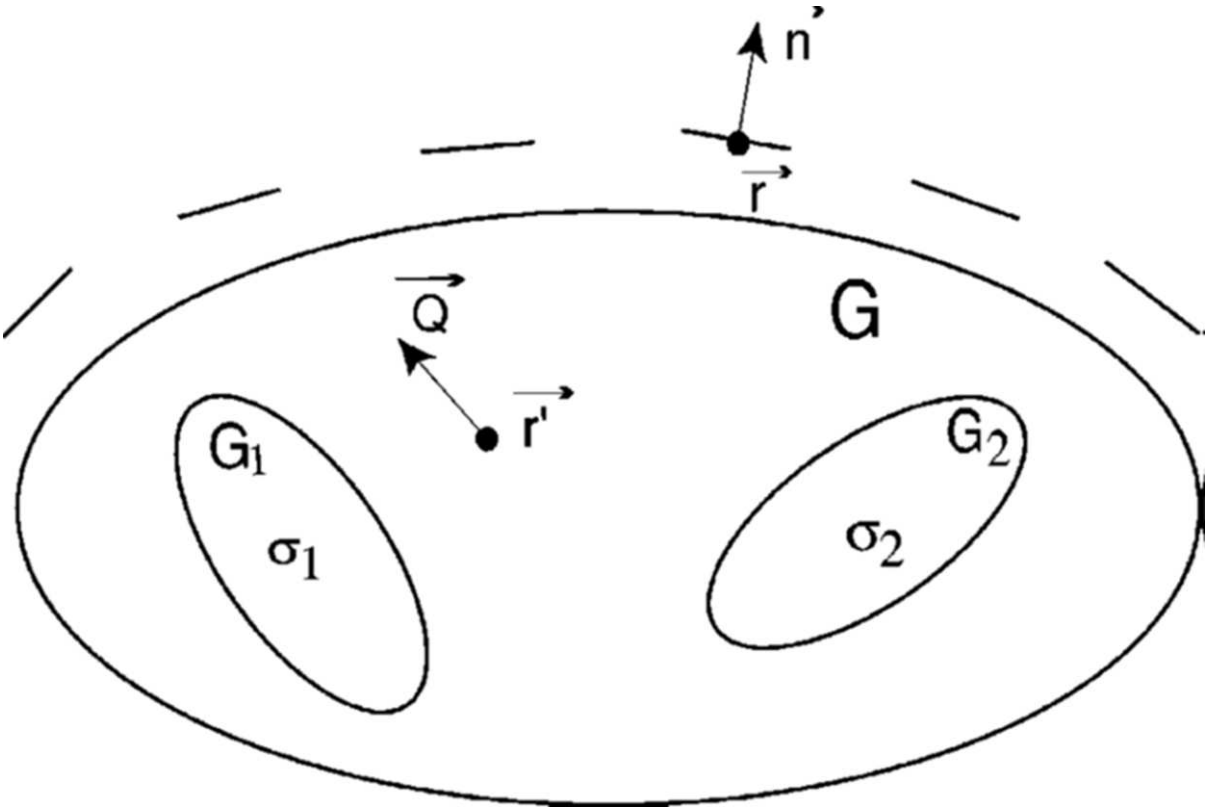

Figure 2.4-8. Schematic diagram showing the relationship between r' (coordinate of the dipole), Q (moment of dipole), r (coordinate of the detector), $n_{\perp}$ (normal to the detector), G (total conductive region), $G_{1\perp}$ (conductive subregion 1), $G_{2\perp}$ (conductive subregion 2), s_1 (conductivity of subregion 1), and s_2 (conductivity of subregion 2) [23]

simultaneous activation of the neuronal current sources positioned very close to each other in common region.

At the same time distributed dipole model was offered as the possible substitution to the current source approximation for the forward problem solution.

2.4.2.2 Distributed Dipole Model

Distributed dipole model in general is simultaneous combination of number of single dipole models. There are several approaches to modelling and implementation of this kind of neuronal current source into the forward problem. First approach is based on the random initial distribution of the dipoles, and their activation according to the position in known specific cortical areas [40]. Second approach is based on the assumption of uniform distribution and the contrary random activation of the dipoles in specific areas. Both approaches are used preliminary in the Inverse Problem solution. Third approach, which is considered mostly in forward problem

solutions, uses the specific configuration of the small group of dipoles in the activation area.

The influence of the different dipoles concentration and position, number of dipoles and orientation has been discovered in literature with the help of distributed dipole models. Sufficient sensitivity of the solution from fluctuation of all mentioned parameters was found in [20, 23, 41-43]. Below is the simple example which illustrates importance of the spatial distribution of the dipoles. Consider two dipoles which have the same magnitude but opposite direction. Imagine these dipoles being placed as close to each other as possible. Simultaneous activation of these dipoles produces zero magnetic field. The same result will take place with two pairs of dipoles, positioned anywhere in the conductive region. So it is obvious that the solution does depend on the internal parameters of the solution method, which are not the parameters of the real object (neuronal current source). There are several ways of limiting the number of parameters and therefore organizing somehow the dipole approximation [20], but all of them lead to unrealistic results by default and does not construct predictable and reliable working model.

2.4.2.3 Distributed Surface and Volume Current Models

Distributed Surface and volume sources have also been used widely in literature [44, 45]. The idea is based on using current density vector distribution inside the given conductive volume representing neuronal current source (see Figure 2.4-9). This method brought new forward simulation algorithms and precise computational results [46]. The main advantage of this approach is in applicability which is absolutely free from any limitations on type and spatial position of the current source. Also forward computations can be performed easily with using almost any solution method. The accuracy of this model in combination with realistic brain model is acceptable in comparison to any other current source approximations.

However, this model has significant disadvantages which restrict the method from being widely implemented. The main problem of the method is its infinite number of parameters. The full current density vector distribution in corresponding region of the brain is necessary in order to simulate even one neuronal current source. Because

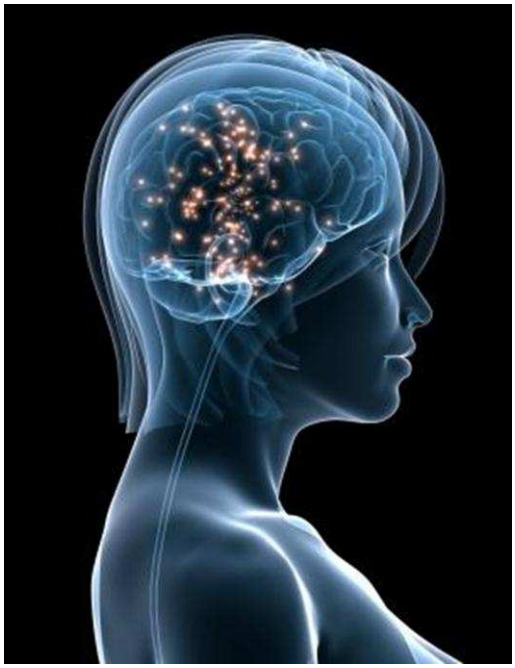

Figure 2.4-9. Example picture showing the volume current density distribution

of the same reason the solution complexity increases exponentially with consideration of more realistic multiple current source activation problems. The accuracy of the method also strongly depends on the source application accuracy. Therefore the final solution error (which is calculated with multiplying the average error by the number of applied parameters) cannot be delivered to be small enough for successful validation.

Due to such implementation complexity and infinite number of unknowns the inverse problem, which is constructed from the forward problem results with distributed current approach, is impossible to solve without additional solution limitations. Typically geometrical or physiological constrains [42] are used in order to apply these limitations. However, having in mind initial complexity of the brain model itself, and combining it with the additional anatomical or physiological complexity, this approach makes solution of the inverse problem to be extremely resource-intensive in terms of time and computational ability. In some cases distributed surface and volume current source model can be identical to distributed dipoles model. This appears when small spatial resolution of provided simulations is considerably low. Described in [44] preliminary study has been done with attempt to avoid computational complexity described before.

2.4.2.4 Other Neuronal Current Source Models

Some other less commonly used attempts of current source modelling were made in literature. The linear-source model was used in paper [26]. This model is based on the assumption that considers the neuronal axon as a small conductive straight line with the constant or quasistatic current. Some simulations with realistic brain model were performed showing the improvement of this model in comparison to the single dipole model. However, this approach is based on the unrealistic neuronal behavior and contradicts with real processes within the neuronal chain or neuronal cluster. So in case of realistic neuronal activation it is quite complicated to construct the modeled source and implement it into the human brain model to satisfy the conditions for accurate solution.

The multipolar expansions were suggested as a reasonable substitution to the traditional dipole model [47]. However the implementation complexity in combination with unrealistic assumptions put this method out of the consideration.

Several other methods were discovered in works [14, 41, 42, 46, 48]. All of them are based on the modified distributed dipoles model. The minor improvement was also shown in comparison to other methods, at the same time none of them are accurate enough for obtaining any realistic solutions for MEG forward problem.

2.4.3 Computational Methods for the Solution of Forward Problem

The mathematical Maxwell equations underlying the modelling processes are unlikely to be solved analytically, especially in the case of realistic brain and source models. The mathematical problem contains sufficient asymmetry of brain model in space as a geometrical object and current source as a realistic representation of the real neuronal current source. Therefore 2D symmetrical representation could not be considered with the forward and inverse problem for MEG. Required Maxwell equations must be solved in 3D space via computational method with the help of computer simulations. There are two major discrete methods for such solution, which are used in wide range of works in this field. They are Boundary Element Method (BEM) and Finite Element Method (FEM).

2.4.3.1 Boundary Element Method (BEM)

The Boundary Element Method is the simplest for programming and interpreting the results [49]. This method was successfully used in works [19-22, 25, 26, 30, 42, 46, 50-54]. The main advantage of this approach is its speed and simplicity for programming and obtaining results, which is clearly shown in papers [21, 54]. The basic idea of the method is that the entire space could be divided onto finite number of solid regions with the uniform homogeneous material properties. Thus the boundary of each region could be extracted and then each boundary is triangulated. Each triangle acts as a boundary element, which has 3 nodes at the vertexes [20]. The distribution of the magnetic field inside the uniform homogeneous region could be easily computed knowing the potential on the boundary of the region, so the main computational part of the method is finding this potential from initial and entire boundary conditions (including current source) and then computing the internal field by knowing algebraic relations. The boundary potential could be calculated by discrete mathematical methods and appropriate 3D geometrical triangulation of the discovered object. The comparison of the boundary element method with other methods was shown for the case of isotropic spherical brain model in paper [19]. The main properties and advantages of BEM were proved:

- Small number of triangles and thus the time of computation is sufficiently small
- Flexibility in programming
- Good accuracy in case of modelling with small number of smooth homogeneous regions

However, the main disadvantage of the method is impossibility to consider anisotropic and/or heterogeneous material properties. As was shown before, the complex anisotropy of the brain matter is very important for consideration. Brain models without these features cannot achieve required accuracy, which is also shown in work [50] for BEM applications. Therefore, it is not possible to use this method for realistic forward modelling. However it is still used for inverse computations in combination with the distributed dipole model due to simplicity of realization.

2.4.3.2 Finite Element Method (FEM)

The Finite Element Method is based on the division of the entire geometrical space onto volume 3D elements [55, 56]. The mathematical solution is basically conducted with parametrical linearization of the complex tensor equations throughout the linear or quadratic space element division and following solution approximation. Each element can be described geometrically as parallelepiped or pyramid. Therefore complex geometrical formation becomes the assembly of simple solvable structures, which makes the problem in general to be formulated in form of the linear matrix equations. This method will is accurately described below in Section 3.3.

FEM is now used in literature more frequently than other approaches simply because of its ability to solve a very wide range of physical problems. A range of computational packages and products were developed based on this method in the field of electromagnetic simulations, such as ANSYS, Nastran, VF Opera. These types of software allow flexible solution of full spectrum of electromagnetic problems, offering exceptional stability, high level of programming optimization, and flexible interface. FEM is not so easy to program in comparison to BEM due to its geometrical basis, but it allows almost unlimited abilities in solving Maxwell equations, managing pre- and post-processing data and changing the parameters of the mathematical model underlying developed algorithms.

FEM in application to forward problem solution for MEG allows fast computations and provides accurate solution for simple problems with spherical brain models as was shown in work [23]. At the same time it is possible to improve and optimize the model at any stage [53]. Paper [14] shows the ability for inhomogeneous anisotropic material properties to be applied, which is the critical advantage as was discussed previously. Due to such wide usage a number of strong algorithms and data were accumulated almost in all areas of engineering computations including cross-platform and cross-software data transferring and result converting [55-58].

In work [53] the comparison of FEM with other methods was carried out. FEM is showed to be better results than other methods according to the accuracy of the solution which was compared to theoretical one. The Table 2-1 shows this comparison with respect to modelling. Here “I” stands for interpolation algorithm.

Finally, as obtained in paper [16], this is the only method with the computational volume for unrestricted number of anisotropic properties in the model, which is necessary to consider in case of white matter fibertracts anisotropy inclusion. The summary of main advantages of the finite element method can be summarized:

- Flexibility in terms of geometrical approximation
- Flexibility in terms of material approximation
- Ability to discover and improve the accuracy of the solution
- Ability to operate with large number of material regions
- Ability to implement complex anisotropic properties of materials

The FEM has only one disadvantage: It is a relatively slow method in comparison to others in terms of computational time. However large computational time values can be avoided by using special techniques e.g. submodelling routine, developed by authors and accurately described in paragraph 3.3.3. Also this method is very friendly to parallel programming technique with combination to large multiprocessor systems.

2.4.3.3 Other Methods

There are some other methods were used in literature to solve the forward problem. They are briefly described below.

Array response kernels method [35] showed applicable results with the very basic modelling, however does not provide the ability of using complex geometrical brain models. Thus realistic model and therefore accurate results cannot be achieved with this method.

Finite Difference Method (FDM) and Finite Volume Method (FVM) showed similarity to FEM [53] in terms of accuracy and it is convenient to use such methods in other fields of bio-electromagnetics. At the same time there is lack of functionality with those methods in terms of element mesh construction. In case of FDM a quadratic shape of the element limits the flexibility of geometrical modelling. FVM in case of electromagnetic equations is basically simplified FEM without interpolation flexibility.

Lead-field interpolation [29, 59] could be used in combination with BEM or FEM to speed up the calculations. Time reduction of a factor of 3 relative to unmodified FEM can be achieved. However, it does not support realistic neuronal current source modelling.

Artificial neural network method [24] could also be used in inverse problem solution. For forward problem this class of methods can operate only in combination with random dipole source modelling.

2.4.4 Main Results and Summary from Literature Survey

According to present literature, a significant interest concerning adequate forward modelling is highlighted. There are fundamental works which show a great importance of forward modelling for MFT based on MEG. At the same time there is lack of realistic simulations in terms of both brain modelling and neuronal current source modelling. Also the importance of data reproduction and patient specific automatic brain model reconstruction was shown, which is at the same time the most significant part of the inverse problem as well.

In addition we must point out the lack of adequate neuronal current source models in literature. The most widely used approach is the current dipole model. This approximation, however does not seem to be accurate enough to produce realistic

TABLE 2-1. COMPARISON OF THE DIFFERENT METHODS WITH RESPECT TO MODELING

	FDM	FEM	FVM	BEM&I	FDM&I	FEM&I	FVM&I
Geometry	-	+	+	+	-	+	-
Boundary conditions	+	+	+	+	-	+	+
Anisotropy	+	+	+	-	+	+	+
Scalpless regions	+	+	+	-	+	+	+
Computation	-	-	-	+	+	+	+

result as discovered in details above and also in 3.4.

The interesting fact must be mentioned in conclusion to the literature survey. Almost no comparison of the forward problem simulation results to the real experimental data have been met in published research papers. This absence of the experimental validation of the forward problem is caused by extreme complexity of the actual experiment. It is also due to medical and research ethics issues together with the novelty of MEG itself as a clinical imaging technique.

However experimental validation was meant to be one of the tasks throughout this report. Therefore attempts for such comparison between the numerical solution and experimental results were made where possible. The estimated errors of the numerical solutions and comparison with analytical computations were made for all cases where it was impossible to make experimental validation.

Chapter 3

Mathematical Modelling of Magnetic Field of the Brain

3.1 Mathematical Formulation of the Forward Problem in MFT Based on MEG

The mathematical model of magnetic fields produced by bioelectric current sources in the brain is based on a set of quasistatic Maxwell's equations which lead to appropriate Poisson's equation. In doing so, it is assumed that the magnetic permeability of brain matter is the same as that of free space ($\mu = \mu_0$). The quasistatic nature of the field is justified by the fact that bioelectrical activities that give rise to magnetic fields are predominantly of low frequency (from below100 Hz to less than 1 kHz). This, together with the material properties of brain matter (e.g., conductivity tensor $\boldsymbol{\sigma}$ and permittivity tensor $\boldsymbol{\varepsilon}$) suggest that in calculating the electric-field intensity $\boldsymbol{E}$ and magnetic flux density $\boldsymbol{B}$ vectors, the time derivative terms $\partial \boldsymbol{E}/\partial t$ and $\partial \boldsymbol{B}/\partial t$ in Maxwell's equations can be ignored [60]. This leads to the following set of simplified Maxwell's equations:

$$\nabla \times \boldsymbol{B} = \mu_0 \boldsymbol{J} \tag{3.1-1}$$

$$\nabla \cdot \boldsymbol{B} = 0 \tag{3.1-2}$$

$$\nabla \times \boldsymbol{E} = 0 \tag{3.1-3}$$

In (3.1-1), the total current density is equal to:

$$\boldsymbol{J} = \boldsymbol{J}_p + \boldsymbol{J}_v = \boldsymbol{J}_p + \boldsymbol{\sigma} \cdot \boldsymbol{E} \tag{3.1-4}$$

where $\boldsymbol{J}_p$ is the primary "excitation" current (or impressed current if at the cellular level) produced by electromotive force (EMF) in the conducting brain tissue. The volume current $\boldsymbol{J}_v = \boldsymbol{\sigma} \cdot \boldsymbol{E}$ is attributed to the effect of the macroscopic electric field $\boldsymbol{E}$ on charge carriers [60]. It has been shown that for a realistic brain model with inhomogeneous conductivity distribution, the magnetic field from this volume current can be comparable with that from the primary current source (e.g., dipole) [18]. Thus, the total current density becomes:

$$\boldsymbol{J} = \boldsymbol{J}_p + \boldsymbol{\sigma} \cdot \boldsymbol{E} = \boldsymbol{J}_p - \boldsymbol{\sigma} \cdot \nabla\varphi \tag{3.1-5}$$

where φ is the electric scalar potential. The previous equations lead to the following Poisson's equation for the quasistatic magnetic field, the solution of which constitutes the solution of the forward problem in MFT based on MEG [60]:

$$\begin{gathered} \nabla \cdot (\boldsymbol{\sigma} \cdot \nabla\varphi) = \nabla \cdot \boldsymbol{J}_p \\ \text{In } \Omega = \Omega(x, y, z) \end{gathered} \tag{3.1-6}$$

Under appropriate boundary conditions equation (3.1-6) is solved for the unknown potential distribution $\varphi = \varphi(x, y, z)$ by the chosen computational method. The complexity of this equation stands by the form of $\boldsymbol{\sigma}(x, y, z)$, which is generally tensor of 3-rd range and depends on $\boldsymbol{r} = (x, y, z)$. The magnetic field $\boldsymbol{B}(\boldsymbol{r})$ at a given point $\boldsymbol{r}$ in the problem domain Ω is then found by using:

$$\boldsymbol{B}(\boldsymbol{r}) = \boldsymbol{B_0}(\boldsymbol{r}) - \frac{\mu_0}{4\pi} \sum_{i=1}^{m} \boldsymbol{\sigma_i} \cdot \int_{G_i} \nabla'\varphi \times \frac{\boldsymbol{R}}{R^3} dv' \tag{3.1-7}$$

$$\boldsymbol{B}_0(\boldsymbol{r}) = \frac{\mu_0}{4\pi} \int_{G_i} \boldsymbol{J}_p(\boldsymbol{r}') \times \frac{\boldsymbol{R}}{R^3} dv' \tag{3.1-8}$$

where the source conductor consists of G_i piecewise homogenous parts, $\boldsymbol{B}_0(\boldsymbol{r})$ is the magnetic field produced only by the primary current $\boldsymbol{J}_p$, $\boldsymbol{R} = \boldsymbol{r} - \boldsymbol{r}'$ and relates to the source regions.

The equation (3.1-6) could be solved by using several approaches. Direct approach allows formally computing potential distribution and finding the values of magnetic field in points of interest [22, 33, 34, 61]. This approach works for very basic brain models (spherical and ellipsoidal) only and does not allow more than several simple current neuronal current sources to be considered. Using direct computations the general properties of described mathematical method were first discovered and a general error of the mathematical model was estimated. Some preliminary work has been done and the range of possible improvements has been obtained with the help of these analytical computations.

In the next Section all possible methods of solution of equations (3.1-6), (3.1-7), and (3.1-8) are discussed in terms of reliability, accuracy and flexibility.

3.2 Various Methods of Solution of the Forward Problem

3.2.1 Direct Analytical Solution for Elliptical Brain Model

As was discussed in Section 2.4, there are several ways to solve equations (3.1-5), (3.1-6), and (3.1-7). First of all, for simple brain models and current sources it is possible to solve these equations analytically. In case of solid elliptical brain models, the geometry of the brain could be described by the equation:

$$\frac{x^2}{\alpha_1^2}+\frac{y^2}{\alpha_2^2}+\frac{z^2}{\alpha_3^2}=1 \tag{3.2-1}$$

where α_i are geometrical parameters of the ellipsoid. Applying current source as a single dipole the magnetic field can be expressed implicitly as [34]:

$$\begin{aligned}\boldsymbol{B}(\boldsymbol{r}) = \frac{\mu_0}{4\pi}\frac{\left[\mathrm{F}_2^1(\rho_r,\mu_r,\vartheta_r)-\mathrm{F}_2^2(\rho_r,\mu_r,\vartheta_r)\right]}{\gamma_1-\gamma_2}\sum_{i=1}^{3}\frac{\hat{\boldsymbol{q}}\cdot\hat{\boldsymbol{e}}_{\boldsymbol{i}}}{\gamma_1-\alpha_i^2}\hat{\boldsymbol{e}}_{\boldsymbol{i}} \\ -\frac{15\mu_0}{4\pi}\sum_{i,j=1;i\neq j}^{3}(\hat{\boldsymbol{q}}\cdot\hat{\boldsymbol{e}}_{\boldsymbol{j}})(\boldsymbol{r}\cdot\hat{\boldsymbol{e}}_{\boldsymbol{j}})(\boldsymbol{r}\cdot\hat{\boldsymbol{e}}_{\boldsymbol{j}})\mathrm{I}_2^{\mathrm{i+j}}(\rho_r)\,\hat{\boldsymbol{e}}_{\boldsymbol{i}}+O\left(\frac{1}{\rho_r^4}\right)\end{aligned} \tag{3.2-2}$$

where $(\rho_r,\mu_r,\vartheta_r)$ refer to the components of $\boldsymbol{r}$ in the ellipsoidal coordinate system ($r_1=\sin\vartheta_r\sinh\mu_r$; $r_2=\cos\vartheta_r\cosh\mu_r$; $r_3=\rho_r$), $\hat{\boldsymbol{q}}$ is the dipole moment, modified by the spatial effects of the anisotropy imposed by the ellipsoid, $\hat{\boldsymbol{e}}_{\boldsymbol{j}}$ is the three-dimension unit vector with '1' in the *j*-th position and zeros elsewhere, γ_1 and γ_2 are the roots of the quadratic equation $\sum_{i=1}^{3}1/(\gamma-\alpha_i^2)$. $\mathrm{I}_2^{\mathrm{i+j}}$ is the second degree elliptical integral of order $i+j$:

$$\mathrm{I}_2^{\mathrm{v}}(\rho) = \int_{\rho^2-\alpha_1^2}^{+\infty} \frac{d\tau}{\left[\varepsilon_2^v\left(\sqrt{\tau+\alpha_1^2}\right)\right]^2 \sqrt{\tau+\alpha_1^2}\sqrt{\tau+\alpha_2^2}\sqrt{\tau+\alpha_3^2}} \tag{3.2-3}$$

$$\varepsilon_2^v(\tau) = \tau^2 - \alpha_1^2 + \gamma_v \tag{3.2-4}$$

$\mathrm{F}_{\mathbf{2}}^{\mathbf{1}}(\rho_r, \mu_r, \vartheta_r)$ and $\mathrm{F}_{\mathbf{2}}^{\mathbf{2}}(\rho_r, \mu_r, \vartheta_r)$ are the second degree exterior solid ellipsoidal harmonics of order 1 and 2 respectively*:*

$$\mathrm{F}_2^v(\rho, \mu, v) = 5\varepsilon_2^v(\rho)\varepsilon_2^v(\mu)\varepsilon_2^v(v)\mathrm{I}_2^v(\rho) \tag{3.2-5}$$

As we see equation (3.2-2) requires some additional computations as well in order to produce a field plots or to calculate specific values. Also this equation does not contain the secondary volume current effects. In order to produce multiple dipole solution the fields from each dipole should be summarized together using additive linearity of the static magnetic field.

Described solution for the elliptical brain model is quite easy to understand but it does not provide any realistic behavior for the magnetic field distribution. In order to follow required range of accuracy, the special computational methods must be used.

3.2.2 Numerical Solution

The idea of the numerical solution is based on discrete division of the integrated space. The magnetic potential $\varphi(\boldsymbol{r})$ as a main unknown is approximated in the entire space through the set of approximating functions. Numerical solution methods, as was discussed are divided in two major groups – volume operating methods and surface operating methods. Other numerical methods, such as boundary integrals, do not work well for electromagnetic simulations.

The most discovered and powerful method from the surface-operating group is Boundary Element Method (BEM). The mathematical formulation of this method for solution could be written in form:

$$\sigma_0\varphi_0(\boldsymbol{r}) = \frac{\sigma_m^- + \sigma_m^+}{2}\varphi(\boldsymbol{r}) + \sum_{k=1}^{N}\frac{\sigma_k^- + \sigma_k^+}{4\pi}\int_{r\prime\in S_k}\varphi(\boldsymbol{r}')\nabla'\left(\frac{1}{R}\right)\cdot\boldsymbol{n_k}(\boldsymbol{r}')ds_k(\boldsymbol{r}') \qquad (3.2\text{-}6)$$

involving the potential $\varphi(\boldsymbol{r})$ on a smooth surfaces S_m separating regions with conductivities σ_m^- , σ_m^+ , with $\boldsymbol{R} = \boldsymbol{r} - \boldsymbol{r}_0$, $R = \|\boldsymbol{R}\|$ and $\nabla'\left(\frac{1}{R}\right) = \frac{\boldsymbol{R}}{R^3}$, where *N* is the number of surfaces, $\boldsymbol{n_k}$ is the unit vector normal to S_k oriented from the region with σ_k^- to the one with σ_k^+ . φ_0 is a potential caused by a known primary current distribution $\boldsymbol{J}_p(\boldsymbol{r})$ in the infinite homogeneous space with conductivity σ_0.

The potential $\boldsymbol{\varphi}$ is discretized using either piecewise constant (P0) or piecewise linear (P1) basis functions χ_i each associated with a surface element (for example a triangle). The continuous integral equation (3) is converted into a corresponding linear equation system by taking a scalar product with test functions ψ_i which are normally chosen to be either the Dirac's $\boldsymbol{\delta}$ (the collocation method), or $\psi_i = \varphi_i$(the Galerkin method). In both cases we obtain a linear equation system:

$$\mathbf{A}\varphi = \mathbf{b} \qquad (3.2\text{-}7)$$

relating $\mathbf{b}$ representing φ_0 and the unknown coefficients of the discretization of φ. The elements of the matrix $\mathbf{A}$ are given by integrals of the type as it stands in the equation (3.2-6).

Although it provides high-speed computations, it has disadvantages mentioned below which makes impossible of using this method in proper realistic simulations:

- Impossibility of performing realistic computations in terms of geometrical properties. As could be observed from the equation (3.2-6), conductivity σ could be used only in form of scalar.

- Sufficient limitation of number of regions could be considered.
- Impossibility of the realistic current source modelling.

The other group of methods is volume-operating methods. The leading method from this group is the Finite Element Method (FEM). It is the most powerful tool for electromagnetic simulations at present. As was discovered and discussed in paragraph 2.4.3, this method allows great flexibility for geometrical modelling as well as for realistic property description and realistic neuronal current source simulations.

3.3 Finite Element Method (FEM) and its Application to Forward Problem in MFT Based on MEG

3.3.1 Basics of the FEM

The idea of the method is described in [55]. According to the mathematical formulation, the considered unknown field variable u in the equation like (3.1-6) can be approximated throughout a set of functions χ_i. Each of these functions has simple structure and most commonly it is the polynomial function of second order. Subdividing the entire space Ω onto the number of simple volumes, it is possible to calculate the distribution of the unknown in the space and approximate each volume as a uniform subspace which has the internal distribution of unknown as χ_i. Considering the shearing boundary conditions of two neighbour elements and providing the conditions for external surface, the linear system of equations could be written and then solved. More formally, in the simple case for 3D problem we can write an equation for our unknown u:

$$u(x,y,z) = \sum_{k=1}^{N} u_k \chi_k(x,y,z) \tag{3.3-1}$$

For the external loading function $f(x,y,z)$ we achieve the same structure as:

$$f(x,y,z) = \sum_{k=1}^{N} f_k \chi_k(x,y,z) \tag{3.3-2}$$

Then, using substitution for our first order differential problem we have the following system of linear first order equations:

$$-\sum_{k=1}^{N} u_k \int_{\Omega} \nabla\chi_k \cdot \nabla\chi_j \, dV = \sum_{k=1}^{N} f_k \int_{\Omega} \chi_k \chi_j \, dV \qquad (3.3\text{-}3)$$

$$for\ j = 1, \dots, N$$

Using the matrix-vector form we obtain:

$$-\mathbf{Lu} = \mathbf{Mf} \qquad (3.3\text{-}4)$$

where matrixes $\mathbf{L}$ and $\mathbf{M}$ are calculated from the equation (3.3-3):

$$L_{kj} = \int_{\Omega} \nabla\chi_k \cdot \nabla\chi_j \, dV$$

$$M_{kj} = \int_{\Omega} \chi_k \chi_j \, dV \qquad (3.3\text{-}5)$$

$$\text{for } j, k = 1, \dots, N$$

Considering the electromagnetic quasistatic simulations (**f** is constant and fully determined), the problem can be described in following form in terms of unknown magnetic potential $\varphi(x, y, z)$:

$$\mathbf{K}\varphi = \mathbf{S} \qquad (3.3\text{-}6)$$

Where $\mathbf{K}$ and $\mathbf{S}$ are the coefficient matrix and boundary condition vector respectively.

3.3.2 Application of FEM for the Solution of the Forward Problem

The most important parameter of the model is the conductivity of the matter $\boldsymbol{\sigma}$ and its distribution in the considered region Ω as follows from (3.1-7). Distribution of tissue conductivity properties leads to sufficient influence in the final magnetic field distribution due to the volume currents, according to the equation (3.1-6). At the same time it is important to follow all geometrical details as the brain itself is very complex structure from geometrical point of view [62], and the geometry of the brain is also confirmed in literature to be sufficient for resulting accuracy [63].

The current source approximation and implementation is also important as the neuronal current behaviour can take very complex forms. For the forward problem solution it is essential to be able to simulate any possible realistic primary current distributions for MEG problem. Let us consider the solution of electromagnetic problem with respect to those parameters, which has some special features. There are two different approaches for Finite Element Modelling (schematically shown in Figure 3.3-1) in application to forward problem.

First approach is based on direct finite element mesh generation from initial data. By the initial data we assume everything related to the model which can be obtained from specific subject for successful modelling. This includes brain images, initial parameters of the model, and problem formulation. Direct mesh generation is useful for obtaining fast results and allows single analysis of unpredictable and complex geometrical structures. The main disadvantage of this method is that there is no option of changing model geometry or mesh distribution according to discovered during the analysis specific assumptions and underlying features. It is also impossible to do a mesh convergence analysis before the actual computations, which is very important for avoiding inaccuracy. The poor accuracy caused by the internal mathematical instability of the solution in case of inaccurate mesh generation cannot be traced as well.

The second approach called Solid Modelling (SM) is more complex, however it allows exceptional flexibility in terms of model optimisation, convergence analysis,

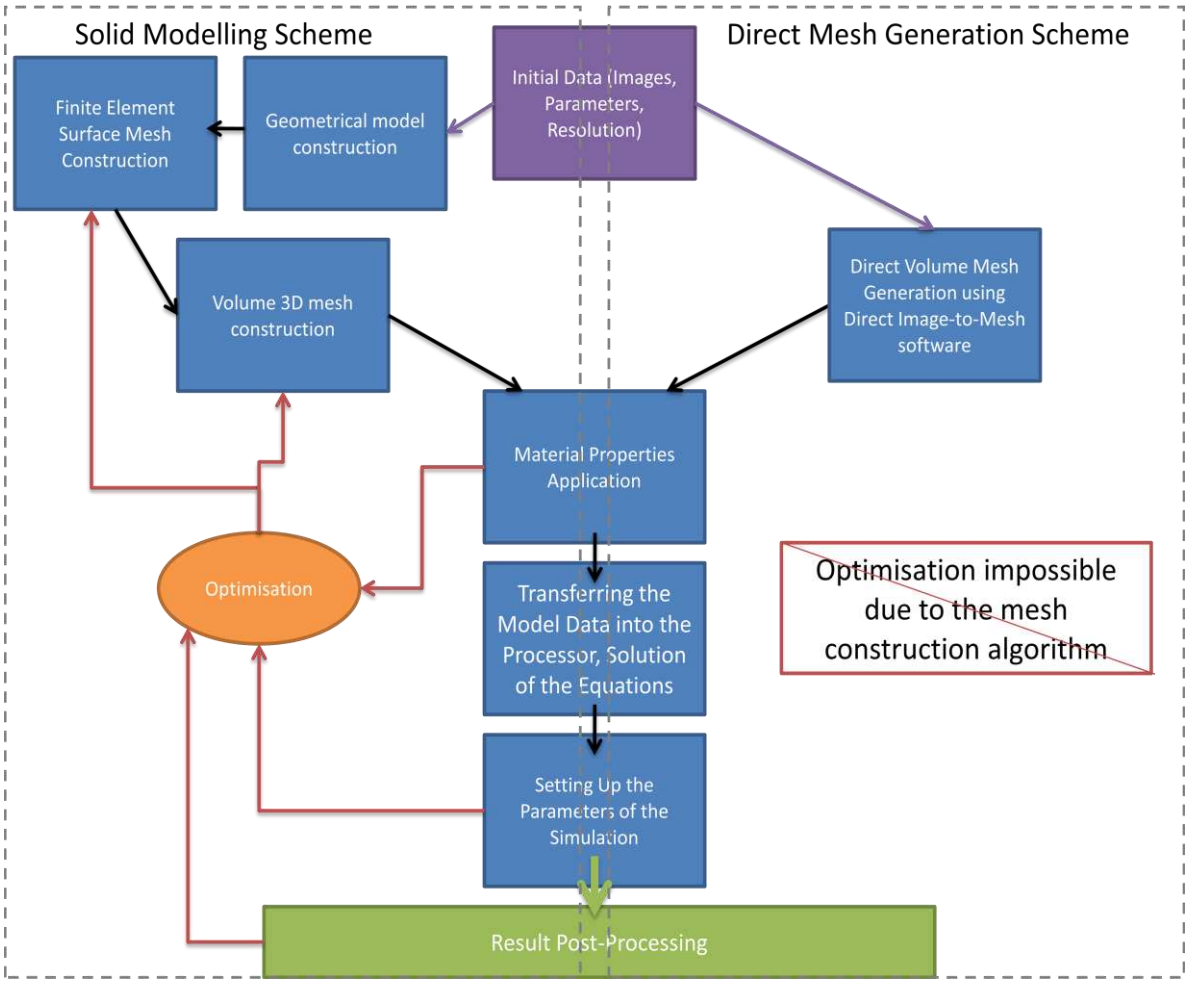

Figure 3.3-1. Diagram showing the procedures of the finite element analysis for electromagnetic problems

mesh reconfiguration, and, which is also important, the submodelling routine (which is discussed in details in paragraph 3.3.3).

This method is based on the initial 3D geometrical parametric modelling. Solid model of the object is created before the mesh generation procedure. Having the parametrical model with required functionality the specific mesh for the problem can be generated, changed, or improved based on the test analysis. All of the indicated optimisation procedures can also be done automatically on the existing common software basis also known as Computer Aided Design (CAD).

All papers listed in literature survey, which are related to finite element modelling with realistic brain shapes use direct mesh generation. This thought to be done

mainly because of the implementation simplicity. However, the accuracy of the method itself for MEG forward problems has not been discovered in literature before.

Major part of analysis presented in this report is based on the finite element solution accuracy and optimisation flexibility. Therefore solid modelling approach is considered and automatic parametric geometrical reconstruction must be introduced before going to the actual modelling part.

3.3.3 Application of Submodelling Technique to Electromagnetics

Submodelling is the common approach which is successfully used in computational mechanics [64] in order to reduce the time of computation with almost no loss in the accuracy of the solution. Present existing technique involves the improvement of the solution (for example stress concentration values in the points of interest) and works only in one direction, from the large scale (coarse model) to the lowest scale (stress concentrator). Term 'scale' here should be referenced to the spatial scale in 3D domain. Our new approach is designed in order to be implemented in electromagnetic problems where the solution must be improved not only in points of interest but also in full computational domain.

3.3.3.1 Description of Direct Submodelling Routine

The well-known existing submodelling routine [64] consists of two major steps which are illustrated in Figure 3.3-2 and described below:

3.3.3.1.1 Solution of the Coarse Problem

First the coarse model is analysed with appropriate boundary conditions. During the solution normal mesh convergence analysis must be performed and minimal FE mesh density must be chosen in order to satisfy the required accuracy for the coarse solution. Result must be checked in the area outside external boundaries of the submodel.

After the solution is computed, all degrees of freedom (DOF) on the boundaries of the submodel are interpolated using element shape functions and then saved.

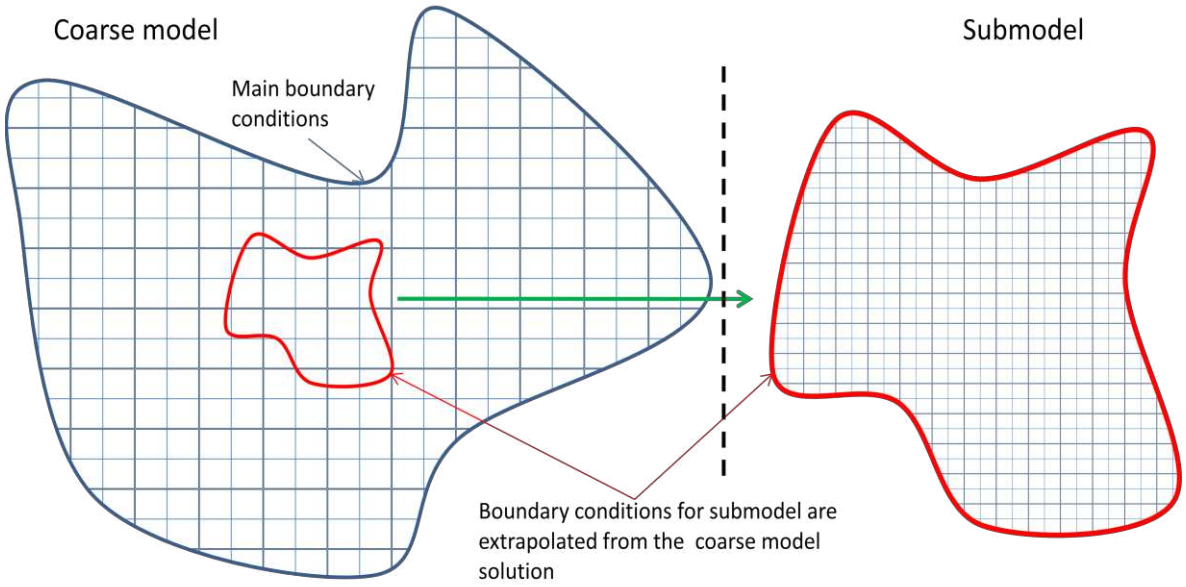

Figure 3.3-2. Direct Submodelling Routine (SR)

3.3.3.1.2 Solution of the Submodel

The second step involves performing the submodel analysis. This analysis is totally independent from the mesh of the coarse model, therefore the mesh density of the submodel must be chosen according to new required accuracy for this particular region. Refined FE mesh could be as dense as it is needed for the solution. The boundary conditions are set up as extrapolated solution values of the coarse model which was saved during previous step. If the main boundary conditions are applicable to the submodel region they must be transferred into it as well.

In electromagnetic computations this procedure can be used for the static problems with external boundary conditions in order to improve the quantities for the required regions of interest. For example, it is widely employed for the static volume conduction problems with relatively small inclusions inside the main isotropic domain.

However, this approach does not allow operation with problems where the point of interest is outside the object of the lowest scale and this object is significant for the solution, e.g. the current or magnetic source.

3.3.3.2 New Combined Submodelling Routine (CSR)

This novel submodelling routine has been developed in order to perform electromagnetic analysis for the multi-scale problems with the electrical or magnetic sources in the smallest scales [65]. These problems include quasistatic coupled electromagnetic problem formulations with the relatively small size of a magnetic dipole, electrical voltage source, or electrical current source implemented within the computational domain. The schematic diagram of the CSR can be seen in Figure 3.3-3.

The full process can be considered as the combination of forward and backward submodelling procedure and described using following steps:

3.3.3.2.1 Solution of the Coarse Problem

This step is similar to the first step of normal SR, with the addition that the submodelling region should be taken around considered electrical or magnetic source. The interpolation boundaries should be relatively far from the source in order to achieve good approximation for the following submodelling solution. The interpolation boundary conditions should also include all degrees of freedom of the solution (magnetic and electric).

3.3.3.2.2 Solution of the Submodel

The submodel solution is performed and the electrical and magnetic fields distribution is obtained in the entire domain. Next step depends on the sort of source being considered.

3.3.3.2.3 Interpolation of the Coarse Model Volume

The entire volume solution of the submodel is then interpolated and transferred as a primary source for the coarse model. Only those (electrical or magnetic) degrees of freedom should be transferred into the coarse model of which the primary source consists of (If primary source is given in form of electric potential or primary current, then only electrical DOFs are transferred). In Figure 3.3-3 the electrical source is the primary so only electrical DOFs is transferred into the coarse model. Note that if both magnetic and electrical DOFs will be interpolated back to the coarse model, the solution of the coarse model will not be improved.

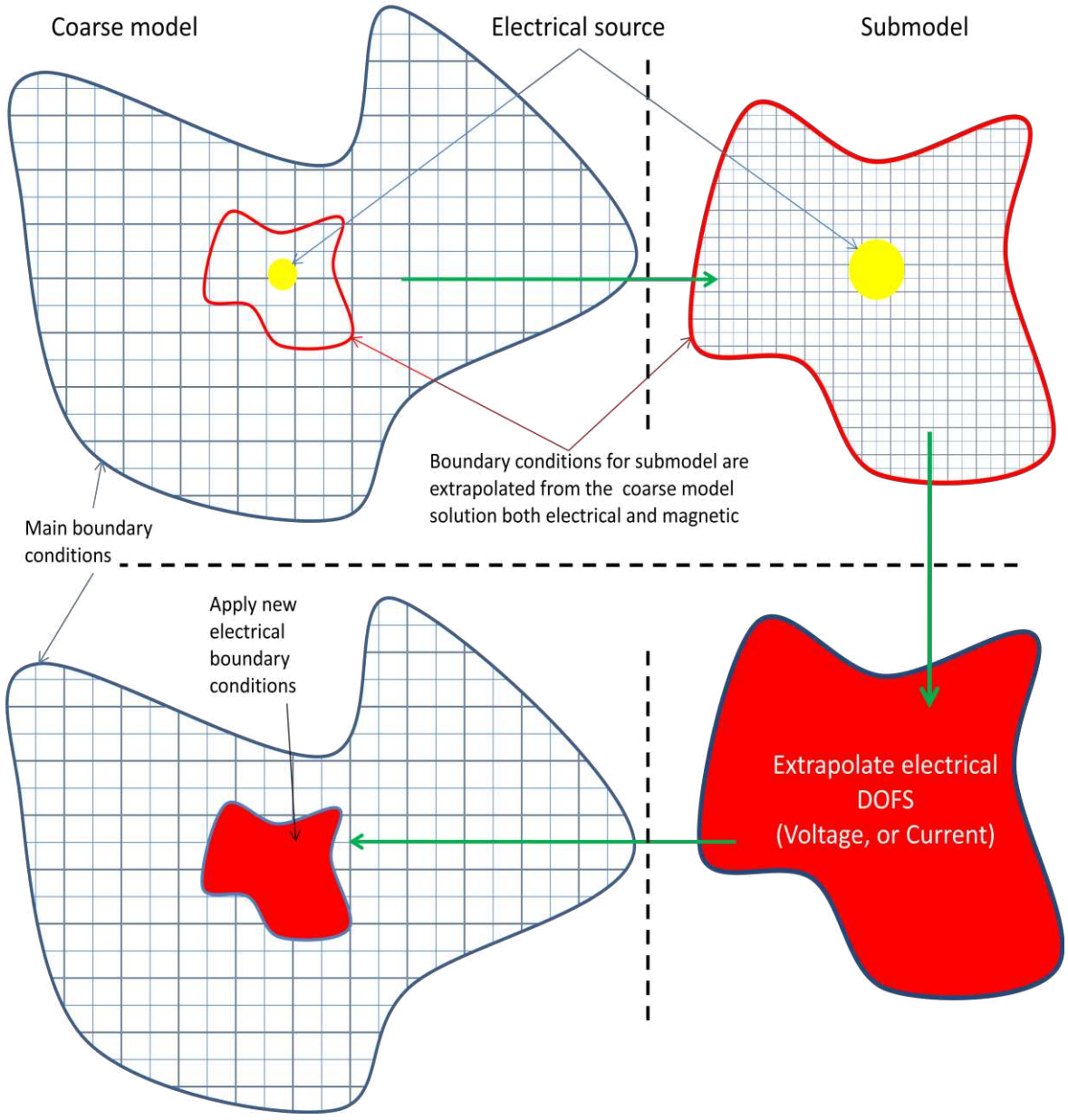

Figure 3.3-3. Combined Submodelling Routine (CSR) in application to the electrical source problem

3.3.3.2.4 Solution of the Coarse Model

After the interpolation and transferring stage is performed, the coarse model should be solved with the electrical or magnetic field distribution as a primary source instead of initial source. Presented approach could be used for multi-source problems, such as bio-electromagnetic EEG, MEG, or ECG forward analysis. In this case the

problem could contain several submodel regions. There are also no restrictions on combination of magnetic and electrical sources in one model.

The CSR has the ability of being applied in analysis of multiple scale problems throughout the application to submodel (for example, in case the source is a mixture of a sub-sources). In this case submodelling sub-domain could be also analysed using CSR.

3.3.3.3 Iterative Submodelling Approach (ICSR)

Iterative Submodelling Combined Routine (ICSR) is developed in order to solve full nonlinear or transient coupled electromagnetic problems with the multi-scale conditions. As the solution process in case of transient analysis and/or nonlinear and iterative, the ICSR operates iteratively on each computational step in time domain. The block-diagram of the ISCR is demonstrated in Figure 3.3-4. The initial step is the same as CSR and then the solution is improved on each *n*-th step until it converges.

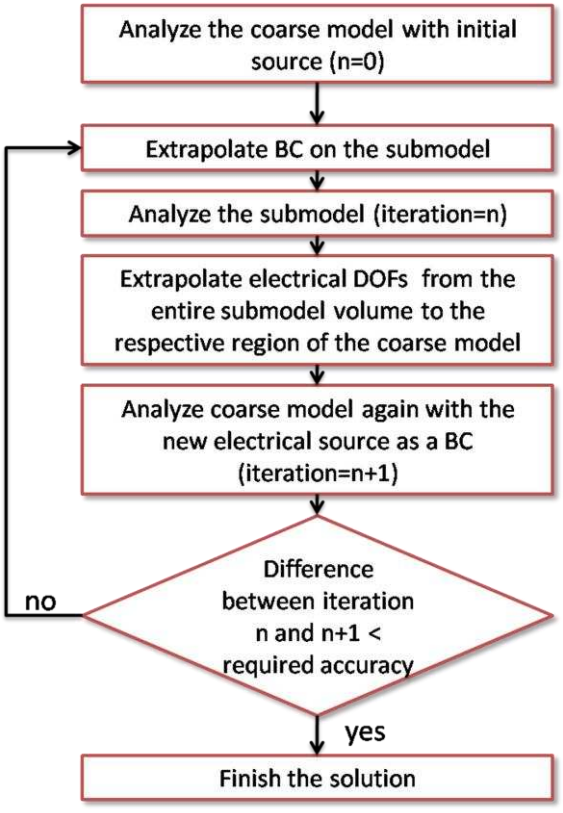

Figure 3.3-4. Block-diagram of Iterative Combined Submodelling Routine (ICSR)

This procedure could be also used in a static analysis with a mesh convergence criteria being run on the second step (second box in Figure 3.3-4). In presented work the performance of ICSR was not tested due to specific areas of application. Transient multi-scale analysis is a very premature field of research and further investigation is required in order to obtain ICSR parameters and optimize its performance for particular cases. Authors believe that for each particular problem new routine optimization analyses must be done.

Most bioelectrical problems are considered quasistatic with a good level of approximation. The frequencies of the signal in biological structures are not higher than 1MHz. So transient effects have no influence on the total solution [15].

3.3.3.4 Multi-Stage Submodelling Approach

Sometimes the source of the interest inside the main model is so small that one submodelling region cannot approximate the solution near the source properly. In this case increasing the size of submodelling region is the only option. However, increasing the size of the submodelling region leads to higher number of elements inside the submodel in order to satisfy required accuracy. This can be avoided by introducing the "submodel-in-the-submodel". Extrapolating this further allows introducing multistage combined submodelling routine (Figure 3.3-5).

This technique in combination with mesh convergence analysis can decrease computational time even more by solving the optimization problem and investigating optimal number of stages and optimal element size in each case.

The complete testing of developed Submodelling approaches is accurately performed and advantages are demonstrated in paragraph 4.4.3 and Section 7.4.

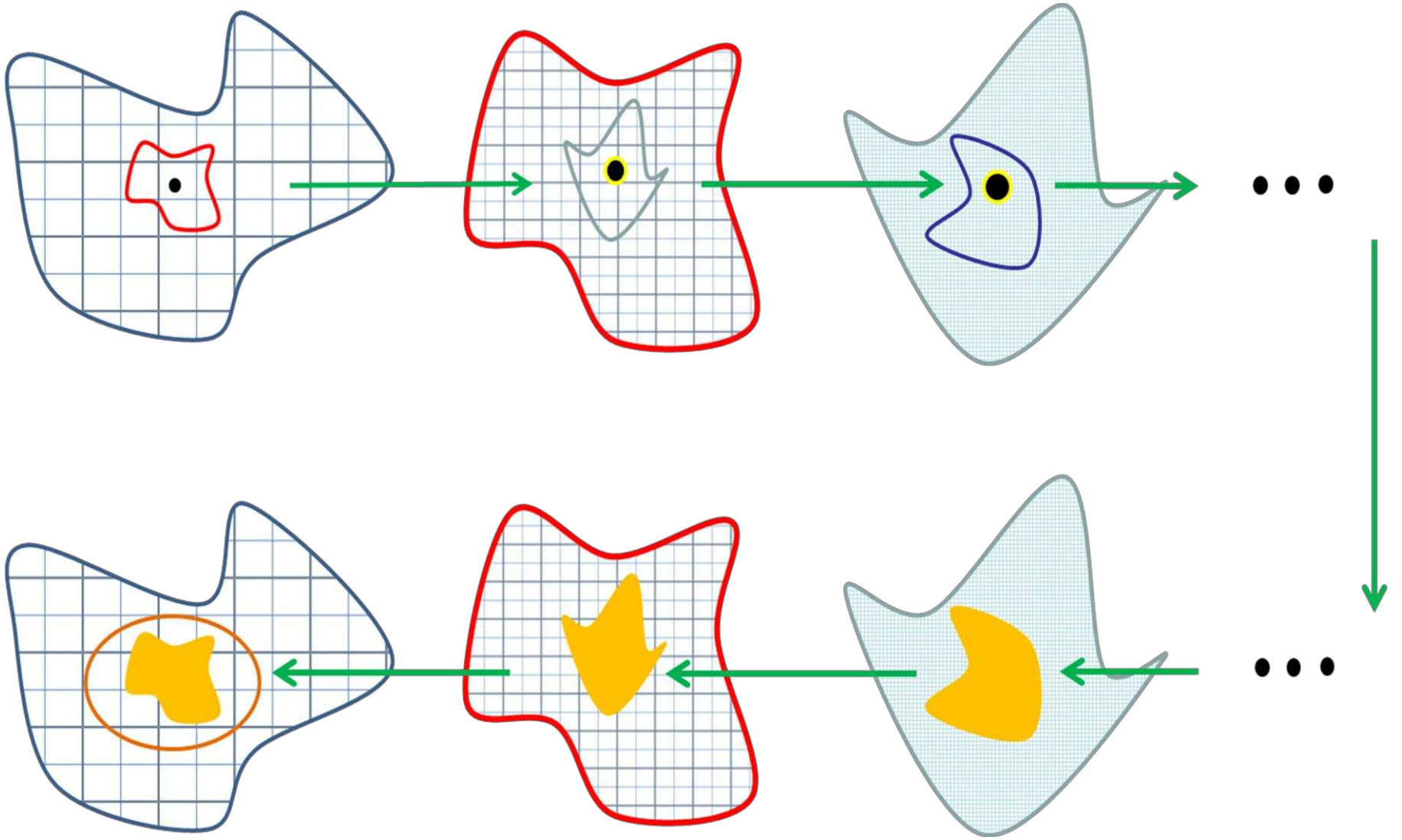

Figure 3.3-5. Combined Multi-stage Submodelling Routine (CMSR) in application to the electrical source problem

3.4 Summary

The mathematical modelling was discussed in this paper. Set of Maxwell equations was evaluated for the problem solution. Analytical and numerical solution methods were highlighted. Finite element method was chosen to be best for the problem. Solid modelling scheme implementation was discovered to be essential prior the actual finite element discretization.

Submodelling technique was discussed and novel submodelling approach designed specifically for electromagnetic analysis was developed. This approach allows significant reduction of computational time for finite element solutions (see Section 7.4 for details).

Chapter 4

Development of Realistic Brain Model

4.1 Development of Realistic-Geometry Brain Model

As was discussed in paragraph 3.3.2 the 3D finite element model was created with solid modelling approach. Parametrical CAD modelling [66] was implemented in order to achieve the ability of different region discretization and perform mesh convergence analysis for the same problem. All algorithms and results highlighted below have been published and more information could be found in author's works [67, 68].

As was discussed earlier human brain geometrical structure is very complex due to the inhomogeneity of external surfaces and anisotropy of the layout of internal tissues. Therefore geometrical reconstruction and following FE meshing of the model is only possible with employing developed computer aided technology. The following automatic algorithm for such construction has been developed and results are performed throughout this Section.

The high-quality MRI is used as initial data of the model reconstruction tool-chain. Commonly full MRI scan consists of about 150 flat 2D slices with 1mm spatial resolution. Conventionally slicing is starting from the top of the head, and finishing with the beginning of the spinal cord. Slices are stacked along z-axis with 2mm gap in between, and all together they are forming the whole-brain volume image (DICOM, REC, or NRRD clinical image formats). According to the underlying physics of MRI technique, each flat 2D image is the complete representation of the internal brain structure in terms of tissue recognition. Physical division on the white and grey matter is used as the first level approximation of the brain matter. Boundaries between these tissues are the most important in our problem in terms of both geometry and material properties; therefore grey/white matter division is kept

throughout the full procedure. The final reconstruction algorithm consists of several steps described below.

4.1.1 Step 1: Detection of 2D External Boundaries on MRI Slices

Initial preparations with MRI images should be done in order to perform following steps. This standard procedure of filtering includes well-known algorithms [69], which were taken directly from literature and/or existing image processing soft-ware:

1) Gaussian noise filtering

2) Optimized black-and-white filtering

All filters were implemented with MIPAV[70] open software platform, developed by Center of Information Technology (CIT) of US National Institute of Health. Other filters can also be applied for sharpness, noise reduction, artefact rejection, and other image improvements (see Appendix 2 for full list of applied filters)

The first actual part of this step after filtering is the white/grey matter detection. The detection algorithm is based on the combination of existing edge detection algorithms [71, 72] and Region Growing algorithm [72, 73]. It was performed in the MIPAV software discussed earlier. Then the edges of white and grey matter is detected automatically and stored in the file as parametrical spline curves in 2D. The result of first two steps can be observed in Figure 4.1-1.

This procedure is repeated for each MRI slice. So the outcome of this step is 150 files with stored parametric edges for both white and grey matter. Note, that the internal edges of grey matter shell be identical to the external edges of white matter. Therefore this step contains comparison and appropriate semi-automatic correction of the white matter boundaries. Obtained boundaries must be manually checked to avoid false detections and boundary intersections.

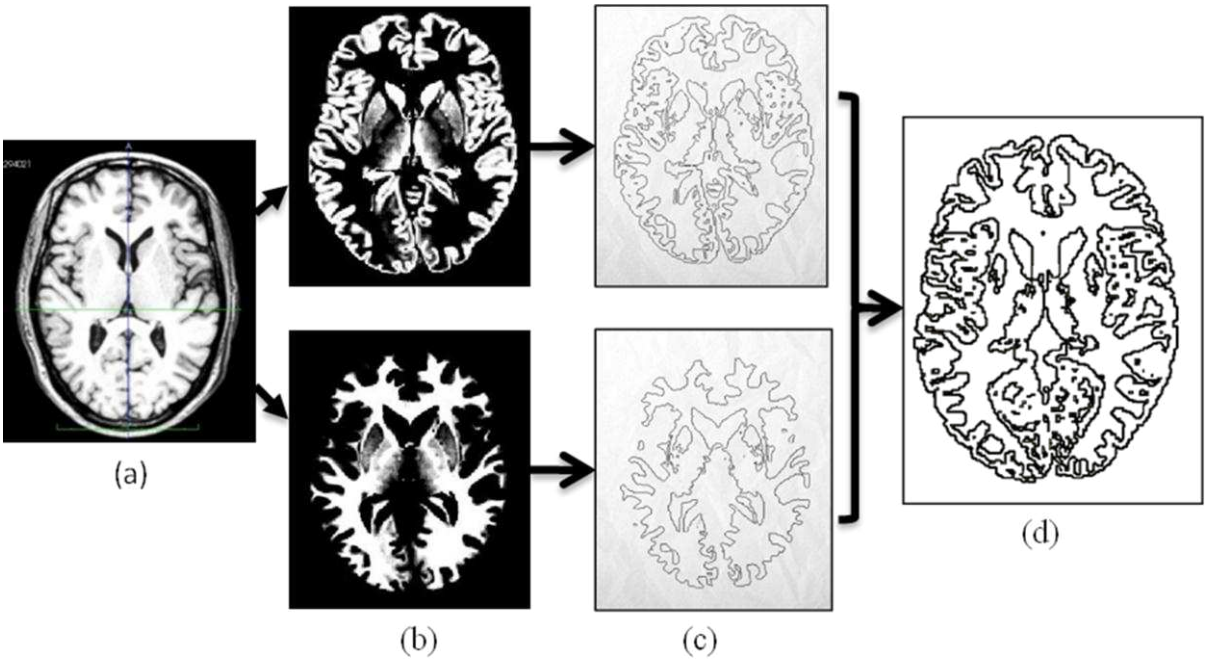

Figure 4.1-1. (a) Typical MRI slice. (b) Accurate detection of edges of grey and (c) white matters. (d) Resulting edges (isolines) of grey and white matters

4.1.2 Step 2: Creation of High-Quality 3D-Surface Model

4.1.2.1 Geometrical Parameterization and Closure

During this step each of the 2D parametric curves is automatically transformed into 3D space by stacking respective slices one on top of each other with the 2mm distance between them according to the resolution step of MRI.

Despite the general geometrical complexity of brain surface, it is isomorphic to a flat plane (it is not self-intersecting) due to its biological nature. Therefore the edges of the white and grey matter are organized, cannot self-intersect, and always form closed contours. The Geometrical Closure Algorithm (GCA) [74] is performed together with the self-intersection automatic checking [75] in order to close all open contours left after previous stages. Resulting 3D spline curves which are combined together is shown in Figure 4.1-2.

4.1.2.2 3D Parametrical Surface Lofting

The most significantly developed part of the geometrical reconstruction is the special Surface Lofting Algorithm. This algorithm allows automatically generating and connecting external surfaces of the white and grey matter of the human brain with previously discussed combination of 3D parametrical curves representing the edges of each slice.

General surface lofting procedure is well-known, commonly used in CAD software and can be found in [76]. Briefly it is the method of surface creation which is based on two curves (beginning of the surface and its end). The network of curves which are perpendicular to the main spline is created with the specified boundary conditions. This network then becomes a NURBS (Non-uniform rational B-spline) surface in 3D. Our approach is based on this method with the specific modifications discussed below.

Each 2D slice contains the boundary of the reconstructed object. Therefore the surface connecting boundaries of one slice with the boundaries of another slice should be created for each pair of slices. Resulting surface boundaries have to be kept with no intersection. The example of this lofting procedure is demonstrated in Figure 4.1-3. Let us assume 3 slices stacked together with one curve (boundary)

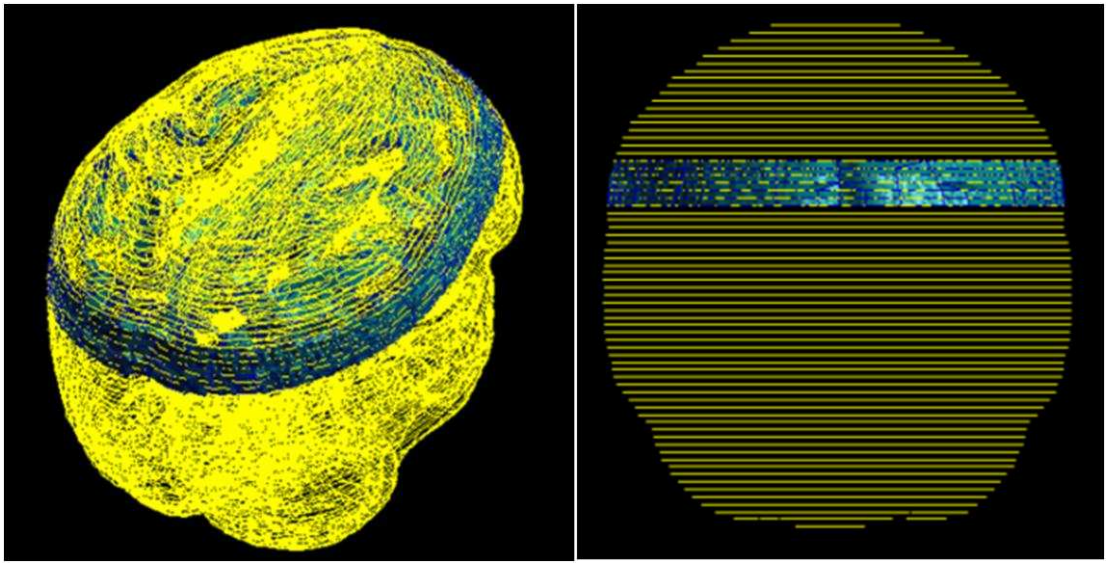

Figure 4.1-2. Parametrical spline curves representing geometrical boundaries of the brain, isometric view (left), and view perpendicular to the slice surface view (right)

being placed on each slice. Let n be the number of the middle slice, hence C_{n-1}, C_n, and C_{n+1} are the curves of $(n-1)$-th, n-th, and $(n+1)$-th slice respectively. Assume that the NURBS surface between $C_{n-1}$and C_n has been already created (blue). The NURBS mesh for this surface contains curves $< D^1_{n-1}, \dots, D^4_{n-1} >$. These curves intersecting with the main curve C_n give the points of intersection (base points) $< P^1_n, \dots, P^4_n >$.

Procedure starts with the evaluation of intersection points for curve C_{n+1}. The number of points in general case is chosen to be exactly the same as for the previous main curve C_n. The position of each point P^m_{n+1} is found by the minimal distance from the point P^m_n to the curve C_{n+1}:

$$P^m_{n+1}: \quad d(P^m_{n+1}, P^m_n) = min\big(d(P^m_n, C_{n+1})\big); \tag{4.1-1}$$

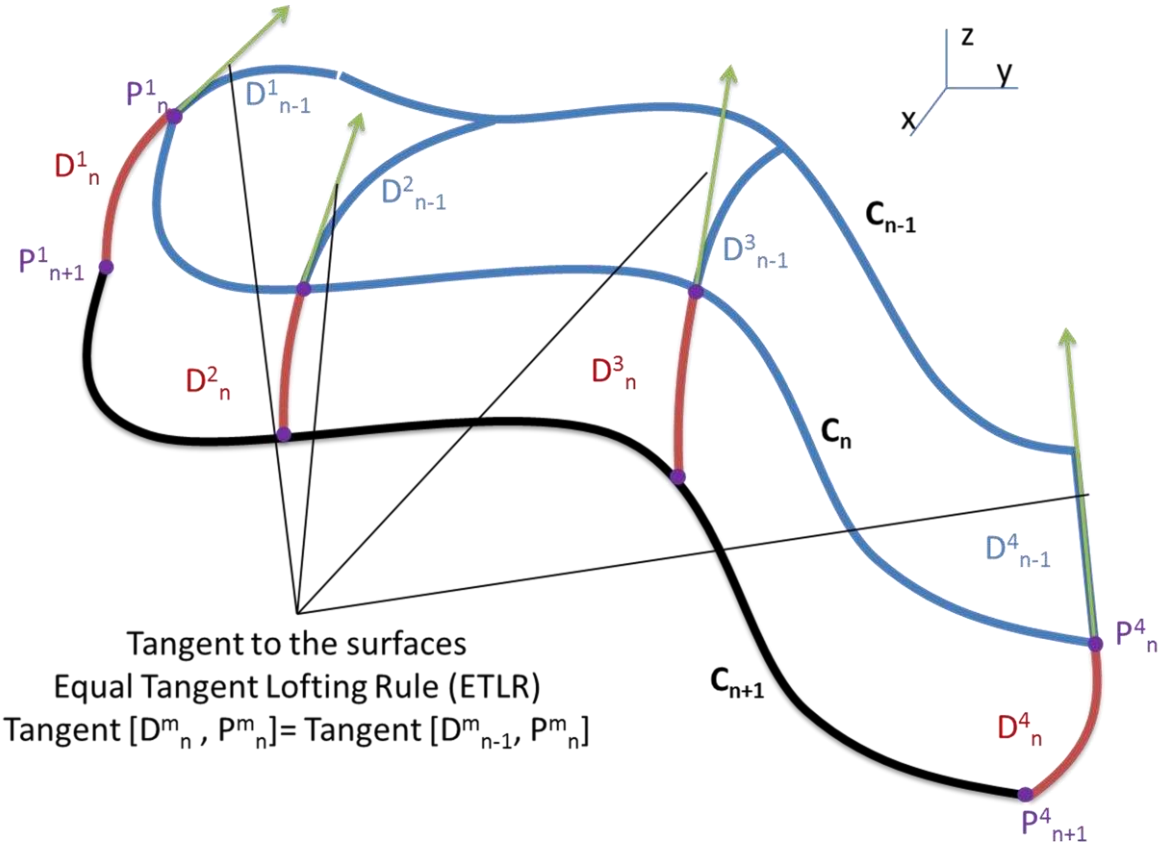

Figure 4.1-3. Lofting procedure for 3 slices (see explanations in text)

where $\mathrm{d}(,)$ is the distance operator in 3D (distance between two points or point and curve).

After all points have been evaluated the NURBS curve $\mathrm{D}_{\mathrm{n}}^{\mathrm{m}}$ (quadratic spline) is created between each corresponding point by the rule of tangential equivalence with the previous NURBS surface:

$$\mathrm{D}_{\mathrm{n}}^{\mathrm{m}} = \mathrm{D}_{\mathrm{n}}^{\mathrm{m}}\{\, \mathrm{P}_{\mathrm{n}}^{\mathrm{m}}; \mathrm{P}_{\mathrm{n+1}}^{\mathrm{m}} \mid t[\mathrm{D}_{\mathrm{n}}^{\mathrm{m}}, \mathrm{P}_{\mathrm{n}}^{\mathrm{m}}] = t[\mathrm{D}_{\mathrm{n-1}}^{\mathrm{m}}, \mathrm{P}_{\mathrm{n}}^{\mathrm{m}}] \,\}; \tag{4.1-2}$$

Here $t[\mathrm{D}\,, \mathrm{P}]$ is the tangent (gradient) operator (tangent to the curve D created from the point P). The boundary conditions on points $\mathrm{P}_{\mathrm{n+1}}^{\mathrm{m}}$ are free.

Assembly of curves $< \mathrm{D}_{\mathrm{n}}^{1}, \ldots, \mathrm{D}_{\mathrm{n}}^{4}; \mathrm{C}_{\mathrm{n}}, \mathrm{C}_{\mathrm{n+1}} >$ is forming the basis for resulting NURBS surface. This procedure is continuously operating from the first slice to the last one until the whole object will be covered by NURBS surfaces. The procedure in general is quite simple if the number of curves is the same at each slice, however for the complex geometry there is a number of common cases must be considered specifically. Due to the fact that all curves in case of MRI-generated object is closed contours, specific algorithms, cases, and exclusions which must be applied, can be collected in following categories.

4.1.2.2.1 One-in-One Transition with Branching (OOTB)

This case operates with two closed contours (one contour is located on each slice). In some cases the minimal distance problem from point to the curve has more than one solution (Distance function will have more than one local minimum near the area, as shown in Figure 4.1-4). In this situation both solutions are preserved and next slice will contain more points. New additional surface is created with three containing curves (red).

4.1.2.2.2 Two-in-One Transition (TOT)

This case appears when n-th slice contains more contours than $(\mathrm{n}+1)$-th. In Figure 4.1-5 the example of this situation is shown. First, the curve $\mathrm{D}_{\mathrm{n}}^{1}$ is evaluated as the shortest straight line between two contours of slice n:

$$D_n^1 = D_n^1\{\, P_n^{1,6}; P_{n_2}^{1,6} \;\mid\; \| P_n^{1,6}, P_{n_2}^{1,6} \| = \min \| C_n^1, C_n^2 \| \,\}; \tag{4.1-3}$$

Then points P_n^1 and P_n^6 are evaluated by the intersection of the perpendicular of the D_n^1 going through its centre, and C_{n+1}^1. Then two triangular surfaces are obtained (red), and the rest of the curves are processed according to the main algorithm.

4.1.2.2.3 Many-to-One Transition (MOT)

This case is processed similar to TOT with the addition of the central flat trimmed surface (Figure 4.1-6, red dashed), which is positioned directly in n-th slice.

4.1.2.2.4 One-two-Many Transition (OMT)

In this situation one of the OOTB, TOT, or MOT procedures is inversed and appropriately applied. Note that only the branching points and corresponding additional straight lines must be found via inverse procedures. For the rest of the regions the normal procedure should follow after the transition region evaluation.

4.1.2.2.5 First and Last Slices

For the first and last slices the trimmed flat surface are generated based on contours. First set of NURBS between first and second slice are generated with the minimal curvature BC on both cases. The final set of NURBS surfaces uses the minimal curvature condition only on the final end (Figure 4.1-7).

4.1.2.2.6 Other Exclusions

There are lots of other different cases and exclusions less commonly have been met during the procedure, but generally it is the problems of programming, counting points, and algorithm implementation.

The entire procedure was implemented using C++ in combination with internal CAD library for standard lofting functions (SolidWorks Mechanical 2008, Dassault Systemes Inc.), CAD geometry processing kernel (Parasolid XT), and visualization platform (MSC.Patran). The result of the procedure during the operation after processing of 7 human brain MRI slices in the middle of the brain can be observed in Figure 4.1-8.

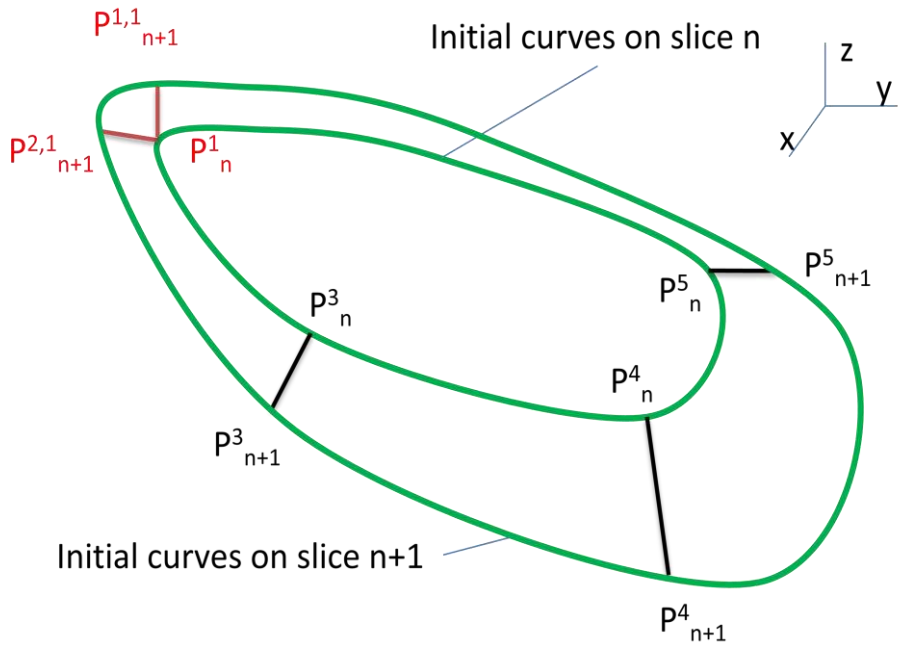

Figure 4.1-4. Points branching in One-to-One transition case

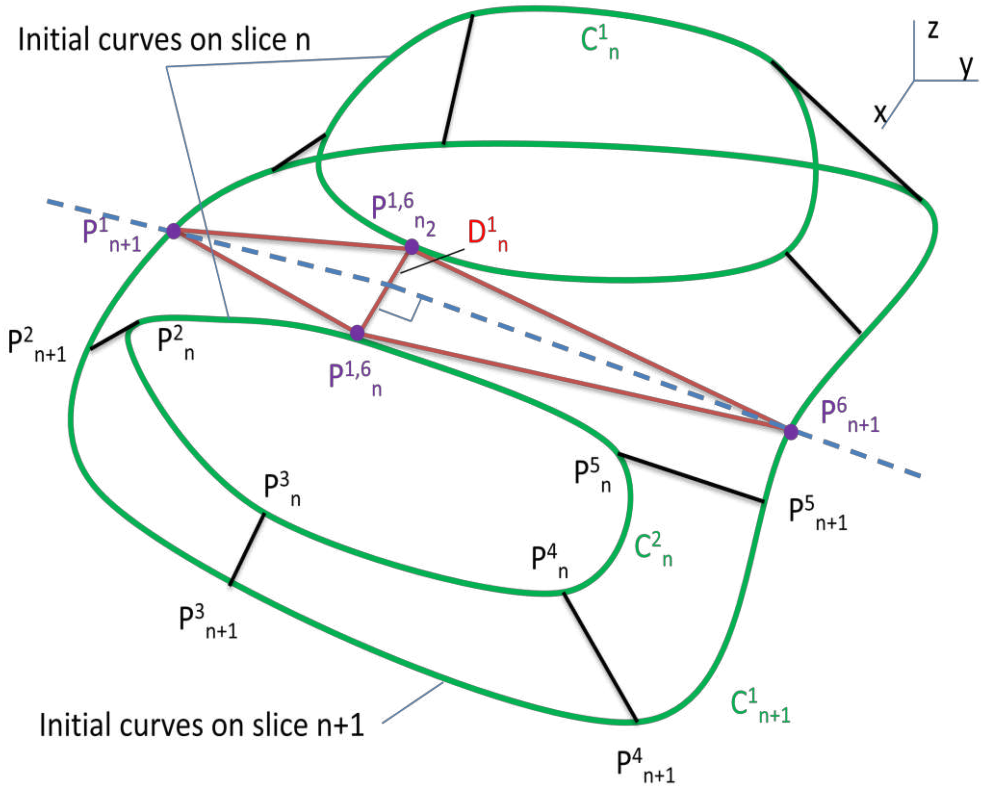

Figure 4.1-5. Two-in-One Transition case

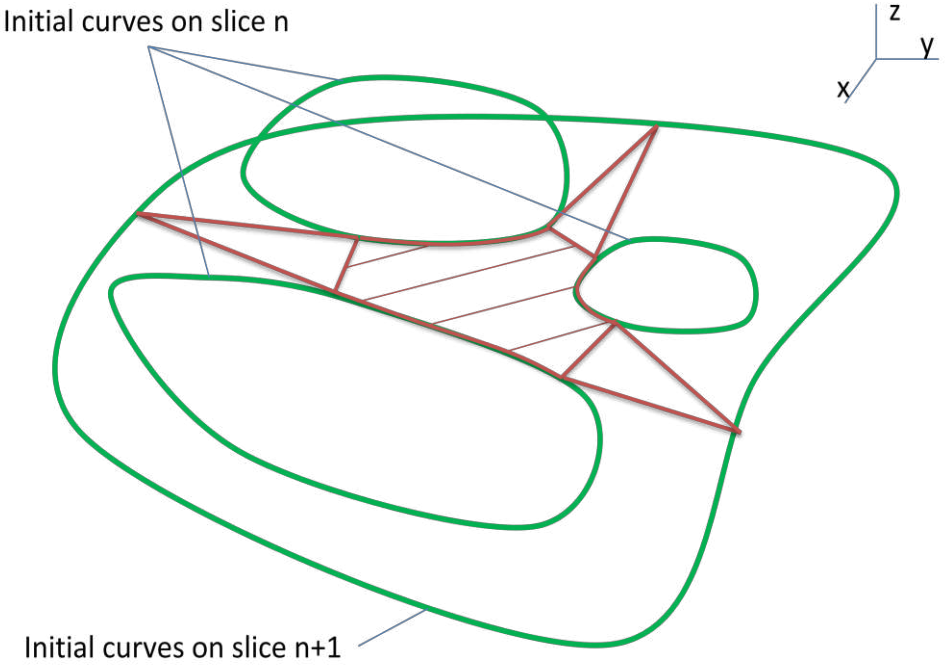

Figure 4.1-6. Many-to-One Transition case

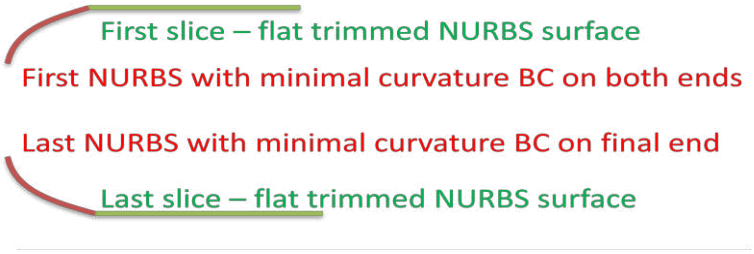

Figure 4.1-7. First and last slices NURBS generation

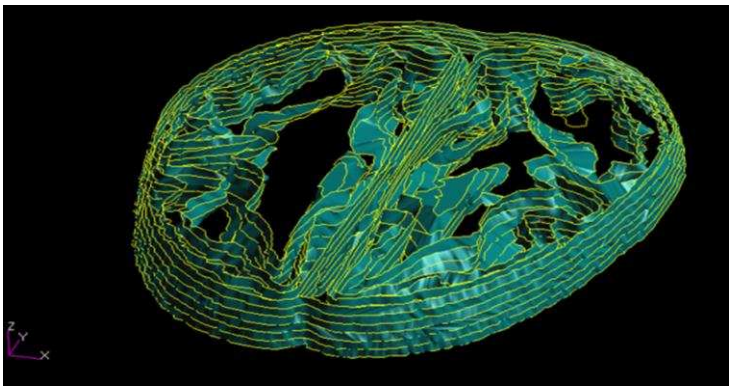

Figure 4.1-8. Automatic Lofting Procedure in process. Human brain grey matter (external) and white matter (internal) NURBS for 7 mid-brain slices

TABLE 4-1. PARAMETERS OF THE SOLID NURBS MODEL OF THE HUMAN BRAIN

Parameter	Value
Number of slices	150
Total number of NURBS surfaces in white matter boundaries	30 000
Total number of NURBS surfaces in grey matter boundaries	10 000

White matter external boundaries for whole-brain model after Lofting Procedure implementation is demonstrated in Figure 4.1-9. Top view represents general overview of NURBS model, and bottom picture shows the model in perpendicular to the slice planes projection. The parameters of the full brain model could be observed in Table 4-2.

The model thus obtained and stored in CAD format and is ready for transferring into any suitable computational environment for subsequent simulation.

4.1.3 Step 3: Obtaining 3D Parametric Ready-to-Perform Model

The reconstructed model is very accurate in terms of geometry, and it reaches the theoretical limits of MRI according to the presented algorithm as there is no accuracy loss during the reconstruction process.

However in some cases less accurate and simplified model may be required (for example in applications like testing solution or for any other proposes, where accuracy is not so important). Specifically for those cases the Smoothing Procedure has been developed. It is optional, and therefore the accuracy of obtaining geometry after this method was not tested. However the method can be applied with required accuracy parameters which is subject to further development.

The procedure is based on temporary triangulation and NURBS smoothing algorithm, which can be performed with the help of any existing reverse engineering

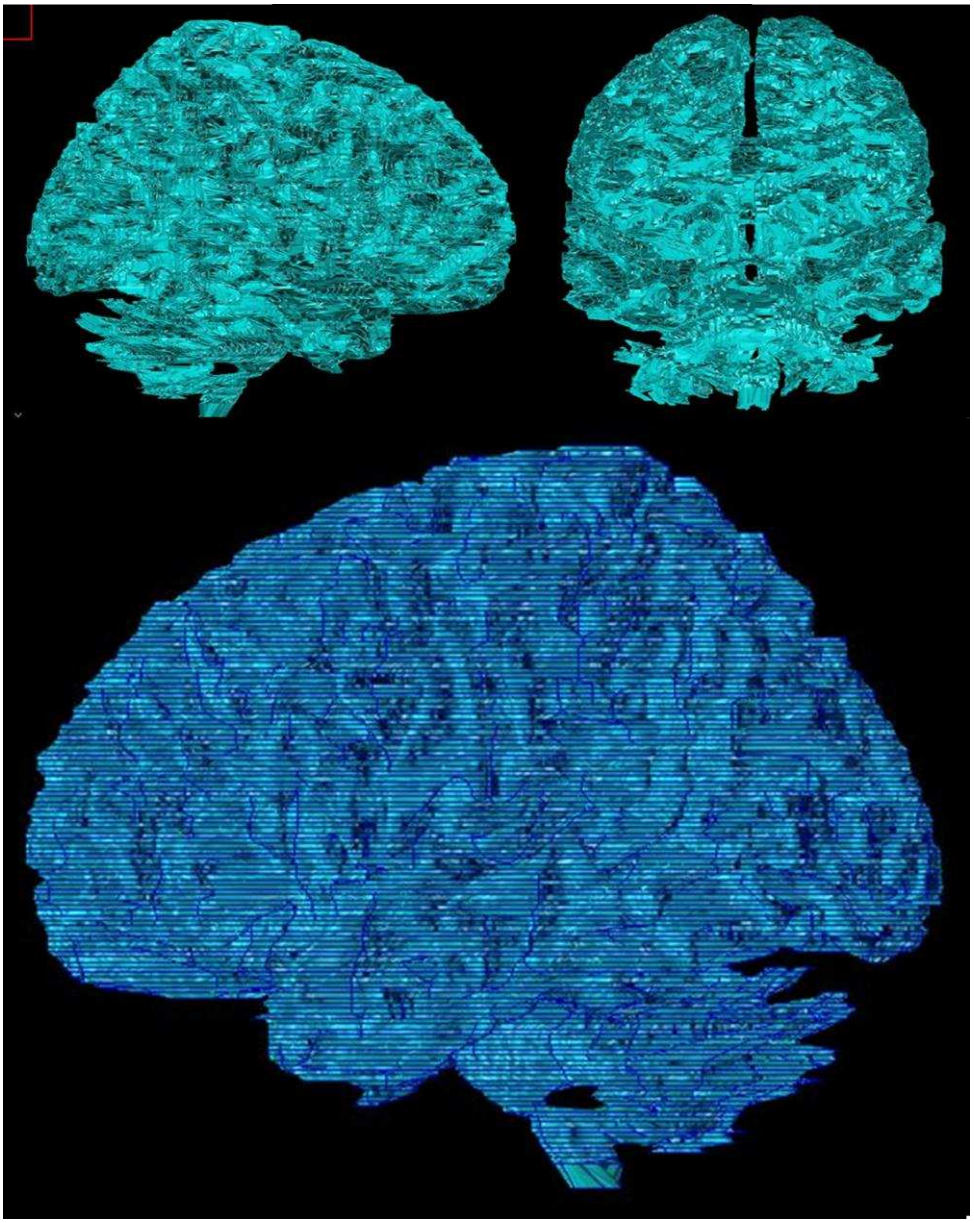

Figure 4.1-9. White matter external NURBS surfaces after Lofting Procedure implementation

software [66]. The whole-brain geometrical model after smoothing procedure application is shown in Figure 4.1-10.

The resulting achieved features with respect to general CAD properties of the brain model are following:

- 640 external NURBS surfaces of Grey matter external boundary
- 560 external NURBS surfaces of White matter external boundary
- Ability to change the model according to the initial data

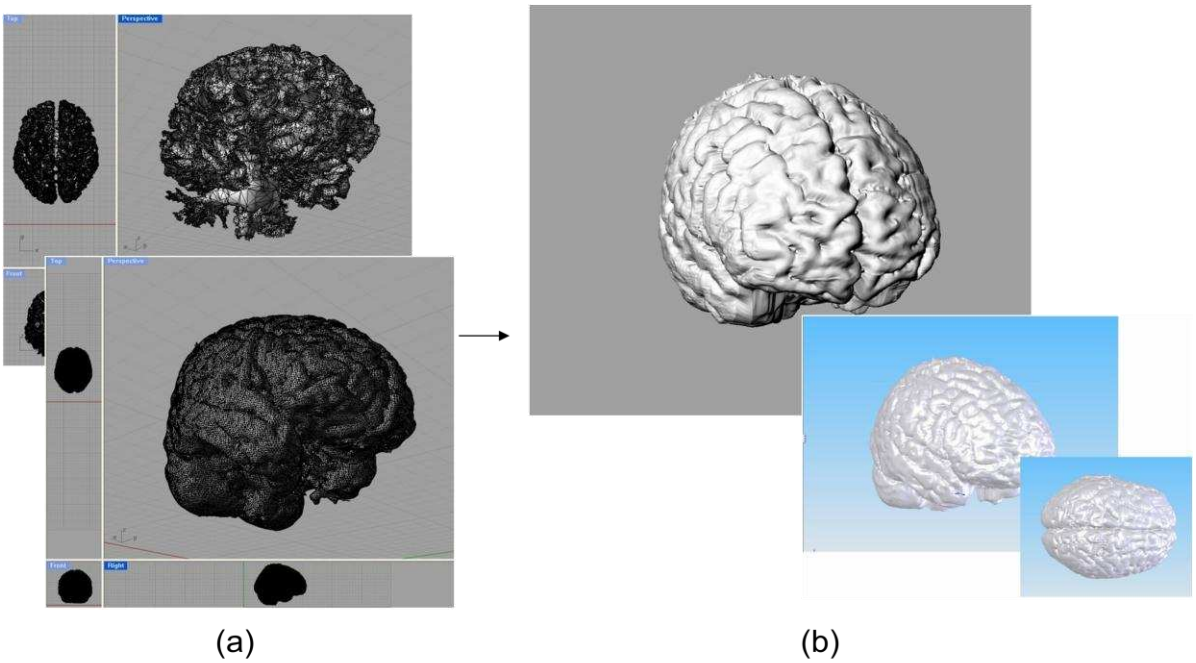

Figure 4.1-10. (a) Polygonal smoothing of the white and grey matter. (b) Solid CAD model representation

- Ability to use Submodelling technique on each study
- Flexibility in choosing the FE system to use
- Flexibility in mesh building, mesh controlling and mesh changing on each step of analysis
- Flexibility in transferring the model into any known geometrical formats

The final CAD human brain model outlines for white and grey matter are visualized in Figure 4.1-11 and Figure 4.1-12 respectively

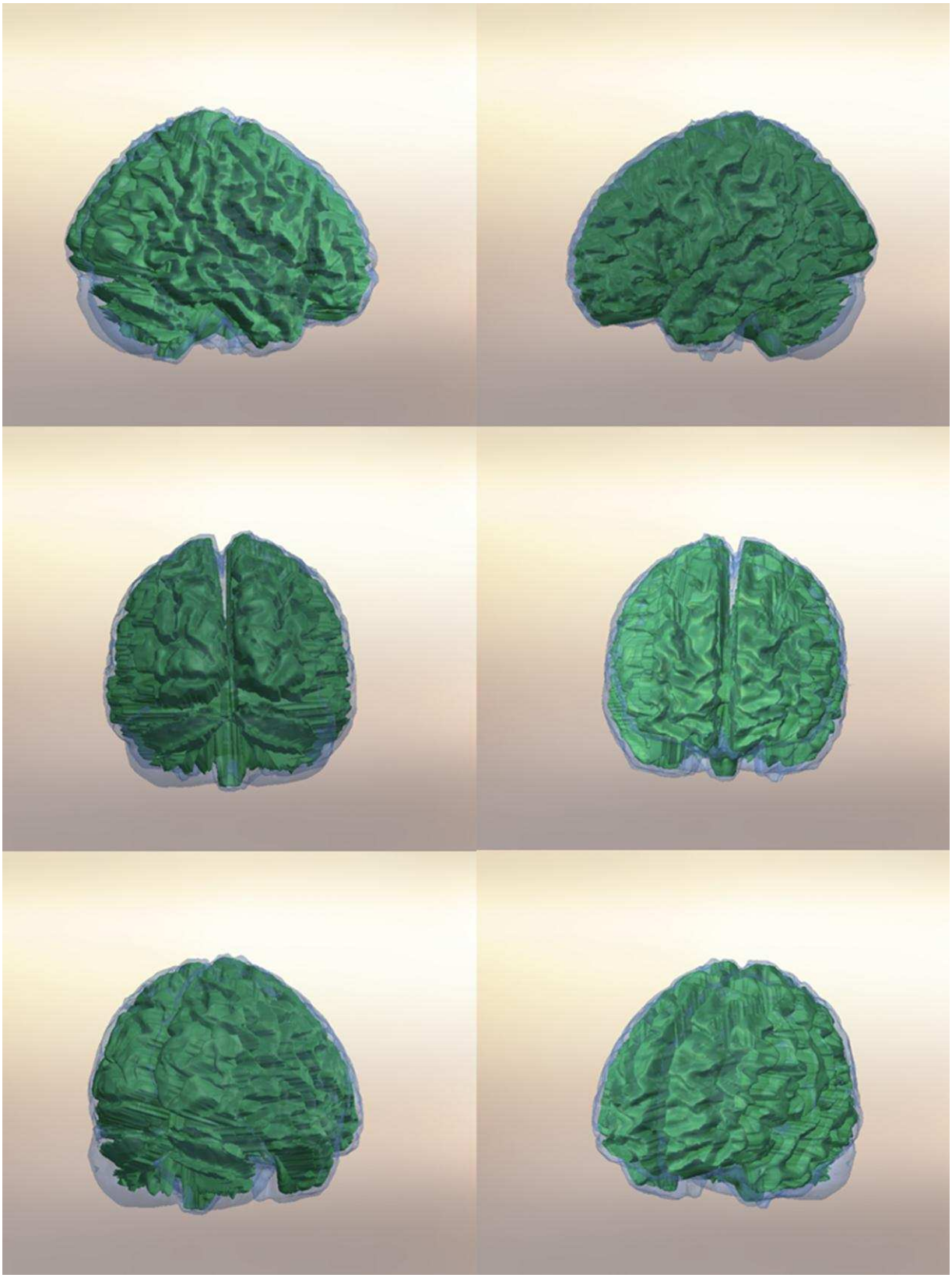

Figure 4.1-11. Final CAD whole-brain model. White matter outline

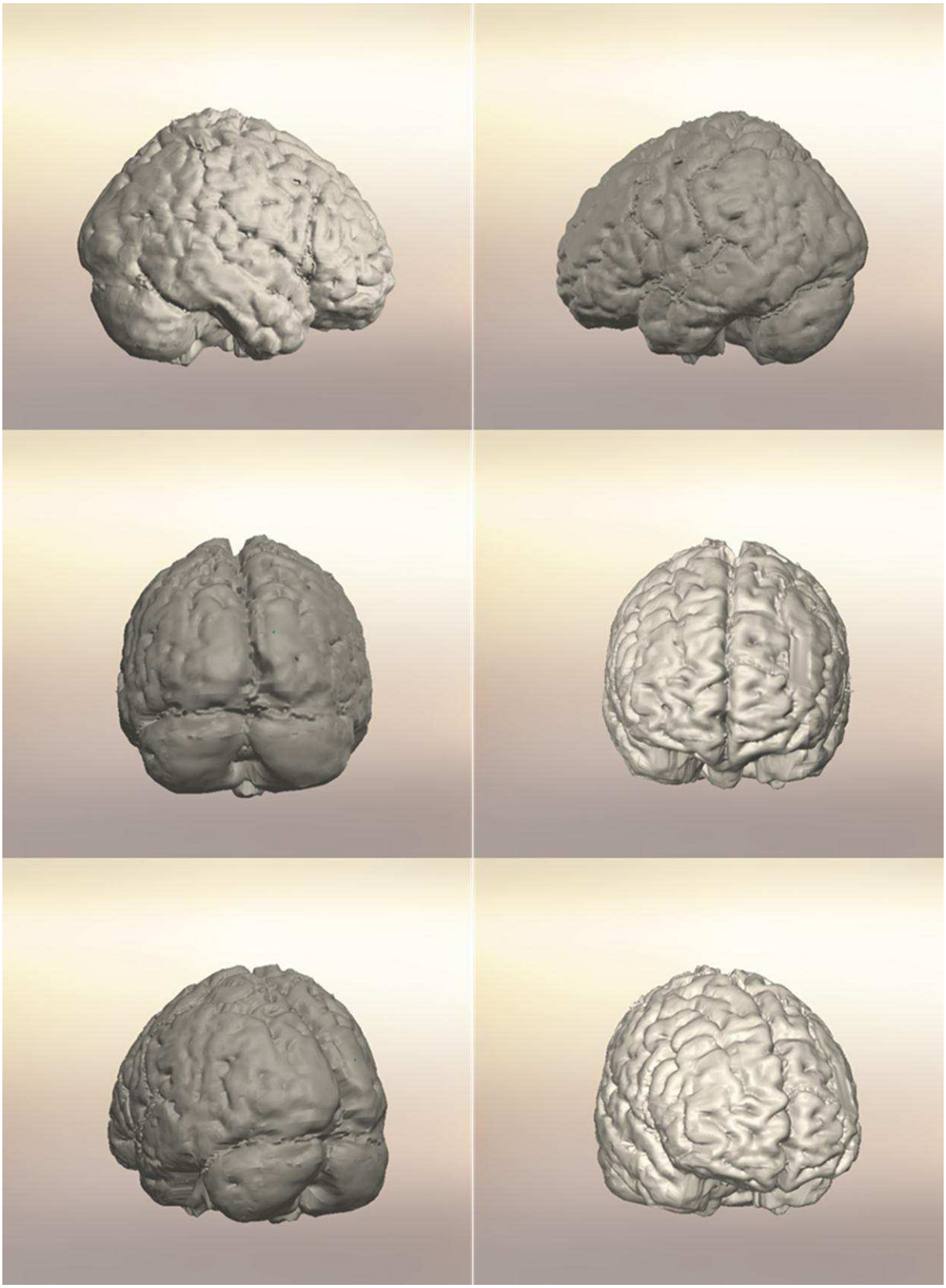

Figure 4.1-12. Final CAD whole-brain model. Grey matter outline

4.2 Test Problem and Results of Simulation for Realistic-Geometry Brain Model with Simple Current Source

Developed in previous Section reconstruction algorithm has been implemented for creation of the brain model of a 24-year male healthy subject, for which MRI brain images were taken from [77] (see Appendix 1 for set of images). The resulting CAD model was transferred into the FE software ANSYS. Then FE mesh generation was performed. The initial parameters of the model can be observed in Table 4-2. In order to determine the optimal parameters of the model and avoid any possible mathematical errors, forward magneto-static analysis in this case was performed in application to MEG tomography with respect to the different mesh density. In Figure 4.2-1 and Figure 4.2-2 the brain FE model and the position of the detection surface is shown. The detection surface has been approximated in form of an ellipsoid. The current source was chosen to be 1mm thin conductor carrying the 1A current was placed in the center of the brain model vertically.

The example of resulting magnetic field produced by single short conductor could be

TABLE 4-2. PARAMETERS OF THE FE MODEL

Parameter	Value
Number of finite elements	100 000 - 1 000 000
Number of degrees of freedom	200 000 - 2 000 000
Solution	Magnetostatic, linear
Accuracy criteria	Mesh size according to the comparison with the analytical solution
Permeability of the media	Air ($\mu = \mu_0$)
Conductivity of the media σ	Not used in magnetostatic analysis

observed in Figure 4.2-4 and Figure 4.2-5. Using these results, the tables of the error depending on mesh size were created and the mesh convergence was discovered (see Figure 4.2-3). At the same time analytical results for different points of the detection surface were calculated and compared for each mesh size with the following equation (simple magnetic field of the short current conductor) [8]:

$$\boldsymbol{B}(\boldsymbol{r}) = \frac{\mu}{4\pi}\frac{I\boldsymbol{R}\times\boldsymbol{L}}{|\boldsymbol{R}|^3} \quad (4.2\text{-}1)$$

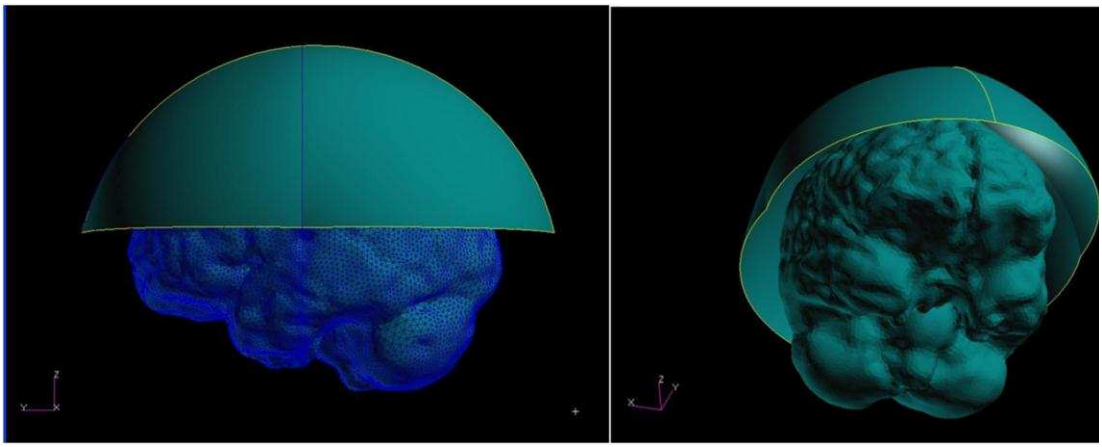

Figure 4.2-1. The position of the detection surface in relation to the brain mode l

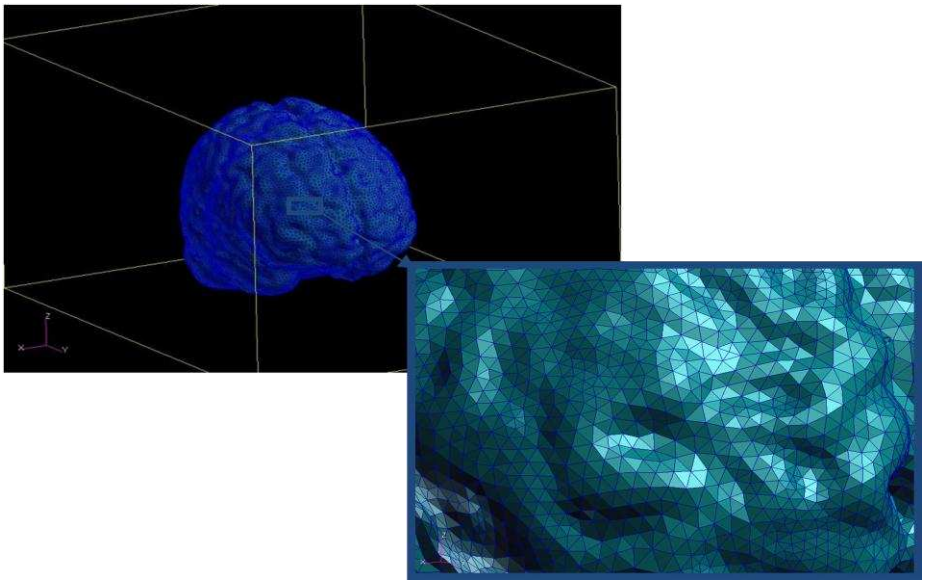

Figure 4.2-2. The FE model and mesh sample

where $\mu = \mu_0$ is the permeability of the media, $\boldsymbol{R} = (\boldsymbol{r} - \boldsymbol{r}')$ is the vector distance from the observation point to the center of the conductor, $I = 1\mathrm{A}$ is the current density, and $\boldsymbol{L}$ is the vector of the conductor length ($|\boldsymbol{L}| = 1\mathrm{mm}$). The optimal mesh size was chosen according to the maximum error criteria of 0.5%. According to the Figure 4.2-3 the size of the element of 3mm with the approximate 500 000 total number of elements satisfies this criteria.

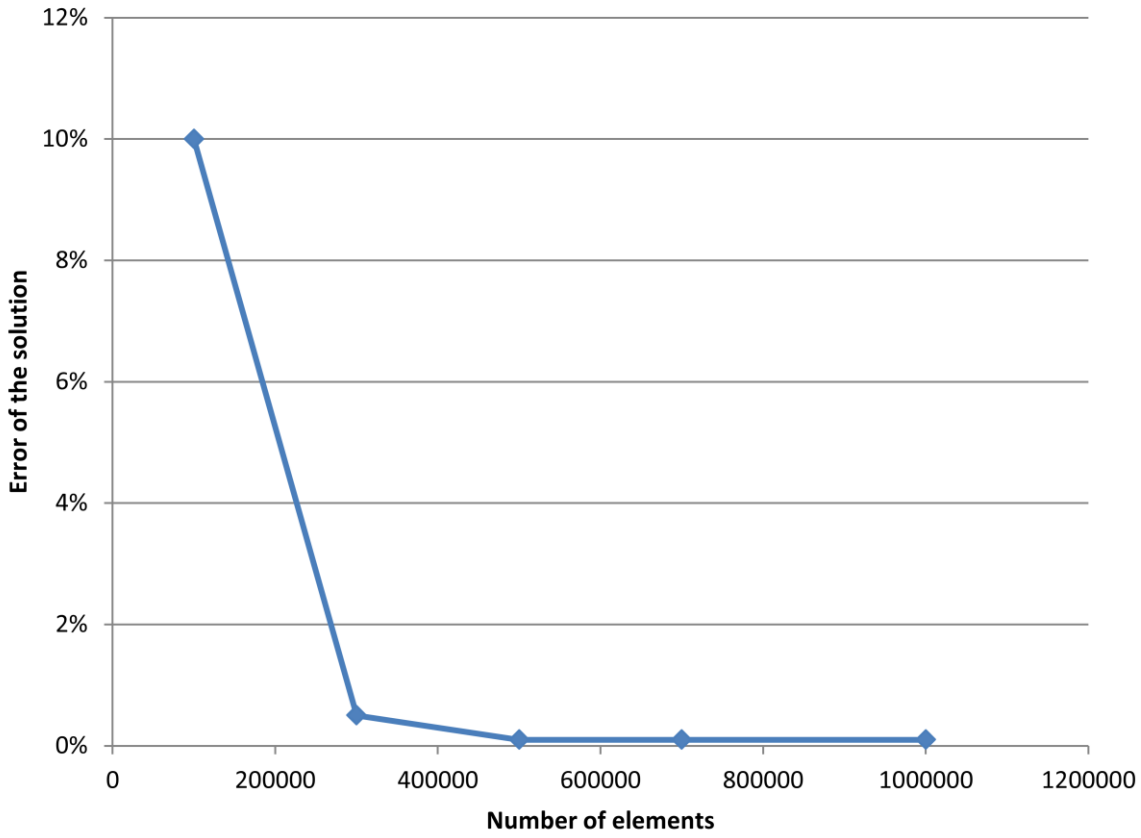

Figure 4.2-3. Mesh convergence graph

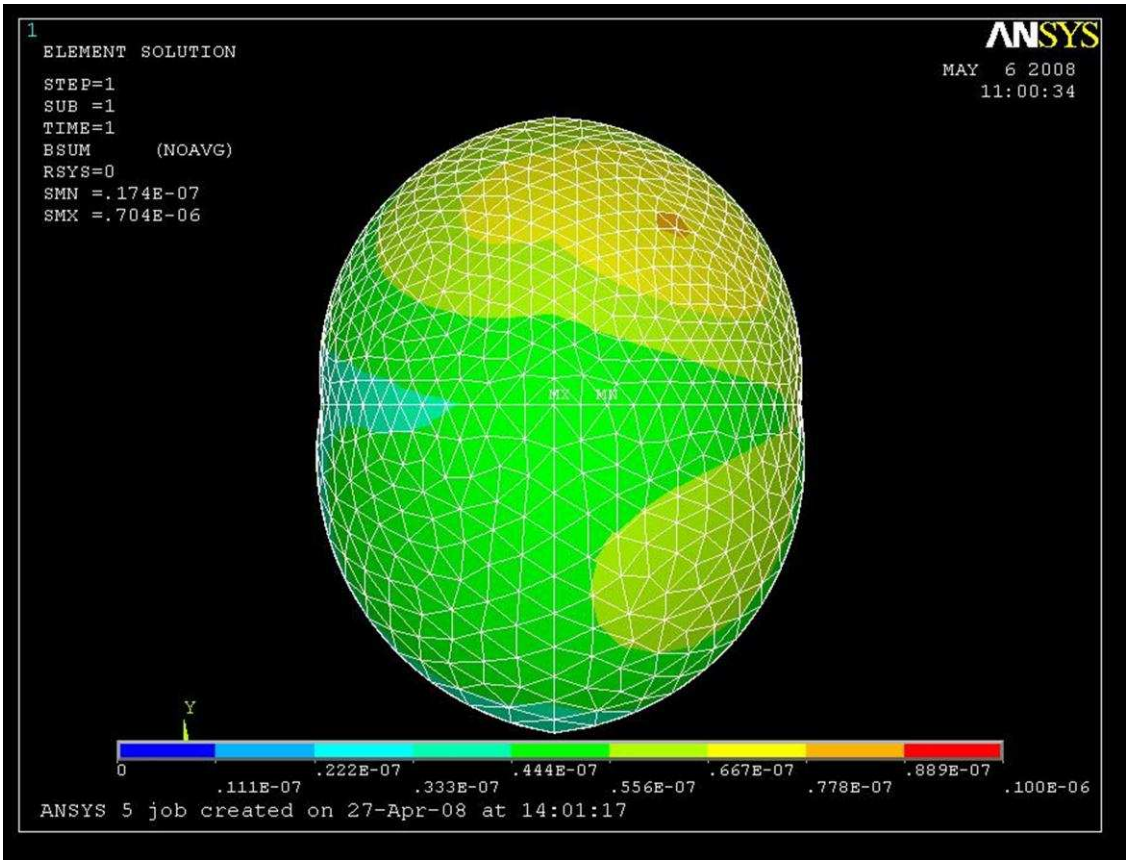

Figure 4.2-4. Magnetic field produced by the vertical straight current source mapped on the detection surface

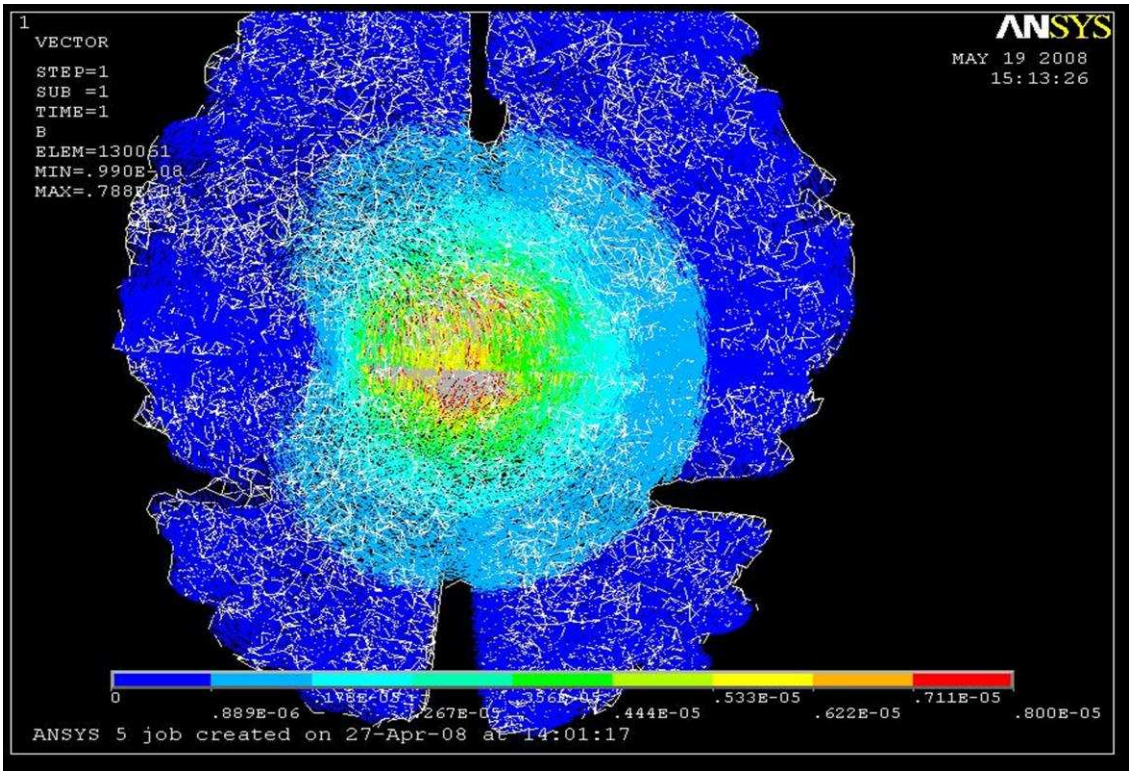

Figure 4.2-5. The resulting magnetic field produced by the vertical straight current source mapped on the central slice (white matter) for the optimal mesh size

4.3 Development of Realistic-Material Property Brain Model

The real brain structure is totally different from the convenient isotropic approximation. The great influence of the secondary volume currents on the solution was clearly shown in [18]. Results obtained in this paper fundamentally prove that sufficient part of the resulting magnetic field is caused by the secondary currents which appear as a result of preliminary electric and magnetic field distribution. Secondary current distribution is linearly dependent on the conductivity of the media according to equation (3.1-7). With respect to human brain anatomy, conductivity properties are fiber-structured and sufficiently anisotropic.

Complex anisotropy is caused by the high axonal density of the white matter and the fact that deactivated axon can provide ion current in only one direction. Although there is no known direct non-invasive way of measuring the conductivity distribution in entire human brain, anisotropic conductivity tensor can be directly linked to the anisotropic diffusion coefficient. This assumption is delivered with the help of knowledge about biological structure of the neuronal axon. It is proved to be accurate and reliable and has been widely used in clinical studies despite its empirical formulation [78].

DT-MRI (Diffusion Tensor MRI) is the only method which provides non-invasive anisotropic diffusion tensor mapping [78-81]. The anisotropic diffusion tensor could be defined as [79, 82]:

$$\mathbf{D} = \mathbf{D}(\mathrm{x}, \mathrm{y}, \mathrm{x}) \tag{4.3-1}$$

This tensor represents the diffusion coefficient function which changes in space. As it is a tensor, it could be described in chosen Cartesian coordinate system by three main directions (eigenvectors) and the values of diffusion along these directions (eigenvalues). This representation can be written in form of diagonal matrix $\mathbf{\Lambda}$ and the matrix of eigenvectors $\mathbf{V}$:

$$\mathbf{D} = \mathbf{V}\boldsymbol{\Lambda}\mathbf{V}^{-1} \tag{4.3-2}$$

$$\boldsymbol{\Lambda} = \begin{bmatrix} \lambda^1 & 0 & 0 \\ 0 & \lambda^2 & 0 \\ 0 & 0 & \lambda^3 \end{bmatrix} \tag{4.3-3}$$

where λ^1, λ^2, λ^3 are the eigenvalues of the diffusion matrix satisfying the relation $\lambda^1 \geq \lambda^2 \geq \lambda^3 \geq 0$, and $\mathbf{V}$ is it's eigenvectors. The structure of the neuronal fiber, which has been studied based on the biological data, has unidirectional form means that the water diffusion is greatest along the direction of the neuronal fiber as it is surrounded by the myelin which is good water ion conductor [39].

Across the myelin shield water ions could not be transported, so the diffusion coefficient has its value near zero along all of the perpendicular to the fiber directions. As neuronal structure in terms of axonal structure is near the same across the white matter, the assumption can be made that conductivity of the media inside the brain is linearly dependent on the diffusion coefficient. In terms of the primary current this directly follows from the fact that myelin direction is definitely equal to the neuronal chain direction, which is the direction of the primary current distribution.

In terms of the secondary current the most conductive material inside the brain is myelin itself, and the mechanism of the secondary conduction is mostly based on the water ions inside the myelin shield. Therefore this assumption does not contradict to the mechanism of ionic current conduction for both cases and can be employed by the following analysis. Assuming equal diffusion coefficients for both types of conductivity we could deliver the law for the conductivity tensor of the brain tissue $\boldsymbol{\sigma}$ as:

$$\boldsymbol{\sigma} = \mathrm{k}\mathbf{D} \tag{4.3-4}$$

and, therefore in Cartesian coordinate system it can be represented:

$$\boldsymbol{\sigma} = \mathrm{k}\mathbf{V}\boldsymbol{\Lambda}\mathbf{V}^{-1} =$$

$$k\,[\boldsymbol{v_1}(\boldsymbol{r}) \quad \boldsymbol{v_2}(\boldsymbol{r}) \quad \boldsymbol{v_3}(\boldsymbol{r})] \begin{bmatrix} \lambda^1(\boldsymbol{r}) & 0 & 0 \\ 0 & \lambda^2(\boldsymbol{r}) & 0 \\ 0 & 0 & \lambda^3(\boldsymbol{r}) \end{bmatrix} \begin{bmatrix} \boldsymbol{v_1}(\boldsymbol{r}) \\ \boldsymbol{v_2}(\boldsymbol{r}) \\ \boldsymbol{v_3}(\boldsymbol{r}) \end{bmatrix}^{-1} \tag{4.3-5}$$

where $\boldsymbol{r} = (x, y, z)$, and $\boldsymbol{v_i}(\boldsymbol{r}) \perp \boldsymbol{v_j}(\boldsymbol{r})$, $i \neq j$. According to the known generalized average values of conductivity for the white and grey matter, which can also be measured via contrast difference between CSF and required tissues, the constant k can be calculated for each study independently in the following form [83]:

$$\mathrm{k} = \frac{\mathrm{k_{white}} + \mathrm{k_{grey}}}{2} \tag{4.3-6}$$

$$\mathrm{k_{white}} = \frac{3\mathrm{N}\sigma_{\mathrm{white}}}{\sum_{\mathrm{i=1}}^{\mathrm{N}}(\lambda_{\mathrm{i}}^1 + \lambda_{\mathrm{i}}^2 + \lambda_{\mathrm{i}}^3)}; \mathrm{k_{grey}} = \frac{3\mathrm{M}\sigma_{\mathrm{grey}}}{\sum_{\mathrm{i=1}}^{\mathrm{M}}(\lambda_{\mathrm{i}}^1 + \lambda_{\mathrm{i}}^2 + \lambda_{\mathrm{i}}^3)}; \tag{4.3-7}$$

where *N, M* are the total number of MRI value volume pixels associated to white and grey matter of the brain respectively.

In Figure 4.3-1 the color representation of the diffusion tensor is presented. The color code on this picture is related to the main diffusivity axis. In other words, the direction of the most diffusive axis in Cartesian coordinate system is highlighted. Red is for mediolateral direction (x), blue is for superiorinterior direction (z), and green is for anteriorposterior direction (y). In Figure 4.3-2 the relative level of anisotropy is plotted to illustrate the complexity of the structure.

The discussed diffusion tensor in application to the brain models used as an example in this report was delivered from the DTMRI dataset downloaded from the

'Asclepios Project' [77, 84]. This data contains averaged dataset characterized normal healthy brain structure, obtained from 40 subjects and is used as a validation atlas for DTI data reconstruction [85].

The automatic algorithm was created for obtaining the conductivity tensor $\boldsymbol{\sigma}(\mathrm{x},\mathrm{y},\mathrm{z})$ directly from the DTMRI dataset (see Appendix 3).

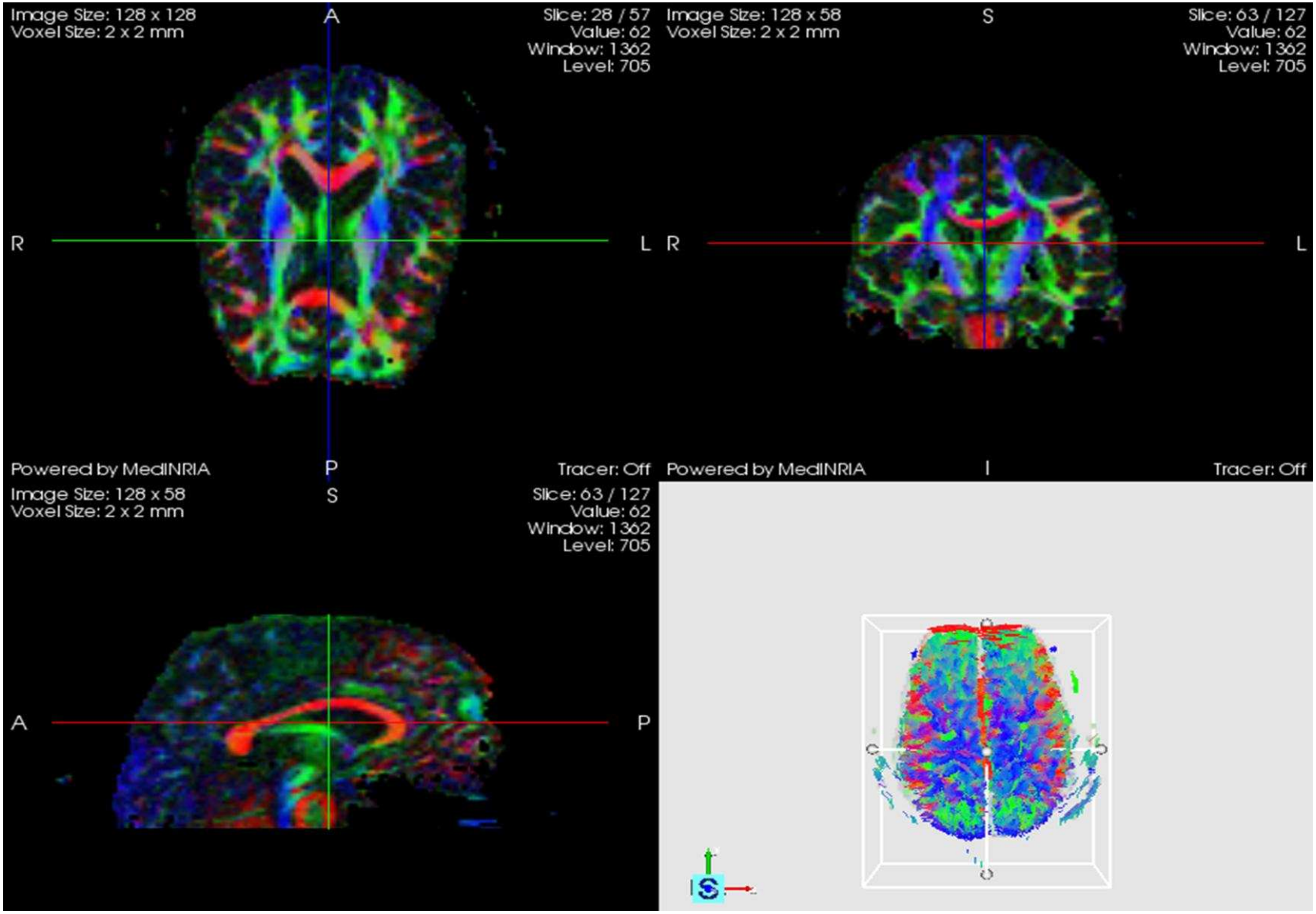

Figure 4.3-1. Anisotropic conductivity distribution. Color palette shows the main axis of anisotropy.

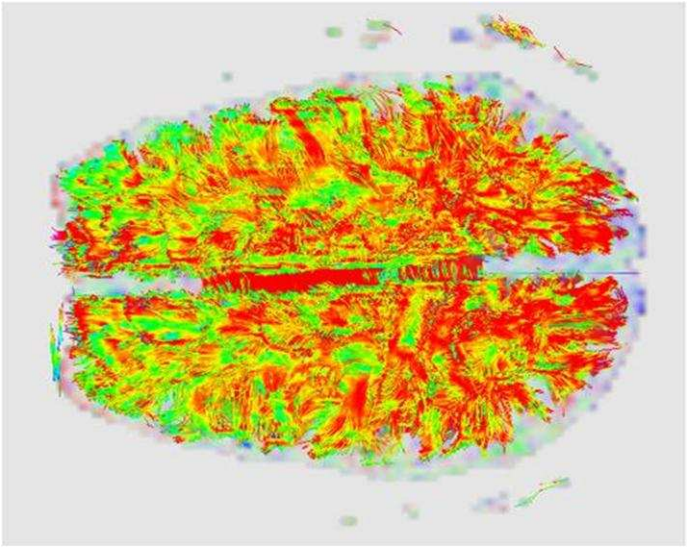

Figure 4.3-2. The level of anisotropy in the brain. From green (isotropic) to red (highly anisotropic)

Resulting properties for each segment of the FE model has been transferred and checked using developed algorithm PITA (Powerful Intersoftware Tensor Algorithm, see Appendix 4 for listing). In Figure 4.3-3 the resulting conductivity tensor for one slice is visualized. Coarse FE model has been used for visual highlighting of conductivity anisotropy. Each box represents the main directions (eigenvectors – orientation of the box) and value (eigenvalue – size of the side) of conductivity tensor for one finite element.

In Figure 4.3-4 the same result is shown in 3D for three different slices of the brain. The difference of the complex anisotropy conductivities between different parts of the brain is clearly illustrated. Also some initial validation of the obtained model and developed algorithm can be illustrated with the help of biological data. For example, the most isotropic region appeared to be the central part of the white matter closer to the spinal cord, which in reality is typically filled with CSF (Cerebrospinal fluid). On the borders of the slices the grey matter macro-isotropy can be detected which correlates to the experimental data. The most anisotropic parts are the thick neuronal channels such as visual nerves (Figure 4.3-3 – almost straight lines throughout the visual cortex), or audial nerves.

Overall, the procedure showed realistic results and fast processing time (around 2 hours for full properties transfer per one DTMRI scan).

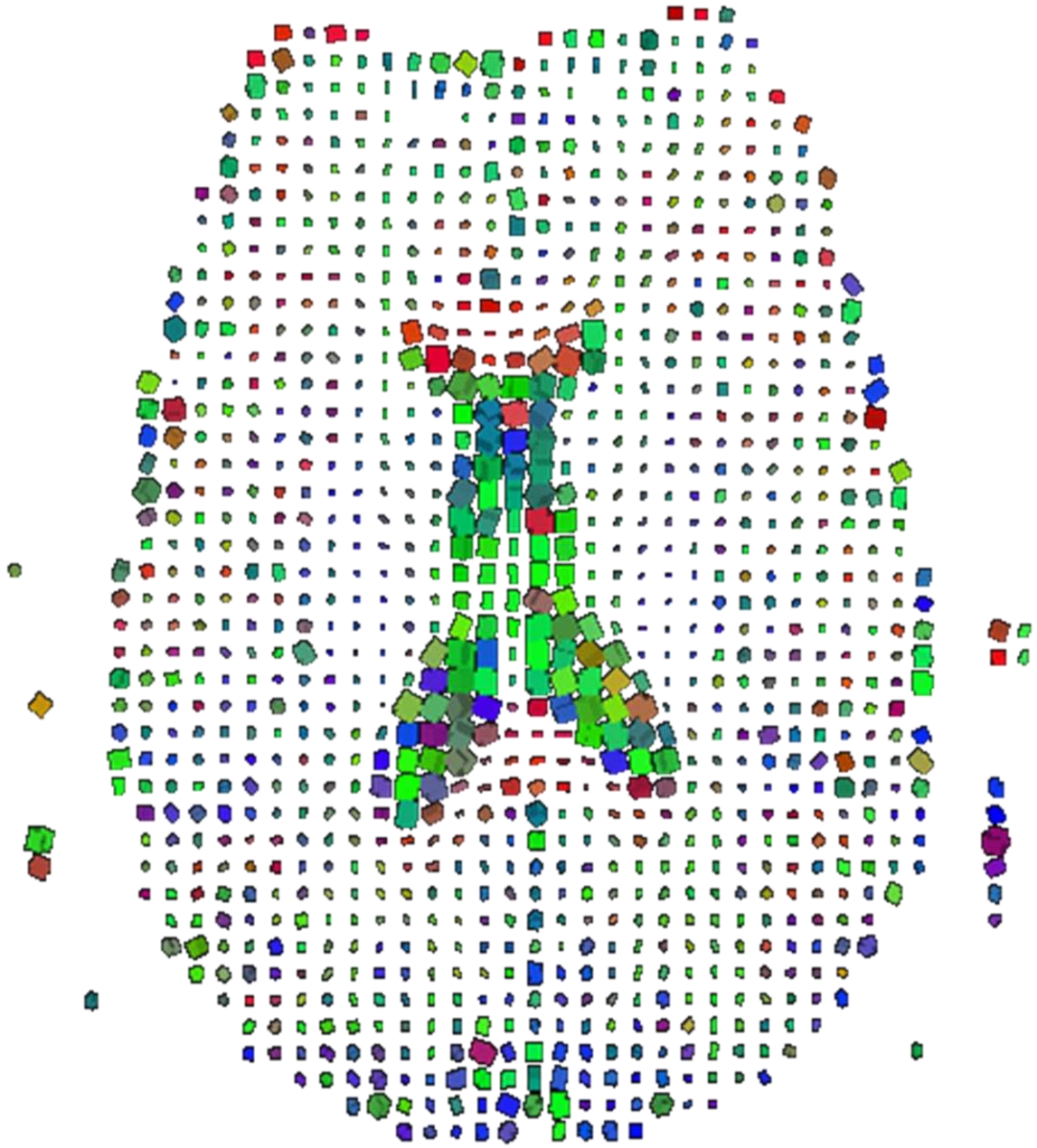

Figure 4.3-3. Example of the anisotropic conductivity tensor data for each element of the space.

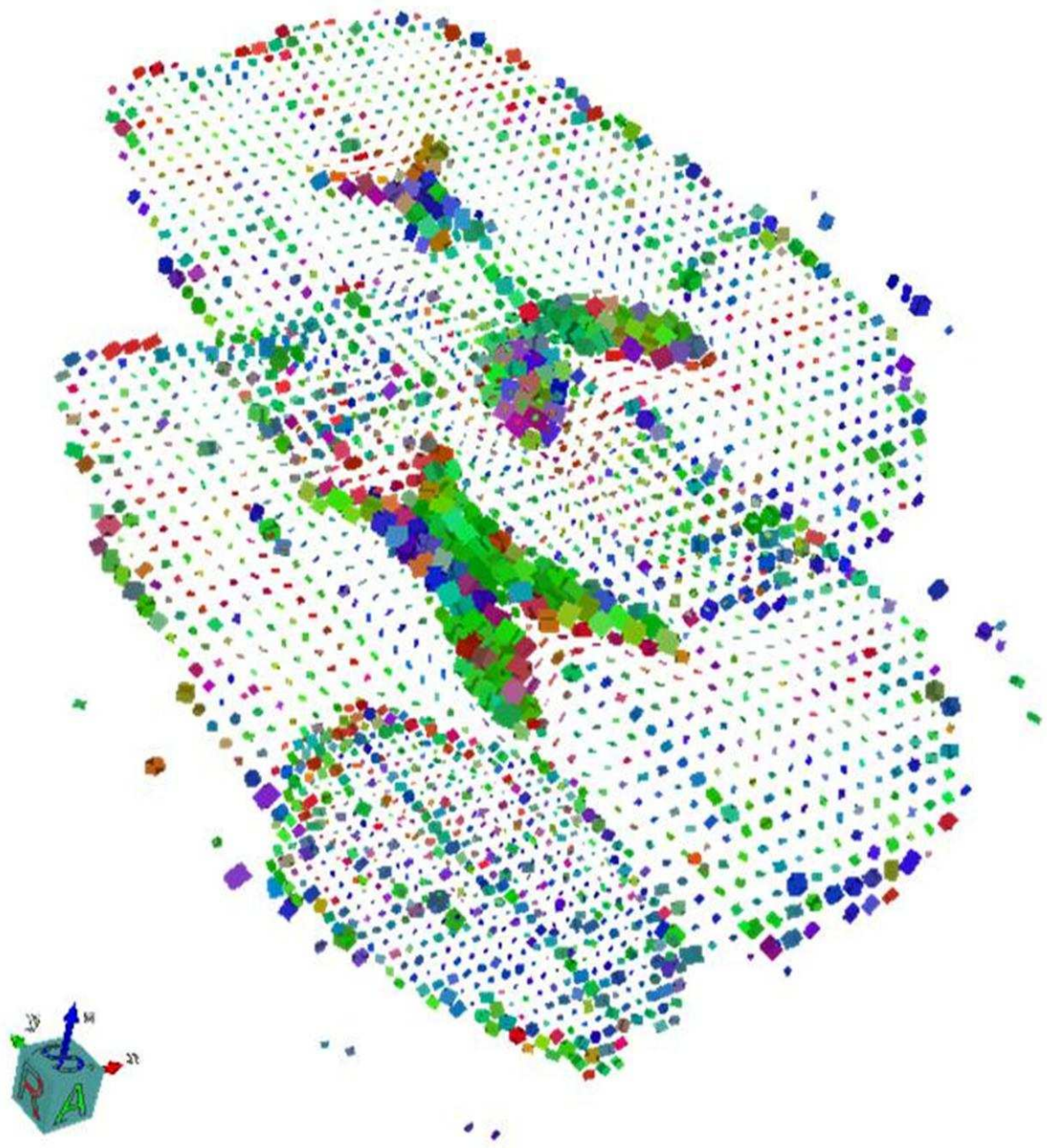

Figure 4.3-4. Three slices of the coarse FE model with the conductivity properties of each element

4.4 Test Problems and Results of Simulations Using Fully Realistic Brain Model and Simple Current Source

The discussed complex anisotropy approach in combination with geometrical reconstruction was implemented in the FE brain model and some test simulations were done in order to evaluate the error for the solution and optimize the model. The initial model parameters were chosen based on the previous mesh convergence results and are described in the following Table 4-3.

4.4.1 Case 1. Electrostatic Formulation

The following problem was introduced as a first testing case in order to check the influence of the complex anisotropic conductivity on the solution. The problem description is shown in Figure 4.4-1. The developed brain model has been placed between two planes with different electric potentials. Resulting electric field distribution has then been calculated. After that the electric current density was obtained for entire brain model volume. The whole vector plot of the current density distribution can be observed in Figure 4.4-2.

In this picture the highly non-uniform structure of current distribution due to the complex anisotropy is clearly seen. The difference is higher in the specific regions of white matter reconfiguration, for example spinal cord entrance region.

The major influence of the complex anisotropy could also be observed by reconstructing current pathways from the current density vector field in order to visualize current flow inside the conductive region. The special algorithm of such reconstruction has been created, the details of which are presented in the next paragraph. This reconstruction was performed for spinal cord and thalamus part. The result of the current path visualization is shown in Figure 4.4-3 , where the general view of the path inside the brain is shown, and Figure 4.4-4, where this path is shown in 3 projections.

The main advantage of the current visualization method is in clear indication of the difference in current flow direction (current path). The paths are all starting almost in the same point, and then separating in space. The strong non-colinearity of the closest paths can be confirmed as they should be parallel in case of no anisotropy influence. Therefore the importance of complex tensor anisotropic properties is proved and clarified.

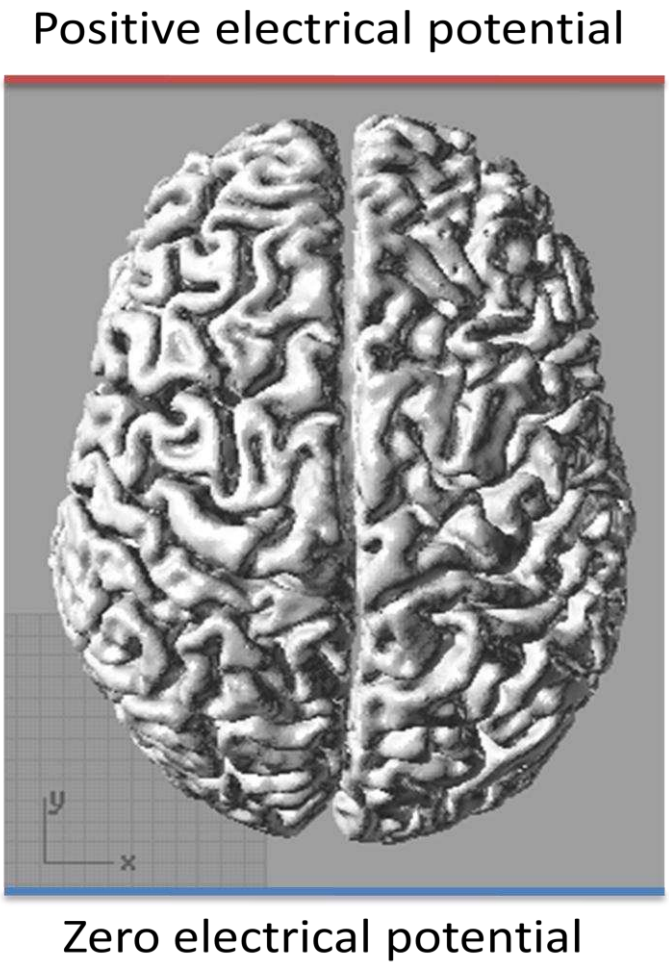

Figure 4.4-1. Formulation of the test problem

TABLE 4-3. PARAMETERS OF THE MODEL WITH ANISOTROPIC PROPERTIES

Parameter	Value
Number of finite elements	~1 300 000
Number of degrees of freedom	~3 000 000
Solution	Electrostatic, linear (case 1)
	Electromagnetic, linear (case 2 and 3. quasistatic approach)
Accuracy criteria	Mesh size according to the previous result
	Submodelling routine introduction
Permeability of the media	Air ($\mu = \mu_0$)
Conductivity of the media σ	Anisotropic realistic conductivity based on the DTMRI data

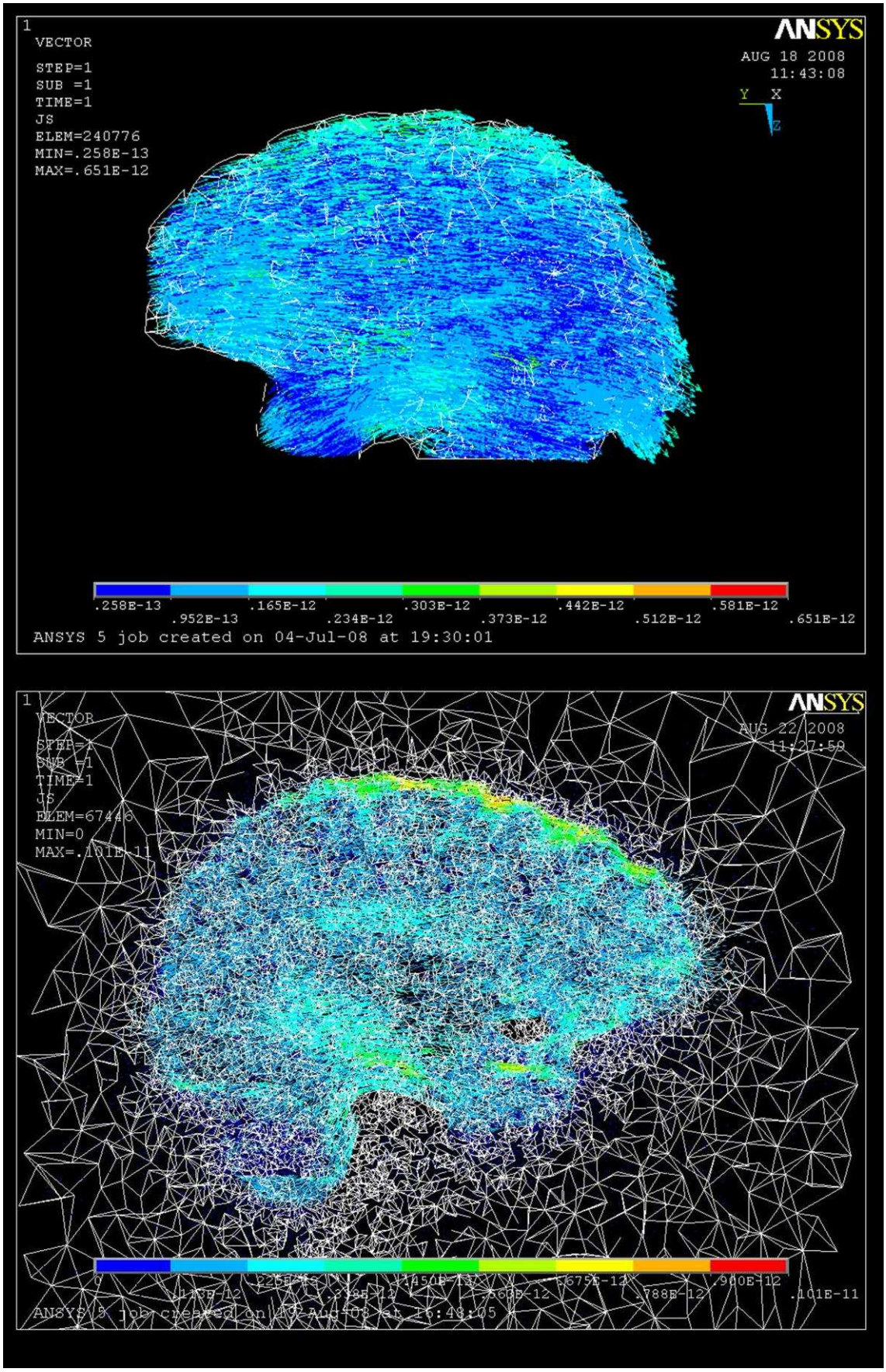

Figure 4.4-2. Results of test simulation: global current density vector plots

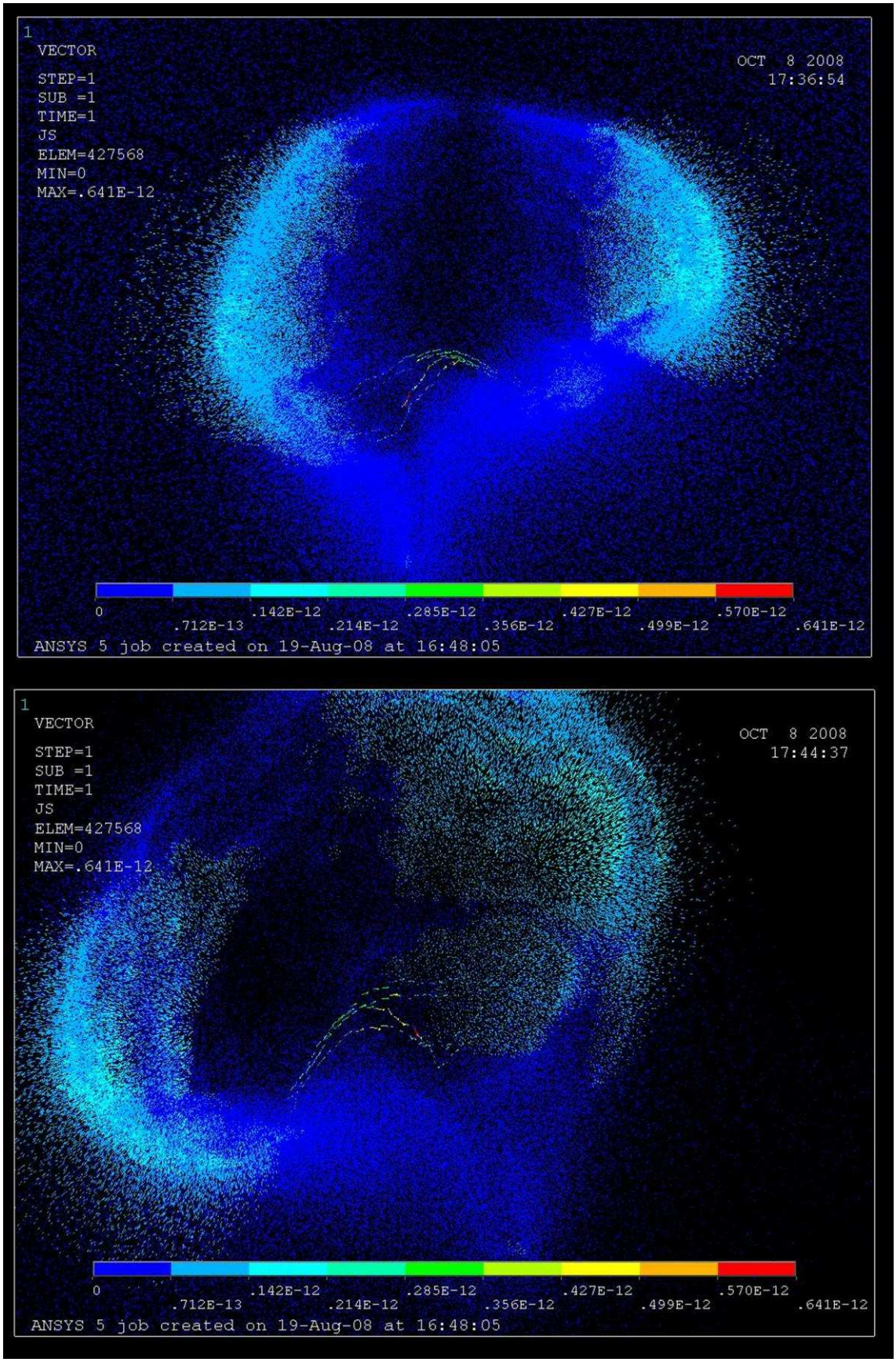

Figure 4.4-3. Results of test simulation: visualization of the current path inside the brain structure

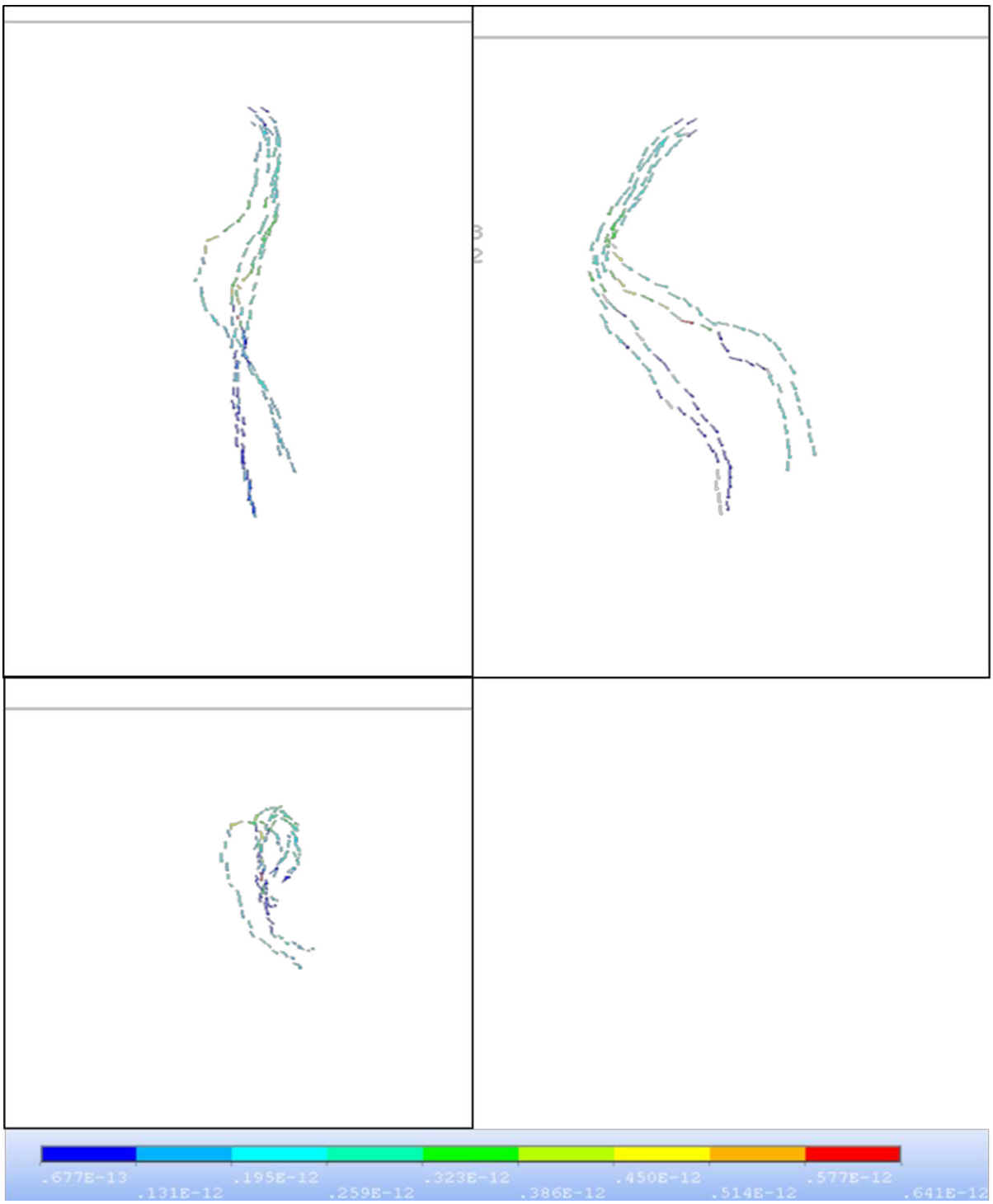

Figure 4.4-4. Results of test simulations: current path topographic views. Color legent represents current density magnitude value. Notice nonlinearity of the path due to anisotropy

4.4.2 Development of Current Path Reconstruction Algorithm

The main idea of the algorithm is based on the equation of motion of the charged particle in the electric field. The trace of this charged particle represents the current path, and at every point follows the direction of vector of the current density.

According to the formulation, the current path is the path that charged particle (electron) is following due to electromotive force. The motion equation can be written with the help of Newton's law:

$$\mathrm{m}\ddot{\boldsymbol{r}} = \boldsymbol{F_e} \tag{4.4-1}$$

where $\boldsymbol{F_e}$ is the electromotive force which can be computed as [8]:

$$\boldsymbol{F_e} = e\boldsymbol{E} \tag{4.4-2}$$

where e is the particle charge, and $\boldsymbol{E}$ is the electric field, related to current density $\boldsymbol{J}$ via following relation [8]:

$$\boldsymbol{J} = \boldsymbol{\sigma} \cdot \boldsymbol{E} \tag{4.4-3}$$

where $\boldsymbol{\sigma} = \boldsymbol{\sigma}(\boldsymbol{r})$ is the conductivity tensor. Substituting (4.4-2) and (4.4-3) into (4.4-1) leads to the following equation for path finding:

$$\mathrm{m}\ddot{\boldsymbol{r}} = e(\boldsymbol{\sigma}^{-1}(\boldsymbol{r}) \cdot \boldsymbol{J}) \tag{4.4-4}$$

In our case, however, $\boldsymbol{E}$ is known vector, so integration can be applied directly to the equation:

$$\ddot{\boldsymbol{r}} = \frac{e}{m}\boldsymbol{E} \tag{4.4-5}$$

And the following set of equations can be obtained:

$$\begin{cases} \boldsymbol{V} = \sqrt{\dfrac{2eU}{m}}\boldsymbol{n} \\ \boldsymbol{r} = \int \boldsymbol{V}dt = \boldsymbol{V}t + \boldsymbol{r_0} \end{cases} \tag{4.4-6}$$

where U is the potential difference, and $\boldsymbol{n}$ is the unit vector characterizing the direction of $\boldsymbol{J}$:

$$\boldsymbol{n} = \frac{\boldsymbol{J}}{|\boldsymbol{J}|} \tag{4.4-7}$$

Knowing initial FEM discretization and assuming U is constant for each particle trace during the time it passes throughout the single element, the following integration scheme for equation (4.4-6) can be implemented with using the existing FE mesh:

$$\begin{cases} \boldsymbol{V_{k+1}} = \sqrt{\dfrac{2eU_{k+1}}{m}}\boldsymbol{n_{k+1}} \\ \boldsymbol{r_{k+1}} = \dfrac{\boldsymbol{V_{k+1}}(t_{k+1} - t_k)}{2} + \boldsymbol{r_k} \end{cases} \tag{4.4-8}$$

where $k = (1, 2, 3, \dots, K)$ is representing the number of the finite element which particle is passing through, and initial position $\boldsymbol{r_0}$ is chosen according to the region of interest (the initial point where the current path is required for visualization can be picked from the screen). In case of steady-state case the current is flowing with the constant path. Therefore each particle in the flow has constant speed magnitude independently on time. Each time step can be then considered to be proportional to

the characteristic size of the respective finite element. Thus equation (4.4-8) becomes:

$$\boldsymbol{r_{k+1}} = H_k \sqrt{\frac{2e < U >}{m}} h\boldsymbol{n_{k+1}} + \boldsymbol{r_k} \tag{4.4-9}$$

where $< U >$ is averaged voltage difference across the path, h is the time constant, and H_k is the characteristic size of the current finite element.

The following particle tracing method is used for practical application (it is also illustrated in Figure 4.4-5). Initially the vectors $\boldsymbol{n_k}$ are calculated throughout the whole domain. Then the starting point $\boldsymbol{r_0}$ is chosen (red arrow on top picture), then the magnitude of vector is calculated which is typically equal to the characteristic size of the finite element. All other parameters are constant throughout the process. The vector, which starts from the center of the current finite element, has the direction of $\boldsymbol{n_k}$ and calculated magnitude (red thin arrow on bottom picture) will point on the finite element which will be next in the chain. Then the process repeats until the domain boundaries have been met or required path length is obtained. All finite elements which have been pointed during the procedure are forming the chain in 3D, and the position of this chain can be approximated by the spline curve (green curve in Figure 4.4-5).

Obtained 3D splines are then painted with the current density magnitude for following visualization. The complete algorithm has been written on ANSYS internal programming language, and its listing is demonstrated in Appendix 5 in details.

The application of the method can be found in this report in different places particularly in Figure 4.4-4.

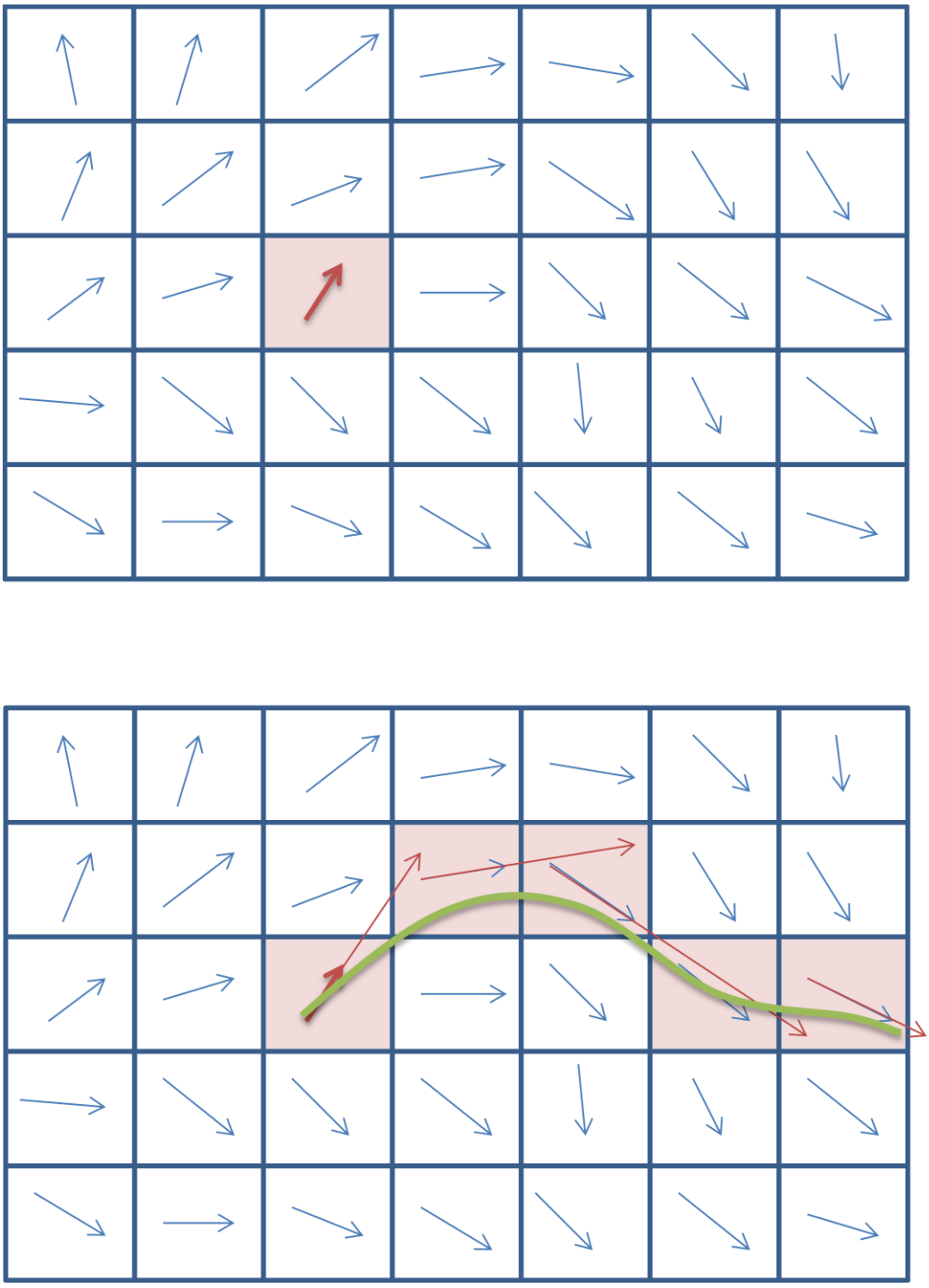

Figure 4.4-5. Current path reconstruction algorithm (see text for explanations).

4.4.3 Case 2. Testing of the Effects of Discrete Solution and Mesh Convergence and the Implementation of the Direct Submodelling Routine

In order to perform the optimization of the model with anisotropic properties and find out the range of application, some of the essential analyses have been performed which are listed below.

4.4.3.1 Modelled Case

The same as in the previous case FE brain model has been used for this analysis (see Table 4-3). The current source was chosen as a straight short conductor (beam) with square cross-sectional area. The size of the beam and problem formulation could be found in Figure 4.4-6.

The values of the conductivity for the current source were varied starting with the

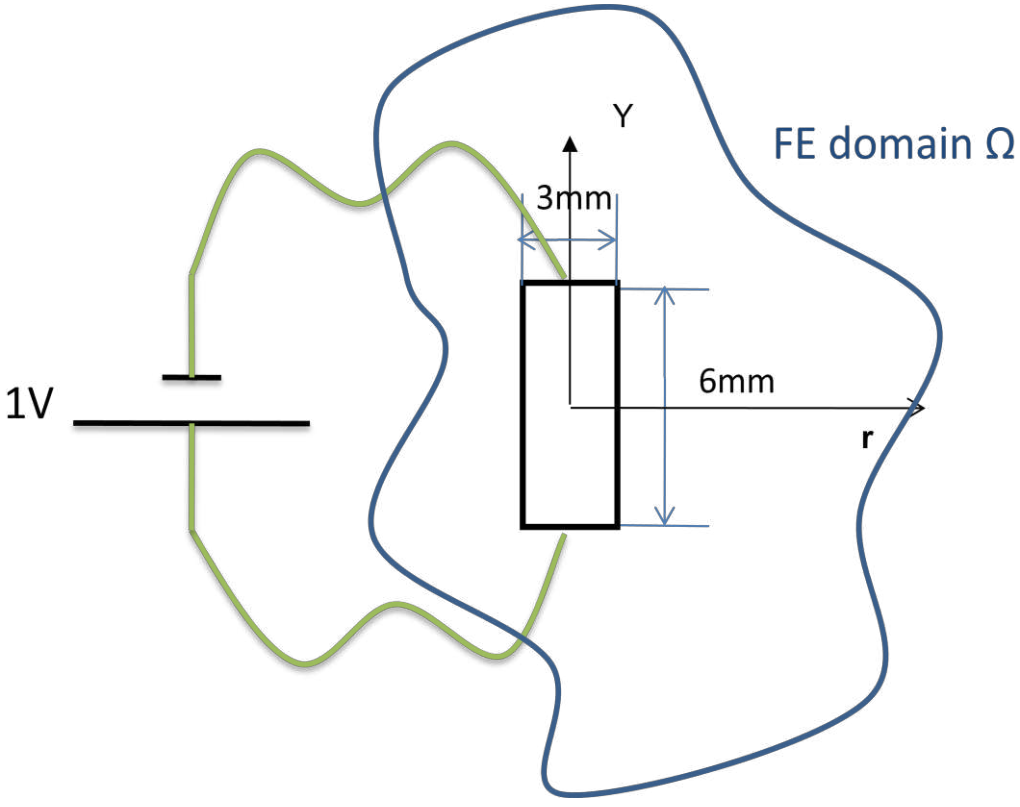

Figure 4.4-6. Current source in the test case problem

conductivity of the copper $6 \cdot 10^7\ \mathrm{S/m}$ in order to perform high conductivity difference between the source and surrounding brain matter. The conductivity values were then gradually reduced to realistic values ($10^3\ \mathrm{S/m}$, $10\ \mathrm{S/m}$, and finally $0.33\ \mathrm{S/m}$). The position of the beam was approximately at the centre of the brain and could be seen in Figure 4.4-7

4.4.3.2 Results of Direct Modelling

The initial mesh density was chosen to satisfy mesh optimization equation for the current source with average element size of 0.5mm. The analyses for several source conductivities were performed.

The analytical solution has been computed for the same parameters of the current source and zero conductivity of the surrounding media. This has been done in order to compare the accuracy of the solution for cases with high conductivity values and

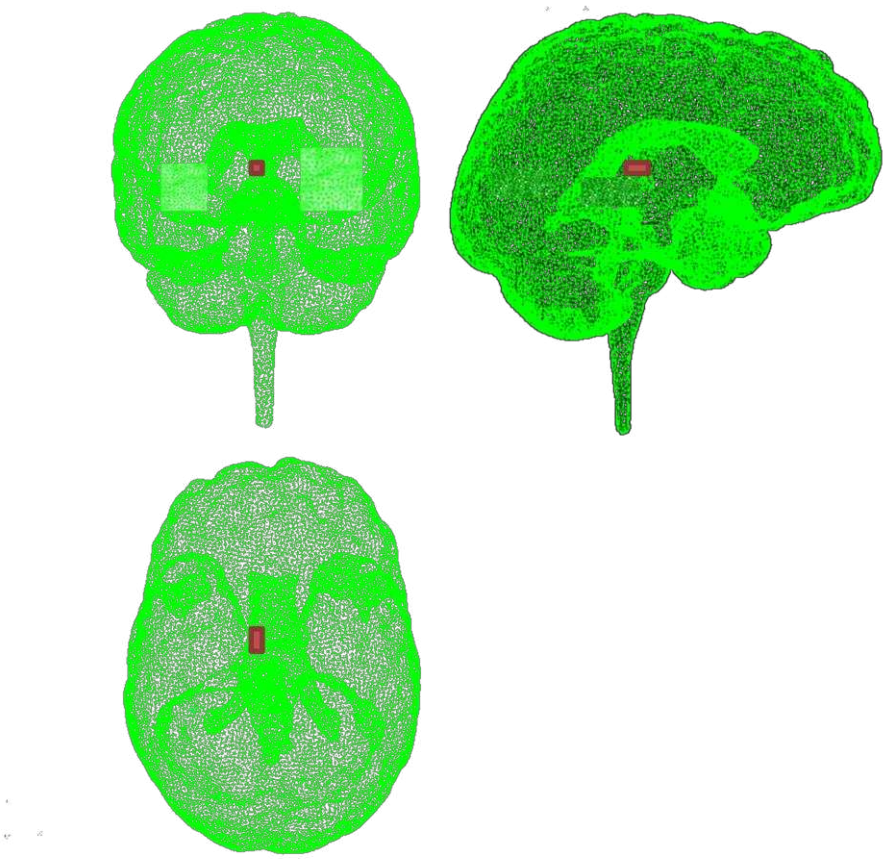

Figure 4.4-7. Position of the current source in test analysis (red rectangle)

to calculate the effect of the low conductivity ratio on the error caused by the mesh discretization. For this analytical case total current I flowing through the current conducting beam could be computed using the Ohm's low:

$$I = \frac{U}{R} = \frac{US\sigma}{l} \tag{4.4-10}$$

where σ is a conductivity of the beam, $S = 3\text{mm} \cdot 3\text{mm} = 9\text{mm}^2$ is a cross-sectional area of the beam, $l = 6mm$ is the length of the beam, and $U = 1V$ is a voltage difference applied to the beam.

In fact, the total current in case of analytical solution must be equal to the total current in case of the numerical solution with complex conductivity according to the energy conservation low. It is possible to compute the total current I_{comp} from the computational experiment, knowing the current density distribution along the $\boldsymbol{r}$ -axis of the beam, and assuming radial symmetry:

$$I_{comp} = \int_0^{r_\text{m}} j(r) \cdot \pi r^2 dr \tag{4.4-11}$$

where r_m is the distance from the center of the beam to the boundary of considered region. The error e then can be computed via the relation:

$$e = \frac{I - I_{comp}}{I} \cdot 100\% \tag{4.4-12}$$

In Figure 4.4-8 computed current density plots are presented in four different numerical cases of beam conductivity. Whilst with the high conductivity ratio between the source and surrounding media produces very accurate solution, the small conductivity ratio produces numerical error in computations. In the bottom left the

smallest conductivity ratio case is showed. The non-realistic effect associated with mesh discretization appears due to improper mesh size.

In Table 4-4 computed total current values are shown for numerical cases with different conductivity ratios. The mesh discretization effect is highlighted very clear for the case 4 where conductivity ratio is almost '1'. The 500% deviation does not seem to be realistic at all. However 0% deviation in case of high conductivity ratio shows the ability of the model to produce realistic results with very high level of accuracy.

The presented cases demonstrate significant importance of the mesh discretization error which appears when parameters of the current source are changed. This illuminates the fact that model behavior should be checked not only in terms of the mesh size for given conductive region but also in terms of the mesh size near the region of simulated current source.

Presented cases show that the mesh size should be sufficiently reduced in order to perform realistic simulations. However, reduction of the mesh size causes increasing of the number elements and degrees of freedom which dramatically increases the time of computation. Also the problematic region for our model is obviously located close to the current source (see the final graph in Figure 4.4-8) as the unrealistic current density peak caused by the mesh discretization is located there. The rest of the model for this type of problem can have the same mesh size as it has before because the current density far from the source shows acceptable behavior and the deviation from the analytical solution is small (around 1-3%). In order to perform fast realistic simulations without additional unnecessary elements and computational time, the submodelling routine has been implemented.

TABLE 4-4. TOTAL CURRENT VALUES AND AVERAGE DEVIATION IN DIFFERENT CASES

Number of sample case	Conductivity of the current source	Conductivity ratio between the source and surrounding brain matter	Total flowing current	Average error *e* of the numerical solution
1	$6 \cdot 10^7$ S/m	10^8	$8.15 \cdot 10^4$ A	0%
2	10^3 S/m	10^4	1.34 A	3%
3	10 S/m	100	$2.45 \cdot 10^{-2}$ A	5%
4	0.33 S/m	~1	$1.11 \cdot 10^{-2}$ A	500%

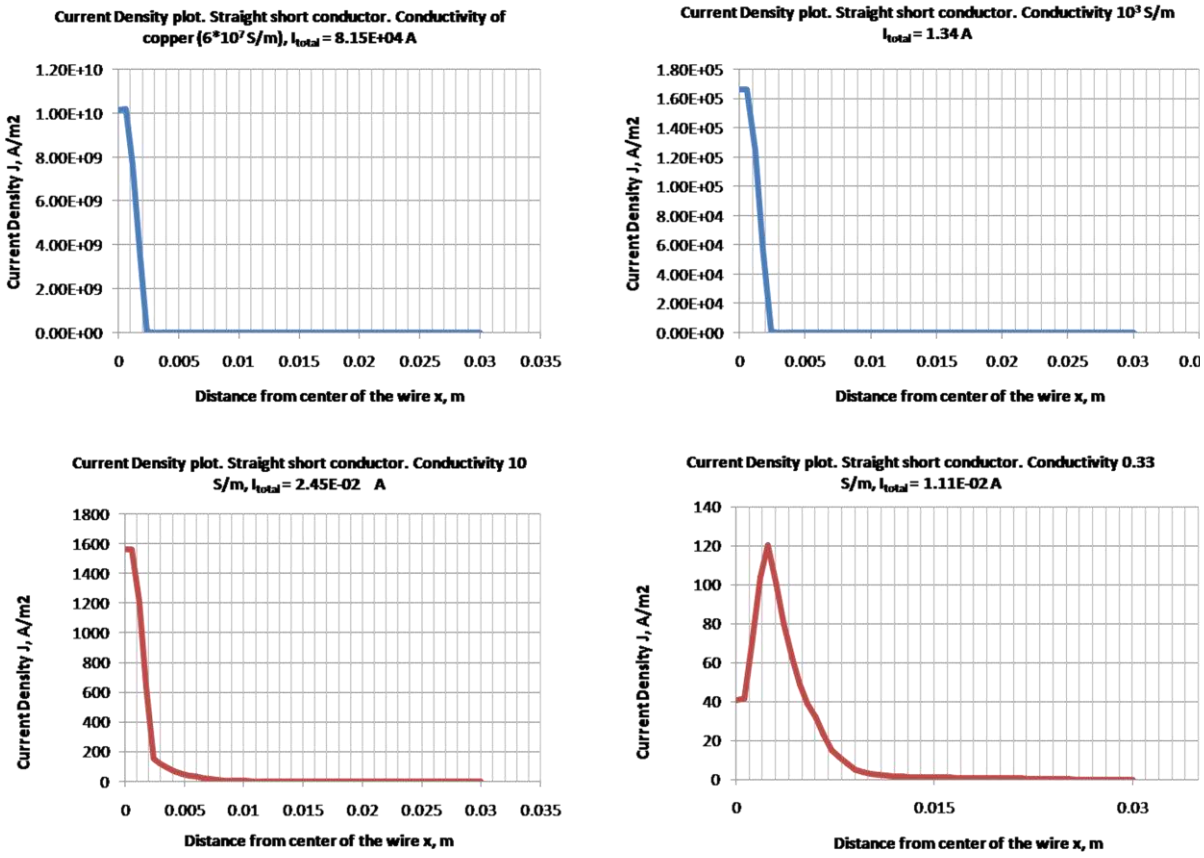

Figure 4.4-8. Current density diagrams for different conductivity values

4.4.3.3 Implementation of Direct Submodelling Routine

The submodelling routine is a computational technique which allows a significant increase in the FE solution accuracy without much increase in computational time. The Idea of this technique is discussed in paragraph 3.3.3.1 and based on the given fact, that the solution accuracy is good enough throughout the full spatial domain apart from the small region of interest. This smaller region of interest could be 'cut-off' from the model and re-meshed with the new mesh size which satisfies requirements of the problem. This new model is usually called the submodel. The initial problem then can be solved for the submodel independently of the main model with the new boundary conditions which are taken from the coarse-mesh solution. The submodelling routine in application to described earlier case is illustrated in Figure 4.4-9.

Note, that in order to perform these analyses the accuracy of the solution for the coarse model in points where the boundary conditions for the submodel are taken must be insured to be high enough.

The straightforward algorithm for this class of problems can be described with the following steps:

- Solve the full model problem with coarse mesh
- Find the region size where the solution becomes inaccurate due to mesh discretization error
- Cut the region of interest (in our case this is the current source region) and form the submodel
- Mesh the submodel with the new improved mesh

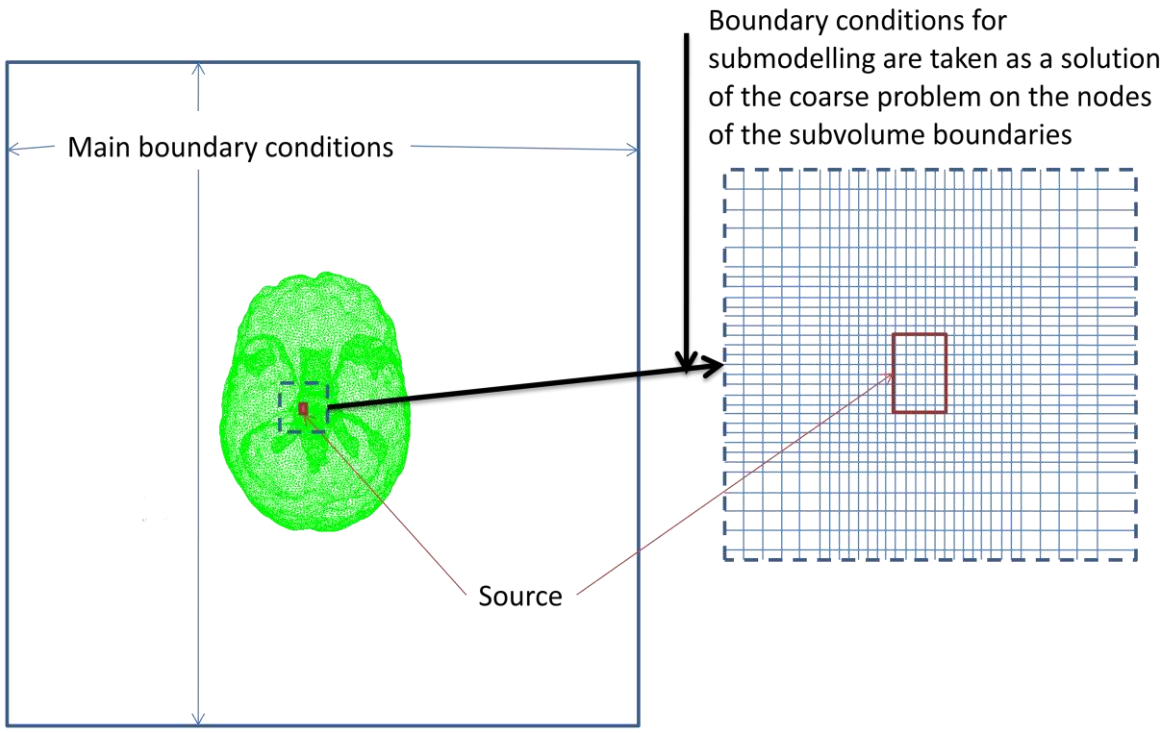

Figure 4.4-9. Direct Submodelling routine description in application to single beam conductance problem

- Transfer the solution in the boundaries of the region from the coarse model as boundary conditions for the submodel.
- Solve the problem for the submodel and transfer the results back to the main model if required.

4.4.3.4 Results and Improvement with using Submodelling Technique

For this particular case the size of the submodel region was 30mm (where the solution is not satisfying the 5% accuracy criterion). Improved mesh size for submodel has been chosen according to the analytical accuracy criteria of 5% as 0.01mm (50 times smaller than the coarse mesh). The improved results can be observed in Figure 4.4-10. The average error e in this case was less than 5%.

This graph also shows the current density distribution caused by volume currents. This effect appears due to almost equivalent conductivities of the beam and the surrounding media and again confirms high importance of the volume currents distribution mentioned before. This result also demonstrates the significance of accurate material properties modeling as those secondary currents are very

sensitive to the complex anisotropic conductivity distribution within the computational domain.

4.4.3.5 Mesh Convergence Analysis

Together with current-based analyses, which were performed in order to optimize the model and satisfy the required accuracy of the solution in terms of electrical field, the solution must also be tested in terms of magnetic field distribution accuracy. In this paragraph the mesh convergence analysis are conducted in order to find the required mesh size for the coarse model with respect to magnetic field flux density as a final result.

During this analysis several cases with different mesh size values were computed. Magnetic field in the critical point of interest for each case was evaluated. The criterion for mesh size optimization was taken according to the required deviation d_e

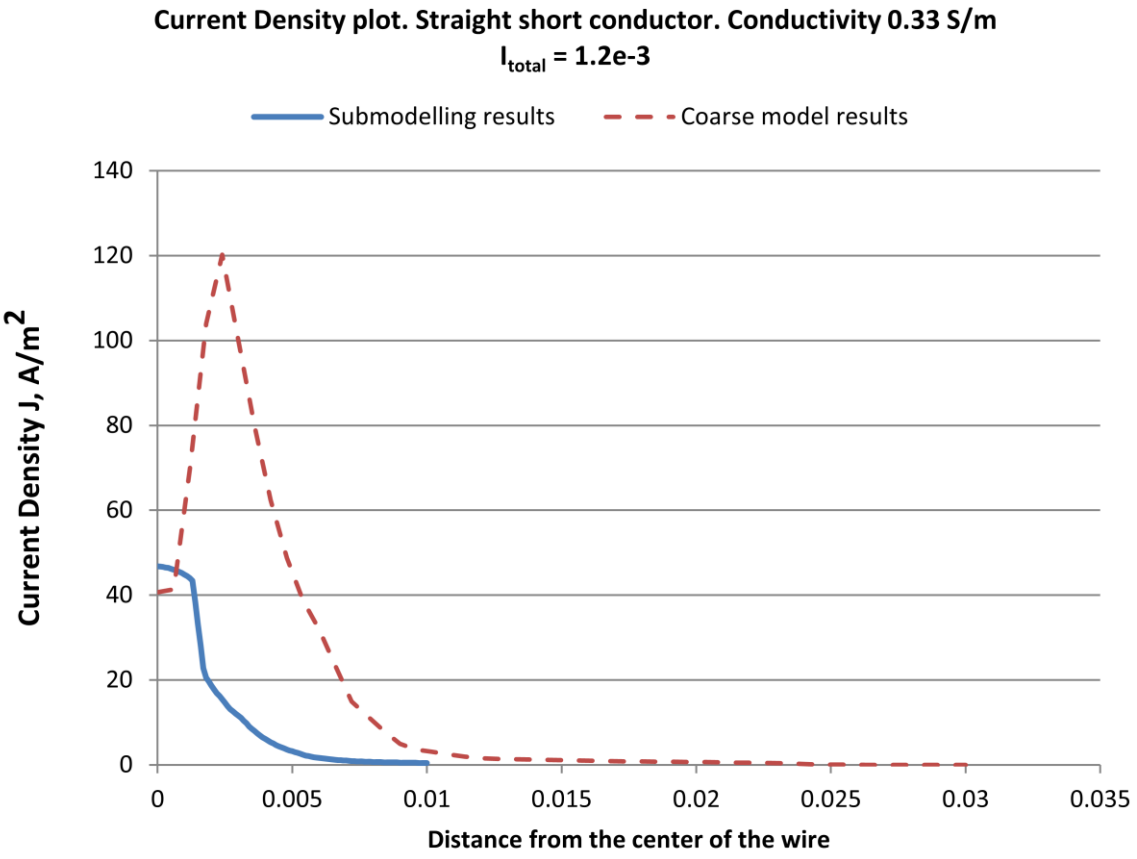

Figure 4.4-10. Improvement of the current density distribution using Submodelling routine

of the result for each case with respect to the following mesh size. The magnetic field flux density deviation requirement was forced to be less than 0.1%:

$$d_e^i = \frac{B_i - B_{i+1}}{B_i} \cdot 100\% < 0.1\% \tag{4.4-13}$$

The test model setup was chosen to be the same as the previous one (see Figure 4.4-6 and Figure 4.4-7) with conductivity of the beam σ=0.33 $\mathrm{S/m}$. Direct submodelling routine has been applied to achieve optimal accuracy. The model was meshed with uniform mesh with the total number of elements in the model representing the mesh quality. Initial case has been meshed with 200,000 elements, which corresponds to the average element size of 5mm. Model then was re-meshed several times with gradual increase of number of elements up to 2,000,000 elements total, which corresponds to the element size of 0.1mm.

In Figure 4.4-11 the results of the mesh convergence test are presented. The point of interest was chosen in the $(\boldsymbol{r}, \boldsymbol{y})$ axis of the beam with following parameters: $|\boldsymbol{y}| = 0; |\boldsymbol{r}| = 6\mathrm{mm}$. At this point magnetic field strongly depends on the mesh discretization effects and it is the most critical point for this solution. Also the analytical solution for the case with non-conductive surrounding media is presented, which has been calculated according to [8] from first principles:

$$B_{analyt} = \mu_0 \frac{I \cdot l}{r^2} \tag{4.4-14}$$

This formula is obtained for the magnetic field flux density solution on the line which passes the center of the conductor, i.e. $|\boldsymbol{y}| = 0$.

The final difference demonstrates the influence of the surrounding matter anisotropic conductivity on the computed magnetic field flux density. The difference for this simple case is 15% which is considered to be very high for basic static solution. Result shows that together with the magnitude of the magnetic field flux density

difference between the case with non-conductive surrounding media and the case with conductive one, there is also significant change in the vector field distribution. This is associated with the strong anisotropy of material properties.

According to presented mesh convergence graph the number of elements *N* of the main model were chosen to be 1000000. This value of *N* delivers the deviation of the solution to be less than 0.1%. *N*=1000000 corresponds to the approximate element size of 0.3mm.

After the mesh convergence analysis has been conducted, the solution was obtained for the current source conductivity σ=10 $\mathrm{S/m}$. This conductivity value of the beam material provides the conductivity ratio of 30 which eliminates the conductivity influence on the solution and allows comparison of the numerical result with analytical computations. The full correlation of the analytical solution to computational result was expected on a relatively far distances from the center of the conductor.

Analytical solution for this case with non-conductive surrounding media was also computed in form (4.4-14). The comparison of the computed and the analytical result is shown in Figure 4.4-12. Notice the point of interest for our problem which is approximately located at the distance of $|\boldsymbol{r}| = 6\mathrm{mm}$ from the centre of the beam. The average error for this region was around 5%, however for the region where $|\boldsymbol{r}| \geq 12\mathrm{mm}$ the computed and analytical results are almost the same (average error was less than 0.5%), and expected correlation was confirmed.

The number of material properties *P* was also studied during mesh convergence analysis. The result is independent of the conductivity ratio. However, the number of common properties was found increased with increasing *N*. The variation of *P* as a function of *N* is shown in Figure 4.4-13.

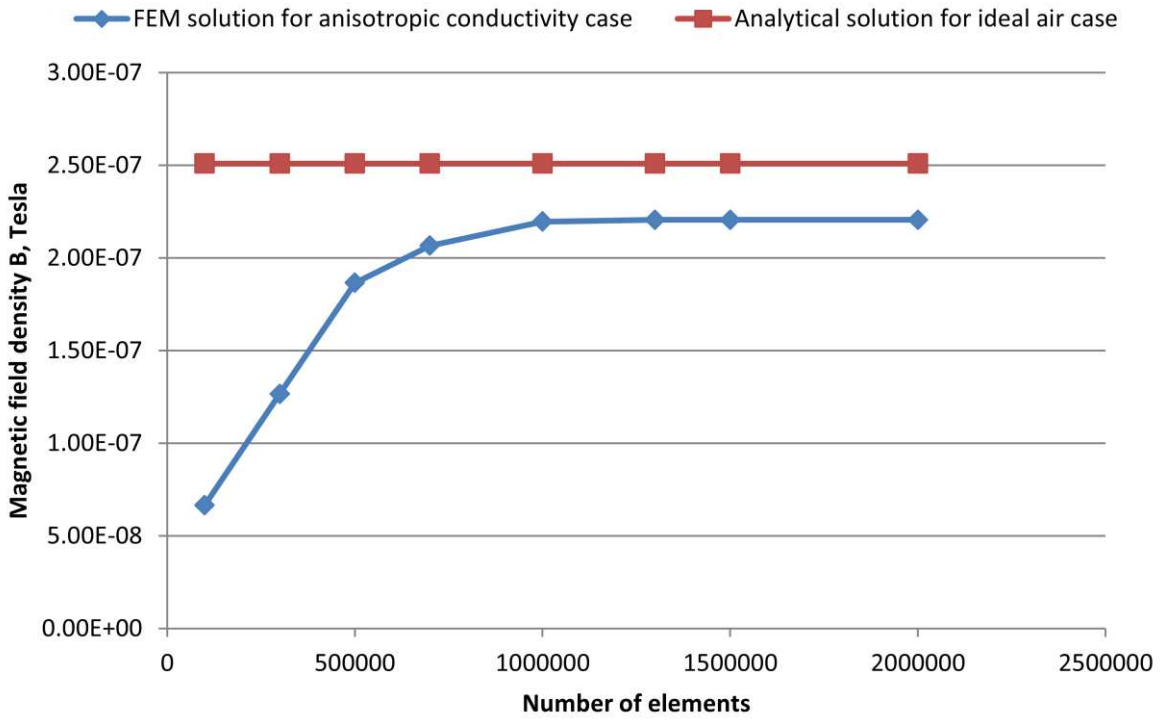

Figure 4.4-11. Mesh convergence graph computed for magnetic field flux density value calculated at the critical point of interest r=0.006m from the center of the conductor

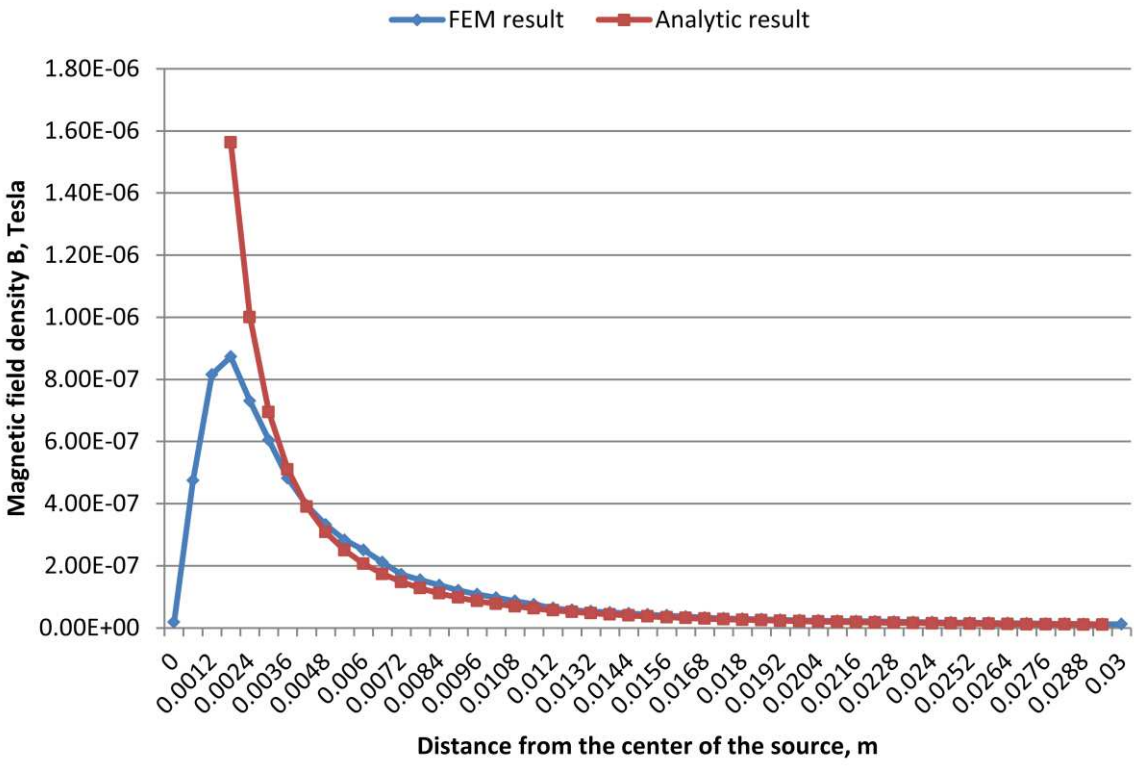

Figure 4.4-12. Magnetic field density diagram for case with conductivity of 10 S/m and optimal mesh

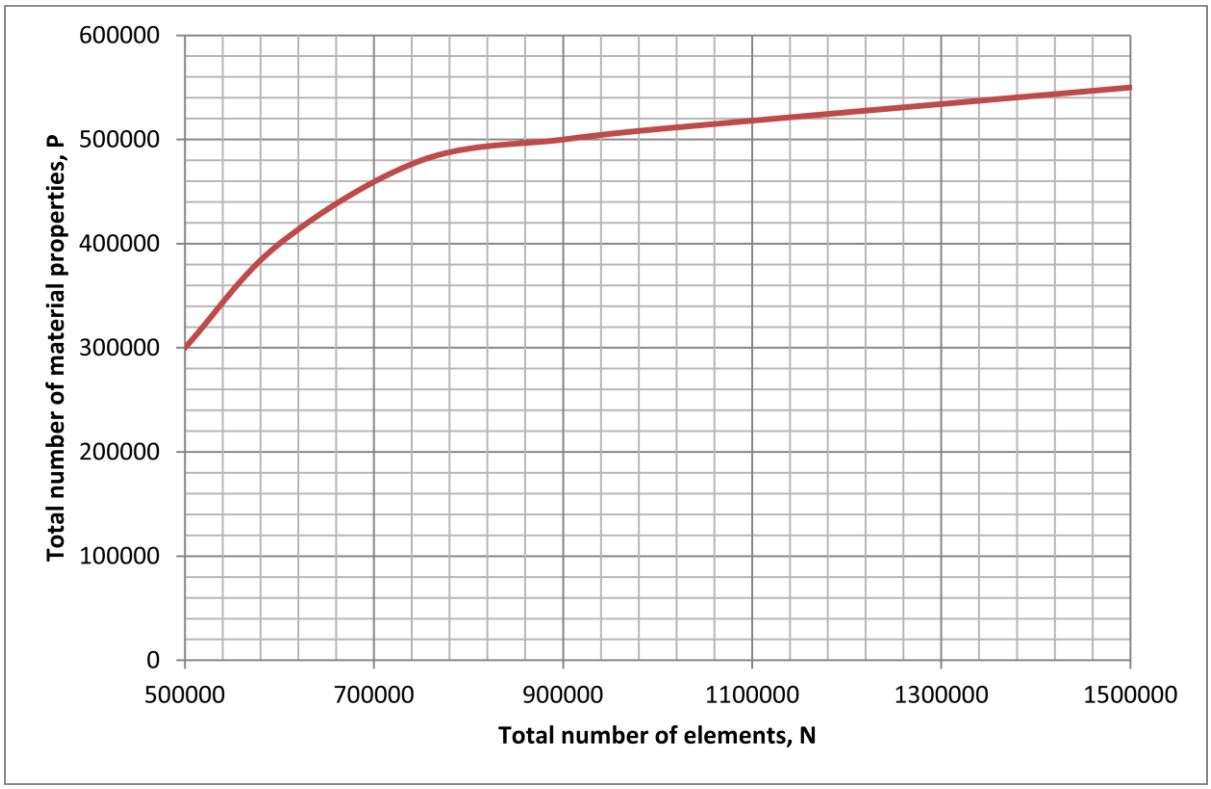

Figure 4.4-13. Optimal number of material properties in the model *P* as a function of total number of FE elements *N*

4.4.4 Conclusions from the Solution of Test Problems and Summary of Optimal Modelling Parameters

The case studies considered earlier highlighted the optimal parameters for modelling and allowed to perform approximate error evaluation for all possible range of solutions. The main target of testing study was to develop as much realistic model as it is possible taking into account reasonable approximations which would not cause decreasing of the accuracy of the solution. All algorithms and reconstruction techniques was developed to be automatic. The solution procedure was also optimized and the automation was performed where it is possible (e.g. submodelling technique was developed and implemented to be fully automatic).

The complex anisotropic conductivity as a property of the model was proved to be a major requirement of the modelling as it shows sufficient influence on the solution. The model has been studied with the wide range of electromagnetic analysis. The error of numerical solution was obtained based on the static electrical analysis. The submodelling technique was implemented and tested in order to reduce the solution error and computational time. The optimal parameters of the mesh and submodel were computed and validated.

The error of the solution in terms of magnetic field flux density was computed based on the mesh convergence analysis. Optimal mesh parameters were obtained and checked.

The optimal parameters for the full range of quasistatic electromagnetic simulations were summarized with the help of convergence criteria and computed numerical errors for both electrical and magnetic components of the solution. These parameters are listed in Table 4-5. There results has also been published in [86]

TABLE 4-5. FINAL OPTIMAL PARAMETERS OF THE BRAIN MODEL

Parameter	Value
Number of elements in the main model	1 000 000
Approximate element size for the main model	0.3mm
Conductivity of the brain region	Complex anisotropic conductivity based on the DT-MRI data
Size of the submodelling region	Approximately 30mm from the center of the current source
Size of the mesh in submodelling region	0.01mm
Error of the current density calculation for chosen parameters	Less than 5%
Error for magnetic field flux density calculation for chosen parameters	Less than 5%

4.5 Summary

The realistic brain model reconstruction routines and tools have been developed in order to perform forward simulations in MFT tomography based on MEG. These tools are proved to deliver the most accurate and realistic brain model in terms of both patient-specific geometry and material properties. The algorithms provide theoretical accuracy of MRI images. At the same time DT-MRI in combination with tensor evaluating technique were implemented to obtain complex anisotropic material properties. The finite element model was studied in different test cases. Estimated errors for the electrical end magnetic solutions were computed. The optimal finite element mesh parameters were obtained. The outline of the finite element discretization with optimal properties is displayed in Figure 4.5-1.

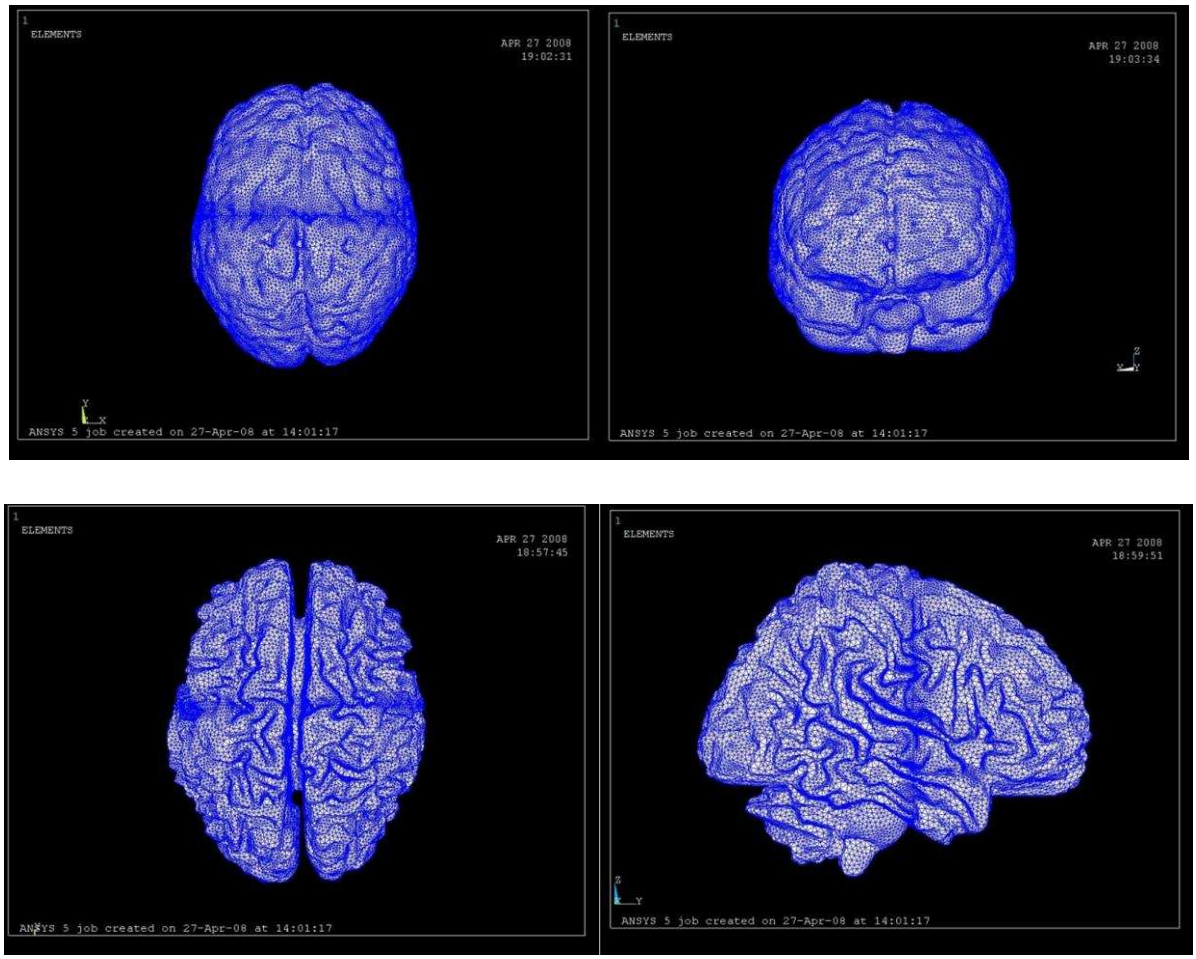

Figure 4.5-1. Outline of the optimal finite element model mesh for Grey (top) and White (bottom) matter respectively

Chapter 5

Modelling of Realistic Neuronal Current Source

There are no accurate representations of the realistic bio-electrical processes which take place inside the brain (see Chapter 6 for details) in literature as far as the realistic neuronal current source is concerned for the solution of the forward problem in MFT based on MEG. This Chapter presents a novel approach which is carefully developed from the neurological and bio-chemical basis specifically for finite element solution of the forward problem.

5.1 Action Potential and Neuronal Currents

5.1.1 Neuronal impulse

Action potential [6] propagates within the neuron due to the special biological mechanism of the cell membrane. Initially the voltage difference between inside and outside the cell is -80mV. When outside electrochemical interactions gives threshold value of 16mV, membrane opens to ionic conductance and action potential starts. Depolarization of the cell during the action potential is caused by the influx of sodium ions across the membrane, and repolarisation is caused by the efflux of potassium ions. The mechanism of membrane conductivity for ions is voltage-gated so action potential works like burning of a fuse. When the action potential reaches its maximum value 40mV, membrane stops provide potassium ions out of the cell and opens to inverse sodium ions propagation. This allows action potential propagates with an approximate velocity 10 m/sec (within the human brain) and only in one direction. The voltage (and hence the current) due to such movement of ions is shown in Figure 5.1-1. This demonstrates one timeframe.

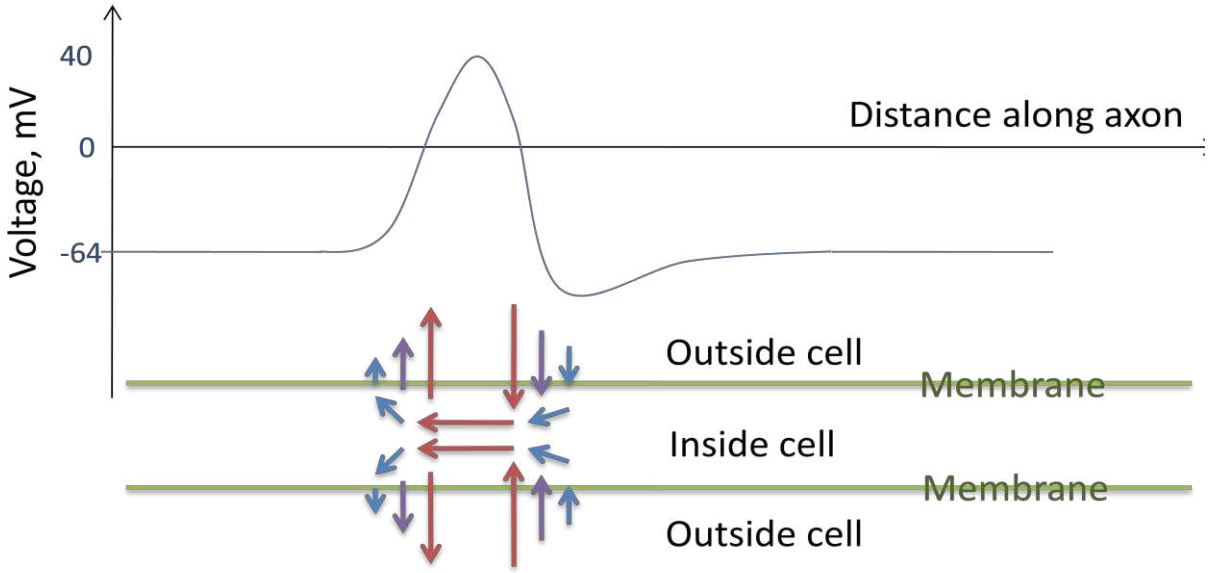

Figure 5.1-1. Action Potential propagation and current distribution

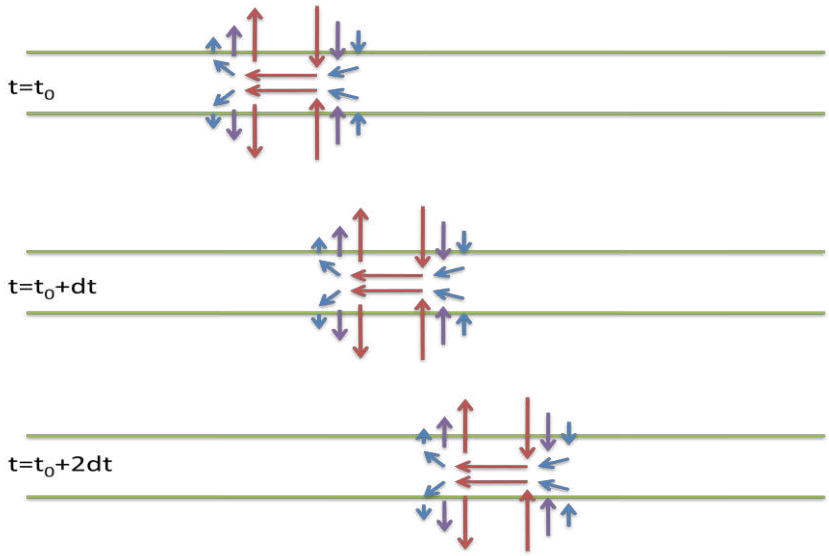

Figure 5.1-2. Current distribution propagation in time

Arrows show the main current distribution due to action potential propagation in the chosen timeframe. The colour of the arrow schematically represents current density value (red-is stronger, blue is weaker). This current distribution picture will be shifted a little bit at the next time step and generally it is moving along the axon axis with the speed of propagation 10 m/sec (as shown in Figure 5.1-2).

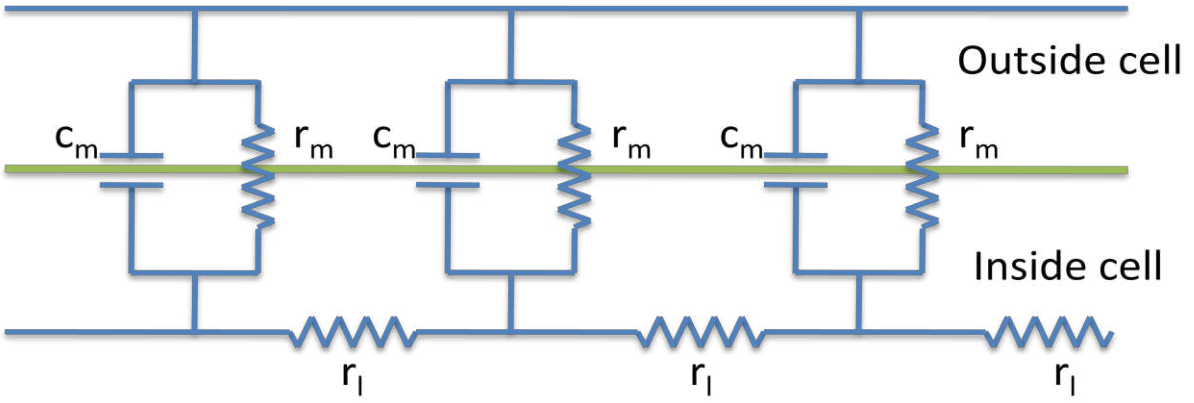

Figure 5.1-3. Cable theory's simplified view of a neuronal fiber; r_m – membrane resistance, r_l – longitudinal resistance, c_m – capacitance due to electrostatic forces

Usually cable theory is used for description of current propagation trough neuronal membrane [87]. As shown in Figure 5.1-3, this could describe the current distribution in neuron with the initial voltage boundary conditions.

The connected RC circuits correspond to adjacent segments of a passive neurite. The extracellular resistances r_e (the counterparts of the intracellular resistances r_i) are not shown, since they are usually negligibly small. The extracellular medium may be assumed to have the same voltage everywhere.

5.1.2 Currents to be Considered for Forward Simulation

Due to the radial symmetry of axon only longitudinal currents can be included in simulation, because there is no primary magnetic field from radial currents. Therefore electromagnetic problem formulation can be illustrated as shown in Figure 5.1-4. Note that this approximation works only for magnetic analysis, for electrical (EEG) potential a different model has to be chosen with respect to the current conductance.

This approach allows going away from difficulty related to cable theory and considering our neuron as a number of short conductors connected to each other. The approximation is also strongly feasible for the myelinated axons where the ionic

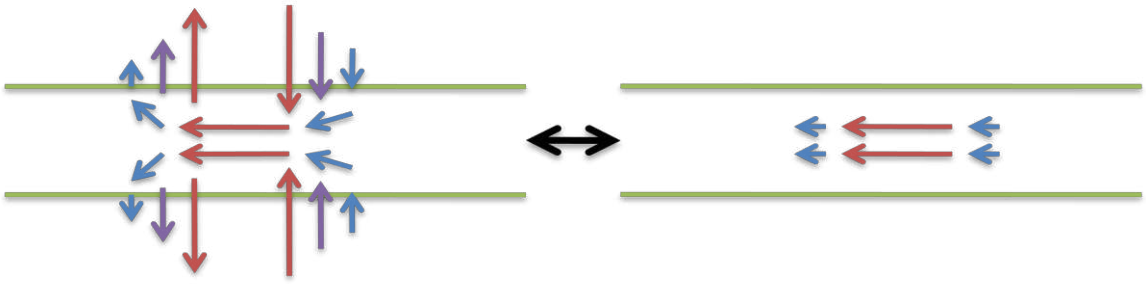

Figure 5.1-4. Equivalent problem formulation for magnetic analysis

influx and outflow is possible only between two myelin formations (In this case the size of each conductor must be chosen as an average size of myelin sheath).

Presented scheme imitates moving impulse along the axon with sequential activation of the voltage sources placed along the axonal path at each short current conductor, therefore allowing the simulation of the action potential propagation. The full simulated voltage loading computational scheme can be visualised as shown in Figure 5.1-5, where dL must be considered according to required time step and therefore accuracy of the solution in case of axons without myelin. In case of myelinated axon, dL must match the exact size of myelin sheath. Voltage function for each sequential voltage source is computed on the basis of neuronal path parameters and parameters of action potential. Generally all sources are taken with equal voltage function shifted in time domain.

Integration of automatic algorithmization and submodelling technique allows practical implementation of this procedure in any finite element software platform, e.g. ANSYS.

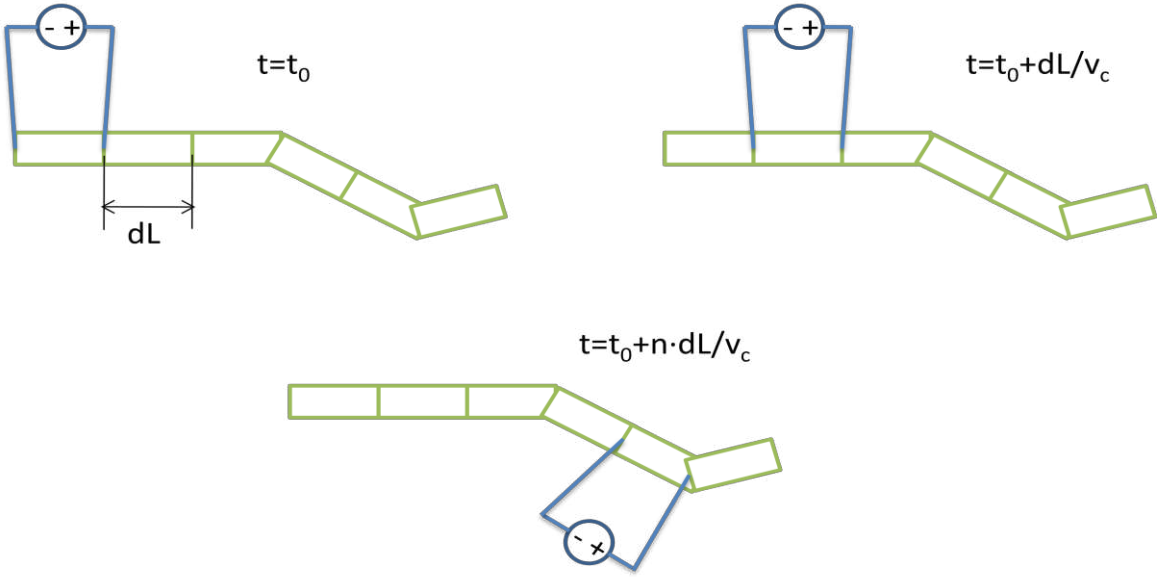

Figure 5.1-5. Computational scheme for forward problem magnetic analysis; V_c is the velocity of action potential propagation (10 m/sec)

5.2 Mathematical Basis for the Approximation of Novel Neuronal Current Source

Mathematical basis of the novel neuronal current source modelling approach is based on the quadratic polynomial approximation of the action potential. Considered space consists of the following type of functions:

$$f(x) = (x - x_0)^2 \tag{5.2-1}$$

Here f is the basic function, x is the coordinate along the path, and x_0 is a constant. In our approach the following structure have been developed as a basis for action potential distribution along the one-dimensional path in a single voltage source position:

$$f_n(x) = U_0[1 - T(x - n\lambda)^2] \tag{5.2-2}$$

This basic function has general characteristics of the actual action potential. Here U_0 is the maximum voltage, λ is the length of one segment (in previous paragraph it is equal to dL), T is the characteristic scale factor, which depends on the initial discretization, and n is the current segment number (Figure 5.1-5).

The Cartesian global 3D coordinate system is not suitable for this application due to high complexity of transformation operators in 3D, therefore the special floating path coordinate system has been used (Figure 5.2-1). Here points of the path are described as vector $\boldsymbol{X}(x)$ with respect to local parameter x representing the distance along the path, the main axis $\boldsymbol{x}(x)$ is always directed collinear to the tangent of the path and the value of x is counted along the neuronal 3D path from its beginning (first neuronal terminal), other axis is the normal $\boldsymbol{n}(x)$ and 3rd vector $\boldsymbol{z}(x)$ respectively:

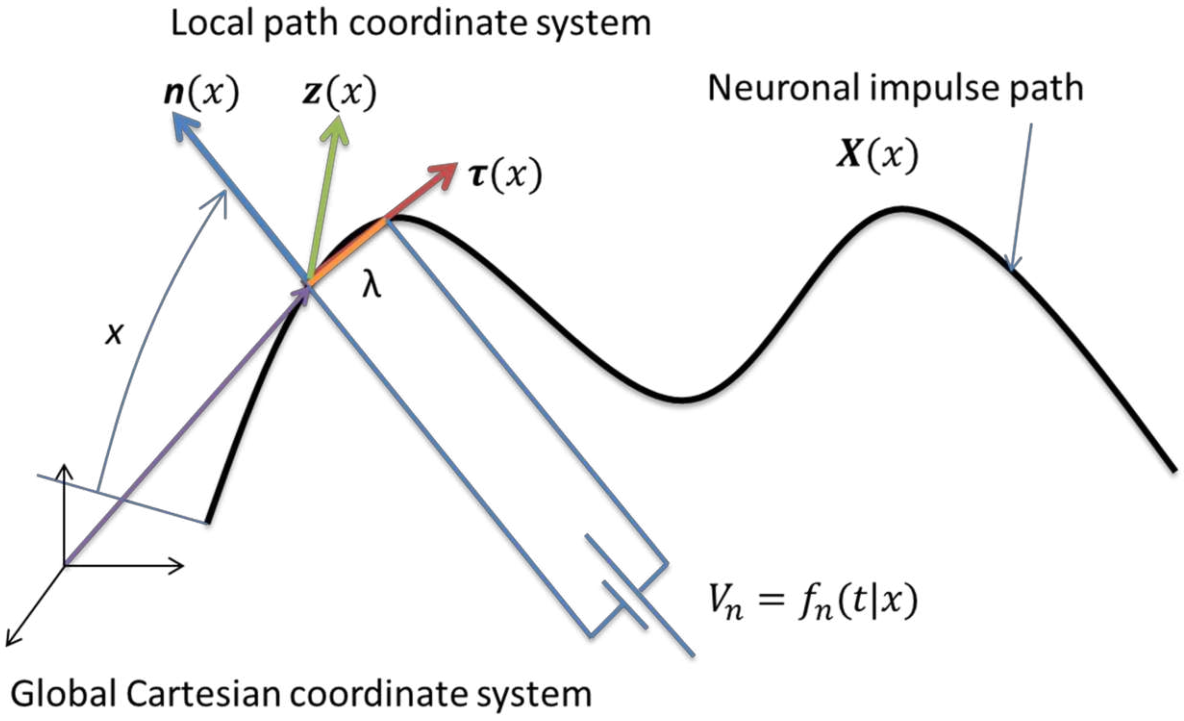

Figure 5.2-1. Floating coordinate system for mathematical computations

$$\boldsymbol{x} = \boldsymbol{\tau}(x)x$$
$$|\boldsymbol{\tau}(x)| = 1 \tag{5.2-3}$$

In terms of the new coordinate system the basic function (5.2-2) can be written, taking into account that all these functions have to be limited in space:

$$f_n(\boldsymbol{x}) = \begin{cases} U_0(1 - T(\boldsymbol{x}(x) - n\lambda\boldsymbol{\tau}(x))^2); & x\epsilon[x_1^n, x_2^n] \\ U_1; & x\epsilon\mathbb{R}\backslash[x_1^n, x_2^n] \end{cases} \tag{5.2-4}$$

Here $x_{1,2}^n$ are the segment limiting constants, and U_1 is the initial axonal voltage. The main advantage of the following functional space (5.2-4) is that it has mathematically one-dimensional behavior in the space domain. This allows transforming the functional space into the time domain and avoiding complexity related to the wave

theory. Due to the constant velocity of action potential propagation space variable can be substituted by the temporal variable t:

$$x = V_0(t - t_0) \tag{5.2-5}$$

were V_0 is the propagation velocity, t_0 is the starting activation time. Therefore (5.2-4) can be transformed to the following form:

$$f_n(t) = \begin{cases} U_0(1 - T(V_0(t - t_0) - n\lambda)^2); & t\epsilon[t_1^n, t_1^n + \gamma_0] \\ U_1; & t\epsilon\mathbb{R}\backslash[t_1^n, t_1^n + \gamma_0] \end{cases} \tag{5.2-6}$$

where γ_0 is the temporal length of the impulse (see Figure 5.2-2), and function f_n now operates in the time domain, and $t_{1,2}^n = x_{1,2}^n / V_0$.

The total voltage at a given time point can be found as a sum of all unit functions operated along the path (note, that spatial position of each segment is known and each function is assigned to corresponding part of the path):

$$\mathcal{F}(t, \mid \lambda, N) = \sum_{n=1}^{N} f_n(t)$$
$$f_n(x)\epsilon\boldsymbol{X}(t, t_0, \lambda, N) \tag{5.2-7}$$

Here N is the total number of functions which is equal to the number of divisions along the path and depends on discretization. The time limiting constants can be found from the limiters of the initial function ($n = 1$):

$$U_1 = U_0(1 - T\left(V_0(t_{1,2}^0 - t_0) - \lambda\right)^2) \tag{5.2-8}$$

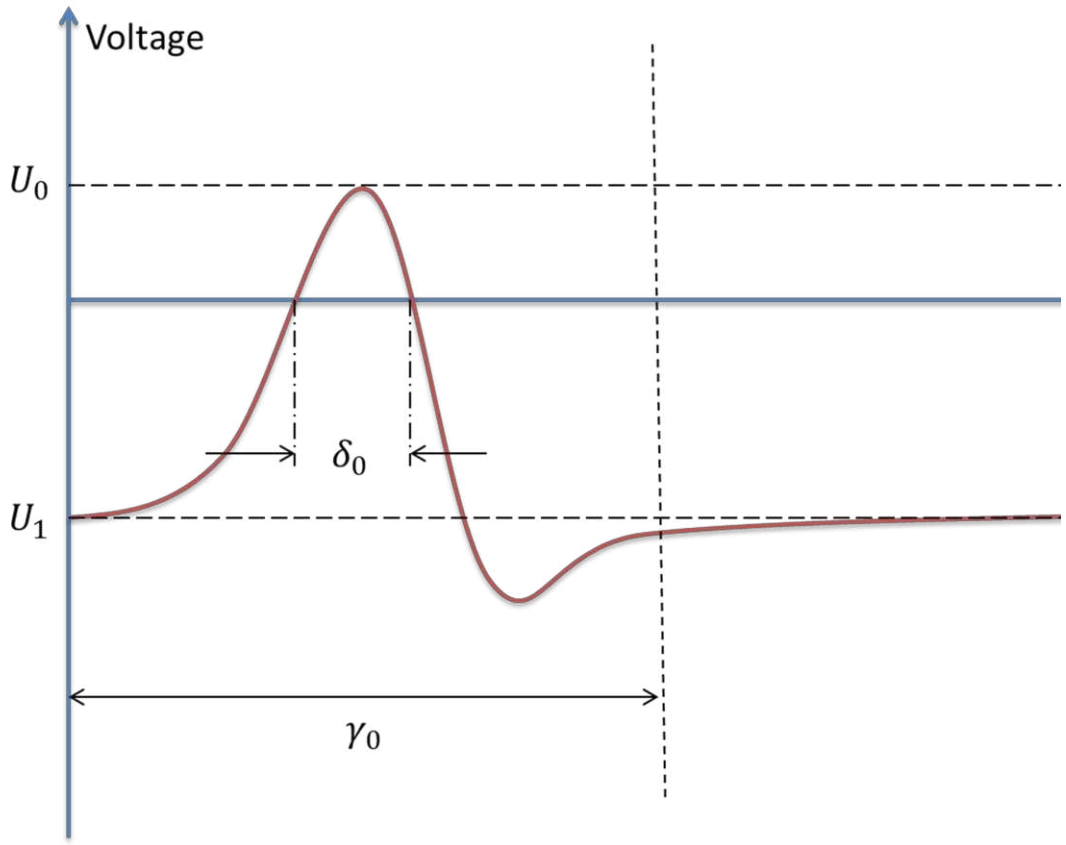

Figure 5.2-2. Mathematical parameters of the action potential approximation

Therefore:

$$t_{1,2}^{0} = \frac{\lambda \pm \sqrt{\frac{1}{T}\left(1 - \frac{U_1}{U_0}\right)}}{V_0} + t_0 \tag{5.2-9}$$

Assuming uniform discretisation of the path (λ is equal everywhere along the path), the only two initial constants must be calculated, and the following can be used for the rest of them:

$$t_{1,2}^{n} = n\frac{\lambda}{V_0} + t_{1,2}^{0} \tag{5.2-10}$$

The characteristic scale factor T can be found from the required action potential form with using zero-to-zero value δ_0 (distance between the zero voltage points along the temporal axis):

$$\left.\begin{array}{l}(t = t_0) => \mathcal{F}(t) = \max = U_0 \\ (t = t_0 + \dfrac{\delta_0}{2}) => \mathcal{F}(t) = 0\end{array}\right\} => T = T(\lambda, N) \qquad (5.2\text{-}11)$$

Substituting (5.2-10) into (5.2-7) and summarizing obtained dependences, the following completely determined set of equations can fully describe the action potential propagation along any neuronal path with known location:

$$\mathcal{F}(t, \mid \lambda, N) = \sum_{n=1}^{N} f_n(t)$$

$$f_n(t) = \begin{cases} U_0(1 - T(V_0(t - t_0) - n\lambda)^2); t\epsilon \left[n\dfrac{\lambda}{V_0} + t_1^0, n\dfrac{\lambda}{V_0} + t_1^0 + \gamma_0\right] \\ U_1; \qquad t\epsilon\mathbb{R}\backslash\left[n\dfrac{\lambda}{V_0} + t_1^0, n\dfrac{\lambda}{V_0} + t_1^0 + \gamma_0\right] \end{cases} \qquad (5.2\text{-}12)$$

$$f_n(x)\epsilon \boldsymbol{X}(t, t_0, \lambda, N)$$

The equations (5.2-12) are specifically designed for finite element discretisation. Below the example parameters which are used for specific white matter neuronal fibres are presented:

$$\gamma = 3\text{msec}; \quad \delta_0 = 0.8\text{msec}$$

$$U_0 = 40\ \text{mV}; \quad U_1 = -64\ \text{mV} \tag{5.2-13}$$

$$\lambda(\text{depends on discretesation}) \sim 0.5\ \text{mm}$$

$$T(\text{depends on discretesation}) \sim 10^6\ \ \text{m}^{-2}$$

5.3 Modelling of Various Neuronal Formations

Let us consider the proposed approach in application to different possible neuronal formations. As was discussed in Chapter 2 there are no single activated neurons inside the brain. Always the group of neurons is activated one by one or at the same time. Also there are three possible formations in terms of electromagnetic simulations. They are thin neuronal fibre (fibertract), myelinated fibertract, and neuronal cluster.

5.3.1 Thin Fibertract

The fibertract is the most common formation of the neurons and it is basically chain of neurons connected one by one, or the entire fibertract is a single long neuronal axon. The action potential impulse comes from the first neuron of the chain and disappears on the last one. For the proposed simulation approach the picture will be exactly as showed in Figure 5.1-5. The main issue for the thin fibertract simulations is in the size of the one segment of the path (λ, or dL). If segment is smaller (closer to the size of real neuron), then the accuracy of the solution is better. For the multiple fibertract simulation the picture can be similar to Figure 5.3-1.

5.3.2 Myelinated Fibertract

Myelinated fibertract is similar to the thin one. The only difference from the electromagnetic point of view is the myelin shield around the axons which protects the ions from the flowing inside and outside the neuron. The neuronal flux is possible only between myelin formations. These types of fibertracts are located within the white matter.

Myelin formations typically all have equal dimensions along the neurotract. So in the computational scheme the size of one neuronal path segment should be exactly equal to the size of the myelin formation (like it is showed in Figure 5.3-2).

5.3.1 Neuronal Cluster

Neuronal cluster is the main formation of the cerebral cortex. The cluster in general is a group of neighbour neurons activated at the same time. Although they are activated simultaneously, the initial impulse is coming from the first starting neuron (usually it is the white matter neuron which is the last neuron of the fibertract) and after single activation impulse disappears. The computational scheme for neuronal cluster can be seen in Figure 5.3-3 and involves one voltage source with multiple parallel connections.

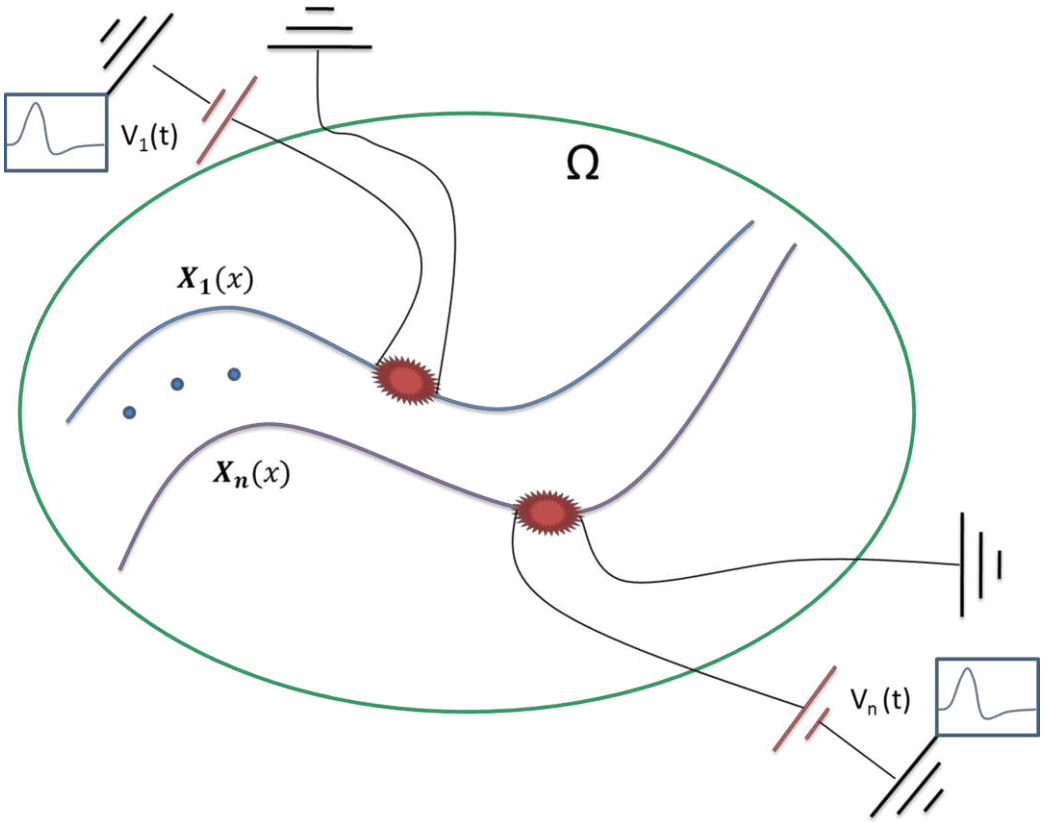

Figure 5.3-1. Multiple thin fiber formulation

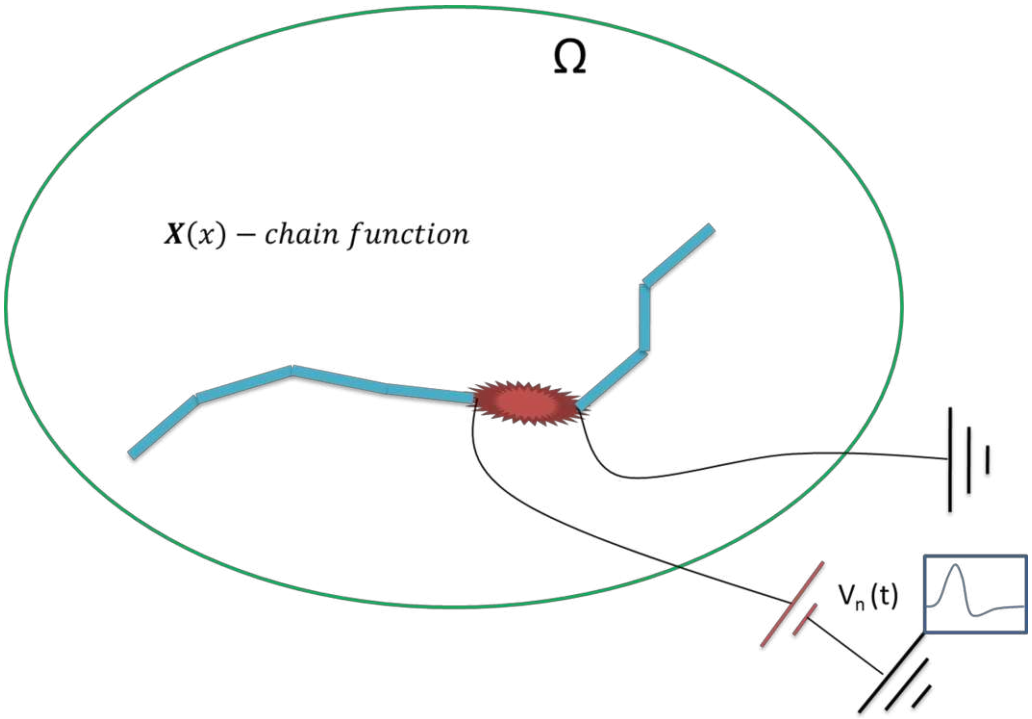

Figure 5.3-2. Myelinated fibertract formulation

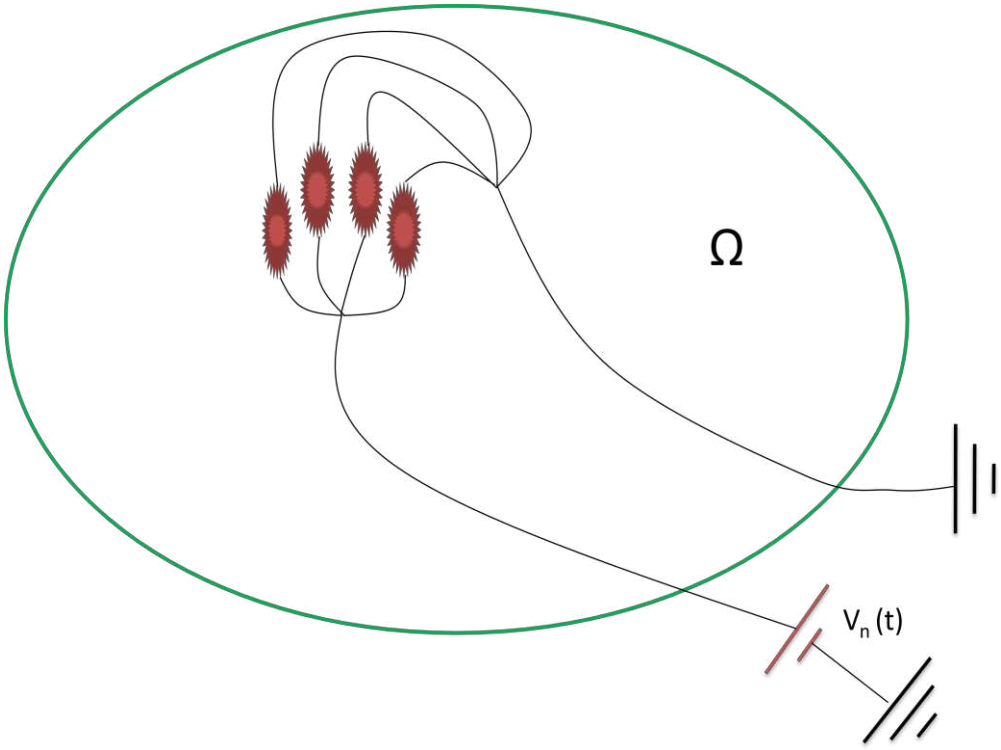

Figure 5.3-3. Neuronal cluster formulation

5.4 Mathematical Basis for the Solution of the Inverse Problem Based on the Novel Neuronal Current Source

This Section shows the ability of the novel neuronal current approach to deliver the proposal for the inverse problem solution. This unique feature of this modelling method has a significant value for the forward problem as none of the traditional current source models can deliver the unique solution not only to forward problem but also to inverse problem. Ability of this presented technique to be inversed also makes forward modelling more feasible in terms of practical applicability.

5.4.1 Neurological Basis – Activation of White Matter Fibertracts

The basis of the new inverse problem solution approach is followed by the neurological data, which determine the white matter as a transferring tissue between different functional brain regions. The functional regions itself consist of grey matter neurons positioned on the cortex. The total number of these neurons exceeds 10^{11}. Total number of trans-neuronal connections is greater than 10^{23} [39]. Even once knowing the exact position of each neuronal cell in the cortex and all possible references the only forward computations would be almost impossible and very resource consumptive with using existing technologies. Inverse computations are not even considered with such large numbers of operating bodies.

However, at present all known imaging modalities use average estimates of the neuronal behaviour and consider neuronal group activation rather than activation of a single neuron. The group of activated neighbour neurons is associated with the specific brain region which is highlighted during the scanning process. This works well for chemical-based modalities or invasive techniques (PET, fMRI), where the brain zone is clearly associated with average amount of processed signal, but cannot be applied to MEG due to impossibility of spatial differentiation. In simple words the received signal is affected by all neurons independently of their spatial location.

From the other side, the signal can be clearly differentiated temporally, which means that long acting signals can be separated from short acting ones, and with this advantage the new inverse approach, which is based on the white matter fibertracts activation, can be suggested. The white matter axons are much longer; the total number of these axons is much less than the number of neurons. Once detected, one fibertract can clearly show the brain region where the signal is coming from and another region where the signal is going to (see Figure 5.4-1 for reference).

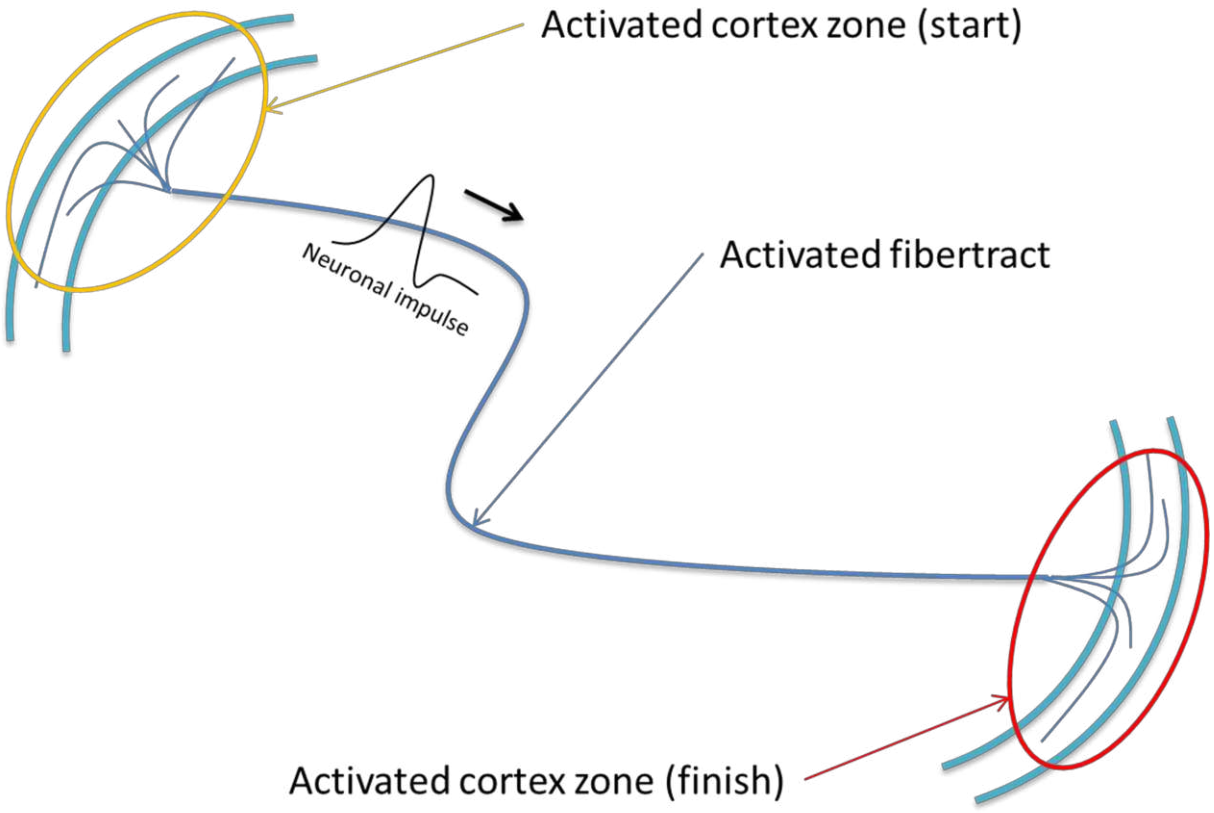

Figure 5.4-1. Novel Inverse Problem approach. White matter fibertracts activation detection, which leads to the activated cortex zones mapping.

5.4.2 Mathematical basis delivery

The Inverse problem solution based on presented novel approach can be constructed with using partial pre-reconstruction for the specific subject. This reconstruction is performed in order to obtain all possible white matter fibertracts within the brain area with the help of DTMRI scanning technology and further white matter DTI reconstruction technique. The idea of the method consists of assuming fibertracts being activated or deactivated at the unknown time points. Due to the specific parameters of the activation function (5.2-13), such as continuity in space and time, in combination with the non-linearity of the path in 3D space, the uniqueness of the solution can be achieved even with several magnetic field measurement points around the head. Number of possible fibertracts is unlimited and depends on the initial discretisation resolution.

Reconstructed white matter pathways are constant physical parameter of the brain structure; therefore the 3D positions and curvature are constant throughout the timeframe of taking the measurements. After MRI scan has been done and DTI reconstruction is performed, mathematically each fibertract curve can be represented as function $\boldsymbol{X}(x)$ in 3D. All fibertracts form a space of pathways:

$$\begin{gathered} \boldsymbol{X_i}(x) \\ x \in (0, \lambda N_i) \\ i = 1, .., M \end{gathered} \tag{5.4-1}$$

where M is the total number of white matter fibertracts within the brain (average number of fibertracts in adult human brain is around 100 millions). The example reconstructed pathways for healthy subject are presented in Figure 5.4-2.

Assume that each fibertract will have activated state while the neuronal impulse is running. Therefore there are no unpredictable starts and cut-offs of the impulse and

uncertainty can be avoided. Thus the activation function can be written for each path with using local path coordinate system topology:

$$\mathcal{F}_i(t, x_i(t, t_1^0), \mid \lambda, N) = \sum_{n=1}^{N} f_n(t)$$

$$f_n(t) = \begin{cases} U_0(1 - T(x_i(t, t_i^0) - n\lambda)^2); & t\epsilon\left[n\frac{\lambda}{V_0} + t_1^0, n\frac{\lambda}{V_0} + t_1^0 + \gamma_0\right] \\ U_1; & t\epsilon\mathbb{R}\backslash\left[n\frac{\lambda}{V_0} + t_1^0, n\frac{\lambda}{V_0} + t_1^0 + \gamma_0\right] \end{cases} \tag{5.4-2}$$

$$f_n(x)\epsilon\boldsymbol{X_i}(t, t_i^0, \lambda, N)$$

Here the coordinate $x_i(t, t_i^0)$ is the path coordinate which depends on the path position, time, and the impulse staring time t_i^0. Also the required discretization has to be performed on this step for each of the path items $\boldsymbol{X_i}(x) = \boldsymbol{X_i}(x, \lambda, N)$. The only unknown here is t_1^0 as all other variables can be calculated by using (5.2-3) in combination with (5.2-5). Therefore with appropriate substitutions voltage function can be written:

$$\mathcal{F}_i = \mathcal{F}_i(t, t_i^0) \tag{5.4-3}$$

where $t_i^0 = t_{1,i}^0$, and therefore for a given action potential and impulse path t_1^0 and t_2^0 can be calculated using:

$$\begin{aligned} t_{1,i}^0 &= t_i^0 \\ t_{2,i}^0 &= t_i^0 + \frac{\lambda}{V_0} \end{aligned} \tag{5.4-4}$$

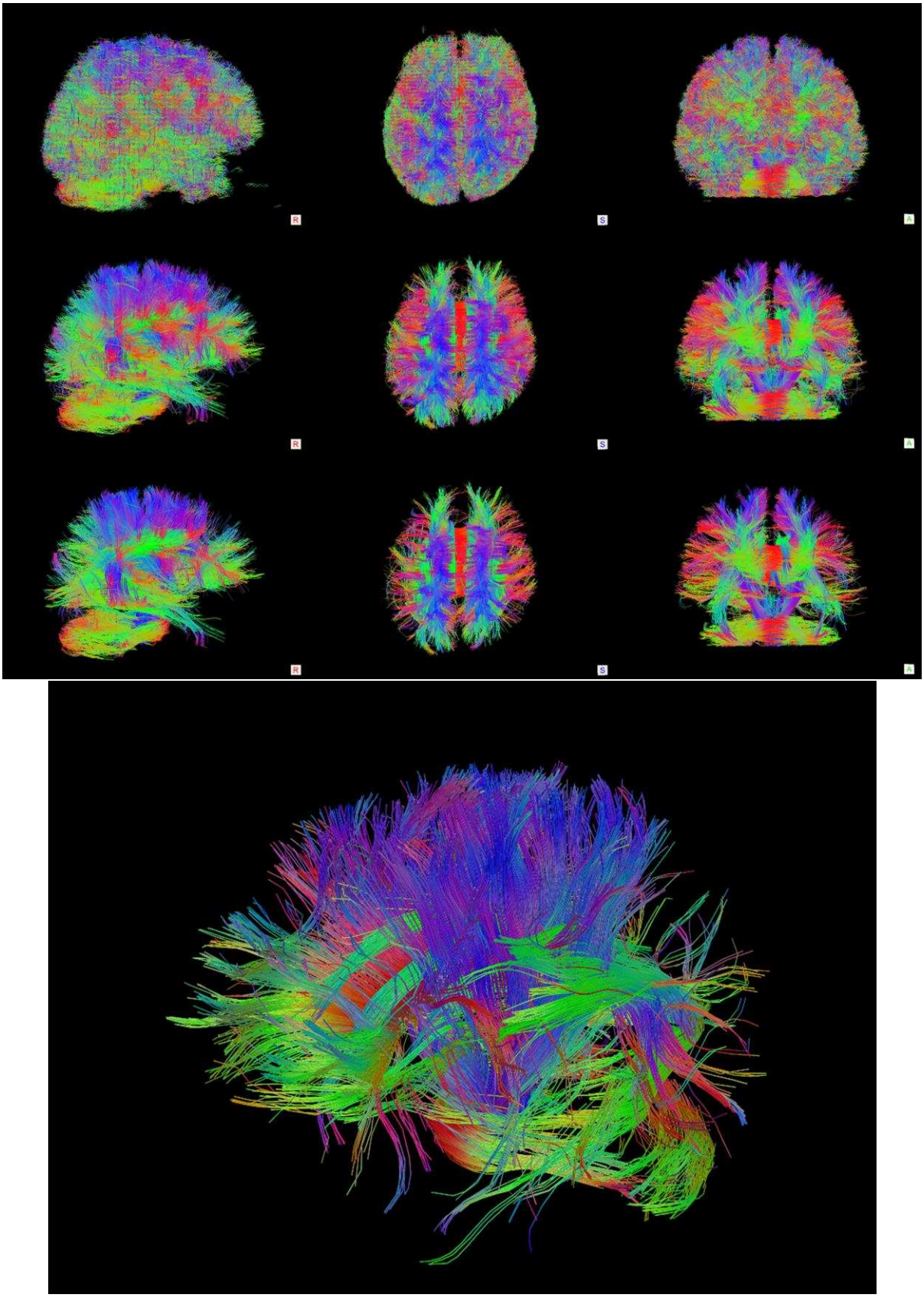

Figure 5.4-2. White matter fibertracts reconstruction X_i. Top row shows whole-brain fibers, middle row shows fibers longer than 18mm, and bottom row shows fibers longer than 30mm. Columns represents from left to right: Right, Sagittal, and Anterior view respectively

The primary current density caused by the voltage distribution can be computed by using Ohm's law in general tensor form:

$$\boldsymbol{J_i}(\boldsymbol{r}', t) = \frac{\mathcal{F}_i(t, t_i^0)}{A}\boldsymbol{\sigma}(\boldsymbol{r}') \cdot \boldsymbol{\tau_i}(t, t_i^0) \tag{5.4-5}$$

where $\boldsymbol{\sigma} = \boldsymbol{\sigma}(\boldsymbol{r})$ is the conductivity tensor obtained from DTMRI, A is the cross-sectional fibertract area, $\boldsymbol{\tau} = \boldsymbol{\tau}(x_i) = \boldsymbol{\tau}(t, t_i^0)$ is the tangential vector to the path from local path coordinate system, which is equal to the normal vector of the area A, and $\boldsymbol{r}'$ is the global coordinate.

Applying the simplified Maxwell equations (3.1-7) and (3.1-8) to our problem, and assuming symmetrical behavior of the secondary currents (see paragraph 5.1.2), the following equation for magnetic field calculation in case of single fibertract can be obtained:

$$\boldsymbol{B_i}(\boldsymbol{r}, t) = \frac{\mu_0}{4\pi}\int_G \boldsymbol{J}_i(\boldsymbol{r}') \times \frac{\boldsymbol{R}}{R^3}dv' = \frac{\mu_0}{4\pi}\int_G \left(\frac{\mathcal{F}_i(t, t_i^0)}{A}\boldsymbol{\sigma}(\boldsymbol{r}') \cdot \boldsymbol{\tau_i}(t, t_i^0)\right) \times \frac{\boldsymbol{R}}{R^3}dv' \tag{5.4-6}$$

the voltage function $\mathcal{F}_i$ does not depend on $\boldsymbol{r}'$**,** therefore can be placed outside of integration. For the simplicity of calculations fibertract area can be averaged and placed out of the integration as a constant. Thus:

$$\boldsymbol{B_i}(\boldsymbol{r}, t) = \frac{\mu_0}{4\pi A}\mathcal{F}_i(t, t_i^0)\int_G (\boldsymbol{\sigma}(\boldsymbol{r}') \cdot \boldsymbol{\tau_i}(t, t_i^0)) \times \frac{\boldsymbol{R}}{R^3}dv' \tag{5.4-7}$$

The integral now contains only known parameters therefore can be easily calculated for known path and conductivity tensor distribution, so replacing it with the linear vector function of t and t_i^0 :

$$\boldsymbol{B_i}(\boldsymbol{r}, t) = \frac{\mu_0}{4\pi A}\mathcal{F}_i(t, t_i^0)\boldsymbol{g_i}(\boldsymbol{r}, t, t_i^0) \tag{5.4-8}$$

$$\boldsymbol{g_i}(\boldsymbol{r}, t, t_i^0) = \int_G (\boldsymbol{\sigma}(\boldsymbol{r}') \cdot \boldsymbol{\tau_i}(t, t_i^0)) \times \frac{\boldsymbol{R}}{R^3} dv'$$

The direction vector $\boldsymbol{\tau_i}(x)$ depends only on the current position on the path in global Cartesian coordinate system. In local path coordinate system it linearly depends on time, because the system is uniform along path length. Action potential moves with constant velocity, so the vector $\boldsymbol{\tau}$ is moving with constant velocity, and therefore it can be described as a constant vector in local coordinate system, in global coordinates it depends on the path parameters, therefore $\boldsymbol{\tau} = \boldsymbol{\tau_i}(t, t_i^0)$.

Due to principal linearity of the problem the total magnetic field will contain the sum of all component magnetic fields, therefore:

$$\boldsymbol{B}(\boldsymbol{r}, t) = \sum_{i=1}^{M} \boldsymbol{B_i}(\boldsymbol{r}, t) = \sum_{i=1}^{M} \frac{\mu_0}{4\pi A} \mathcal{F}_i(t, t_i^0) \boldsymbol{g_i}(\boldsymbol{r}, t, t_i^0) \tag{5.4-9}$$

The structure of the function $\mathcal{F}_i(t, t_i^0)$ already contains all required activation parameters which all depend on t_i^0. Now mathematically the inverse problem can be converted into the problem of finding all t_i^0 for required time frame $[t_0, t_m]$, where t_0 is the global measurement starting time, and t_m is the global measurement final time. Note, that in case of fibertract non-activation throughout the measurement the appropriate activation starting time in activation function becomes $t_i^0 = t_m$, controlling the zero influence of this fibertract on total magnetic field.

All functions contained in the equation (5.4-9) are continuous with respect to the time domain; therefore time discretisation can be performed in order to solve this problem. Together with multiple sensor locations the discrete problem can be written:

$$\boldsymbol{B}(\boldsymbol{r_j}, t_k) = \sum_{i=1}^{M} \frac{\mu_0}{4\pi A} \mathcal{F}_i(t_k, t_i^0) \boldsymbol{g_i}(\boldsymbol{r_j}, t_k, t_i^0)$$

$$k = 1..K; p = 1..P \tag{5.4-10}$$

$$P \cdot K = M$$

Here P is the number of sensors, K is the number of measurements taken throughout the time (depending on the size of the problem and accuracy of the equipment, it is possible to choose optimal K). All together number of equations M must be equal to the total number of possibly activated fibertracts (or more than number of fibertracts in case of any error minimization analysis). Generally entire fibertracts set is supposed for any problem, however total number of fibertracts can be reduced if only specific brain region is considered and knowing that there is no magnetic field produced by other fibers.

Each neuronal path is determined using the bi-parametrical cubic spline approximation, and therefore can be described as a piecewise analytical function of second order in Cartesian coordinate system. Thus, applying substitution for the local coordinate system the following equation can be written:

$$\boldsymbol{X_i}(x) = \boldsymbol{P_2^i}(x_k - x_0)^{\boldsymbol{3}} + \boldsymbol{P_1^i} \tag{5.4-11}$$

Where $\boldsymbol{P_{1,2}^i}$ are the vectors consist of piecewise analytical coefficients characterizing the pathway parameters. Applying substitution (5.2-5) to (5.4-11) and knowing linear dependence of the vector $\boldsymbol{\tau_i}$ to the $\boldsymbol{X_i}(x)$, the following dependences can be obtained:

$$\boldsymbol{X_i}(t_k, t_i^0) = \boldsymbol{P_2^i}(t_k - t_i^0)^{\boldsymbol{3}} + \boldsymbol{P_1^i}$$

$$\boldsymbol{\tau}(t_k, t_i^0) = \boldsymbol{Q_2^i}(t_k - t_i^0)^3 + \boldsymbol{Q_1^i} \tag{5.4-12}$$

where $\boldsymbol{Q}_{1,2}^{\boldsymbol{i}}$ are also the constant piecewise coefficient vectors. Substitution of (5.4-12) to (5.4-8) gives the following expression for $\boldsymbol{g_i}$:

$$\boldsymbol{g_i}(\boldsymbol{r}, t_k, t_i^0) = \int_G \left(\boldsymbol{\sigma}(\boldsymbol{r}') \cdot \left(\boldsymbol{Q_2^i}(t_k - t_i^0)^3 + \boldsymbol{Q_1^i}\right)\right) \times \frac{\boldsymbol{R}}{R^3} dv' \tag{5.4-13}$$

Algebraic operations allow this expression to be transferred into the following:

$$\boldsymbol{g_i}(\boldsymbol{r}, t_k, t_i^0) = (t_k - t_i^0)^3 \int_G \left(\boldsymbol{\sigma}(\boldsymbol{r}') \cdot \boldsymbol{Q_2^i}\right) \times \frac{\boldsymbol{R}}{R^3} dv' + \int_G \left(\boldsymbol{\sigma}(\boldsymbol{r}') \cdot \boldsymbol{Q_1^i}\right) \times \frac{\boldsymbol{R}}{R^3} dv' \tag{5.4-14}$$

The both integrals do not depend on time and therefore can be pre-calculated numerically with initial space discretization for each path individually:

$$\begin{aligned} \boldsymbol{A_i}(\boldsymbol{r}) &= \int_G \left(\boldsymbol{\sigma}(\boldsymbol{r}') \cdot \boldsymbol{Q_2^i}\right) \times \frac{\boldsymbol{R}}{R^3} dv' \\ \boldsymbol{B_i}(\boldsymbol{r}) &= \int_G \left(\boldsymbol{\sigma}(\boldsymbol{r}') \cdot \boldsymbol{Q_1^i}\right) \times \frac{\boldsymbol{R}}{R^3} dv' \end{aligned} \tag{5.4-15}$$

The expression (5.4-14) now can be written in simple form:

$$\boldsymbol{g_i}(\boldsymbol{r}, t_k, t_i^0) = (t - t_i^0)^2 \boldsymbol{A_i}(\boldsymbol{r}) + \boldsymbol{B_i}(\boldsymbol{r}) \tag{5.4-16}$$

Knowing that for each time and path point expression (5.4-2) becomes a sum of quadratic polynomials of the following form:

$$\begin{aligned} f_n^i(t_k) = (t_k - t_i^0)^2[-U_0 T V_0^2 p_i^n] + (t_k - t_i^0)[2U_0 T V_0 n\lambda p_i^n] + p_i^n[U_0 \\ - U_0 T n^2 \lambda^2] + U_1(1 - p_i^n) \end{aligned} \tag{5.4-17}$$

$$p_i^n = \begin{cases} 1; & t_k \epsilon \left[n\frac{\lambda}{V_0} + t_i^0, n\frac{\lambda}{V_0} + t_i^0 + \gamma_0 \right] \\ 0; & t_k \epsilon \mathbb{R} \backslash \left[n\frac{\lambda}{V_0} + t_i^0, n\frac{\lambda}{V_0} + t_i^0 + \gamma_0 \right] \end{cases}$$

Summarizing all known coefficients to the pre-calculated piecewise analytical constant functions C_i^k, D_i^k, the overall function can be obtained in the following form:

$$\mathcal{F}_i(t_k, t_i^0) = P_i(t_k - t_0)\left\{C_i^k (t_k - t_i^0)^2 + D_i^k\right\} + U_1\left(1 - P_i(t_k - t_i^0)\right) \tag{5.4-18}$$

$$P_i = \begin{cases} 1; & t_k \epsilon [t_i^0, t_i^0 + N\lambda] \\ 0; & t_k \epsilon \mathbb{R} \backslash [t_i^0, t_i^0 + N\lambda] \end{cases}$$

Substituting (5.4-18) and (5.4-16) into (5.4-10) the following system can be obtained:

$$\boldsymbol{B}(\boldsymbol{r_j}, t_k) = \frac{\mu_0}{4\pi A} \sum_{i=1}^{M} \left(P_i(t_0)\left(C_i^k (t_k - t_i^0)^2 + D_i^k\right) + U_1\left(1 - P_i(t_i^0)\right)\right) \cdot \left((t - t_i^0)^2 \boldsymbol{A_i}(\boldsymbol{r_j}) + \boldsymbol{B_i}(\boldsymbol{r_j})\right)$$

$$k = 1..K; j = 1..J \tag{5.4-19}$$

$$J \cdot K = M$$

$$P_i = \begin{cases} 1; & t_k \epsilon [t_i^0, t_i^0 + N\lambda] \\ 0; & t_k \epsilon \mathbb{R} \backslash [t_i^0, t_i^0 + N\lambda] \end{cases}$$

where $P_i = P_i(t - t_i^0)$ can be considered as a Heaviside step function. The (5.4-19) is the fully invertible system of the equations with respect to the variable t_i^0.Normally it

can be solved by applying Laplace transformation because it contains only polynomial functions and a step function with unknown parameter. Applying the Laplace transform to (5.4-19) the system of equations becomes simple and inverse solution can be performed by solving the following linear system with respect to $e^{-t_i^0}$:

$$\boldsymbol{B}_j^n = \mathcal{L}\{\boldsymbol{B}(\boldsymbol{r}_j, t_k), n\} = \frac{\mu_0}{4\pi A}\sum_{i=1}^{M}\left[e^{-t_i^0}\left(\frac{\boldsymbol{W}_i^n(\boldsymbol{r}_j)}{s_n^5} + \frac{\boldsymbol{R}_i^n(\boldsymbol{r}_j)}{s_n^3} + \frac{\boldsymbol{H}_i^n(\boldsymbol{r}_j)}{s_n}\right) + \frac{\boldsymbol{G}_i^n(\boldsymbol{r}_j)}{s_n}\right] \tag{5.4-20}$$

$$n = 1..K; k = 1..K; j = 1..J$$

$$J \cdot K = M$$

Here $\boldsymbol{W}_i^n(\boldsymbol{r}_j)$, $\boldsymbol{R}_i^n(\boldsymbol{r}_j)$, $\boldsymbol{H}_i^n(\boldsymbol{r}_j)$, and $\boldsymbol{G}_i^n(\boldsymbol{r}_j)$ are constant pre-calculated vectors for given n, j and i.

If necessary, the averaging throughout the integration over a short period of time can be made; thus cutting off external noise and chaotic currents within the brain associated with other cognitive activity, and at the same time avoiding Laplace transformation method.

5.5 Summary

The realistic neuronal current source model has been developed. This model includes neurological and biological parameters of the real neuronal formations and satisfies the following requirements:

- High-quality (during the model construction only physical assumptions were made)
- Flexibility in terms of modelling of different structures (It is possible to simulate all range of existed neuronal formations)
- Flexibility in terms of properties (model has several important parameters which could be changed according to the real simulated neuronal formation)
- Finite element compatibility

Discussed approach also could be implemented into the EEG tomography problems; however different assumptions must be made for the considered currents because the symmetric approach does not work for electrical analyses.

The effect of approach implementation into the forward problem solution is carefully studied in Chapter 7.

Also the mathematical basis of the inverse problem solution which is based on the white matter fibertract activation detection is presented and its features were highlighted. This basis demonstrates the unique property of presented approach to be inversed and makes forward problem computations more feasible in terms of practical applications.

Chapter 6

Effects of Realistic Brain Model on the Solution of the Forward Problem

6.1 Problem with Traditional Current Sources

The brain model development approach discussed in Chapter 4 has been used for realistic forward simulations based on experimental data. The data was obtained from SPM dataset of Cambridge MEG laboratory at MRC CBU [88]. This dataset has been delivered by medics and contains high-quality MEG and EEG data for the healthy 25-old patient, male [89]. Also MRI scan have been obtained for this subject before the experiment which has been used for realistic geometrical brain model development.

MEG data from the patient were recorded during medical experiment involving showing the specific picture to the patient. The data contains recorded potentials and approximation pictures on the detection surface. Also high-quality fMRI were recorded during the experiment which allowed physiological correlation of displaying working parts of the cerebral cortex in the same time with the MEG signal collection. This gives the opportunity to literally know which areas are responsible for magnetic field production and the signal of which was displayed on MEG images.

The resulting fMRI and EEG data were processed and current source positions were mapped. Using this result three most active points were chosen as main primary current sources. The potentials in each current source were obtained using inverse EEG procedure developed by SPM lab and available in open source community for downloading [88]. These three activated zones and electric potential changing in

time for each zone are shown in Figure 6.1-1. These sources were implemented in the brain model as current sources with spherical shape.

All processed external data which were received from dataset, applied in simulations as an input, and compared with simulated results is:

1) Location of the neuronal current sources and their parameters
2) MEG experimentally recorded data associated with these sources activation
3) MRI and DTMRI of the brain for the subject for which the data was recorded

For each source the zero potential was applied on one hemisphere and the actual potential has been set on another hemisphere. The potentials were taken from the experimental data mentioned before (Figure 6.1-2).

This current source formulation is identical to the dipole formulation in case of radius of the sphere is small enough in comparison with the size of the model. In our simulations such small radius was chosen to be 0.5mm. The radius of the detection surface is approximately 200mm which satisfies this condition (radius ratio is 400). The positions of current sources implemented into the FE model could be seen in Figure 6.1-3. With respect to the activated brain zones these sources are placed in the most activated points.

The brain model was built with the parameters listed in Table 4-5 and is shown in Figure 6.1-4 together with the position of the detection surface. The detection surface is formed by the positions of 155 MEG detectors around the head according to the specifications of MEG tomography machine which has been used in data acquisition.

Although the current source approximation which is used in this model makes sense in terms of the computational approach (easy-to-implement, fast computing), it does not, however, consider less activated brain parts. The proposed modelling targets general accuracy and results are compared mostly with visual similarity. Obtained accuracy could be sufficiently improved in future if needed. The additional parameter of the simulation is the length of computation time range T = 600ms (calculated from the starting of the first potential). The result could be computed for each specific time frame independently because quasistatic approach is considered.

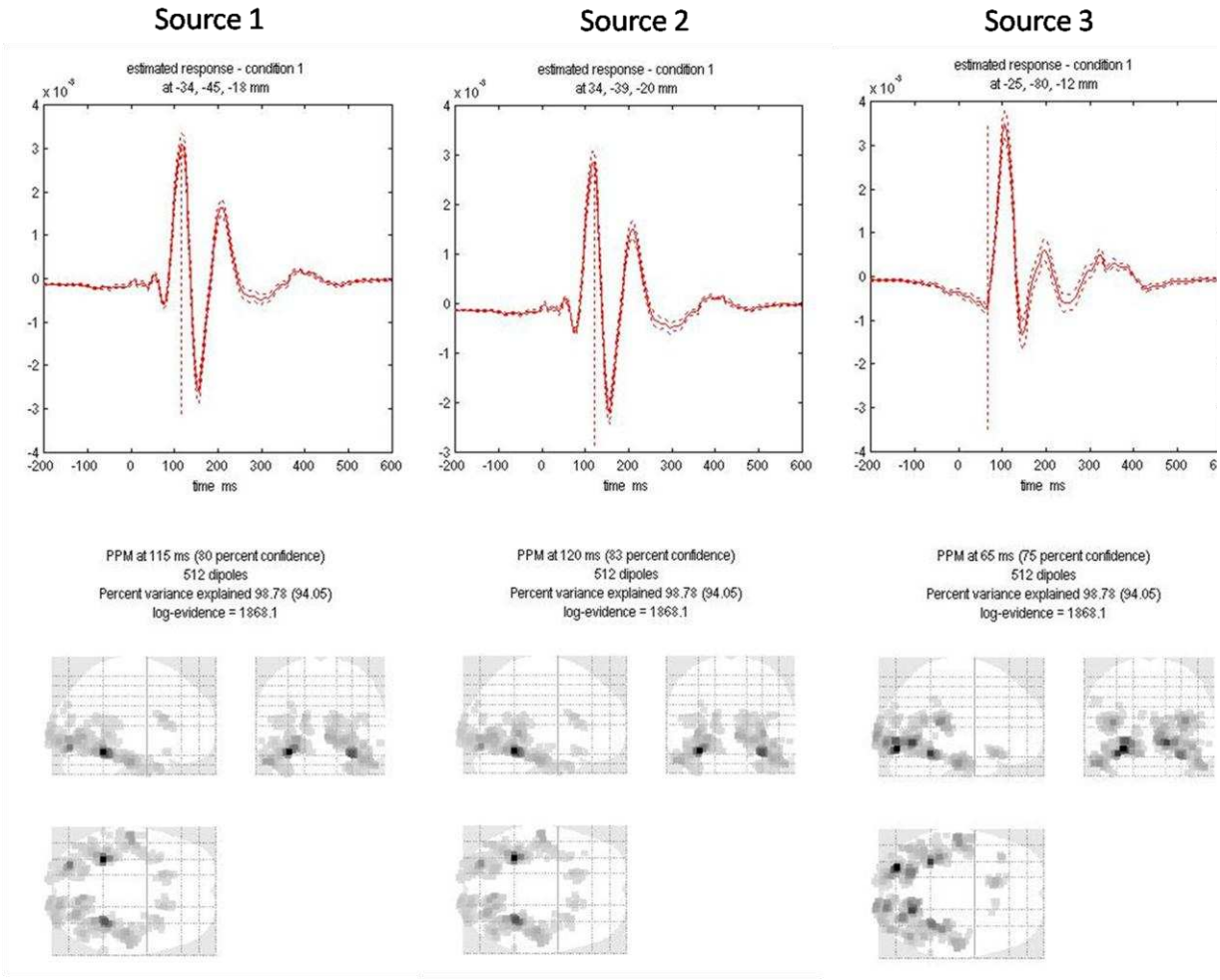

Figure 6.1-1. Voltage load, obtained from SPM dataset for each of the current source and assumed distribution (black points on the images matches the modeled sources in FEM)

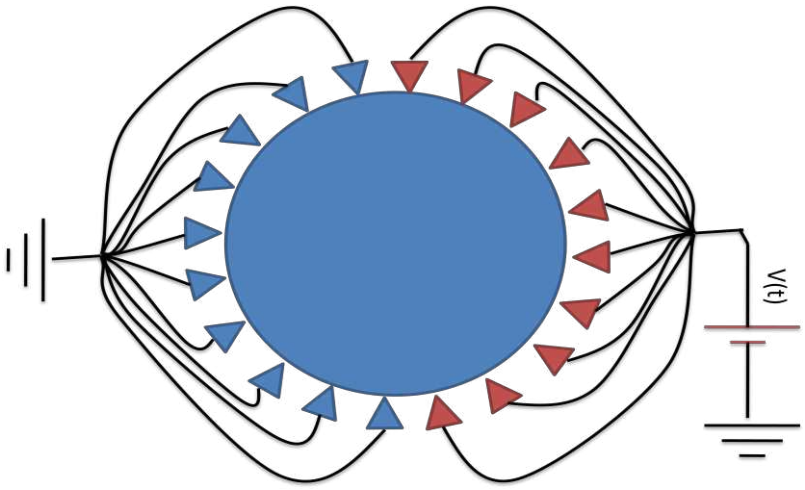

Figure 6.1-2. Current source modeling approximation

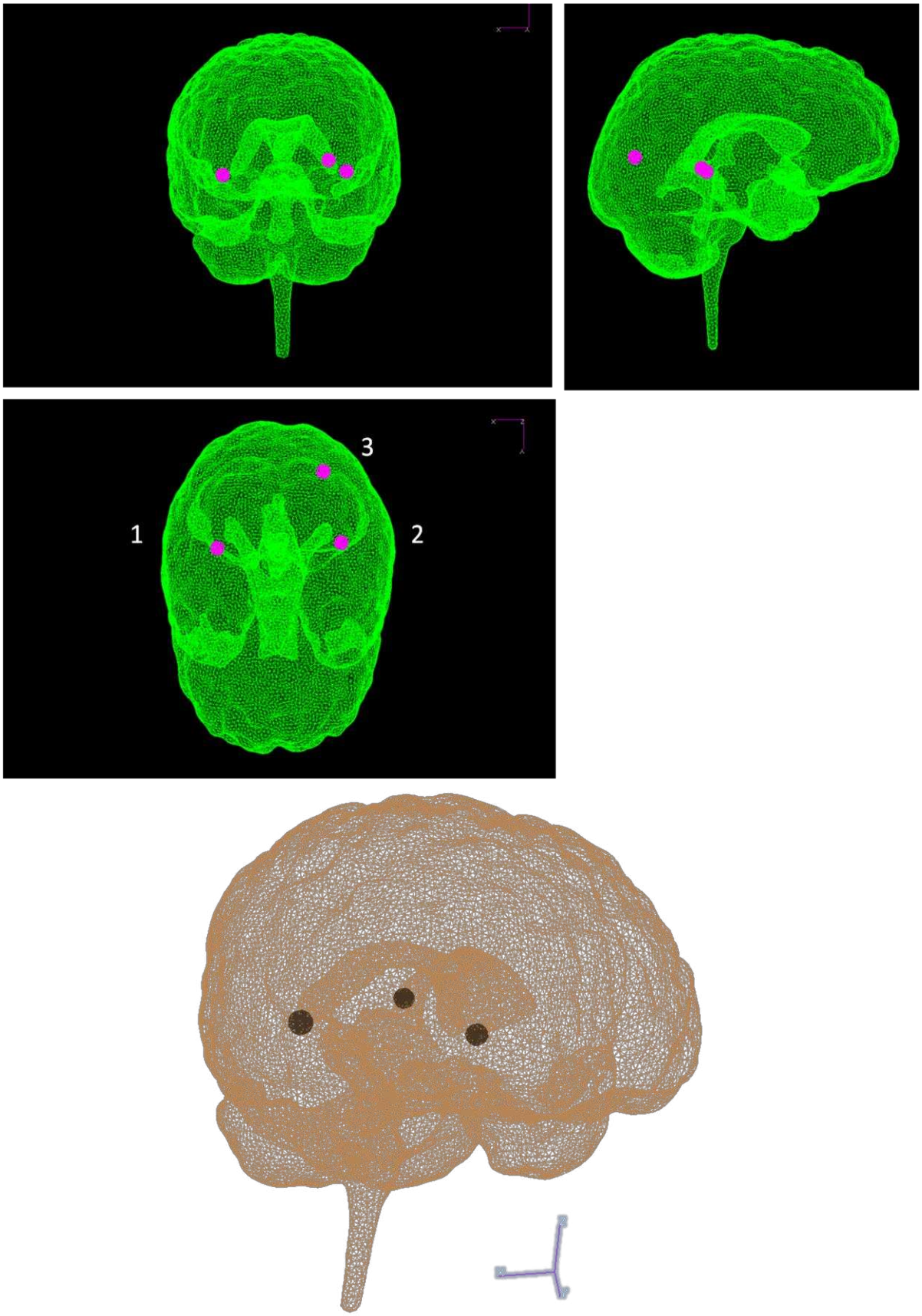

Figure 6.1-3. Position of the current sources ‘1’,’2’, and ‘3’ in FE model

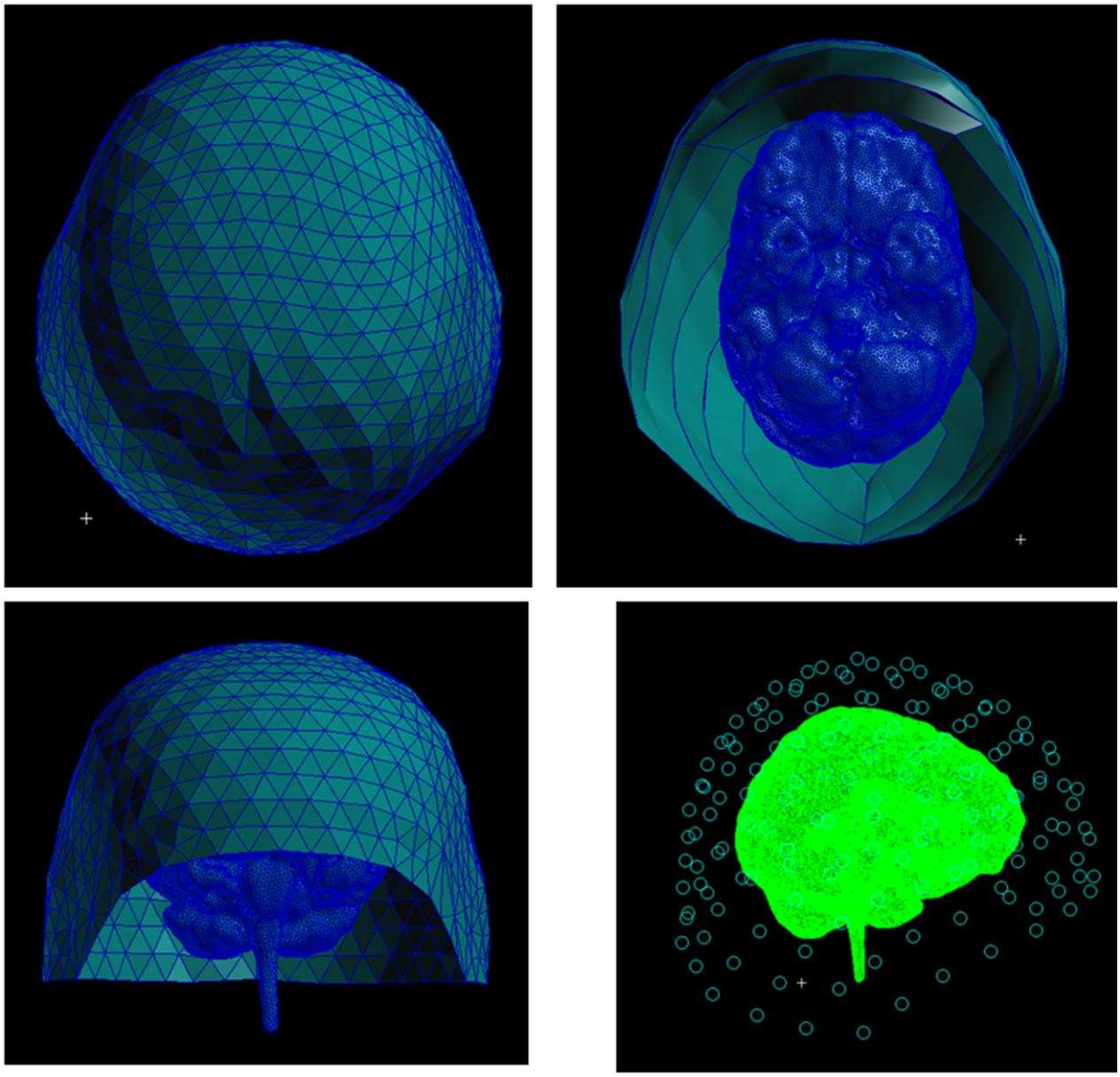

Figure 6.1-4. Position and form of the detection surface (bottom left - actual positions of the SQUID sensors)

6.2 Results of Simulation

The most significant timeframe in terms of model validation is t=200ms as at this time point the potentials in current sources have their maximum values (see Figure 6.1-1). Therefore all obtained results are listed for this timeframe. In Figure 6.2-1 the resulting magnetic flux density vector plot is displayed on the detection surface. In Figure 6.2-2 and Figure 6.2-3 the current density vector plot inside the brain is presented in order to illustrate the complexity of volume currents which take place in these computations.

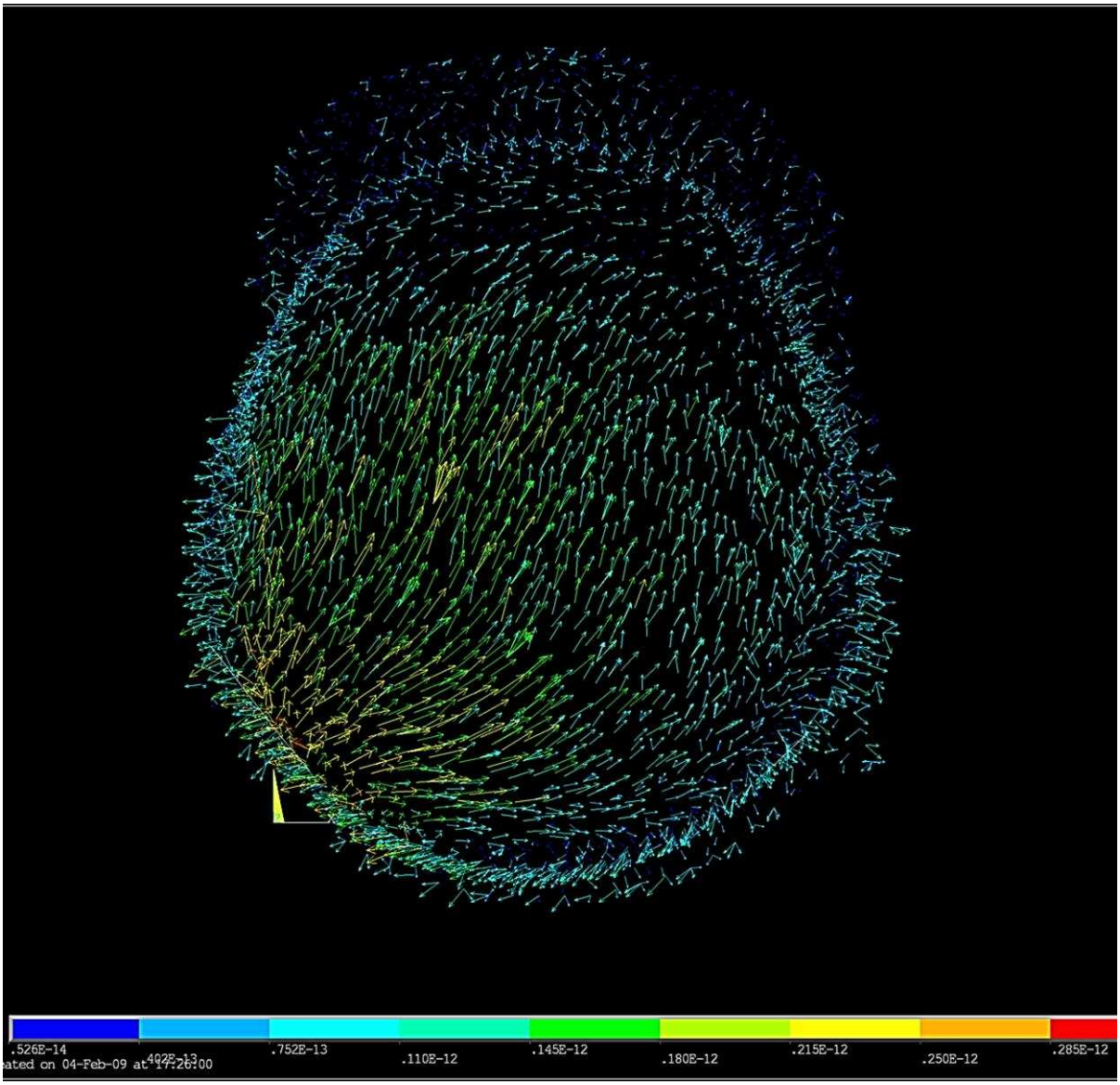

Figure 6.2-1. Results. Magnetic field flux density vector distribution on the detection surface

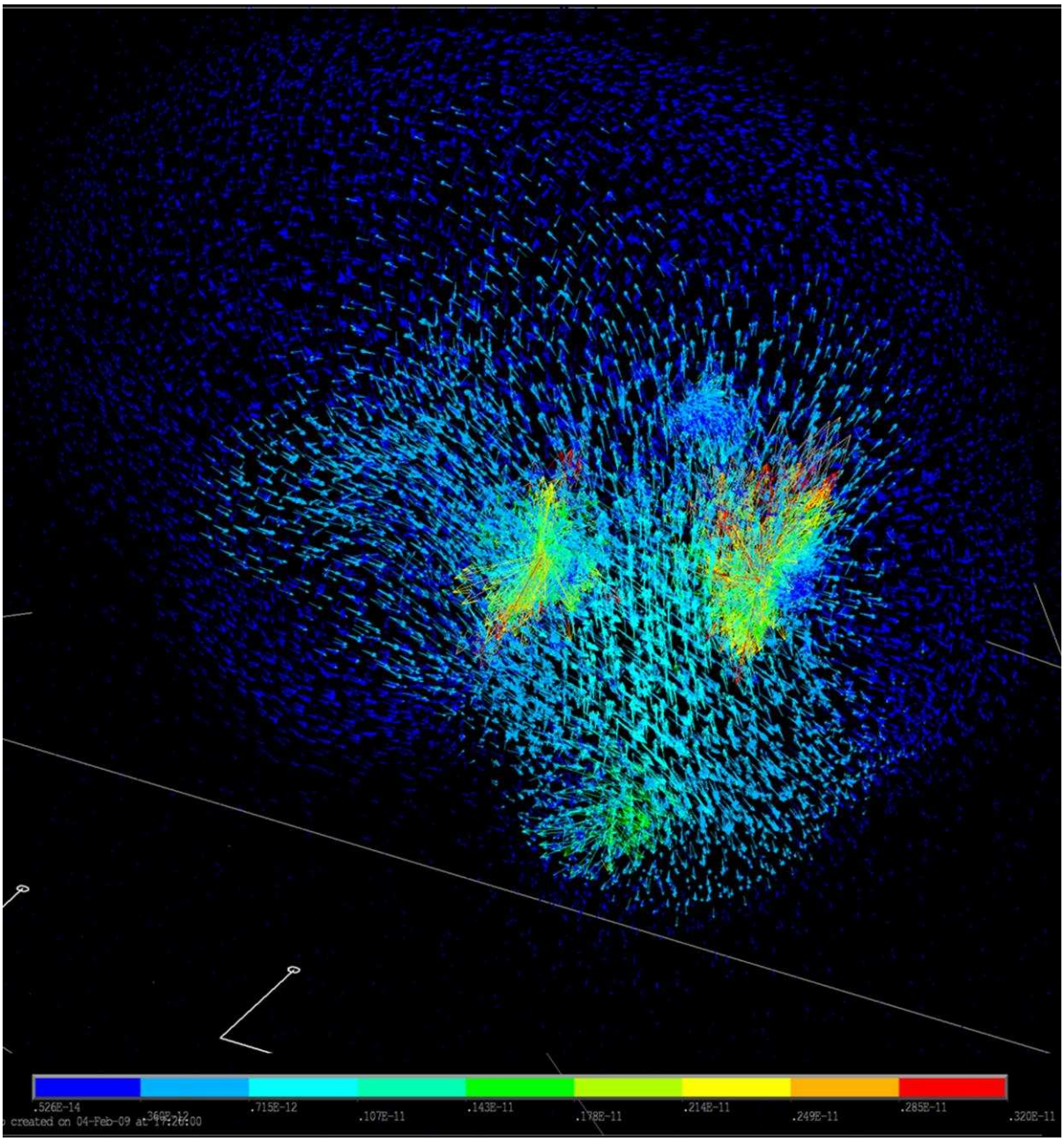

Figure 6.2-2. Results. Current density vector plot inside the brain structure

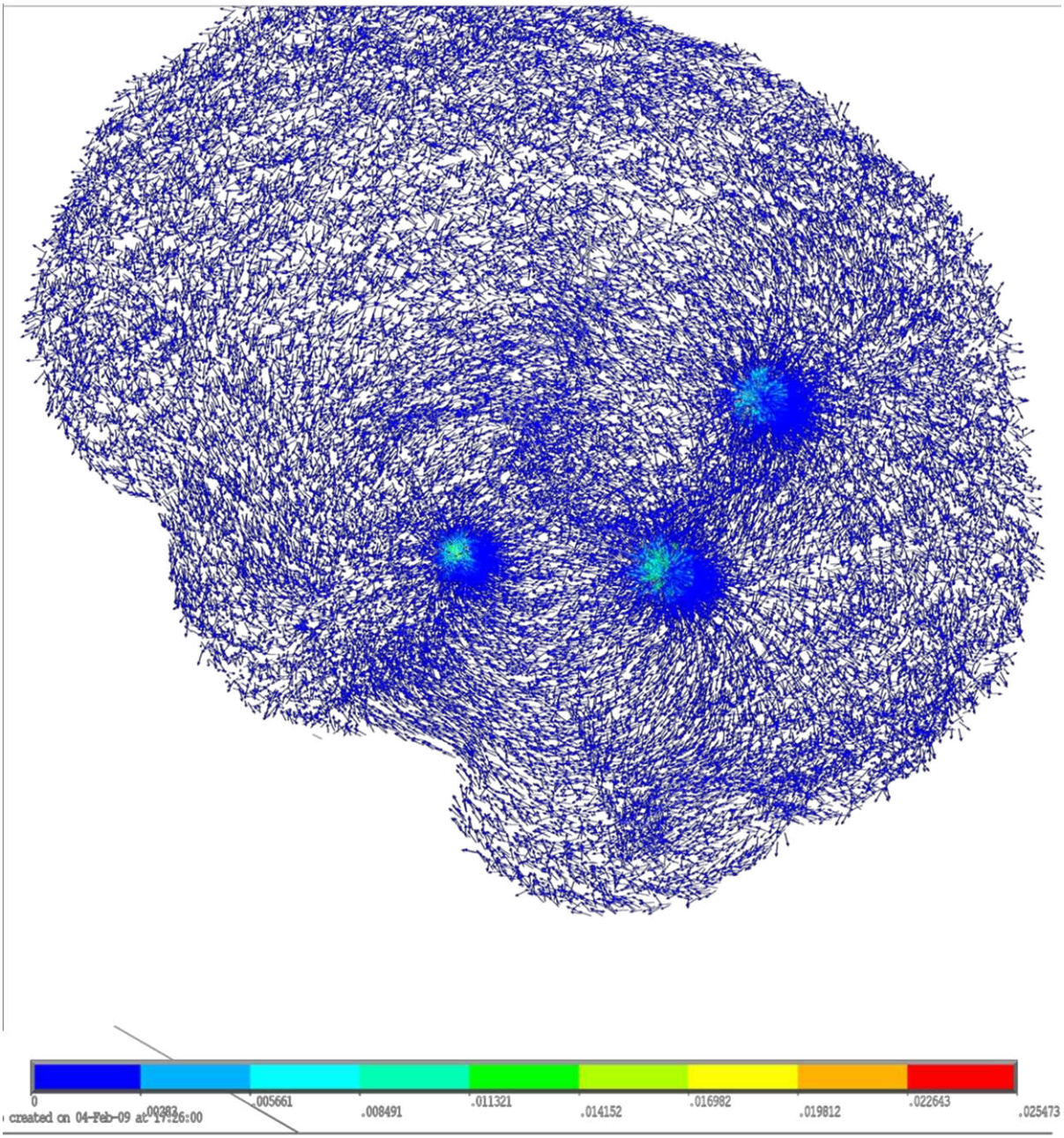

Figure 6.2-3. Result. Current density intensive plot

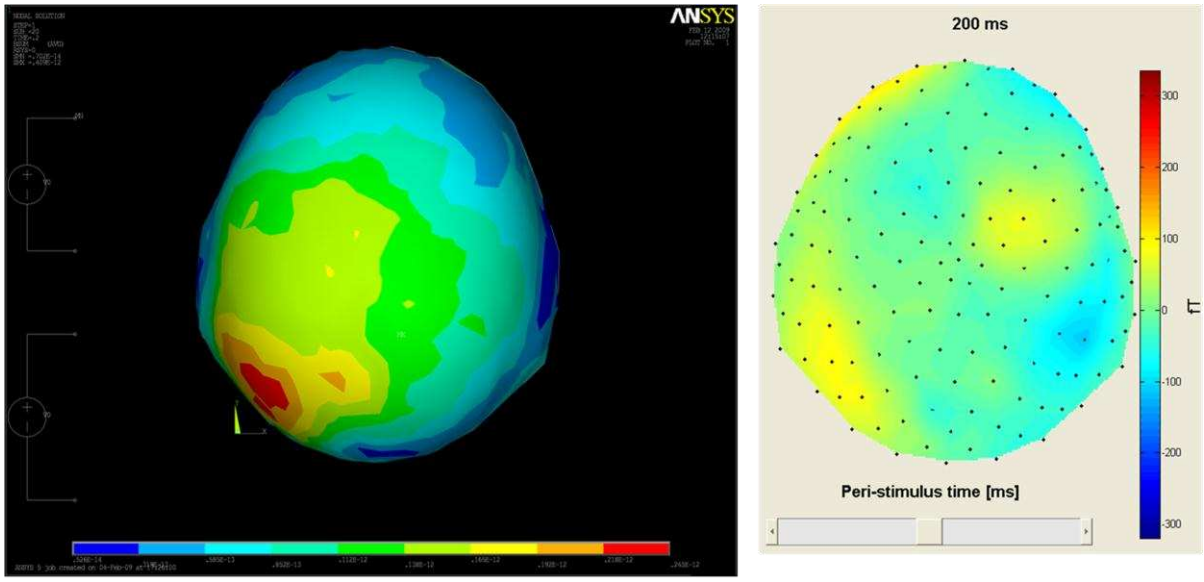

Figure 6.2-4. Comparison of the FEM result (left) and real experimental result (right). Magnetic field flux density plot on the detection surface. Time frame - 200ms.

The magnetic field flux density magnitude was mapped on the detection surface and compared to the experimental MEG results (Figure 6.2-4). The point with the maximal value of the magnetic field flux density is located in the left posterior part of the detection surface. The point of minimal magnetic field flux density is found in the right posterior region. From the medical point of view it is very useful result as the sources were taken from the visual cortex (visual experiment have been done for the subject) and we could conclude that the information was processed in the left hemisphere of the brain cortex which appears in the resulting magnetic field. In both computed and experimental plots maximum and minimum points are almost in the same position. The maximum magnitude of the magnetic field flux density in the computational result is 245fT which is less than in experimental result (approximately 300fT). This difference is caused by the unrealistic computational approach for the current source approximation as was mentioned before. Less activated parts were not considered in simulations so we could approximate their influence on the solution by the difference of the experimental and computed result which could be calculated in percentage as normal deviation d_{ex} with the following equation:

$$d_{ex} \approx \frac{\left|B_{exp} - B_{num}\right|}{B_{exp}} = 18\% \tag{6.2-1}$$

where B_{exp} is the maximum experimental magnetic flux density value, and B_{num} is the maximum numerical magnetic flux density value. This is, however, a very approximate result as the total error of the solution must be taken into account.

Overall error could be computed as an average deviation of the error for each timeframe for the solution by following formulae:

$$e_a = \frac{\sum_{k=1}^{M} \sqrt{\sum_{i=1}^{N} \left(\frac{B_{i,k}^{exp} - B_{i,k}^{num}}{B_{i,k}^{exp}} \right)^2}}{M} \cdot 100\% \tag{6.2-2}$$

Here $N = 155$ is the number of detectors, $M = 200$ is a total number of timeframes where the result is obtained, $B_{i,k}^{exp}$ and $B_{i,k}^{num}$ is a magnitude of the magnetic flux density in i-th detector for k -th timeframe, experimental and numerical respectively. For our result the estimated overall error were computed:

$$e_a = \mathbf{40}\% \tag{6.2-3}$$

This error shows the summarized average influence of objective errors for the numerical solution in comparison to real experimental results. The particular error of the method e_m can be also estimated knowing the influence of the low-active brain zones which was not included into the simulations:

$$e_m = e_a - d_{ex} = \mathbf{22}\% \tag{6.2-4}$$

6.3 Summary

For the developed realistic brain model the three-source problem was solved and compared to the experiment. During these computations the following points were highlighted:

- The great influence of the volume currents and therefore complex anisotropic conductivity was showed
- The numerical result according to the visual examination of the magnetic field plot is very similar to the experimental one despite the fact that current source approximation was not realistic
- The influence of low-activated brain zones was computed in form of the deviation $d_{ex} = 18\%$
- The overall error was estimated for this particular case as $e_a = 40\%$
- Based on the above assumptions the average error of the method can be computed: $e_m = 22\%$

These values however have only estimated meanings. But it allows approximate the influence of the current source improper modelling with using a following method. The error of the solution for the test case discussed in paragraph 4.4.3 for chosen parameters can be computed and was less than 5%. So the estimate error e_{cs} for the current source modelling could be evaluated as a difference between the summarized method error and finite element error:

$$e_{cs} = e_m - 5\% = \mathbf{17}\% \tag{6.3-1}$$

This means that the error caused by the current source modelling approach (**17%**) has the same range order as the actual error caused by not considering of the low-activated brain zones (**18%**). Thus this error is objectively too big for this kind of solutions.

Having this type of proposed current source models (which is identical to dipole models) could cause total ignorance of these low-activated parts during the forward or inverse solution. So the dipole model therefore cannot be considered as an appropriate neuronal current source model not in theoretical computations nor in clinical practice, which confirms previous assumptions.

Chapter 7

Effects of Realistic Source Model on the Solution of the Forward Problem

7.1 Formulation of the Problem for Realistic Fibertract Modelling

The discussed in Chapter 5 proposal for the neuronal current source modelling was implemented into the forward solution for single fibertract activation problem. The position and shape of the neuronal path is shown in Figure 7.1-1.The path was divided according to the computational approach, described above, onto 20 segments along its length. The length of each segment is 0.5cm with 10cm overall length of the path. The cross-sectional diameter of the path was chosen to be 1 mm with approximate area of $1mm^2$. This has been done to show the dependence of magnetic field from the neuronal path thickness and to evaluate real fiber track diameter based on realistic data. Voltage difference was applied to each segment according to the parabolic interpolation of the action potential, which could be seen in Figure 7.1-2.

Here the last three segments are shown assuming similar behavior for the rest of them. The voltage value for non-activated segments is -0.064V. It was set up according to biological data [6]. The maximum value is corresponded to the maximum value of the action potential of 0.04V. The rest of the brain was considered as a conductor with zero voltage boundary conditions.

The other parameters of the finite element forward simulations in this case and some technical data are shown in Table 7-1.

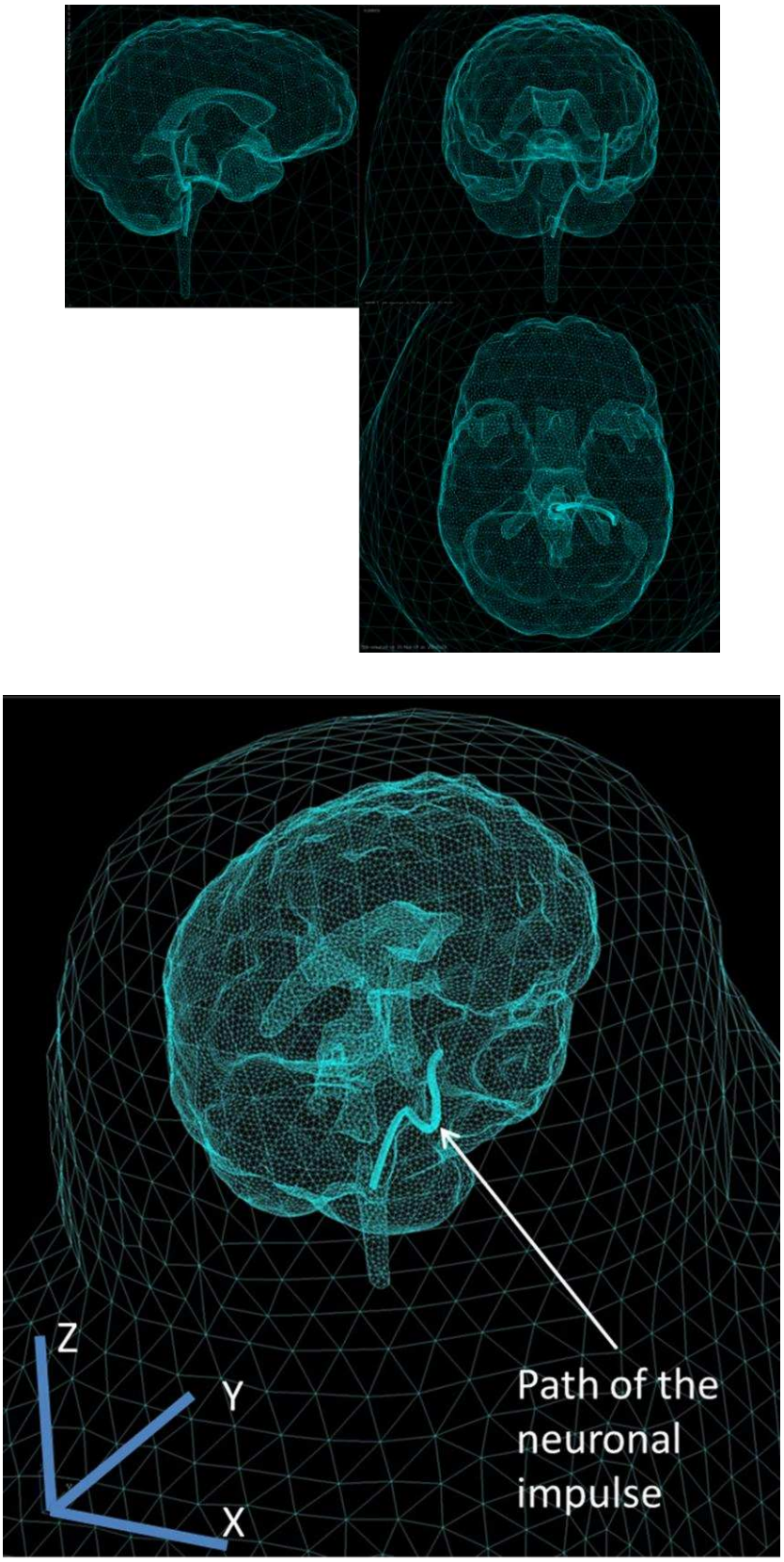

Figure 7.1-1. Brain model view with defined neuronal impulse path

TABLE 7-1. PARAMETERS OF THE SIMULATIONS FOR NEUROTRACT (FIBERTRACT) ACTIVATION

Parameter	Value
Solution	Time-dependent electromagnetic
Time period of simulations	0.01s
Number of time steps for simulation	200
Accuracy criteria	Test for Mesh Convergence of 5%

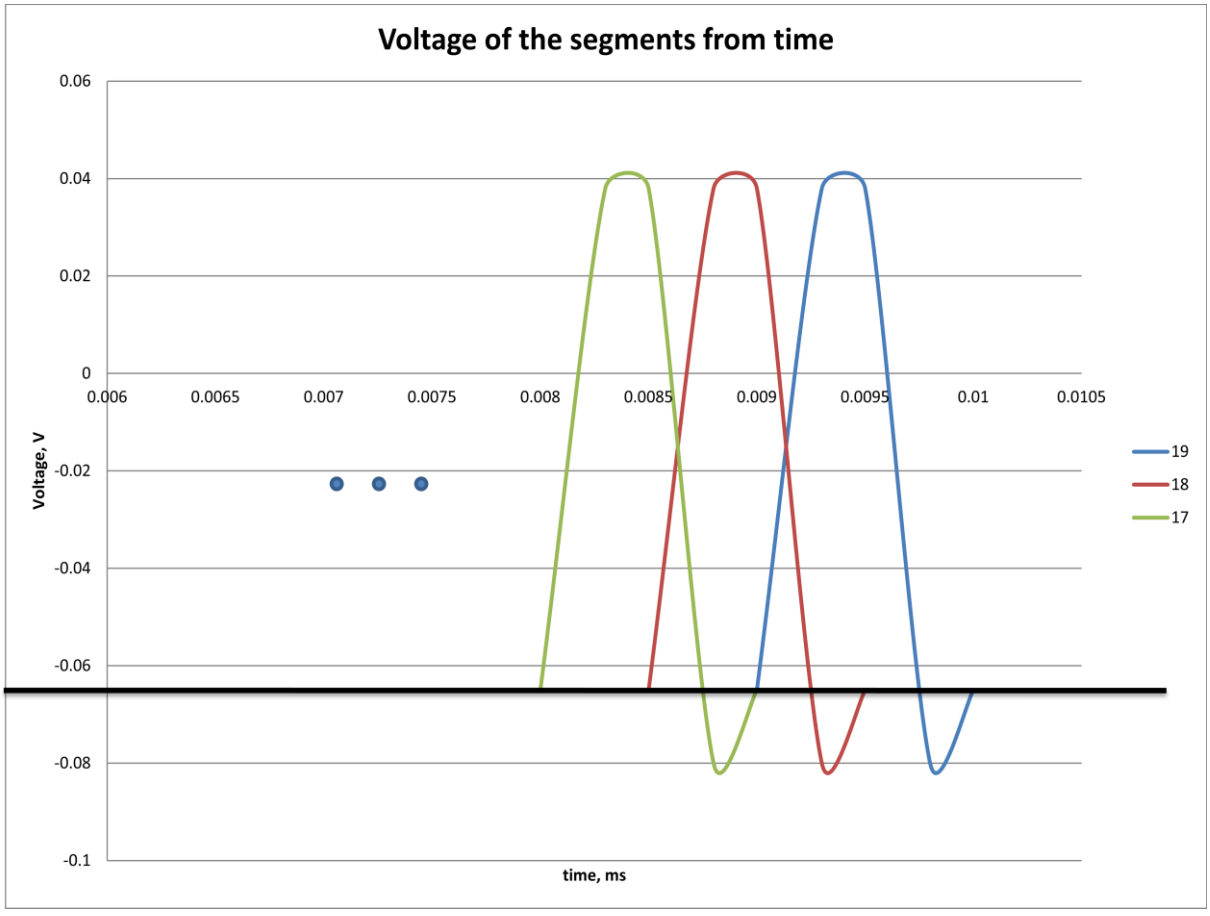

Figure 7.1-2. Voltage applied to the segments of the path. Here the last three segments are shown – number 17 (green), 18 (red), and 19 (blue). A black baseline shows the voltage of deactivated segments.

7.2 Results of Simulation for Activated Fibertract Problem

In Figure 7.2-1 the current density vector distribution at several time frames is shown. The current density propagation along the path during the time of propagation can be traced. The charge transition according the action potential mechanism can be observed, and the current which passes through membrane of the cell is clearly seen (Figure 7.2-2 and Figure 7.2-3).

For the resulting magnetic field measurements 5 points were chosen according to the real positions of detectors in MEG machine (they are displayed in Figure 7.2-4). The magnetic field flux density was obtained at these points during the simulation, and the results are presented on the diagram (Figure 7.2-5). Presented values on the graph are the magnitudes of the magnetic flux density vector $\boldsymbol{B}(\boldsymbol{r})$, where $\boldsymbol{r}$ represents the position of each detection point. The distances from each point to the beginning and to the end of the path are presented in Table 7-2.

The typical behavior of the MEG magnetic sensor output is obtained from the graph. Observed magnetic field graphs and patterns are highlighting the fact that real experimental recorded data most likely contains the white matter fibertracts impulses. This was also confirmed with realistic diameter fibertract simulations performed later in section 7.5.

Presented results proved that inverse problem solutions, which are currently consider only cortical activity, have to deal the consideration of white matter action potentials in combination with the cortical ones.

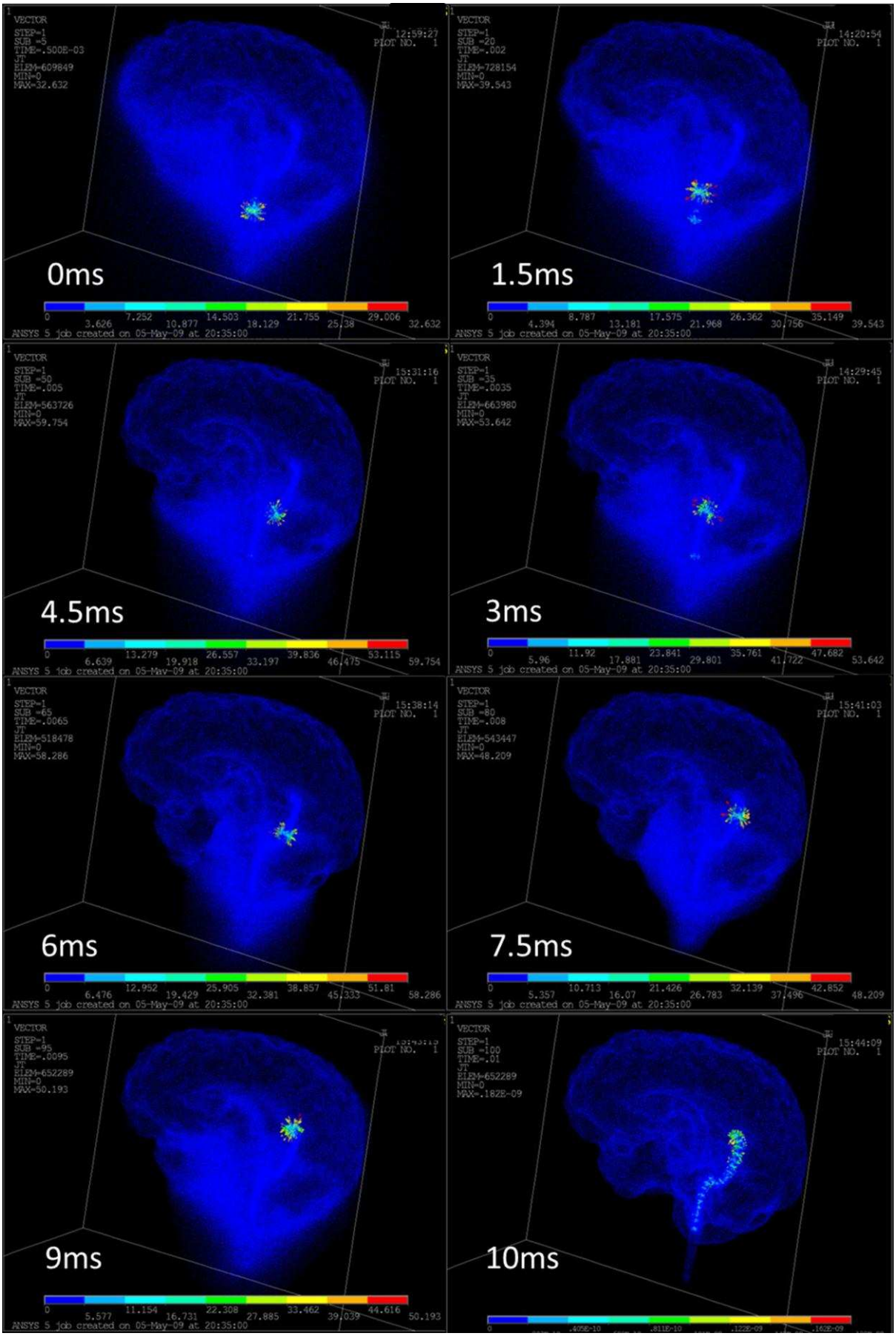

Figure 7.2-1. Electric current density visualization. From initial time 0ms (top left) to the final time 10ms (bottom right) respectively

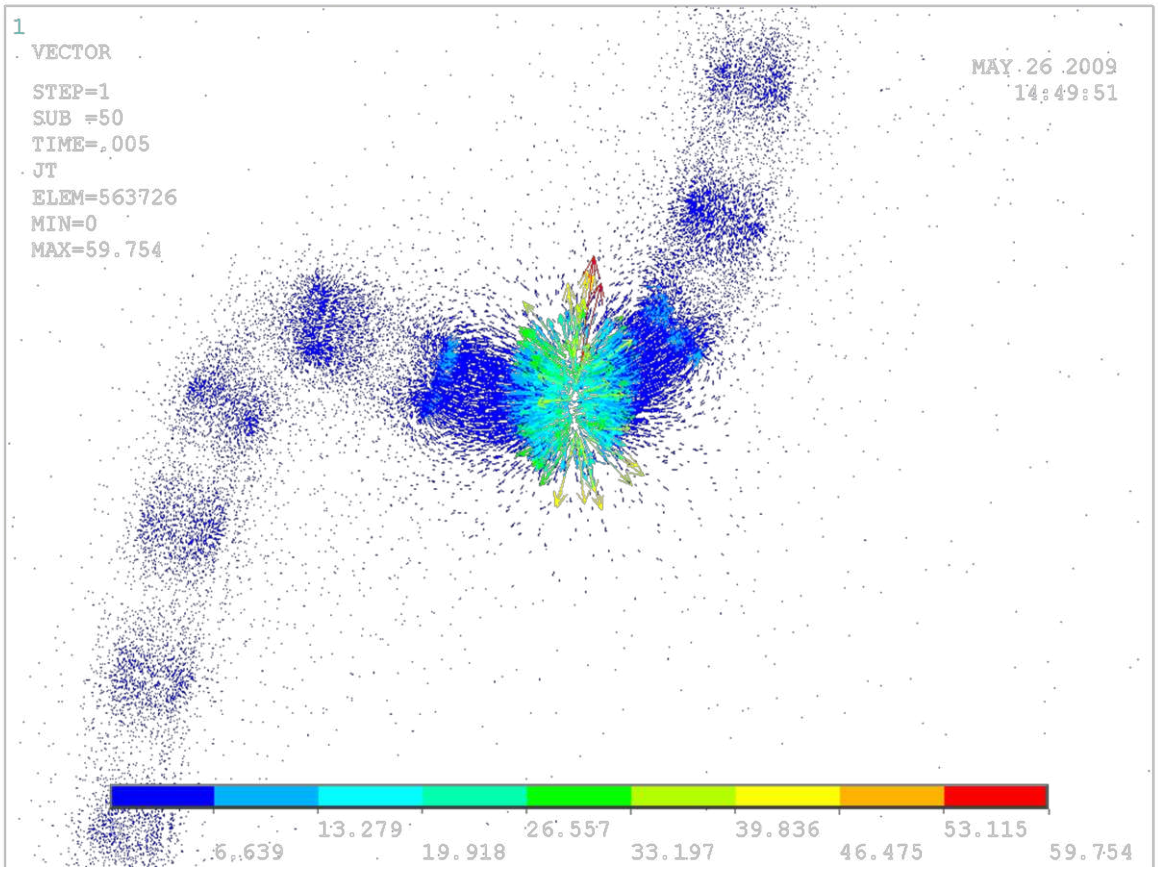

Figure 7.2-2. Current density vector distribution. Time point t=5ms. Vector sizes depend on magnitude

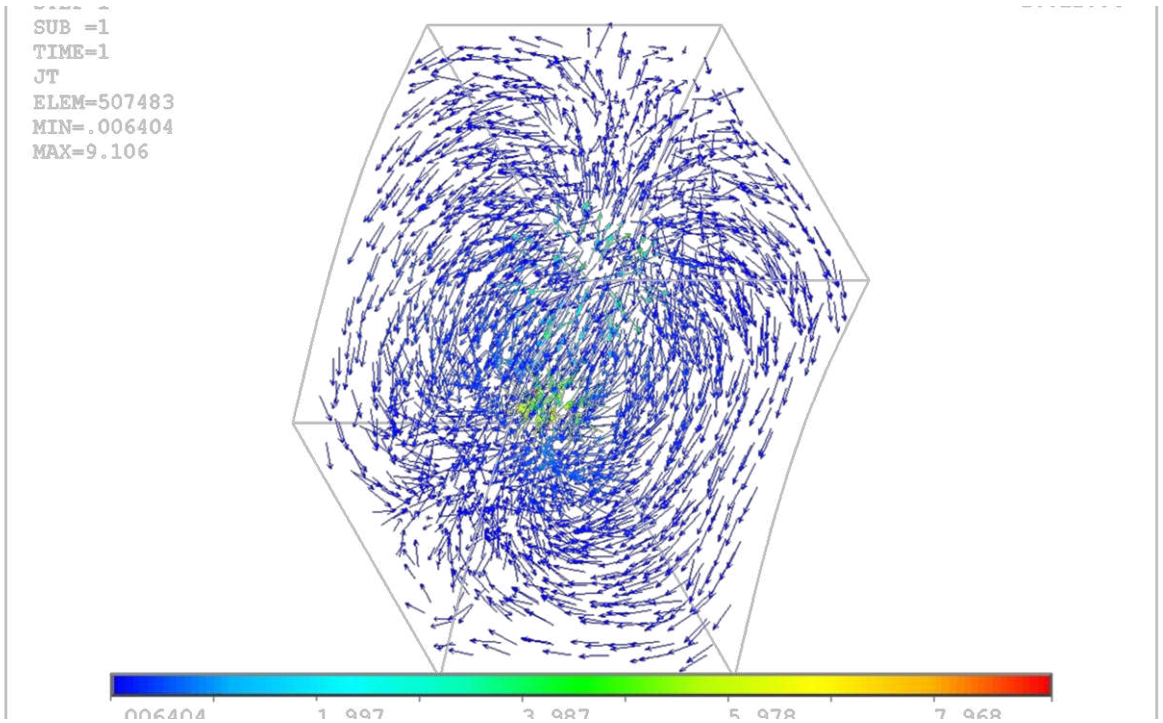

Figure 7.2-3. Current density vector distribution. Closer look at an arbitrary chosen time frame t=1.5ms. Constant vector sizes.

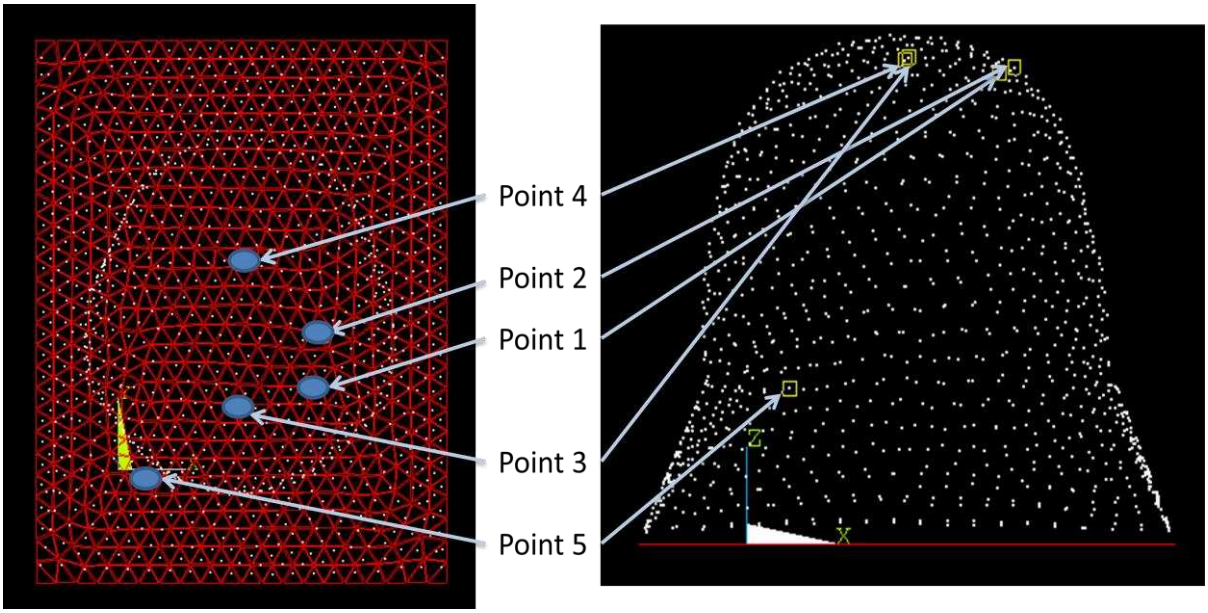

Figure 7.2-4. Position of the observed points for magnetic field measurements on the MEG detectors surface

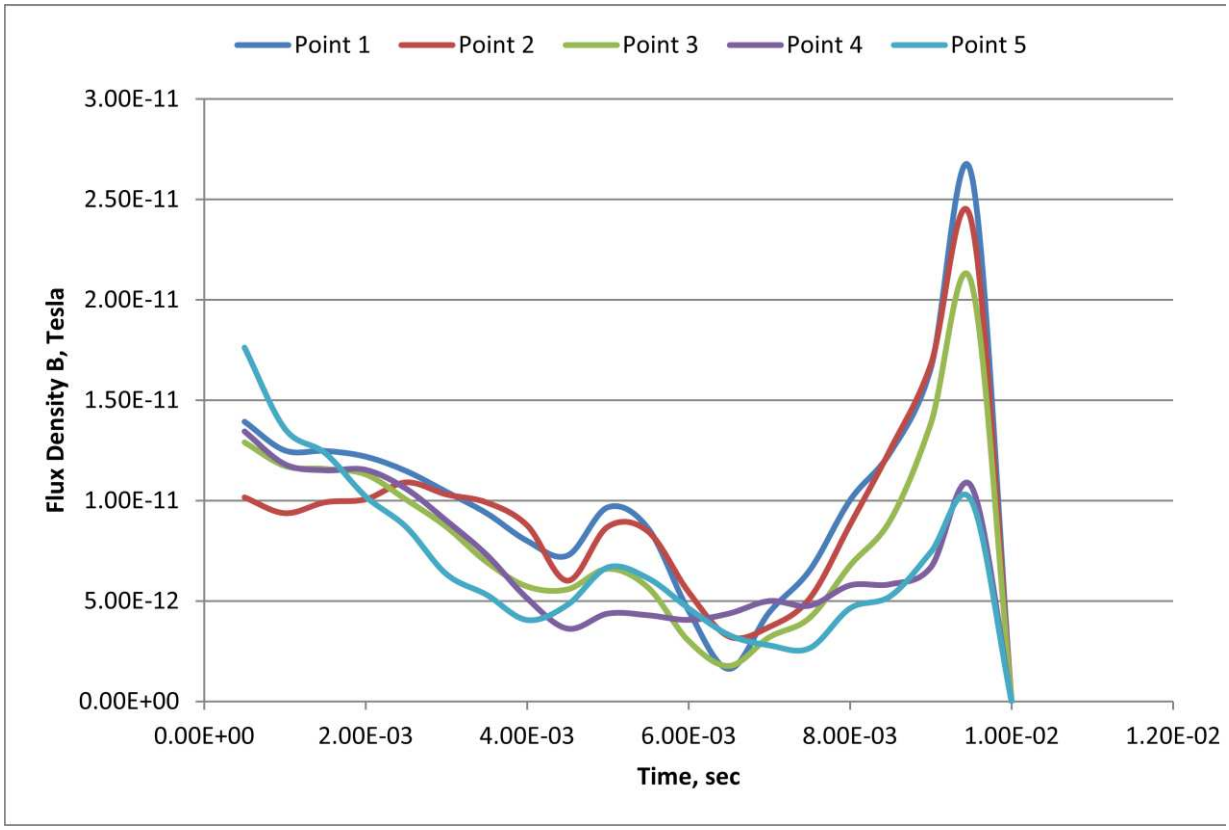

Figure 7.2-5. Magnetic field flux density for each corresponding detecting point

Table 7-2. Absolute distances from the measuring point to the path

Point number	Distance to the beginning of the path, m	Distance to the end of the path, m
1	0.15181	0.08089
2	0.15493	0.08060
3	0.15221	0.09201
4	0.15820	0.10631
5	0.11411	0.12142

7.3 Computation of Fibertract Diameter - Analytical Approach

Numerical results obtained magnetic field flux density magnitude B as approximately $1{\sim}25 \cdot 10^{-12}$T based on the abstract 1mm diameter fibertract. However, the realistic magnetic field flux density B_{real} has its range around $10{\sim}40 \cdot 10^{-15}$ T. The dependence of the magnetic field from the fibertract diameter can be calculated theoretically, and then it can be approximated with the help of numerical solution and compared with experimental results.

Short part of the fibertract can be represented as a uniform isotropic beam of the size *dL* (as it is shown in Figure 5.1-5). This beam has a cross-sectional area *S* and resistivity of the material $\rho = 1/\sigma$. The total current in the beam due to applied voltage difference V could be found:

$$I = \frac{V \cdot S}{\rho \cdot dL} \tag{7.3-1}$$

The magnetic field due to this current in the same conductive region will depends on *I* linearly (which is obviously follows from (3.1-8), substituting $\boldsymbol{J_p} = I \cdot \boldsymbol{n}$, where $\boldsymbol{n}$ is a unit direction vector), i.e.:

$$\boldsymbol{B}(\boldsymbol{r}) = \boldsymbol{k}(\boldsymbol{r}) \cdot I \tag{7.3-2}$$

where $\boldsymbol{k}(\boldsymbol{r})$ does not depend on *I*, and therefore substituting (7.3-1) into (7.3-2):

$$\boldsymbol{B}(\boldsymbol{r}) = \boldsymbol{k}'(\boldsymbol{r}) \cdot S \tag{7.3-3}$$

Thus we obtain the linear dependence between $\boldsymbol{B}$ – the magnetic field flux density around the head and S – the cross-sectional area of the fibertract. For 1mm^2 cross-sectional area we have got $B = \|\boldsymbol{B}\| \approx 1{\sim}25 \cdot 10^{-12}\mathrm{T}$. Thus to find realistic fibertract size we can use the formula:

$$S_r = S \cdot \frac{B_{real}}{B} \cong 1\mathrm{mm}^2 \cdot \frac{1{\sim}25 \cdot 10^{-15}\mathrm{T}}{10{\sim}40 \cdot 10^{-12}\mathrm{T}} \cong 0.025{\sim}2.5 \cdot 10^{-3}\mathrm{mm}^2 \tag{7.3-4}$$

So the diameter of the fibertract can be found:

$$d_r = \sqrt{S_r} \cong 15{\sim}150 \cdot 10^{-3}\mathrm{mm} \cong \mathbf{5{\sim}50\mu m} \tag{7.3-5}$$

The measured *in vivo* diameter of the fibertract is **13~20µm** [90]. This means the obtained result showed good correspondence with real experimental data. Therefore numerical simulations are proved to be fully in range of experimental values.

7.4 Employing ubmodelling for Estimating the Realistic Size Fibertract Simulations

Previously discussed Combined Submodelling Routine (paragraph 3.3.3.2) was implemented in order to sufficiently decrease computational time with no almost loss of accuracy. Proposed following analysis is designed to obtain the rate of computational resources improvement and the maximum error of the solution.

The problem discussed here is exactly the same as in previous case (Section 7.1), with only one neuronal segment consideration for simplicity propose. In Figure 7.4-1 the outline of the brain is shown together with the boundaries of the submodelling region and neuronal current source. Neuronal source is considered in form of novel approach (action potential) with voltage difference of 50mV. Thickness of the neuronal path is set up unrealistic of 0.5mm in order to test CSR on the solution. It is obvious that the efficiency of the CSR is increasing with the increasing of the scale difference, so for realistic micron sizes of the neuronal axon's thickness the relative estimated time of computations will be decreased sufficiently more.

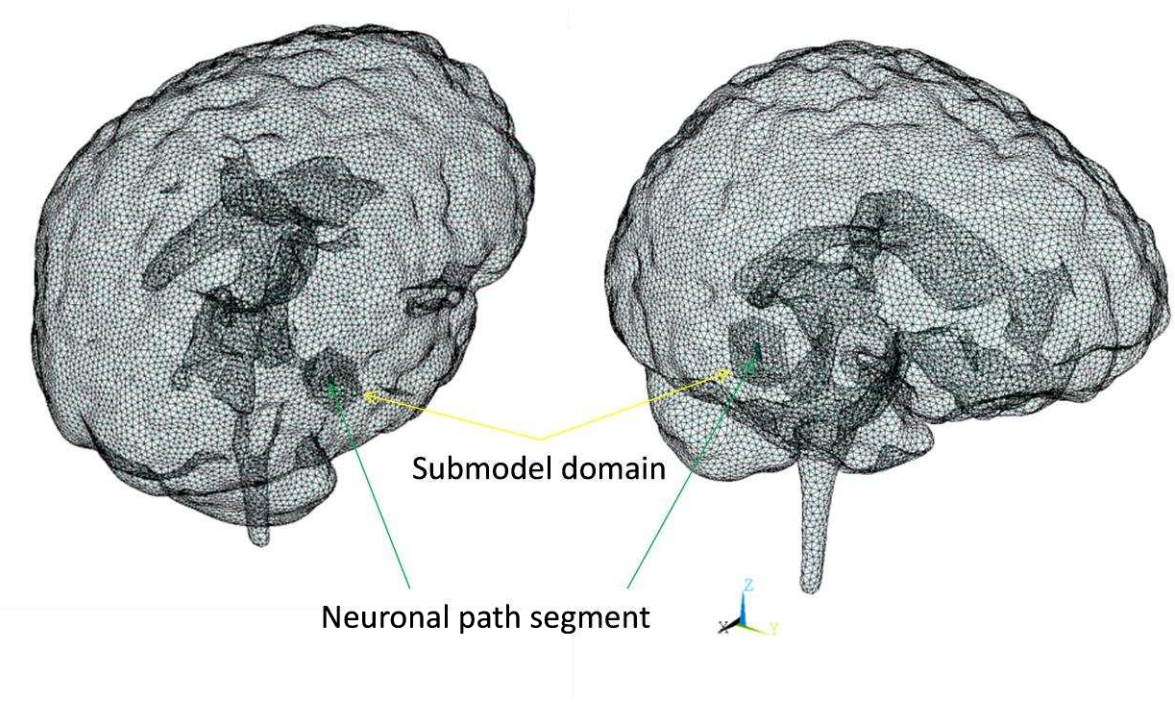

Figure 7.4-1. Outline of the brain model and position for the submodelling region and neuronal source

As discussed earlier, the submodel region was chosen as a small volume surrounding the current source, and the rest of the brain region was proposed having insufficient influence on the solution with further mesh improvements. Therefore two models were used in further computations: coarse initial model of the whole brain, and fine proper meshed submodel region. The problem is quasistatic; therefore for testing proposes only one step of integration could be performed as a static solution.

Mesh with around 800,000 elements has been generated for the coarse model (relatively poor for the multi-scale solution). This number of elements satisfies the mesh convergence criteria with the single scale in considered geometry of the brain model without neuronal current source inside. 300,000 elements has been found fine enough to satisfy accuracy requirements for the submodel mesh.

The model with very fine mesh of 10,000,000 elements has been used in order to generate direct solution for comparison. Obtained results with using SCR have been then compared to those without using submodelling but with the fine mesh instead (conservative approach). For this simulation the fine model containing 10,000,000 elements have been considered as the optimal according to the conservative mesh convergence criteria.

7.4.1 Simulation Results and Comparison

The computational set-up has been made and then quasistatic Maxwell equations were solved in the FE domain. The results were obtained for both fine mesh model and CSR model and compared.

InFigure 7.4-2 and Figure 7.4-4 the intensity of magnetic field flux density is performed on the detection surface around the head (points of interest for the solution). It is clearly shown that coarse model itself gives very poor result. However, after the CSR being applied the result is almost the same (maximum error of 5%) as in the fine model.

Sufficient improvement of current density distribution with applied CSR is shown in Figure 7.4-3. This distribution has been found to be the main reason for inadequate results for cases with poor mesh density near current source area.

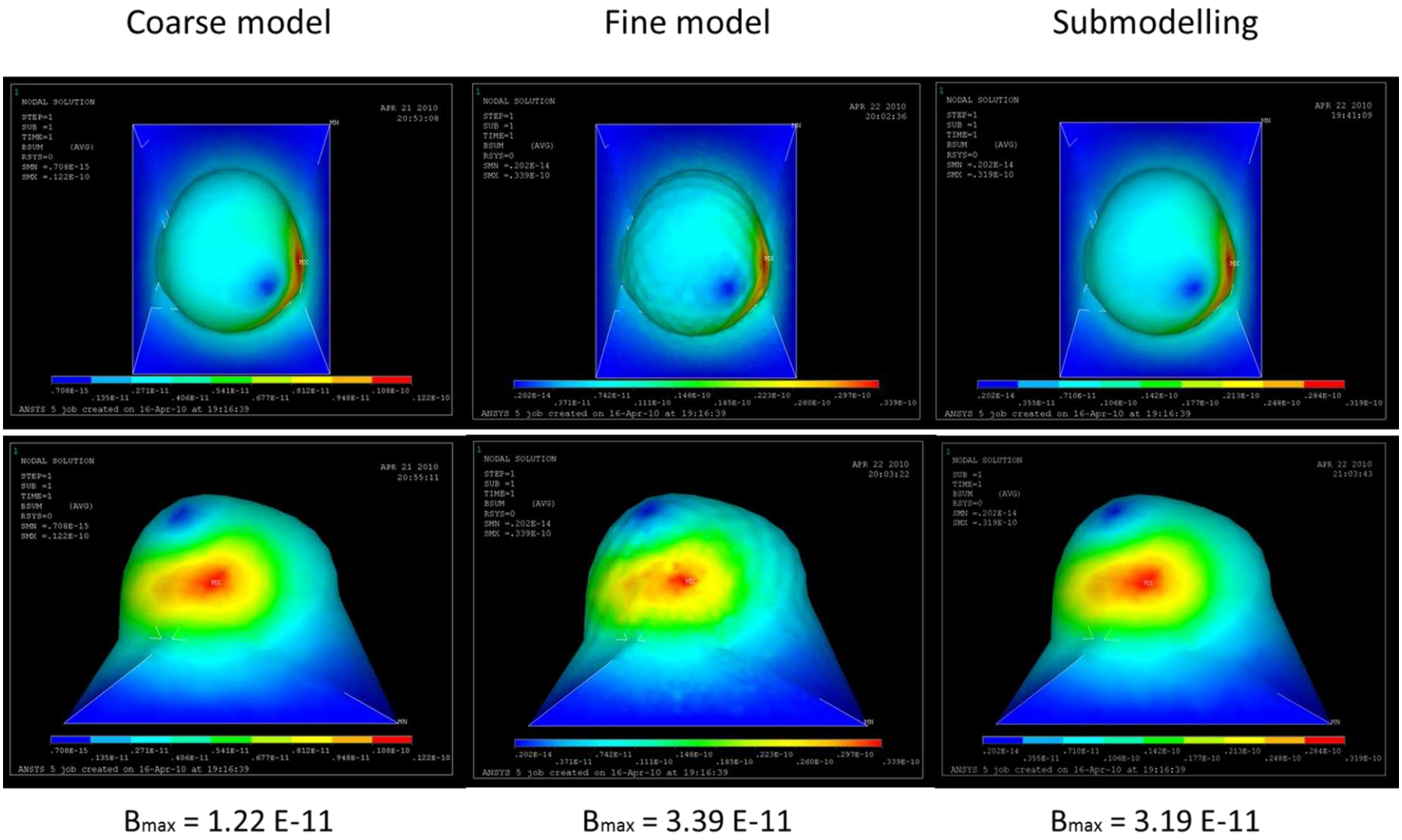

Figure 7.4-2. Results of simulations. Comparison between the initial coarse model solution (left), fine model solution (middle), and CSR solution (right). Rows represent top and side views respectively

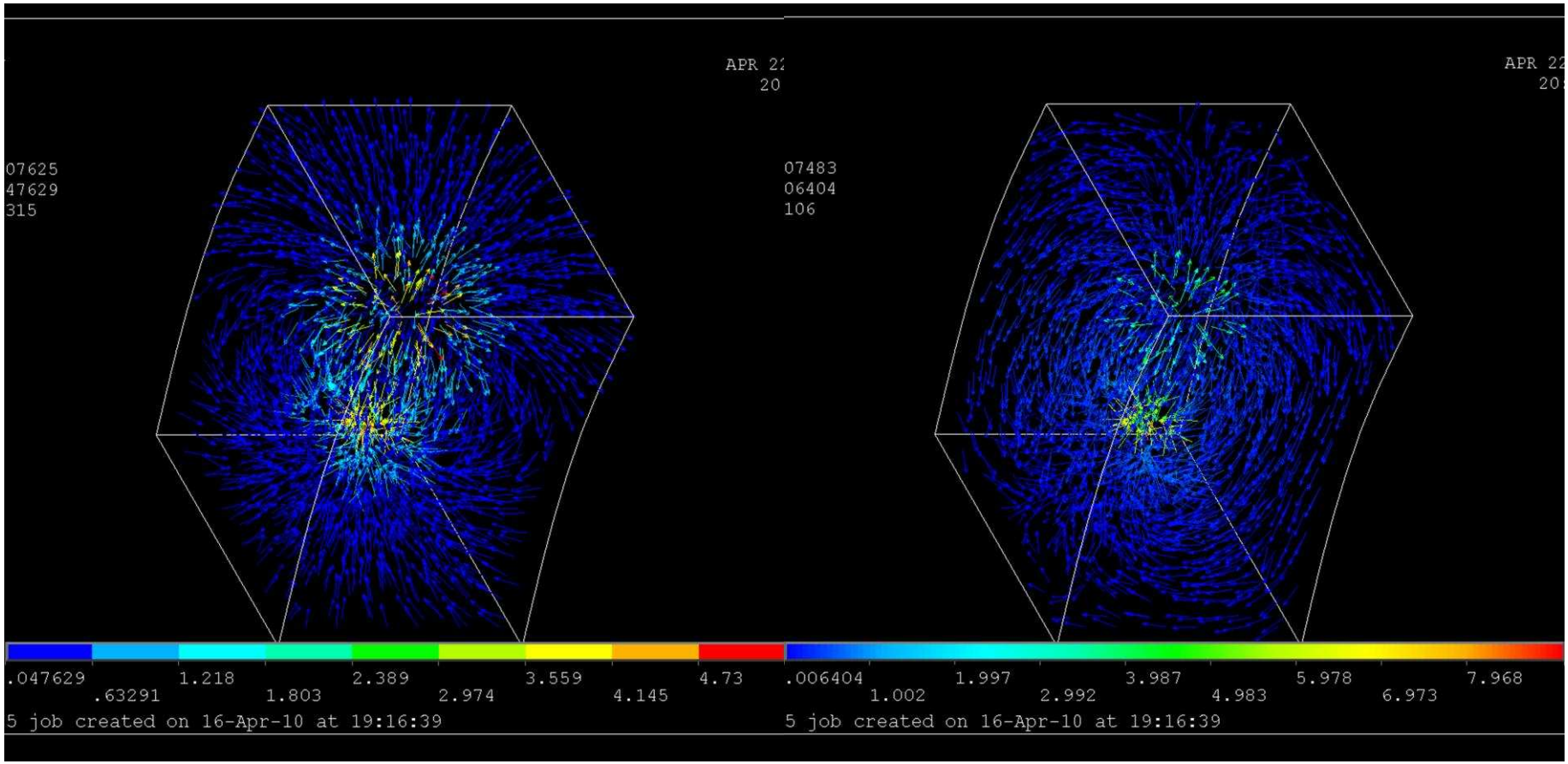

Figure 7.4-3. Current density distribution inside the submodelling region of the coarse model. Direct coarse model solution (left), and solution after CSR (right)

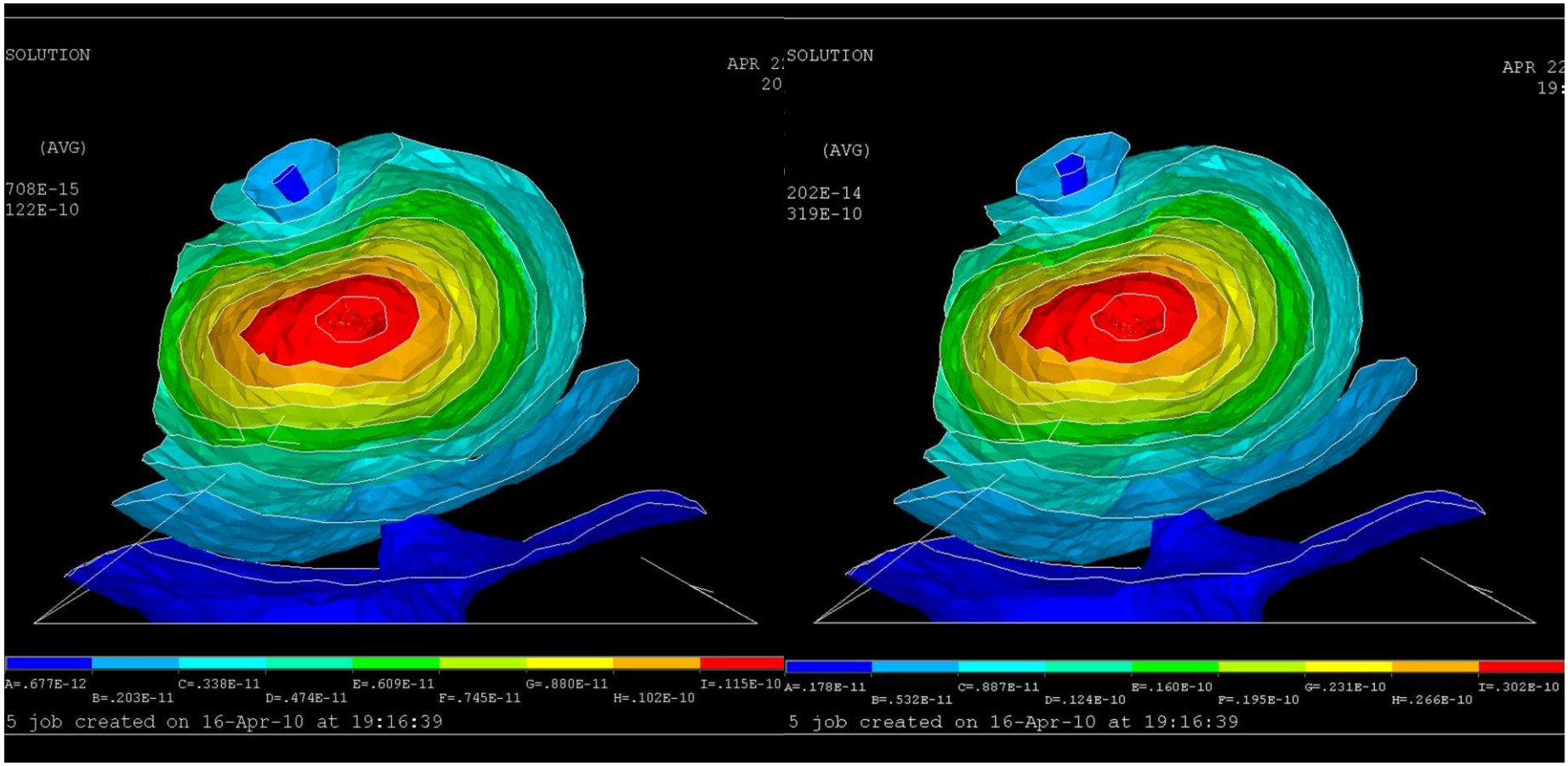

Figure 7.4-4. Magnetic flux density isosurface plot for coarse model (left) and with submodelling approach (right)

Table 7-3. The comparison table and CSR efficiency

Parameter	Fine model	CSR model
Number of elements	10 mln	0.8 (+0.3) mln
Magnetic field flux density maximum value	$3.39 \cdot 10^{-11}$ T	$3.19 \cdot 10^{-11}$ T
Maximum error of the CSR solution	5%	
Average error of the CSR solution	0.3%	
Time of computation	168 hours	1.5 hours
Rate of computational time acceleration	100	

The magnetic flux density isosurfaces (Figure 7.4-4) also shows incorrect spatial magnetic field distribution in coarse model. This has been sufficiently improved with CSR model (note the difference in the top configuration of the isosurface and slightly different angle of the toroid-like bodies of the equilibrium-valued surface representing magnetic field flux density).

The average resulting CSR error for this case has been evaluated using the following relation:

$$e = \frac{\sum_{\Omega}\left(\frac{\left|B_i^{fine} - B_i^{CSR}\right|}{B_i^{fine}}\right)}{N}, \tag{7.4-1}$$

where B_i^{fine} and B_i^{CSR} is the values of magnetic field flux density in the nodes of the detection surface Ω, and N is the total number of nodes contained in this surface.

Overall comparison results are summarized in Table 7-3 where the time of calculation for both fine and CSR models is presented.

7.4.2 Summary

The combined submodelling routine (CSR) and iterative combined submodelling routine (ICSR) have been developed for multi-scale bio-electrical problems. Routines allow sufficient reduction of computational time with almost no loss in solution accuracy. These routines have very wide field of implementation especially in bio-electromagnetic problems where multiple scale is significant for consideration. The CSR was tested on the forward solution of the fibertract activation problem. Comparison between the solution for initial fine finite element model with appropriate mesh density required for direct analysis, and CSR applied to the same problem highlighted enormous ability of CSR to significantly reduce computational time (approximately 100 times) with almost no loss of solution accuracy. The average error of the CSR solution has been found to be 0.3% for chosen size of submodelling region.

Performed analysis shows the potential of CSR to decrease computational time even more, if the difference between the considered dimension scales is higher than in performed example.

Future investigation is planned in order to evaluate error and optimal parameters for ICSR which has also implementation in transient and non-linear electromagnetic multi-scale problems, for example in microelectronics.

7.5 Improved Solution of the Fibertract Activation Problem

With the help of submodelling the dependence between the fibertract diameter and magnetic field was obtained using the realistic neuronal current source approach. The results are displayed in Figure 7.5-1 together with the analytical curve. Analytical equation has been developed for reference proposes and is based on the rough computations that were made in Section 7.3, and follows directly from (7.3-3):

$$\boldsymbol{B}(\boldsymbol{r}) = \boldsymbol{k}'(\boldsymbol{r}) \cdot d^2 \tag{7.5-1}$$

where d is the fibertract diameter, and $\boldsymbol{k}'(\boldsymbol{r})$ is the coefficient which is independent from the diameter. The result (Figure 7.5-1) shows close correlation between

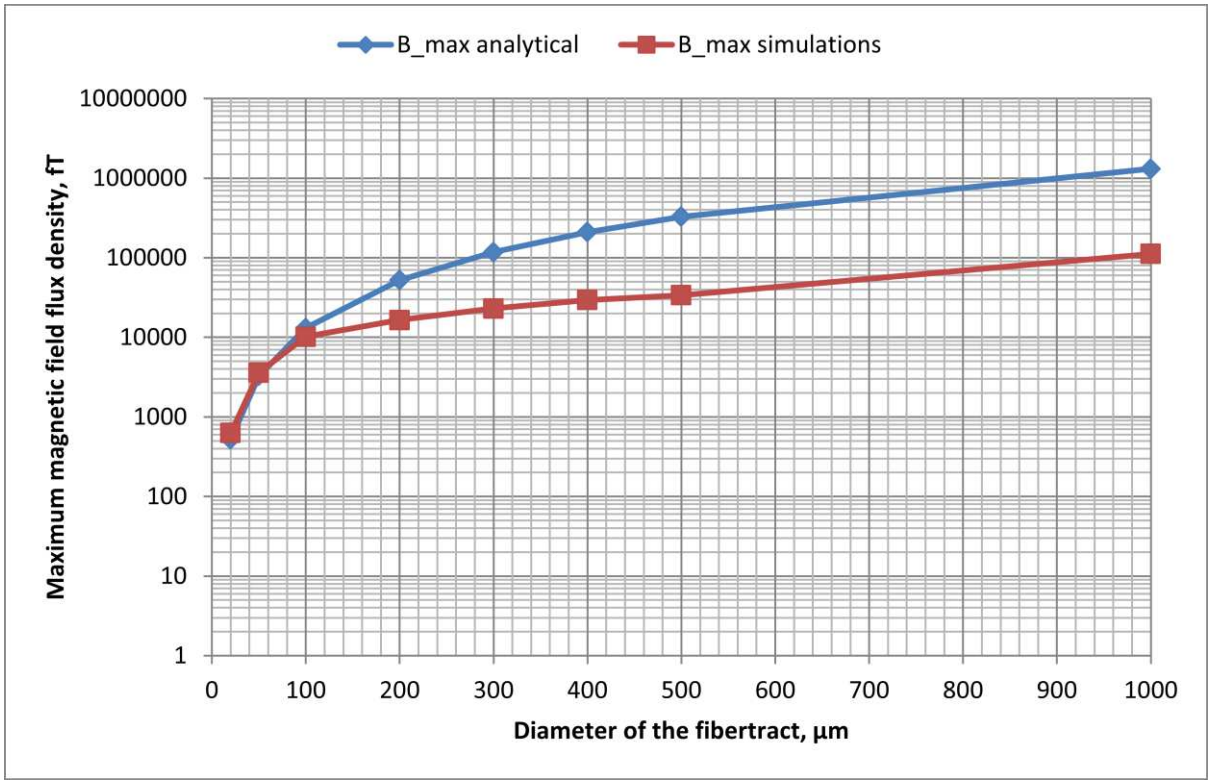

Figure 7.5-1. Comparison between analytical and simulated curve of dependence between the maximal magnetic field in the sensor and fibertract diameter

analytical approach and computer simulations in case of very small fibertract sizes. However for fibertract diameter value greater than 100μm the difference between analytical and simulated result is significant. Such difference for comparatively large fibertract diameter is caused by specific current distribution which was not taken into account during analytical computations. Obviously, the single beam current cannot be considered with this type of analysis. Delivered results show that realistic current distribution is significant for consideration especially in case of similar conductivity of the main conductive body (such as neuronal current source) and surrounding media.

The final simulated magnetic field plot in case of realistic fibertract size of **20μm** is displayed in Figure 7.5-2. Visual observation of the mapped activity and signal magnitude comparison show similarity to the average experimental results made with similar conditions (The pattern of magnetic field has its peak value nearby the activated zone). The comparative analysis of the result shows close correlation between the modelled white matter fibertract activity and the outputs of the SQUID magnetic sensors, used in MEG. The magnitude of the magnetic field flux density has the same order and also is in close correlation to the averaged experimentally collected data. Obtained result confirms that white matter activity has sufficient influence on the output data and thus must be considered in the forward and inverse solutions.

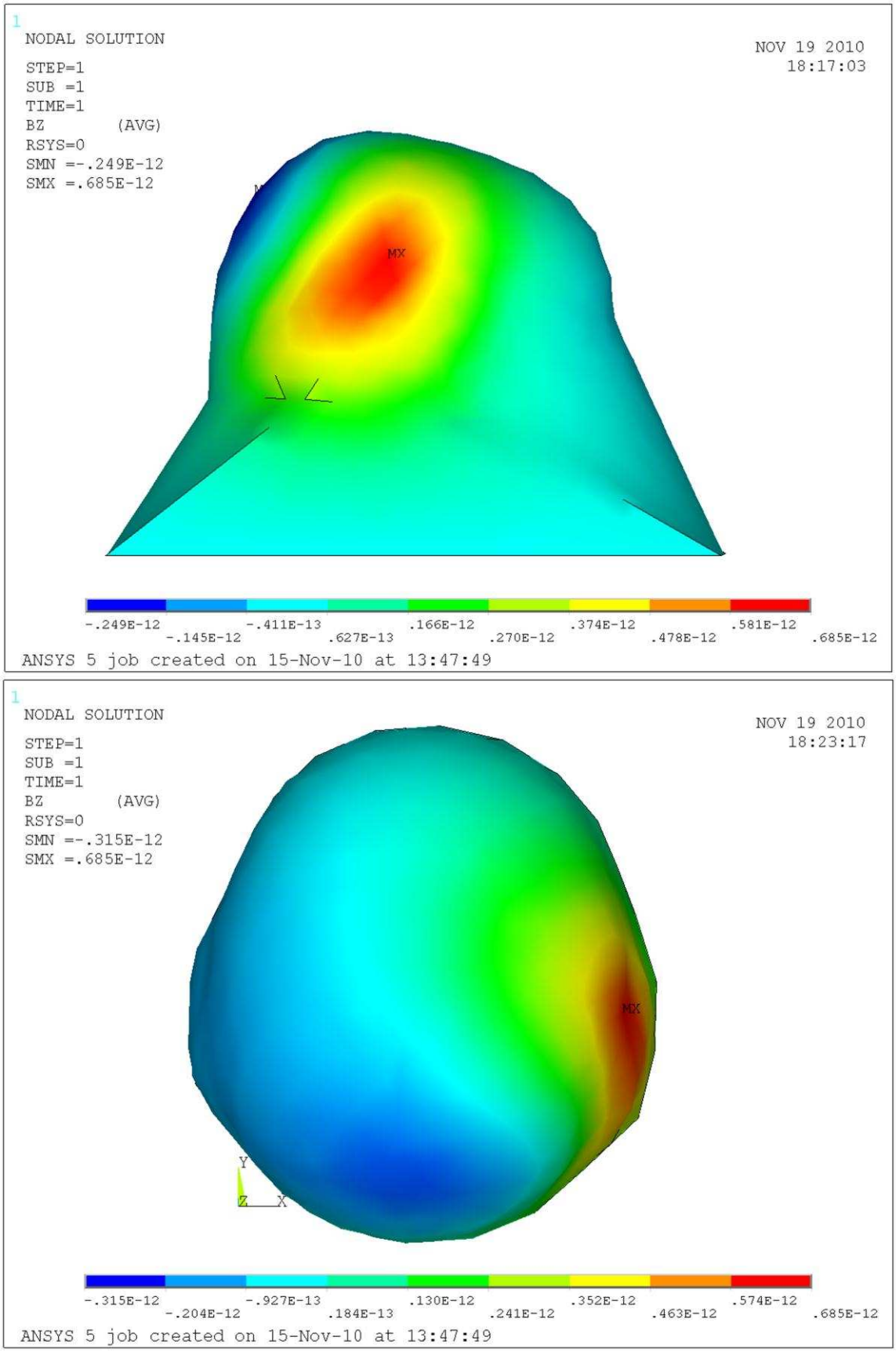

Figure 7.5-2. Magnetic field flux density normal to the sensor surface plot in case of realistic fibertract diameter simulations

7.6 Summary

The novel realistic current source development approach was implemented to solve the single fibertract problem. It is based on the accurate biological and electromagnetic assumptions, and has been designed to simulate the realistic behaviour of the electromagnetic processes inside the human brain. This approach has been implemented into the realistic brain model and forward simulations have been performed. Resulting current density distribution and magnetic field distribution around the head were obtained.

Resulting magnetic fields and current density plots allows discovering the influence of the electromagnetic processes in neuronal fibertract on the forward problem solution. Performed result investigation confirms the importance of the white matter potentials of being carefully used in both forward and inverse solutions. This leads to the general proposal of the white matter fibertracts consideration in combination with traditionally considered grey matter cortical neurons.

Current density plots showed very high difference between our realistic approach and the dipole model. Magnetic field plots allowed visual observation of the magnetic field behaviour in each detector which has also been showed.

Proposed method in application to FEM shows good stability and allows providing simulations with high complexity in terms of neuronal behaviour and internal structure. Submodelling routine has been applied and tested during the simulations. Results confirmed sufficient computational time reduction in all cases of multi-scale electromagnetic problems.

Chapter 8

General Conclusions and Further Work

8.1 General Conclusions

As a result of conducted research the methodologies and tools for forward problem solution were developed, tested, and successfully implemented. The following aims with correspondent objectives have been achieved:

1) The methodologies for the human brain modelling for forward solution MFT based on MEG were delivered:
    a. *Realistic human brain reconstruction procedure and corresponding software for practical implementation*. Resulting computer model reaches the highest possible resolution of existing non-invasive scanning techniques in terms of geometry. Reconstructing procedure also accurately follows realistic anisotropic conductivity properties.
    b. *The human brain model* reconstructed with these techniques is known to be the most accurate among existing models for considered propose in terms of both geometrical and material properties.
2) Methodologies for neuronal current source modelling for forward and inverse problem in MFT based on MEG have been developed:
    a. *Novel neuronal current source modelling approach*. This approach has been built from bio-electrical basis and allows finite element modelling of the neuronal currents with the extraordinary rate between the accuracy and computational complexity.
    b. *The inverse solution method* with the outstanding potential has been also proposed. This proposal underpins the significance of the novel neuronal current source modelling approach.

c. *Algorithms and procedures for practical implementation* of the neuronal current source model into the human brain model for the full branch of possible problems related to the forward problem solution have been delivered.

3) Developed methodologies have been tested and analysed. The error and accuracy analysis have been performed. Optimisation has been performed for every introduced method. Direct and indirect experimental validation has been conducted where possible. Number of practically useful tools for wide range of application fields have been developed and tested:
   a. *Novel submodelling routine for multi-scale finite element analysis*. This computational technique has been developed for sufficient acceleration of the forward problem solution. The acceleration rate of over 100 times has been achieved with much more in potential.
   b. *CAD transfer module.* Allows the model to be saved in a standard CAD format and to be used in any existing computational software with CAD support.
   c. *Cross-software property extraction algorithm.* Allows DT-MRI image processing with extraction and transition of complex material properties of the human brain.
   d. *Current path reconstruction algorithm.* Allows current path reconstruction and visualisation. It can be used for the full range of electromagnetic conductance problems.
   e. *Neuronal path finite element application tool-chain.* Allows automatic implementation of the novel neuronal current source approach into the finite element model. The tool-chain allows the set of 3D neuronal current paths to be used as an input and implements novel neuronal current source approach directly to the brain model.

All techniques and described methods can also be used in other fields of forward electromagnetic simulations, especially in cases with material properties complexity and multi-scale geometrical definitions.

8.2 Further Work

Further work and research is planned in the following directions:

1) More accurate direct experimental validation and practical confirmation of the developed techniques with the help of neurosurgeons and neuroscientists.
2) Inverse problem further development and accurate solution. Clinical validation.
3) Clinical method for fibertract thickness measurement further development and practical application

Clinical specialists are required for experimental data and consultancy access in all activities mentioned above.

References

[1] W. Roentgen, *Diagnostic imaging 100 years ago*, Servir, vol. 44, pp. 207-10, Jul-Aug 1996.

[2] T. H. Newton and D. G. Potts, *Radiology of the skull and brain, Vol 2 : Angiography*. St. Louis: Mosby, 1974.

[3] F. Hyder, *Dynamic brain imaging : multi-modal methods and in vivo applications*. New York, N.Y.: Humana ; [London : Springer, distributor], 2009.

[4] D. Cohen, *Magnetoencephalography: evidence of magnetic fields produced by alpha-rhythm currents*, Science, vol. 161, pp. 784-6, Aug 23 1968.

[5] J. E. Zimmerman, T. M. Flynn, United States. National Bureau of Standards., and United States. Office of Naval Research., *Applications of closed-cycle cryocoolers to small superconducting devices : proceedings of a conference held at the National Bureau of Standards, Boulder, Colorado, October 3-4, 1977*. Washington: U.S. Dept. of Commerce, National Bureau of Standards : for sale by the Supt. of Docs., U.S. Govt. Print. Off., 1978.

[6] M. F. Bear, B. W. Connors, and M. A. Paradiso, *Neuroscience : exploring the brain*, 2nd ed. ed. Baltimore, Md.: Lippincott Williams & Wilkins, 2001.

[7] A. M. Winkler, P. Kochunov, J. Blangero, L. Almasy, K. Zilles, P. T. Fox, R. Duggirala, and D. C. Glahn, *Cortical thickness or grey matter volume? The importance of selecting the phenotype for imaging genetics studies*, Neuroimage, vol. 53, pp. 1135-46, Nov 15 2010.

[8] J. D. Kraus, *Electromagnetics*, 4th ed. ed.: McGraw-Hill, 1991.

[9] K. Penanen, I. Hahn, and B. H. Eom. (2007) Improved Sensing Coils for SQUIDs. *NASA Tech Briefs*.

[10] A. Schnabel, M. Burghoff, S. Hartwig, F. Petsche, U. Steinhoff, D. Drung, and H. Koch, *A sensor configuration for a 304 SQUID vector magnetometer*, Neurol Clin Neurophysiol, vol. 2004, p. 70, 2004.

[11] Available: http://www.supraconductivite.fr/en/index.php?p=applications-medical-meg

[12] J. Vrba, S. E. Robinson, and J. McCubbin, *Forward solution ambiguity for fMEG model*, Neurol Clin Neurophysiol, vol. 2004, p. 87, 2004.

[13] T. Greitz, C. Bohm, E. Hellstrand, M. S. Hamalainen, R. Hari, L. J. Ilmoniemi, R. Seitz, and O. V. Lounasmaa, *Use of a computerized brain atlas in magnetoencephalographic activation studies*, Neuroreport, vol. 5, pp. 449-52, Jan 12 1994.

[14] J. Haueisen, C. Ramon, M. Eiselt, H. Brauer, and H. Nowak, *Influence of tissue resistivities on neuromagnetic fields and electric potentials studied with a finite element model of the head*, IEEE Trans Biomed Eng, vol. 44, pp. 727-35, Aug 1997.

[15] B. He, *Modeling and imaging of bioelectrical activity : principles and applications*. New York: Kluwer Academic/Plenum Publishers, 2004.

[16] S. Kim, T.-S. Kim, Y. Zhou, and M. Singh, *Influence of Conductivity Tensors on the Scalp Electrical Potential: Study With 2-D Finite Element Models*, IEEE TRANSACTIONS ON NUCLEAR SCIENCE, vol. 50, p. 7, 2003.

[17] R. Van Uitert, C. Johnson, and L. Zhukov, *Influence of head tissue conductivity in forward and inverse magnetoencephalographic simulations using realistic head models*, IEEE Trans Biomed Eng, vol. 51, pp. 2129-37, Dec 2004.

[18] R. Van Uitert, D. Weinstein, and C. Johnson, *Volume currents in forward and inverse magnetoencephalographic simulations using realistic head models*, Ann Biomed Eng, vol. 31, pp. 21-31, Jan 2003.

[19] M. Clerc, A. Dervieux, R. Keriven, O. Faugeras, J. Kybic, and T. e. Papadopoulo, *Comparison of BEM and FEM methods for the E/MEG problem*, Biomag, 2002.

[20] A. Crouzeix, B. Yvert, O. Bertrand, and J. Pernier, *An evaluation of dipole reconstruction accuracy with spherical and realistic head models in MEG*, Clin Neurophysiol, vol. 110, pp. 2176-88, Dec 1999.

[21] J. Kybic, M. Clerc, O. Faugeras, R. Keriven, and T. Papadopoulo, *Fast multipole acceleration of the MEG/EEG boundary element method*, Phys Med Biol, vol. 50, pp. 4695-710, Oct 7 2005.

[22] J. C. Mosher, R. M. Leahy, and P. S. Lewis, *EEG and MEG: forward solutions for inverse methods*, IEEE Trans Biomed Eng, vol. 46, pp. 245-59, Mar 1999.

[23] P. H. Schimpf, C. Ramon, and J. Haueisen, *Dipole models for the EEG and MEG*, IEEE Trans Biomed Eng, vol. 49, pp. 409-18, May 2002.

[24] M. Sun and R. J. Sclabassi, *The forward EEG solutions can be computed using artificial neural networks*, IEEE Trans Biomed Eng, vol. 47, pp. 1044-50, Aug 2000.

[25] S. Tissari and J. Rahola, *Error analysis of a Galerkin method to solve the forward problem in MEG using the boundary element method*, Comput Methods Programs Biomed, vol. 72, pp. 209-22, Nov 2003.

[26] I. S. Yetik, A. Nehorai, C. H. Muravchik, and J. Haueisen, *Line-source modeling and estimation with magnetoencephalography*, IEEE Trans Biomed Eng, vol. 52, pp. 839-51, May 2005.

[27] B. Yvert, A. Crouzeix-Cheylus, and J. Pernier, *Fast realistic modeling in bioelectromagnetism using lead-field interpolation*, Hum Brain Mapp, vol. 14, pp. 48-63, Sep 2001.

[28] Z. Akalin, C. E. Acar, and N. G. Gencer, *Development Of Realistic Head Models For Electromagnetic Source Imaging of The Human Brain*, Proceedings of the 23rd Annual EMBS International Conference, 2001.

[29] G. Nolte, *The magnetic lead field theorem in the quasi-static approximation and its use for magnetoencephalography forward calculation in realistic volume conductors*, Phys Med Biol, vol. 48, pp. 3637-52, Nov 21 2003.

[30] L. Rao, R. He, Y. Li, S. Liu, and W. Yan, *Computations of Electroencephalography and Magnetoencephalography for Real Head Model*, IEEE transactions on Magnetics, vol. 36, p. 4, july 2000 2000.

[31] M. N. S. Saita, N. Niki, N. Nakasato, T. Yoshimoto, *An Estimation Algorithm of Neuromagnetic Sources in the Cortical Region Using Realistically-Shaped Head Model*, 1999.

[32] C. H. Wolters, A. Anwander, X. Tricoche, D. Weinstein, M. A. Koch, and R. S. MacLeod, *Influence of tissue conductivity anisotropy on EEG/MEG field and return current computation in a realistic head model: a simulation and visualization study using high-resolution finite element modeling*, Neuroimage, vol. 30, pp. 813-26, Apr 15 2006.

[33] P. Kemppainen and M. Peters, *On the forward solution of electroencephalography and magnetoencephalography*, Clin Phys Physiol Meas, vol. 12 Suppl A, pp. 95-9, 1991.

[34] D. Gutierrez, A. Nehorai, and H. Preissl, *Ellipsoidal head model for fetal magnetoencephalography: forward and inverse solutions*, Phys Med Biol, vol. 50, pp. 2141-57, May 7 2005.

[35] D. Gutierrez and A. Nehorai, *Array response kernels for EEG and MEG in multilayer ellipsoidal geometry*, IEEE Trans Biomed Eng, vol. 55, pp. 1103-11, Mar 2008.

[36] F. B. Sachse, C. D. Werner, K. Meyer-Waarden, and O. Dossel, *Development of a human body model for numerical calculation of electrical fields*, Comput Med Imaging Graph, vol. 24, pp. 165-71, May-Jun 2000.

[37] N. von Ellenrieder, P. A. Valdes-Hernandez, and C. H. Muravchik, *On the EEG/MEG forward problem solution for distributed cortical sources*, Med Biol Eng Comput, vol. 47, pp. 1083-91, Oct 2009.

[38] C. Lee, C.-H. Im, K. Choi, and H.-K. Jung, *Estimation of Solution Accuracy From Leadfield Matrix in Magnetoencephalography*, IEEE TRANSACTIONS ON MAGNETICS, vol. 43, p. 4, 2007.

[39] M. F. Bear, B. W. Connors, and M. A. Paradiso, *Neuroscience : exploring the brain*, 3rd ed. ed. Baltimore, Md.: Lippincott Williams & Wilkins, 2007.

[40] K. Jerbi, S. Baillet, J. C. Mosher, G. Nolte, L. Garnero, and R. M. Leahy, *Localization of realistic cortical activity in MEG using current multipoles*, Neuroimage, vol. 22, pp. 779-93, Jun 2004.

[41] J. C. de Munck, P. C. Vijn, and F. H. Lopes da Silva, *A random dipole model for spontaneous brain activity*, IEEE Trans Biomed Eng, vol. 39, pp. 791-804, Aug 1992.

[42] C. H. Im, H. K. Jung, and N. Fujimaki, *Anatomically constrained dipole adjustment (ANACONDA) for accurate MEG/EEG focal source localizations*, Phys Med Biol, vol. 50, pp. 4931-53, Oct 21 2005.

[43] A. Rodriguez-Rivera, B. D. Van Veen, and R. T. Wakai, *Statistical performance analysis of signal variance-based dipole models for MEG/EEG source localization and detection*, IEEE Trans Biomed Eng, vol. 50, pp. 137-49, Feb 2003.

[44] J. Malmivuo and R. Plonsey, *Bioelectromagnetism : principles and applications of bioelectric and biomagnetic fields*. New York ; Oxford: Oxford University Press, 1995.

[45] K. H. Pettersen, A. Devor, I. Ulbert, A. M. Dale, and G. T. Einevoll, *Current-source density estimation based on inversion of electrostatic forward solution: effects of finite extent of neuronal activity and conductivity discontinuities*, J Neurosci Methods, vol. 154, pp. 116-33, Jun 30 2006.

[46] F. H. Lin, J. W. Belliveau, A. M. Dale, and M. S. Hamalainen, *Distributed current estimates using cortical orientation constraints*, Hum Brain Mapp, vol. 27, pp. 1-13, Jan 2006.

[47] K. Jerbi, J. C. Mosher, S. Baillet, and R. M. Leahy, *On MEG forward modelling using multipolar expansions*, Phys Med Biol, vol. 47, pp. 523-55, Feb 21 2002.

[48] J. B. Nixon, P. E. Rasser, M. D. Teubner, C. R. Clark, and M. J. Bottema, *Numerical model of electrical potential within the human head*, INTERNATIONAL JOURNAL FOR NUMERICAL METHODS IN ENGINEERING, vol. 56, p. 14, 2003.

[49] C. A. Brebbia, *The boundary element method for engineers*. London/New York: Pentech Press/Halstead Press, 1978.

[50] Z. Akalin-Acar and N. G. Gencer, *An advanced boundary element method (BEM) implementation for the forward problem of electromagnetic source imaging*, Phys Med Biol, vol. 49, pp. 5011-28, Nov 7 2004.

[51] N. v. Ellenrieder, C. H. Muravchik, and A. Nehorai, *MEG Forward Problem Formulation Using Equivalent Surface Current Densities*, IEEE TRANSACTIONS ON BIOMEDICAL ENGINEERING, vol. 52, p. 8, 2005.

[52] J. Kybic, M. Clerc, O. Faugeras, R. Keriven, and T. Papadopoulo, *Generalized head models for MEG/EEG: boundary element method beyond nested volumes*, Phys Med Biol, vol. 51, pp. 1333-46, Mar 7 2006.

[53] G. W. Pruis, B. H. Gilding, and M. J. Peters, *A comparison of different numerical methods for solving the forward problem in EEG and MEG*, Physiol Meas, vol. 14 Suppl 4A, pp. A1-9, Nov 1993.

[54] N. G. Gencer and I. O. Tanzer, *Forward problem solution of electromagnetic source imaging using a new BEM formulation with high-order elements*, Phys Med Biol, vol. 44, pp. 2275-87, Sep 1999.

[55] S. S. Rao, *The finite element method in engineering*, 4th ed. ed. Oxford: Butterworth-Heinemann, 2005.

[56] Y. W. Kwon and H. Bang, *The finite element method using MATLAB*, 2nd ed. ed. Boca Raton ; London: CRC Press, 2000.

[57] E. Madenci and I. Guven, *The finite element method and applications in engineering using ANSYS*. New York: Springer, 2006.

[58] V. K. Jirsa, K. J. Jantzen, A. Fuchs, and J. A. Kelso, *Spatiotemporal forward solution of the EEG and MEG using network modeling*, IEEE Trans Med Imaging, vol. 21, pp. 493-504, May 2002.

[59] S. Tissari and J. Rahola, *A precorrected-fFT method to accelerate the solution of the forward problem in magnetoencephalography*, Phys Med Biol, vol. 48, pp. 523-41, Feb 21 2003.

[60] M. Hamalainen, R. Hari, R. J. Ilmoniemi, J. Knuutila, and O. V. Lounasmaa, *Magnetoencephalography-theory, instrumentation, and applications to noninvasive studies of the working human brain*, Rev. Modern Phys., vol. 65, p. 84, 1993.

[61] Y. Salu, *Implementing a consistency criterion in numerical solution of the bioelectric forward problem*, IEEE Trans Biomed Eng, vol. 27, pp. 338-41, Jun 1980.

[62] Y. Lai, W. van Drongelen, L. Ding, K. E. Hecox, V. L. Towle, D. M. Frim, and B. He, *Estimation of in vivo human brain-to-skull conductivity ratio from simultaneous extra- and intra-cranial electrical potential recordings*, Clin Neurophysiol, vol. 116, pp. 456-65, Feb 2005.

[63] N. von Ellenrieder, C. H. Muravchik, and A. Nehorai, *Effects of geometric head model perturbations on the EEG forward and inverse problems*, IEEE Trans Biomed Eng, vol. 53, pp. 421-9, Mar 2006.

[64] I. ANSYS. (2010, Submodelling. *Release 11.0 Documentation for Ansys*. Available: http://www.kxcad.net/ansys/ANSYS/ansyshelp/Hlp_G_ADV4UN.html

[65] K. Y. Aristovich and S. H. Khan, *A new submodelling technique for multi-scale finite element computation of electromagnetic fields: Application in bioelectromagnetism* J. Phys.: Conf. Ser., vol. 238, eds. S. H. Khan, K. T. V. Grattan, L. Finkelstein, and P. Kyriacou 2010.

[66] *CAD/CAM/CAE technology, 2009*. Warrendale: SAE International, 2009.

[67] K. Y. Aristovich and S. H. Khan, *Automatic procedure for realistic 3D finite element modelling of human brain for bioelectromagnetic computations* J. Phys.:

Conf. Ser., vol. 238, eds. S. H. Khan, K. T. V. Grattan, L. Finkelstein and P. Kyriacou, 2010.

[68] S. H. Khan, K. Y. Aristovich, and A. I. Borovkov, *Solution of the Forward Problem in Magnetic-Field Tomography (MFT) Based on Magnetoencephalography (MEG)*, IEEE TRANSACTIONS ON MAGNETICS, vol. 45, p. 4, 2009.

[69] L. Landini, V. Positano, and M. F. Santarelli, *Advanced image processing in magnetic resonance imaging*. Boca Raton, FL: CRC/Taylor & Francis, 2005.

[70] CIT. *MIPAV software* [web-page]. Available: http://mipav.cit.nih.gov/index.php

[71] J. A. Green, *Optimal edge detection and digital picture processing*, 2nd ed. Wichita, Kan.: Greenwood Research, 1994.

[72] J. C. Russ, *The image processing handbook*, 5th ed. Boca Raton: CRC/Taylor and Francis, 2007.

[73] S. V. Vaseghi, *Advanced digital signal processing and noise reduction*, 4th ed. New York: J. Wiley & Sons, 2008.

[74] M. d. Berg, *Computational geometry : algorithms and applications*, 3rd ed. Berlin: Springer, 2008.

[75] J. E. Goodman and J. O'Rourke, *Handbook of discrete and computational geometry*, 2nd ed. Boca Raton: Chapman & Hall/CRC, 2004.

[76] J. D. Boissonnat and M. Teillaud, *Effective computational geometry for curves and surfaces*. New York ; Berlin: Springer, 2007.

[77] T. A. project. Available: http://www-sop.inria.fr/asclepios/

[78] Y. Jung, A. A. Samsonov, W. F. Block, M. Lazar, A. Lu, J. Liu, and A. L. Alexander, *3D diffusion tensor MRI with isotropic resolution using a steady-state radial acquisition*, J Magn Reson Imaging, vol. 29, pp. 1175-84, May 2009.

[79] W. Van Hecke, J. Sijbers, S. De Backer, D. Poot, P. M. Parizel, and A. Leemans, *On the construction of a ground truth framework for evaluating voxel-*

based diffusion tensor MRI analysis methods, Neuroimage, vol. 46, pp. 692-707, Jul 1 2009.

[80] C. D. Kroenke, E. N. Taber, L. A. Leigland, A. K. Knutsen, and P. V. Bayly, *Regional patterns of cerebral cortical differentiation determined by diffusion tensor MRI*, Cereb Cortex, vol. 19, pp. 2916-29, Dec 2009.

[81] H. Yasmin, S. Aoki, O. Abe, Y. Nakata, N. Hayashi, Y. Masutani, M. Goto, and K. Ohtomo, *Tract-specific analysis of white matter pathways in healthy subjects: a pilot study using diffusion tensor MRI*, Neuroradiology, vol. 51, pp. 831-40, Dec 2009.

[82] P. J. Basser, J. Mattiello, and D. LeBihan, *MR diffusion tensor spectroscopy and imaging*, Biophys J, vol. 66, pp. 259-67, Jan 1994.

[83] K. Wang, S. Zhu, B. A. Mueller, K. O. Lim, Z. Liu, and B. He, *A new method to derive white matter conductivity from diffusion tensor MRI*, IEEE Trans Biomed Eng, vol. 55, pp. 2481-6, Oct 2008.

[84] Asclepios. (2009). *MedINRIA*. Available: http://www-sop.inria.fr/asclepios/software/MedINRIA/

[85] T. V. Boon Thye Thomas Yeo, Pierre Fillard, Xavier Pennec, Polina Golland, Nicholas Ayache, and Olivier Clatz, *DTI Registration with Exact Finite-Strain Differential*, Proceedings of the IEEE International Symposium on Biomedical Imaging: From Nano to Macro (ISBI'08), May 2008 2008.

[86] K. Y. Aristovich, S. H. Khan, and A. I. Borovkov, *Investigation of optimal parameters for finite element solution of the forward problem in magnetic field tomography based on magnetoencephalography*, J. Phys.: Conf. Ser., vol. 307, 2011 2011.

[87] W. Rall, C. Koch, and I. Segev, Eds., *Cable Theory for Dendritic Neurons* (Methods in Neuronal Modeling: From Synapses to Networks. Cambridge: Bradford Books, MIT Press, 1989, p.^pp. Pages.

[88] M. cambridge. (2007). Available: http://imaging.mrc-cbu.cam.ac.uk/meg/CbuMeg

[89] D. J. Mitchell and R. Cusack, "MEG response to visual item load, in short-term memory and attentional monitoring tasks," in *Biomagnetism – Interdisciplinary Research and Exploration*, Y. K. Kakigi I, Kuriki S, Ed., ed: Hokkaido University Press, 2008, pp. 209-211.

[90] S. Sircar, *Principles of medical physiology*. Stuttgart ; New York: Thieme, 2008.

[91] T. Chaira and A. K. Ray, *Fuzzy image processing and applications with MATLAB*. Boca Raton, Fla.: CRC, 2010.

[92] C. Collet, J. Chanussot, and K. Chehdi, *Multivariate image processing*. London: Wiley-ISTE, 2010.

[93] A. M. Baskurt, *Three-dimensional image processing (3DIP) and applications*. Bellingham: SPIE, 2010.

[94] J.-C. Bertein and R. Ceschi, *Discrete stochastic processes and optimal filtering*, 2nd ed. ed. London: ISTE ; Hoboken.

[95] A. Mohamad-Djafari, *Inverse problems in vision and 3D tomography*. London: ISTE ; Hoboken.

[96] M. Petrou and C. Petrou, *Image processing : the fundamentals*, 2nd ed. ed. Oxford: Wiley, 2010.

[97] F. Y. Shih, *Image processing and pattern recognition : fundamentals and techniques*. Hoboken, N.J.: Wiley ; Chichester : John Wiley [distributor], 2010.

[98] K. H. Yap and S. W. A. i. p. Perry, *Adaptive image processing : a computational intelligence perspective*, 2nd ed. ed. Boca Raton, Fla.: CRC ; London : Taylor & Francis [distributor], 2010.

[99] D. Fofi and K. S. Niel, *Image processing : machine vision applications III*. Bellingham, Wash.: SPIE, 2010.

[100] U. Qidwai and C. H. Chen, *Digital image processing : an algorithmic approach with MATLAB*. Boca Raton: Chapman & Hall, 2010.

APPENDIX 1

Set of MRI Images Used for Realistic Human Brain Model Reconstruction

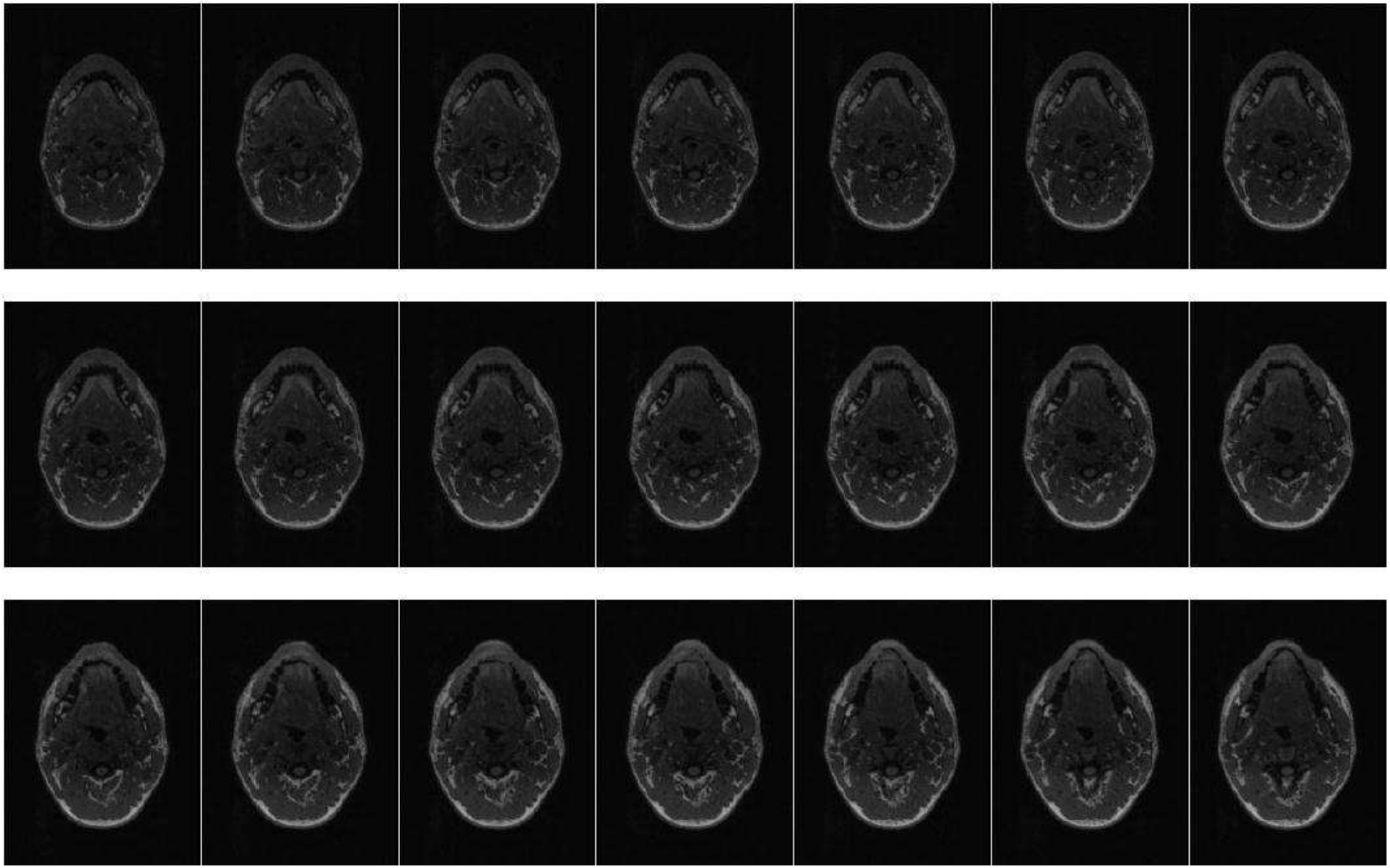

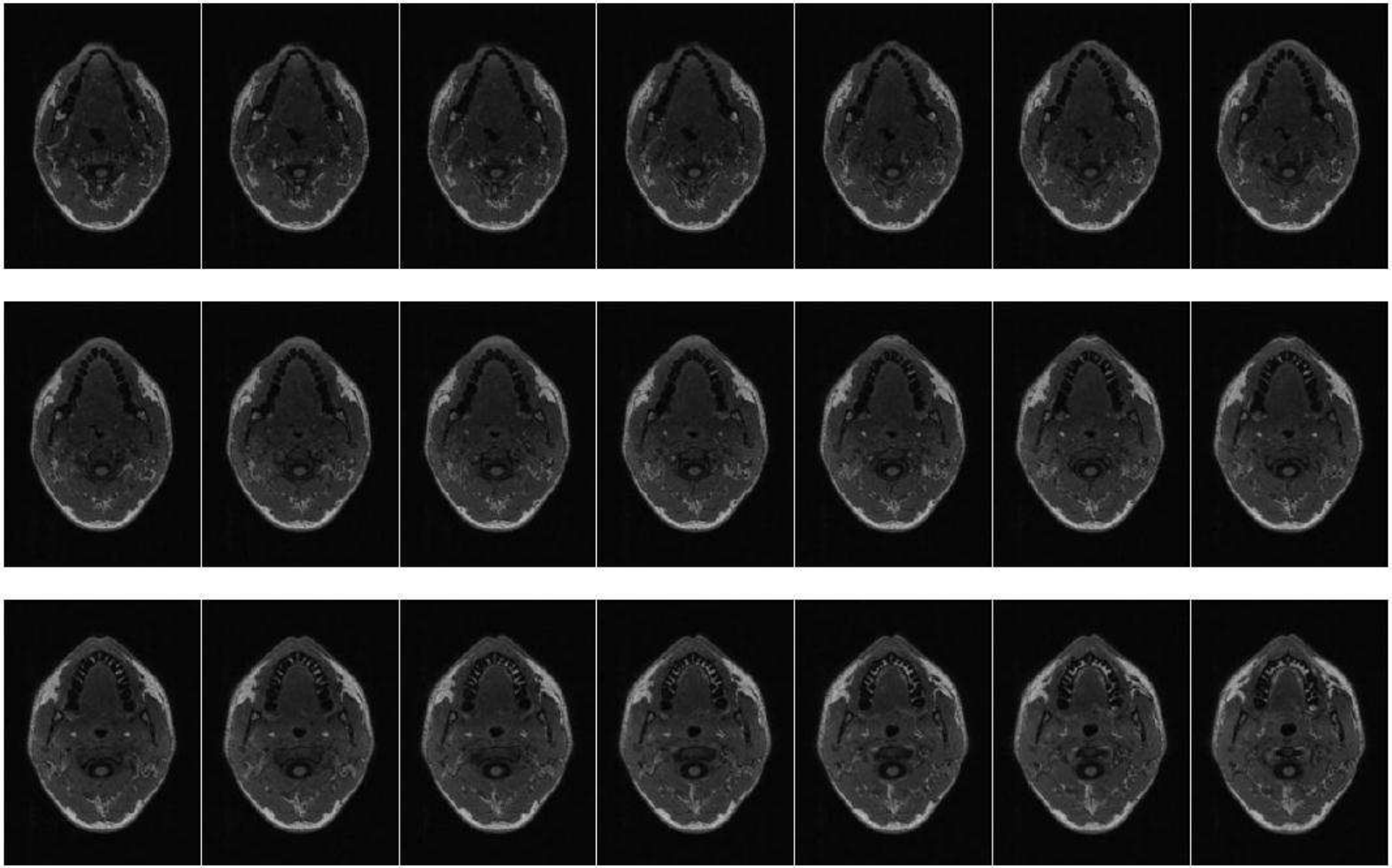

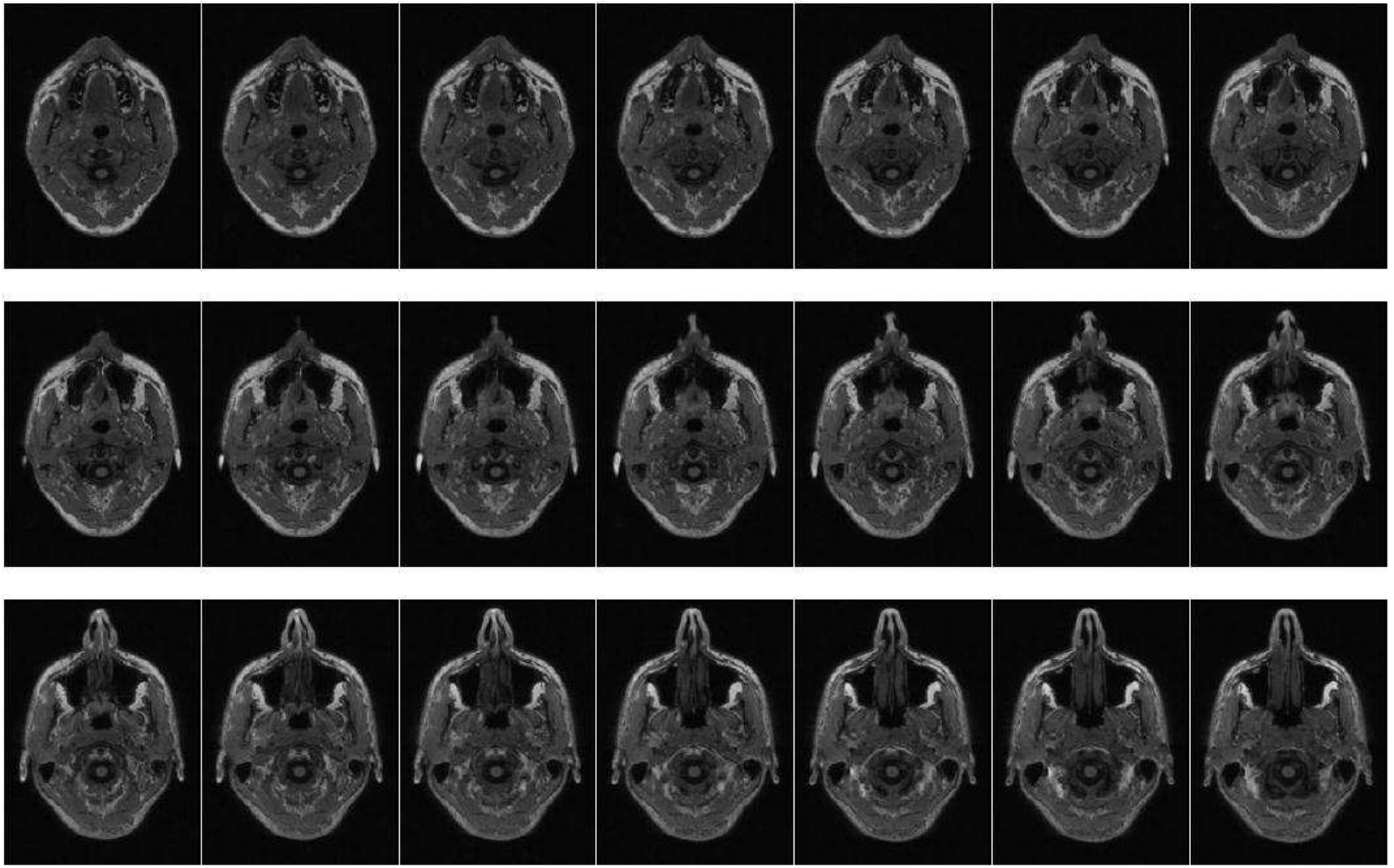

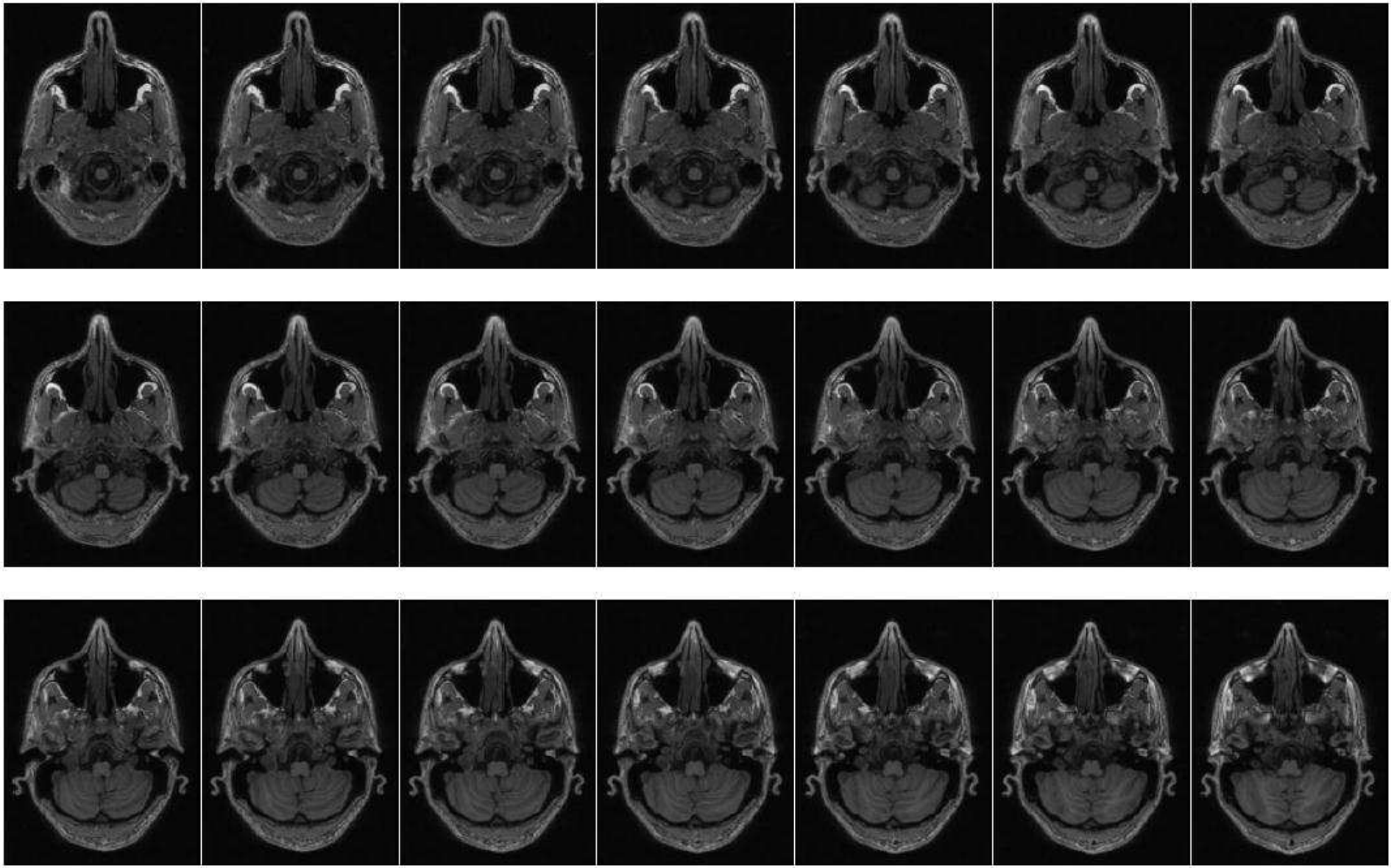

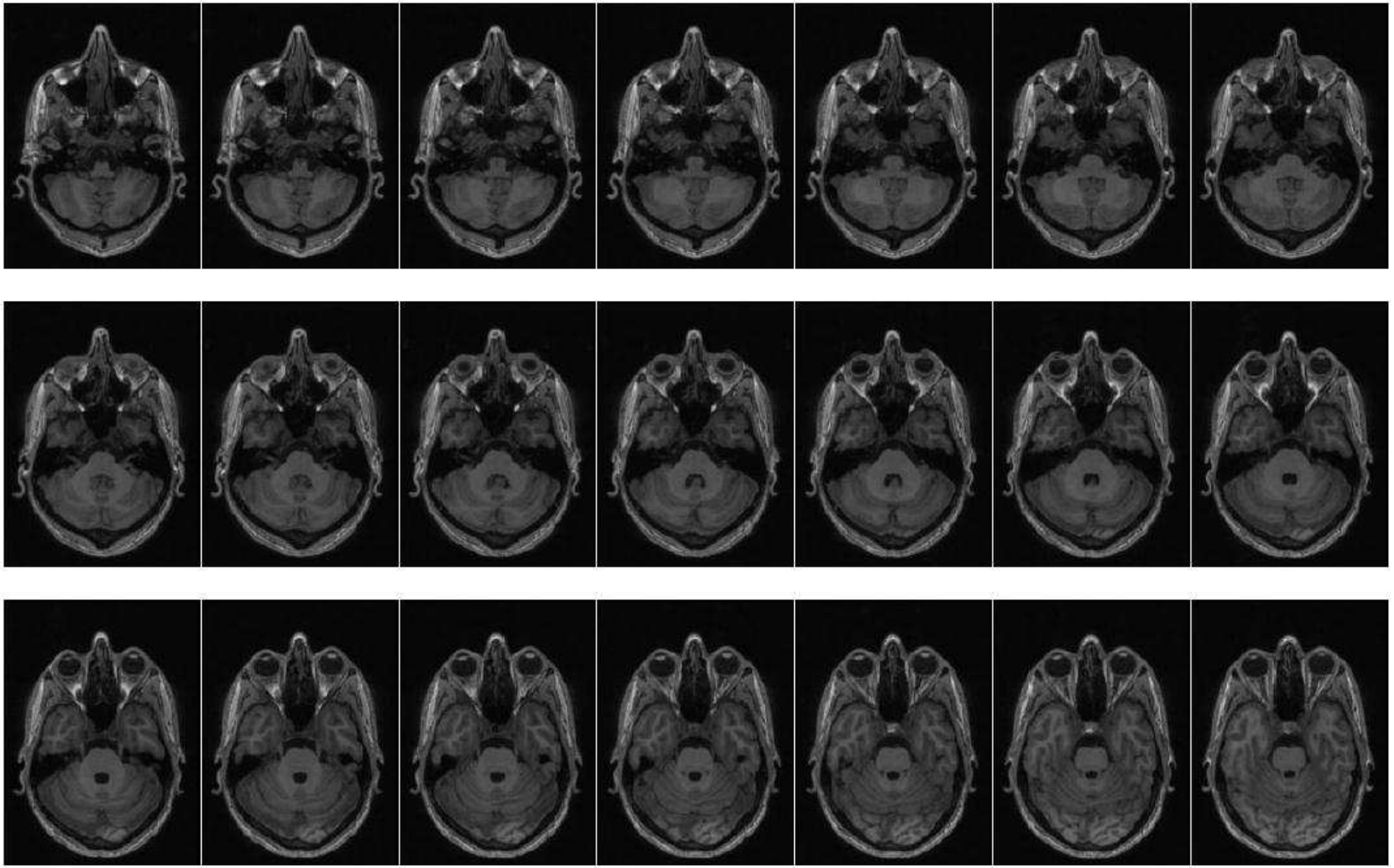

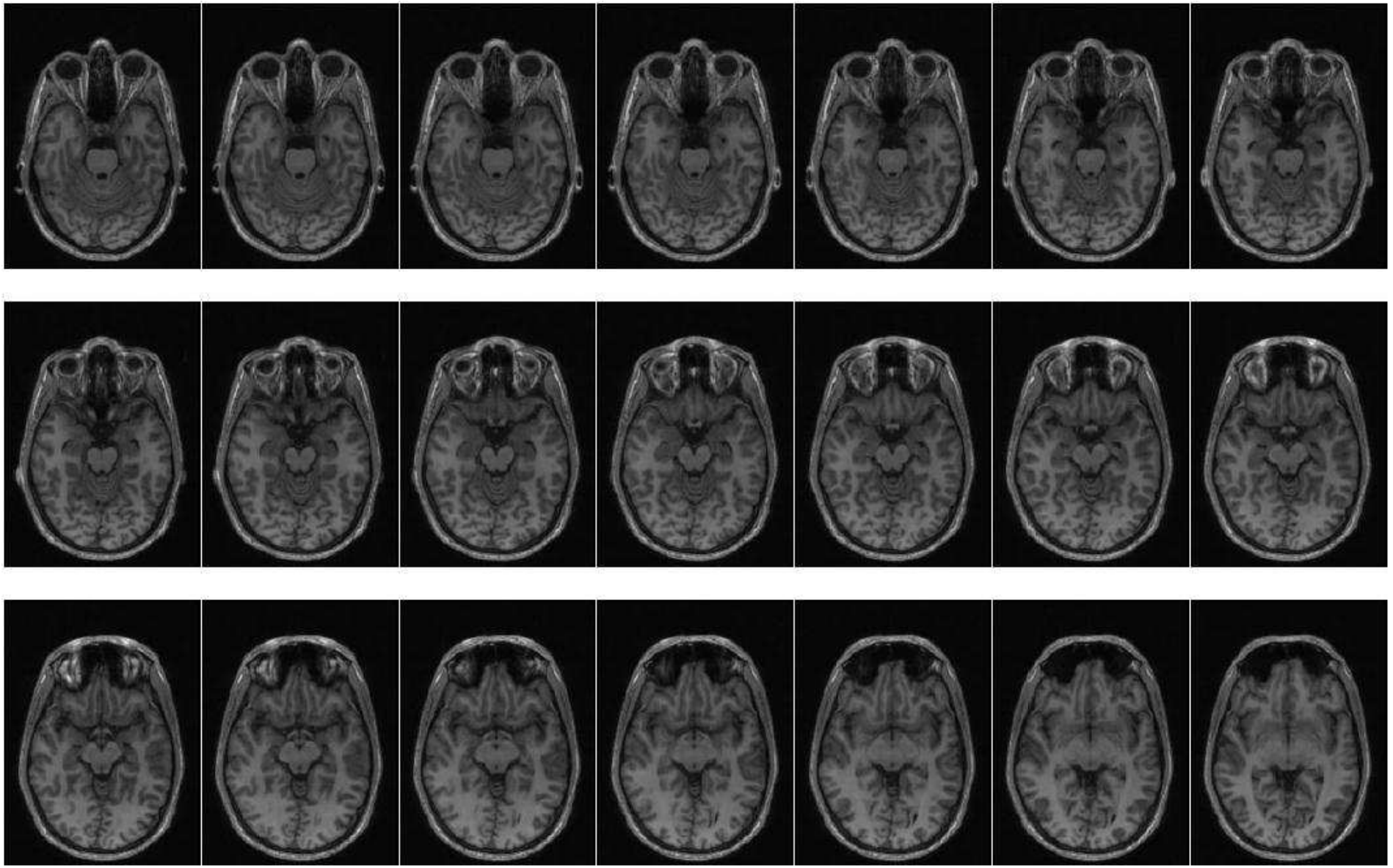

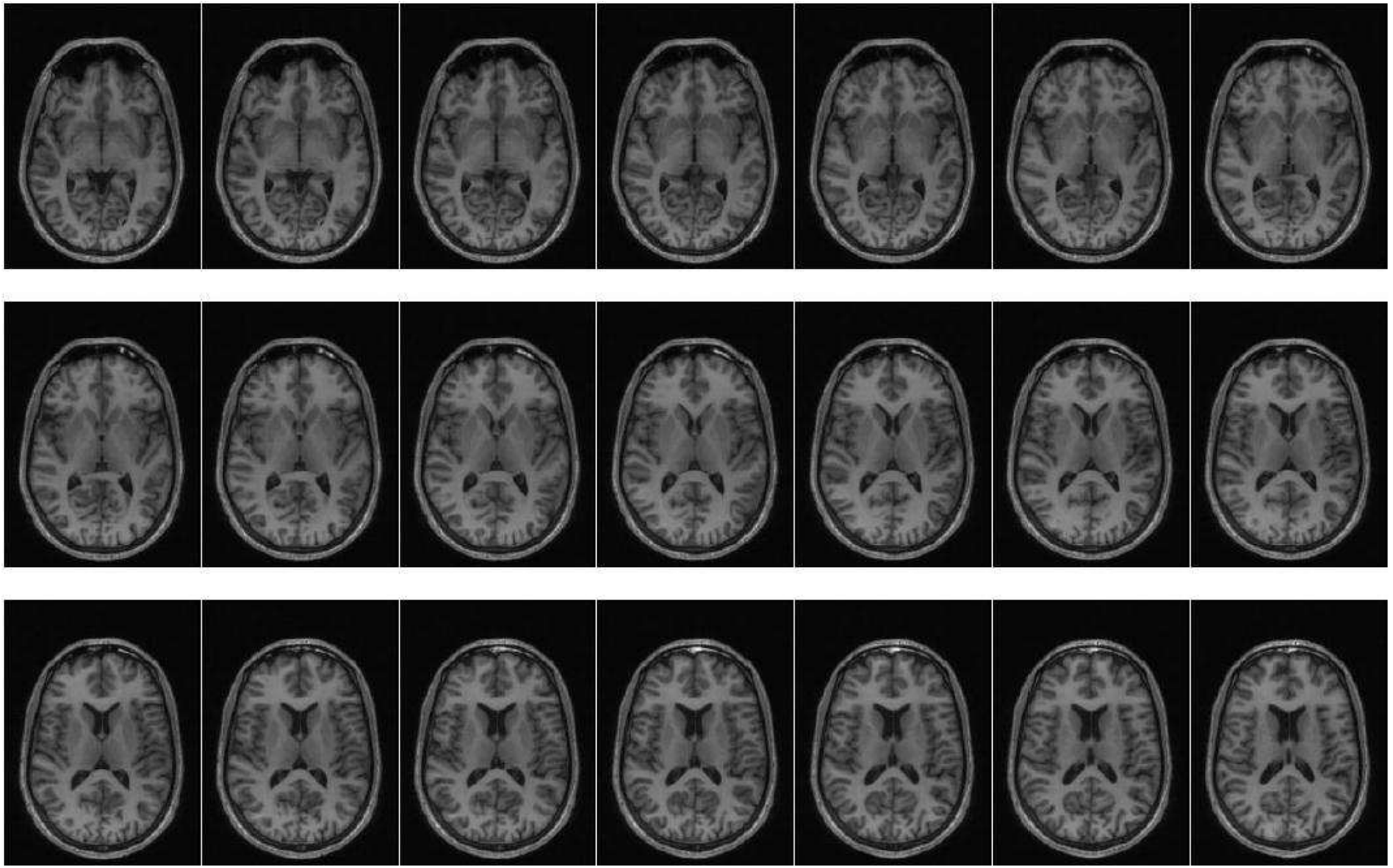

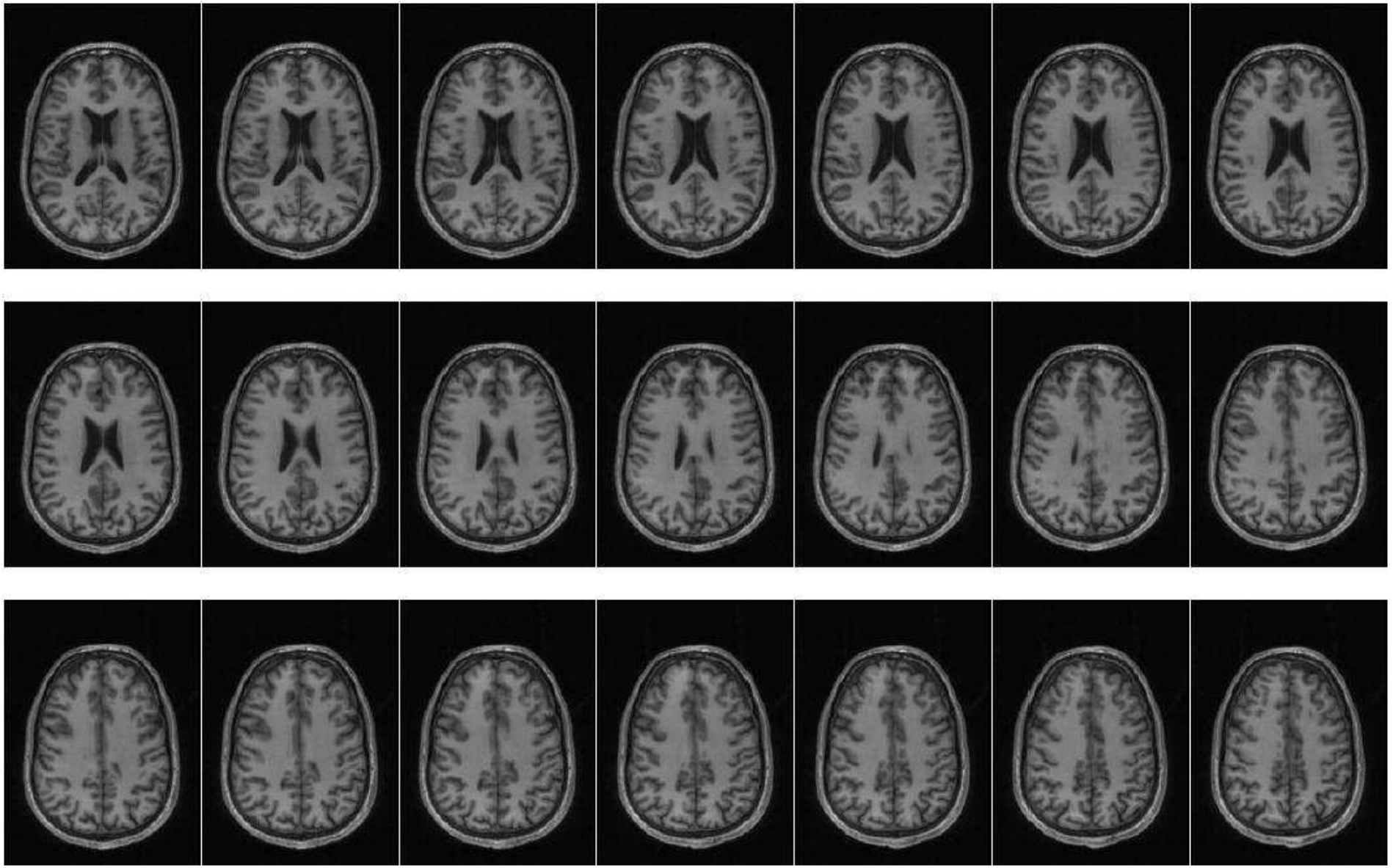

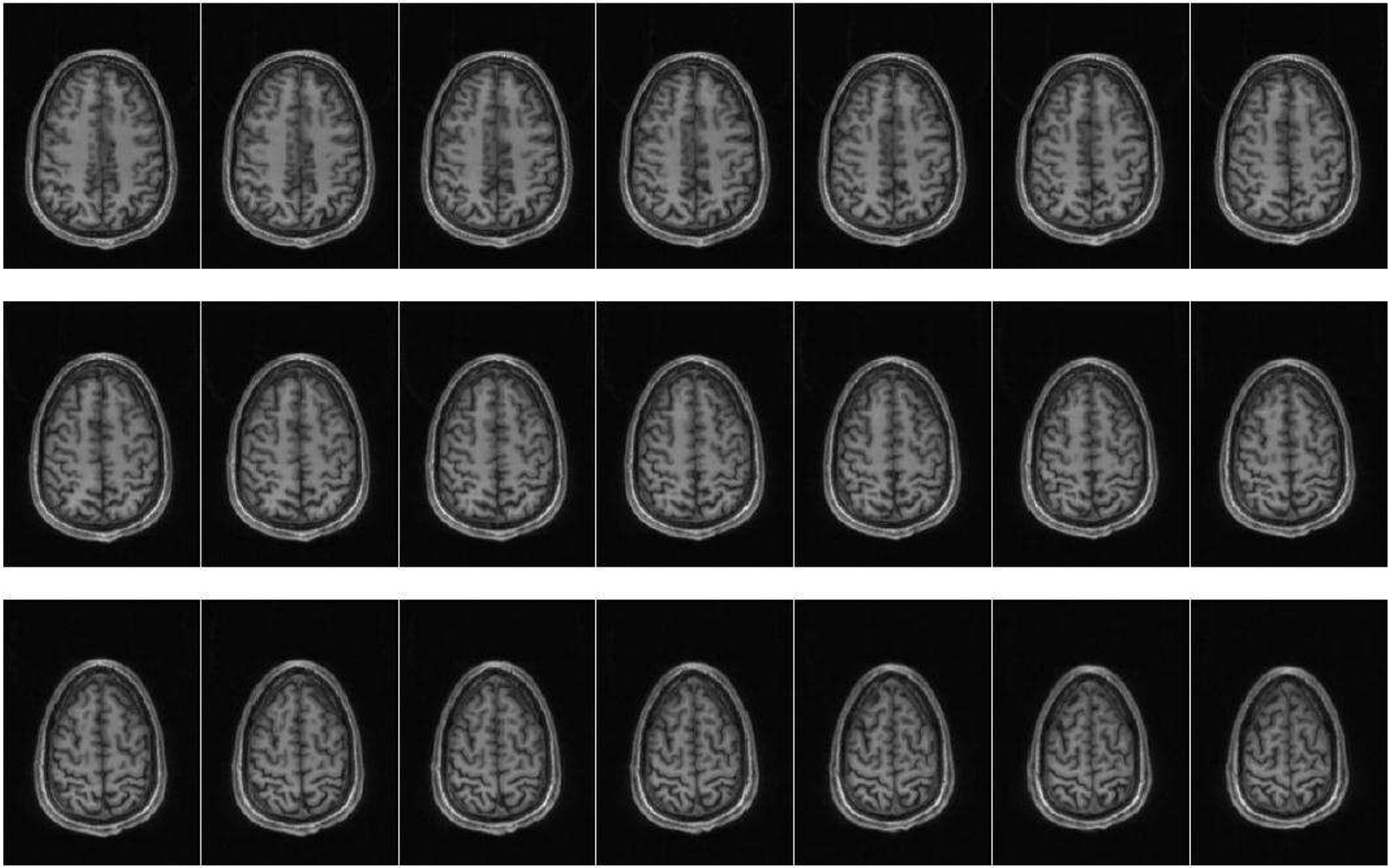

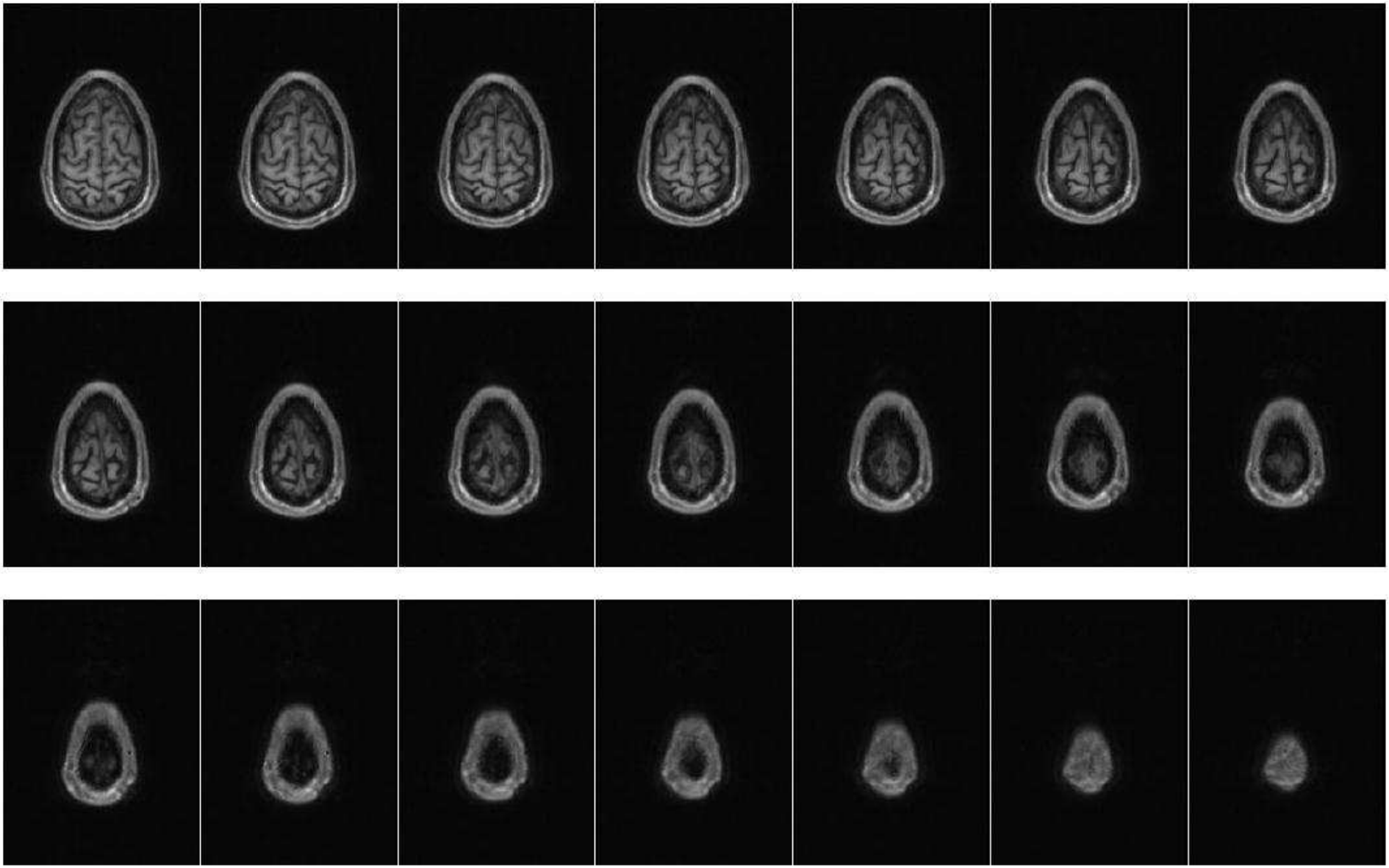

APPENDIX 2

List of MRI Filtering Algorithms

- Rescale, Resample filter based on matrices algorithm [91]
- Shrink-wrap filtering technique [92]
- Noise Reduction Filter [93, 94]
- Smoothing Filters [93, 94]
- Metal Artifact Reduction Filter [95, 96]
- Morphological Filters [95, 97]
- Paint/Unpaint filter for removing artefacts [95, 97]
- Confidence Connected Region Growing Masking [91, 98]
- Flood Fill Masking [94, 99, 100]
- Cavity Fill Masking [94, 99, 100]
- Island Removal for automatic artifact reduction [94, 99, 100]
- Thresholding filter [96, 100]
- Boolean Operations Masking tool [96, 100]
- Overlap Check [96, 100]
- Multi-Part Anti-Aliasing processing tool [96, 100]

APPENDIX 3

Tensor Conductivity Reconstruction Algorithm

File **Main.m** *– Developed by © 2009 Kirill Aristovich*

```
clear;
[T,sp,origin] = ReadInrTensorData('tensor.inr');
sizeT=size(T);
f=fopen('ten_NotZ_met_DB.txt','w');
in=0;
for i=1:sizeT(1)
   for j=1:sizeT(2)
      for k=1:sizeT(3)
         if (T{i,j,k} (1,1)~= 0 && T{i,j,k}(2,2) ~=0 && T{i,j,k}(1,1)~=0)
            fprintf(f, '%i %i %i %f %f %f\n', i*2,j*2,153-k*2,T{i,j,k}(1,1), T{i,j,k}(2,2), T{i,j,k}(3,3));
            in=in+1;
         end
      end
   end
end
fclose(f);
ff=fopen('ten_NotZ_met_DB_param.txt','w');
fprintf(ff,'number of rows = %f\n',in);
fclose(ff);
```

File **LoadINR.m** *– Developed by © Kirill Aristovich from Open Source INR lib by ©2008 INRIA*

```
error(nargchk(1,2,nargin));

%- if input is already an image then no loading is needed
if isnumeric(name)
   A = name;
   return
end

%- check if file exists
if ~exist(name,'file')
   %- check for gz
   if exist([name '.gz'],'file')
      name=[name '.gz'];
   else
      error('[LoadInr] Image file does not exist');
   end
end

%- check for compressed image
if strcmp(name(end-2:end),'.gz')
   h.compressed='gz';
   r_name=[tempname '.inr'];
   %fprintf('Decompressing to %s\n',r_name);
   unix(['gunzip -c ' name ' > ' r_name]);
else
   h.compressed='none';
   r_name=name;
end

%- check for analyze or minc image
if strcmp(r_name(end-3:end),'.img')|strcmp(r_name(end-3:end),'.hdr')...
      |strcmp(r_name(end-3:end),'.mnc')
   if nargin > 1
      %error('[LoadInr] Option not supported for analyse images');
      %- to come soon...
      h=[];
   end
   [dim, vox, scale, type, offset, origin, descrip] = spm_hread(r_name);
   [pathstr, name, ext] = fileparts(r_name);
   h = struct('xdim',dim(1),...
            'ydim',dim(2),...
            'zdim',dim(3),...
            'vdim',1,...
            'vx',vox(1),...
            'vy',vox(2),...
            'vz',vox(3),...
            'scale',scale,...
            'mtype',spm_type(type),...
```

```
            'name',r_name,...
            'path',pathstr,...
            'shortname',[name ext]);
    A = spm_read_vols(spm_vol(r_name));
    return
end

fid = fopen(r_name,'r');
if (fid > 0)

  %- allocate buffer
  [header,count]=fread(fid,256,'char');
  header=char(header)';
  if(count~=256)
    error(sprintf('[LoadInr] Fatal image read problem (%s).',name))
  end
  if(~strcmp(header(1:12),'#INRIMAGE-4#'))
    error(sprintf('[LoadInr] Unknown image type (%s).',name))
  end
  h.version=header(2:11);

  while isempty(findstr(header,'##}'))
    [head,count]=fread(fid,256,'char');
    if(count~=256)
      error(sprintf('[LoadInr] Fatal image read problem (%s).',name))
    end
    header=[header char(head)'];
  end

  % x dimension
  pos=findstr(header,'XDIM=');
  if(isempty(pos)|size(pos,2)~=1)
    error(sprintf('[LoadInr] Invalid header XDIM (%s).',name));
  end
  pos_=find(0+header(pos:end)==10);
  h.xdim=str2num(header(pos+5:pos_(1)-2+pos));
  if isempty(h.xdim)
    error(sprintf('[LoadInr] Invalid XDIM (%s).',name));
  end

  % y dimension
  pos=findstr(header,'YDIM=');
  if(isempty(pos)|size(pos,2)~=1)
    error(sprintf('[LoadInr] Invalid header YDIM (%s).',name));
  end
  pos_=find(0+header(pos:end)==10);
  h.ydim=str2num(header(pos+5:pos_(1)-2+pos));
  if isempty(h.ydim)
    error(sprintf('[LoadInr] Invalid YDIM (%s).',name));
  end
```

```
% z dimension
pos=findstr(header,'ZDIM=');
if(isempty(pos)|size(pos,2)~=1)
  error(sprintf('[LoadInr] Invalid header ZDIM (%s).',name));
end
pos_=find(0+header(pos:end)==10);
h.zdim=str2num(header(pos+5:pos_(1)-2+pos));
if isempty(h.zdim)
  error(sprintf('[LoadInr] Invalid ZDIM (%s).',name));
end

% v dimension
pos=findstr(header,'VDIM=');
if(isempty(pos)|size(pos,2)~=1)
  error(sprintf('[LoadInr] Invalid header VDIM (%s).',name));
end
pos_=find(0+header(pos:end)==10);
h.vdim=str2num(header(pos+5:pos_(1)-2+pos));
if isempty(h.vdim)
  error(sprintf('[LoadInr] Invalid VDIM (%s).',name));
end
%  if h.vdim~=1
%    error(sprintf('[LoadInr] Only scalar images supported (%s).',name));
%  end

% image type
pos=findstr(header,'TYPE=');
if(isempty(pos)|size(pos,2)~=1)
  error(sprintf('[LoadInr] Invalid header TYPE (%s).',name));
end
pos_=find(0+header(pos:end)==10);
h.type=(header(pos+5:pos_(1)-2+pos));
if isempty(h.type)
  error(sprintf('[LoadInr] Invalid TYPE (%s).',name));
end
switch h.type
case 'unsigned fixed'
  ty = 'uint';
case 'float'
  ty= 'float';
case 'signed fixed'
  ty= 'int';
otherwise
  error(sprintf('[LoadInr] Unknown image type (%s).',name));
end


% number of bits
pos=findstr(header,'PIXSIZE=');
```

```
if(isempty(pos)|size(pos,2)~=1)
  error(sprintf('[LoadInr] Invalid header PIXSIZE (%s).',name));
end
pos_=find(0+header(pos:end)==32);
h.pixsize=(header(pos+8:pos_(1)-2+pos));
if isempty(h.pixsize)
  error(sprintf('[LoadInr] Invalid PIXSIZE (%s).',name));
end
ty=[ty h.pixsize];
switch h.pixsize
case '8'
  sy=1;
case '16'
  sy=2;
case '32'
  sy=4;
case '64'
  sy=8;
otherwise
  error(sprintf('[LoadInr] Unknown number of bits (%s).',name));
end
h.pixbytesize=sy;
h.mtype=ty;

% cpu name
pos=findstr(header,'CPU=');
if(isempty(pos)|size(pos,2)~=1);
  error(sprintf('[LoadInr] Invalid header CPU (%s).',name));
end
pos_=find(0+header(pos:end)==10);
h.cpu=(header(pos+4:pos_(1)-2+pos));
if isempty(h.cpu)
  error(sprintf('[LoadInr] Invalid CPU (%s).',name));
end
switch h.cpu
case 'decm'
  m_format='ieee-le';
case 'sun'
  m_format='ieee-be';
otherwise
  error(sprintf('[LoadInr] Unknown machine type (%s).',name));
end

% ************************************
% Extra fields, not needed to read image
% ************************************
% x pixelsize
pos=findstr(header,'VX=');
if(length(pos)>1)
  error(sprintf('[LoadInr] Invalid header VX (%s).',name));
```

```
end
if(~isempty(pos))
  pos_=find(0+header(pos:end)==10);
  h.vx=str2num(header(pos+3:pos_(1)-2+pos));
  if isempty(h.vx)
    error(sprintf('[LoadInr] Invalid VX (%s).',name));
  end
end
% y pixelsize
pos=findstr(header,'VY=');
if(length(pos)>1)
  error(sprintf('[LoadInr] Invalid header VY (%s).',name));
end
if(~isempty(pos))
  pos_=find(0+header(pos:end)==10);
  h.vy=str2num(header(pos+3:pos_(1)-2+pos));
  if isempty(h.vy)
    error(sprintf('[LoadInr] Invalid VY (%s).',name));
  end
end
% z pixelsize
pos=findstr(header,'VZ=');
if(length(pos)>1)
  error(sprintf('[LoadInr] Invalid header VZ (%s).',name));
end
if(~isempty(pos))
  pos_=find(0+header(pos:end)==10);
  h.vz=str2num(header(pos+3:pos_(1)-2+pos));
  if isempty(h.vz)
    error(sprintf('[LoadInr] Invalid VZ (%s).',name));
  end
end
% scale
pos=findstr(header,'SCALE=');
if(length(pos)>1)
  error(sprintf('[LoadInr] Invalid header SCALE (%s).',name));
end
if(~isempty(pos))
  pos_=find(0+header(pos:end)==10);
  h.scale=header(pos+6:pos_(1)-2+pos);
  if isempty(h.scale)
    error(sprintf('[LoadInr] Invalid SCALE (%s).',name));
  end
end

% find commentlines
com=[char(10) '#'];
pos=findstr(header,com);
% store comments in struct not yet implemented
```

```
% Store name in header structure
h.name=name;
[h.path,h.shortname,h.ext] = fileparts(h.name);

% save file position, close file, reopen in
% in specified machine mode
fpos=ftell(fid);
fclose(fid);
% store image data offset (in bytes) in header structure
h.offset=fpos;

if(nargin>1)
  if(ischar(slice))
    switch slice
      %read header only
    case 'header'
      A=[];
      return
    otherwise
      error('[LoadInr] Invalid option');
    end
  end
end


fid=fopen(r_name,'r',m_format);


% read only slice asked for
if(nargin>1)
  if(h.vdim~=1)
    error('[LoadInr] Vectorial Slice loading not yet supported');
  end
  if(length(slice)>2)
    error('[LoadInr] Invalid slice specification, [start slice, end slice]');
  end
  if(length(slice)==1)
    slice(2)=slice(1);
  else
    if(slice(1)>slice(2))
      error('[LoadInr] Invalid slice order');
    end
  end
  if((slice(1)>0)&(slice(2)<=h.zdim))
    fseek(fid,fpos+(h.xdim*h.ydim*h.pixbytesize*(slice(1)-1)),-1);
    [B,count]=fread(fid,h.xdim*h.ydim*(slice(2)-slice(1)+1),ty);
    % check if all bytes could be read
    if(count~=(h.xdim*h.ydim*(slice(2)-slice(1)+1)))
```

```
      error('[LoadInr] Image size problem');
      exit;
    end
    A=reshape(B,h.xdim,h.ydim,slice(2)-slice(1)+1)';
  else
    error('[LoadInr] Invalid slice number')
  end
 else
  % read complete image
  fseek(fid,fpos,-1);
  s=h.xdim*h.ydim*h.zdim*h.vdim;
  [B,count]=fread(fid,s,ty);
  % check if all bytes could be read
  if(count~=s)
    error('[LoadInr] Image size problem');
    exit;
  end
  if(h.vdim==1)
    A=reshape(B,h.xdim,h.ydim,h.zdim);
  else
    A=permute(reshape(B,h.vdim,h.xdim,h.ydim,h.zdim),[2,3,4,1]);
  end
  %A=permute(reshape(B,h.xdim,h.ydim,h.zdim),[2,1,3]);
 end
 fclose(fid);
else
 error(sprintf('[LoadInr] Image ''%s'' could not be opened',name));
end

if strcmp(h.compressed,'gz')
  if ~strcmp(r_name,name)
    unix(['\rm -f ' r_name]);
  end
end


File ReadInrTensorData.m – Modified by (c) Kirill Aristovich from Open Source INR lib by (c) 2008
INRIA
function [T,sp,origin] = ReadInrTensorData(filename)

 % Usage:
 %
 % [T, sp, origin] = ReadInrTensorData(filename)
 %
 % T: Tensor field (cells) -> access by brackets, i.e., T{10,10,10}.
 % sp: spacing (voxel size)
 % origin: origin of the image in real world coordinates


[I,H] = loadinr(filename);
```

```
sp = [H.vx, H.vy, H.vz];
origin = [0 0 0];

dims = size(I);

% tensor dimension
NTensor = size(I,4);
N = (sqrt( 8*NTensor + 1 ) - 1)/2;

T = cell(dims(1:3));


for k=1:dims(3)
   for j=1:dims(2)
      for i=1:dims(1)

         v = I(i,j,k,:);
         t = zeros(N,N);
         ind = 1;

         for nc=1:N
           for nl = 1:nc
            t(nl,nc) = v(ind);
            t(nc,nl) = t(nl,nc);
            ind = ind+1;
          end
         end

          T{i,j,k} = t;

      end
   end
end
```

APPENDIX 4

PITA (Powerful Intersoftware Tensor Algorithm)

```
! PITA algorithm. Copyright © by Kirill Aristovich
!
!___________test
maxrow=10
*DIM, TAB,,maxrow,6
*VREAD, TAB(1,1),C:\test\ten_NotZ,txt,,jik,6,maxrow
(F4.0,F4.0,F4.0,F10.6,F10.6,F10.6,'%\')

*DIM, Tensor,array,250,250,250,4

*DO, i,1,maxrow
   ii=TAB(i,1)
   jj=TAB(i,2)
   kk=TAB(i,3)
   tensor(ii,jj,kk,1)=TAB(i,4)
   tensor(ii,jj,kk,2)=TAB(i,5)
   tensor(ii,jj,kk,3)=TAB(i,6)
   tensor(ii,jj,kk,4)=i

   material = NINT(i/100)+1
   MPTEMP
   MPTEMP, material, i
   MPDATA, KXX, material, TAB(i,4)
   MPTEMP
   MPTEMP, material, i
   MPDATA, KYY, material, TAB(i,5)
   MPTEMP
   MPTEMP, material, i
   MPDATA, KZZ, material, TAB(i,6)
*ENDDO

*DO, i,1,maxrow

*enddo


*GET, elm_max, ELEM,0,NUM,MAX
*GET, elm_min, ELEM,0,NUM,MIN

*DO, N,elm_min,elm_max
   * GET, elm_x, ELEM, N, CENT, X
   * GET, elm_y, ELEM, N, CENT, Y
   * GET, elm_z, ELEM, N, CENT, Z
   elm_x = NINT(elm_x*1000)
   elm_y = NINT(elm_y*1000)
```

```
   elm_z = NINT(elm_z*1000)

   elm_material =  nint( tensor(elm_x,elm_y,elm_z,4) ) + 1
   EMODIF, N, MAT, elm_material
*enddo

*GET, node_max, NODE,0,NUM,MAX
*GET, node_min, NODE,0,NUM,MIN

*DO, N,node_min,node_max
   * GET, node_x, node, N, LOC, X
   * GET, node_y, node, N, LOC, Y
   * GET, node_z, node, N, LOC, Z
   node_x = NINT(node_x*1000)
   node_y = NINT(node_y*1000)
   node_z = NINT(node_z*1000)

   node_temp = tensor(node_x,node_y,node_z,4)
   D,N,TEMP,node_temp
*enddo
!___________eo_test
```

```
! Main Body
/BATCH
/NOPRINT
!
/COM ANSYS input file created by the MSC ANSYS input file translator (
/COM PAT3/ANSYS 15.0.038 ) on May      05, 2009 at 20:35:21.
!
/PREP7
!
!
/TITLE, ANSYS 5 job created on 05-May-09 at 20:35:00
_____________________________________________
List of nodes
_____________________________________________
/COM Defining Element Types
!
ET,1,SOLID97,6, 0, 0, 0, 0, 0
!
MP,RSVX,1,3.3
MP,MURX,1,1
!
MP,RSVX,5,3
MP,MURX,5,1
!
MP,RSVX,2,3e13
MP,MURX,2,1
!
MP,RSVX,3,3e13
MP,MURX,3,1
!
/COM Turn off shape checking until all elements written
SHPP, OFF
!
!
/COM Element props and connectivity for Region:1
!
MAT,   1
TYPE,   1
_____________________________________________
List of elements and properties
_____________________________________________


NUMCMP,NODE
NUMCMP,ELEM

maxrow=3164
*DIM, TAB,,maxrow,6
*VREAD, TAB(1,1),K:\ANSYS_with_properties\Trace_MAY_2009\ten_NotZ_met_DB,txt,,jik,6,maxrow
(F4.0,F4.0,F4.0,F10.6,F10.6,F10.6,'%\')

*DIM, Tensor,arr4,256,256,250,4


!*DO, i,1,250
```

```
!   *DO, j,1,250
!      *DO, k,1,250
!         *DO, t,1,4
!            tensor(i,j,k,t)=0
!         *ENDDO
!      *ENDDO
!   *ENDDO
!*ENDDO


*DO, i,1,maxrow
   ii=TAB(i,1)
   jj=TAB(i,2)
   kk=TAB(i,3)
   tensor(ii,jj,kk,1)=ABS(1./TAB(i,4))
   tensor(ii,jj,kk,2)=ABS(1./TAB(i,5))
   tensor(ii,jj,kk,3)=ABS(1./TAB(i,6))

   material = i+5
   tensor(ii,jj,kk,4)=material


   MP, RSVX, material, ABS(1./TAB(i,4))
   MP, RSVY, material, ABS(1./TAB(i,5))
   MP, RSVZ, material, ABS(1./TAB(i,6))
   MP, MURX, material, 1

*ENDDO

/COM
/COM Element Properties starting
/COM
*GET, elm_max, ELEM,0,NUM,MAX
*GET, elm_min, ELEM,0,NUM,MIN

*DO, N,elm_min,elm_max
   * GET, elm_x, ELEM, N, CENT, X
   * GET, elm_y, ELEM, N, CENT, Y
   * GET, elm_z, ELEM, N, CENT, Z
   elm_x = NINT((elm_x+35)/0.96094)
   elm_y = NINT((elm_y+24)/0.96094)
   elm_z = NINT((elm_z-113)/2.2)

   elm_x = 8*NINT(elm_x/8)+2
   elm_y = 8*NINT(elm_y/8)+2
   elm_z = 8*NINT(elm_z/8)-1


   i=0

   * IF, elm_x, GE, 1, AND, elm_x, LE, 256, THEN
   * IF, elm_y, GE, 1, AND, elm_y, LE, 256, THEN
   * IF, elm_z, GE, 1, AND, elm_z, LE, 256, THEN
         i=nint (tensor(elm_x,elm_y,elm_z,4))
         !*MSG, UI, i
```

```
        !integer = %I
   * ENDIF
   * ENDIF
   * ENDIF

   *GET, elm_material, ELEM, N, ATTR, MAT

   * IF, i,ne,0, THEN
   * IF, elm_material,eq,1,THEN
      elm_material =  i
   * ENDIF
   * ENDIF

   EMODIF, N, MAT, elm_material


*enddo
/COM Element Properties finished

/COM FINISHED TRANSFER
/COM ;)
FINISH
```

APPENDIX 5

Current Path Reconstruction Algorithm

```
! Path reconstruction algorithm. Copyright by © Kirill Aristovich
NUM=30

*DIM,ELEM_N,ARRAY,100,NUM

! -----Initial Point----------
X0=100
Y0=150
Z0=150
! ------Length of the quadrant-------
h=5

X_max=250
Y_max=300
Z_max=350

n_x = X_max/h
n_y = Y_max/h
n_z = Z_max/h


*GET, elm_max, ELEM,0,NUM,MAX
*GET, elm_min, ELEM,0,NUM,MIN

*DIM,ELEMENT,arr4,n_x+1,n_y+1,n_z+1,1000

*DO, N,elm_min,elm_max

   X = CENTRX(N)
   Y = CENTRY(N)
   Z = CENTRZ(N)

   *IF, X,ge,0,AND,Y,ge,0,THEN

      i_x = NINT(X/h)+1
      i_Y = NINT(Y/h)+1
      i_Z = NINT(Z/h)+1

      *IF, ELEMENT(i_x,i_y,i_z,1),LT,1,THEN
         ELEMENT(i_x,i_y,i_z,1)=0
      *ENDIF

      ELEMENT(i_x,i_y,i_z,1)= ELEMENT(i_x,i_y,i_z,1)+1
      i=ELEMENT(i_x,i_y,i_z,1)
      ELEMENT(i_x,i_y,i_z,i+1)=N
   *ENDIF
```

```
*ENDDO


*DO, g,1,NUM

   X0=100-g*3-1 + 30*NINT((g-4.5)/10)
   Y0=150
   Z0=150 + 40*NINT((g-4.5)/10)

*DO, K,1,100

   i_x = NINT(X0/h)+1
   i_Y = NINT(Y0/h)+1
   i_Z = NINT(Z0/h)+1

   i_min_x = i_x-1
   i_max_x = i_x+1

   *IF, i_min_x, lt, 1, THEN
      i_min_x=1
   *ENDIF

   *IF, i_max_x, gt, n_x+1, THEN
      i_max_x=n_x+1
   *ENDIF

   i_min_y = i_y-1
   i_max_y = i_y+1

   *IF, i_min_y, lt, 1, THEN
      i_min_y=1
   *ENDIF

   *IF, i_max_y, gt, n_y+1, THEN
      i_max_y=n_y+1
   *ENDIF

   i_min_z = i_z-1
   i_max_z = i_z+1

   *IF, i_min_z, lt, 1, THEN
      i_min_z=1
   *ENDIF

   *IF, i_max_z, gt, n_z+1, THEN
      i_max_z=n_z+1
   *ENDIF

   N0=1


   *DO, i, i_min_x,i_max_x
   *DO, j, i_min_y,i_max_y
   *DO, t, i_min_z,i_max_z
      p_max=ELEMENT(i,j,t,1)
```

```
      *DO, p, 2, p_max
        Cx=CENTRX(ELEMENT(i,j,t,p))
        Cy=CENTRY(ELEMENT(i,j,t,p))
        Cz=CENTRZ(ELEMENT(i,j,t,p))

        Cnx=CENTRX(N0)
        Cny=CENTRY(N0)
        Cnz=CENTRZ(N0)

        *IF,(Cx-X0)*(Cx-X0)+(Cy-Y0)*(Cy-Y0)+(Cz-Z0)*(Cz-Z0), le,(Cnx-X0)*(Cnx-X0)+(Cny-Y0)*(Cny-Y0)+(Cnz-
Z0)*(Cnz-Z0),THEN
          N0=ELEMENT(i,j,t,p)
        *ENDIF
      *ENDDO

    *ENDDO
    *ENDDO
    *ENDDO

    ELEM_N(K,g)=N0

    *GET, Jx, ELEM, N0, JS, X
    *GET, Jy, ELEM, N0, JS, Y
    *GET, Jz, ELEM, N0, JS, Z


    J=sqrt(Jx*Jx+Jy*Jy+Jz*Jz)

    *IF, J, ne,0, THEN
      Jx=3*Jx/J
      Jy=3*Jy/J
      Jz=3*Jz/J
    *ELSE
      Jx=0
      Jy=0
      Jz=0
    *ENDIF


    X0=NINT(CENTRX(N0)+Jx)
    Y0=NINT(CENTRY(N0)+Jy)
    Z0=NINT(CENTRZ(N0)+Jz)

*ENDDO

*ENDDO

ESEL,NONE

*DO, g,1,NUM
*DO, k,1,100
  ESEL,A,ELEM,,ELEM_N(k,g)
*ENDDO
*ENDDO
```